National Library of Canada
Bibliothèque nationale du Canada

Canadian Theses Service
Service des thèses canadiennes

Ottawa, Canada
K1A 0N4

NOTICE

The quality of this microform is heavily dependent upon the quality of the original thesis submitted for microfilming. Every effort has been made to ensure the highest quality of reproduction possible.

If pages are missing, contact the university which granted the degree.

Some pages may have indistinct print especially if the original pages were typed with a poor typewriter ribbon or if the university sent us an inferior photocopy.

Reproduction in full or in part of this microform is governed by the Canadian Copyright Act, R.S.C. 1970, c. C-30, and subsequent amendments.

AVIS

La qualité de cette microforme dépend grandement de la qualité de la thèse soumise au microfilmage. Nous avons tout fait pour assurer une qualité supérieure de reproduction.

S'il manque des pages, veuillez communiquer avec l'université qui a conféré le grade.

La qualité d'impression de certaines pages peut laisser à désirer, surtout si les pages originales ont été dactylographiées à l'aide d'un ruban usé ou si l'université nous a fait parvenir une photocopie de qualité inférieure.

La reproduction, même partielle, de cette microforme est soumise à la Loi canadienne sur le droit d'auteur, SRC 1970, c. C-30, et ses amendements subséquents.

NL-339 (r. 88/04) c

Canada

National Library of Canada
Bibliothèque nationale du Canada

Canadian Theses Service
Service des thèses canadiennes

Ottawa, Canada
K1A 0N4

The author has granted an irrevocable non-exclusive licence allowing the National Library of Canada to reproduce, loan, distribute or sell copies of his/her thesis by any means and in any form or format, making this thesis available to interested persons.

The author retains ownership of the copyright in his/her thesis. Neither the thesis nor substantial extracts from it may be printed or otherwise reproduced without his/her permission.

L'auteur a accordé une licence irrévocable et non exclusive permettant à la Bibliothèque nationale du Canada de reproduire, prêter, distribuer ou vendre des copies de sa thèse de quelque manière et sous quelque forme que ce soit pour mettre des exemplaires de cette thèse à la disposition des personnes intéressées.

L'auteur conserve la propriété du droit d'auteur qui protège sa thèse. Ni la thèse ni des extraits substantiels de celle-ci ne doivent être imprimés ou autrement reproduits sans son autorisation.

ISBN 0-315-55457-6

Canada

THE UNIVERSITY OF ALBERTA

THE DESIGN AND FABRICATION OF OPTIMIZED MISSING TISSUE COMPENSATORS

by

DONALD MURRAY ROBINSON (C)

A THESIS

SUBMITTED TO THE FACULTY OF GRADUATE STUDIES AND RESEARCH

IN PARTIAL FULFILMENT OF THE REQUIREMENTS OF THE DEGREE

OF DOCTOR OF PHILOSOPHY

IN

MEDICAL PHYSICS

DEPARTMENT OF PHYSICS

EDMONTON, ALBERTA

FALL, 1989

THE UNIVERSITY OF ALBERTA

RELEASE FORM

Name of Author: DONALD M. ROBINSON

Title of Thesis: THE DESIGN AND FABRICATION OF OPTIMIZED MISSING TISSUE COMPENSATORS

Degree: DOCTOR OF PHILOSOPHY

Year this Degree Granted: 1989

Permission is hereby granted to THE UNIVERSITY OF ALBERTA LIBRARY to reproduce single copies of this thesis and to lend or sell such copies for private, scholarly, or scientific research purposes only.

The author reserves other publication rights, and neither the thesis nor extensive extracts from in may be printed or otherwise reproduced without the author's written permission.

Don Robinson

10839 - 66 Avenue

Edmonton, Alberta, T6H 1Y1

Date: July 15, 1989

THE UNIVERSITY OF ALBERTA

FACULTY OF GRADUATE STUDIES AND RESEARCH

The undersigned certify that they have read, and recommend to the Faculty of Graduate Studies and Research, for acceptance, a thesis entitled

The Design and Fabrication of

Optimized Missing Tissue Compensators

submitted by Donald Murray Robinson in partial fulfilment of the degree of Doctor of Philosophy in Physics

.....
Supervisor

.....

.....

.....

.....

.....
External Examiner

Date June 22, 1989

This work is dedicated to my father
in loving memory

Abstract

The introduction of an attenuating medium into a photon beam serves both to reduce the intensity of the primary beam and to create secondary radiation due to scatter. When retracted missing tissue compensators are employed to compensate for irregular surface contour or internal inhomogeneities, they are often fabricated without regard to the scattered radiation that they introduce into the system. Experimental evaluation of a retracted compensator designed for use with an anthropomorphic phantom reveals an inability to provide true compensation.

The study of a mathematically describable conical geometry has clearly demonstrated the need for improved compensator design. Experimental results obtained with this geometry can be reproduced with good agreement, by theoretical calculations based on primary and first order scattered radiation. This method of analysis may be extended to predict the shape of a compensator which will produce an optimized dose distribution at a given depth in a phantom. An optimized compensator was constructed based on these theoretical considerations and excellent agreement was observed between theory and experiment. Dramatic improvement in restoration of bolus dose is obtained with this optimized compensator.

Finally, an anthropomorphic phantom of the neck region has been constructed and the performance of a compensator designed according to current clinical methods for this geometry has been evaluated. The performance of an optimized compensator specific to this geometry is presented and good agreement between theoretical predictions and

experimental results(data) is observed. Dramatic improvement in bolus dose restoration over that obtained with the clinically designed compensator is realized.

Acknowledgements

I would like to express my sincere gratitude to the following people who made this work possible:

My mother and father for their encouragement and support.

My supervisor, Dr. J. W. Scrimger, for his guidance, encouragement, and patience.

Dr. J.J. Battista for his enthusiasm and many stimulating blackboard sessions.

Colin Field for saving my life more than once in the land of vax.

Ernest Mah and Claire McCartney for their invaluable assistance in navigating the mysteries of vax and also keeping me sane.

Finn Mortensen for the experimental apparatus and phantoms which he patiently produced for me.

John Isitt for his enthusiastic help and instruction in the mold room.

Wayne Logus and Brent Long for their assistance with many of the technical aspects of this work.

Sig Laban, Don Burdeniuk, and Len Johnson for their assistance and instruction with many aspects of the theory and operation of the accelerators.

Ken and Sue Light and Dylan and Bev Coe for their friendship and encouragement for which words are insufficient to express my gratitude.

Dawn for late night coffee and a helping hand when it was most needed.

The financial support of the Alberta Heritage Foundation for Medical Research and the Alberta Cancer Board and the Department of Physics at the University of Alberta is gratefully acknowledged.

TABLE OF CONTENTS

CHAPTER PAGE

I Introduction 1

1.1 Rationale and Introduction to the study 2

1.2 Interaction of Radiation with Matter 5

1.2.1 Photon Interactions 5

1.2.2 Electron Interactions 21

1.3 Radiation Sources 28

1.3.1 Cobalt-60 28

1.3.2 Medical Linear Accelerators 30

1.4 Dosimetry 34

1.4.1 Basic Concepts 34

1.4.2 Ionization Based Dosimetry 36

1.4.2.1 Standard Air Chamber 36

1.4.2.2 Practical Ion Chambers 39

1.4.3 Solid State Detectors 40

1.4.4 Thermoluminescent Dosimetry 41

1.5 General Introduction and Review of Previous Work on Compensators 42

II Experimental Results with Conical Compensators 60

2.1 Experimental Parameters 61

2.1.2 Radiation Sources 67

2.1.2.1 Cobalt-60 67

2.1.2.2 6MV 68

2.1.2.3 15MV 68

2.1.3 Dosimetry Devices 69

2.2 Experimental Results 77
2.3 Analysis and Discussion of Results 77
III Theoretical Analysis 102
3.1 Rationale and Introduction 103
3.2 The Analytical Model 104
3.3 Analytic Results 115
3.4 Analysis and Discussion of Results 138
IV Optimized Compensators 157
4.1 Theoretical Considerations 158
4.2 Results and Analysis 161
V An Anthropomorphic Geometry 176
5.1 Experimental Parameters 177
5.2 Experimental Results 182
5.3 Optimized Compensation 194
VI Conclusions 203
References 205

List of Tables

Table 1.1	Photon interactions with matter	6
Table 2.1	Important physical characteristics of the semiconductor detector	72
Table 2.2	Maximum departure from bolus dose in the conical geometry. Comparison between that predicted on the basis of replacement of missing primary attenuation only and that observed experimentally	100
Table 3.1	Interaction cross sections for the materials water, polystyrene, aluminum, and lead at photon energy of 1.25MeV	109
Table 3.2	Interaction cross sections for the materials water, polystyrene, aluminum, and lead at photon energy 5.0MeV	110
Table 5.1	Mean deviation (percentage) from bolus dose in the uncompensated and compensated configurations	195

LIST OF FIGURES

Figure		page
1.01	Coherent (or Rayleigh) scattering	8
1.02	The photoelectric effect	9
1.03	Photoelectric cross sections for water and lead	11
1.04	Compton scattering	12
1.05	The angular distribution of compton scattered photons	15
1.06	The angular distribution of compton recoil electrons	16
1.07	The effect of binding energy on the Klein-Nishina cross sections for 300keV photons in lead	18
1.08	The relative importance of photon interactions	20
1.09	Photon interaction cross sections for water	22
1.10	Photon interaction cross sections for lead	23
1.11	The decay scheme of Cobalt-60	29
1.12	The major components of a linear accelerator	31
1.13	The principle components of a treatment head	33
1.14	Schematic representation of a Standard air chamber	37
1.15	The effect of bolus on isodose curves. (a) Isodose curves without bolus. (b) Isodise curves with bolus on the phantom surface	44
1.16	An X-ray beam incident normal to the surface of a homogeneous phantom	45
1.17	A plot of dose as a function of depth for the geometry of Figure 1.16	47

1.18 Anterior view of the anthropomorphic phantom 54
1.19 Cross-sectional view of the anthropomorphic phantom 55
1.20 Measurements at layer #4 located 8.5cm below 100cm SSD 56
1.21 Measurements at layer #7 located 14cm below 100cm SSD 57
2.01 The conical geometry showing its main components 62
2.02 Diagramatic representation of the conical geometry 63
2.03 Design of the p-type right angle silicon detector 70
2.04 Energy response of the right angle semiconductor detector 73
2.05 Diode response versus ion chamber response at low photon energies (measured) 74
2.06 Diode response versus ion chamber response across the field at Cobalt-60 at 17cm depth (measured) 76
2.07 Uncompensated dose as a % of bolus dose at 9cm depth (measured) (a) Cobalt-60, (b) 6MV, (c) 15MV..... 78
2.08 Compensated dose as a % of bolus dose for geometric cone at 9cm depth (measured) (a) Cobalt-60, (b) 6MV, (c) 15MV 79
2.09 Compensated dose as a % of bolus dose for aluminum cone at 9cm depth (measured) (a) Cobalt-60, (b) 6MV, (c) 15MV 80
2.10 Compensated dose as a % of bolus dose for lead cone at 9cm depth (measured) (a) Cobalt-60, (b) 6MV, (c) 15MV 81
2.11 Uncompensated dose as a % of bolus dose at 12cm depth (measured) (a) Cobalt-60, (b) 6MV, (c) 15MV 82
2.12 Compensated dose as a % of bolus dose for geometric cone at 12cm depth (measured) (a) Cobalt-60, (b) 6MV, (c) 15MV 83
2.13 Compensated dose as a % of bolus dose for aluminum cone at 12cm depth (measured) ((a) Cobalt-60, (b) 6MV, (c) 15MV 84

2.14 Compensated dose as a % of bolus dose for lead cone at 12cm depth (measured) (a) Cobalt-60, (b) 6MV, (c) 15MV 85
2.15 Uncompensated dose as a % of bolus dose at 15cm depth (measured) (a) Cobalt-60, (b) 6MV, (c) 15MV 86
2.16 Compensated dose as a % of bolus dose for geometric cone at 15cm depth (measured) (a) Cobalt-60, (b) 6MV, (c) 15MV 87
2.17 Compensated dose as a % of bolus dose for aluminum cone at 15cm depth (measured) ((a) Cobalt-60, (b) 6MV, (c) 15MV 88
2.18 Compensated dose as a % of bolus dose for lead cone at 15cm depth (measured) (a) Cobalt-60, (b) 6MV, (c) 15MV 89
2.19 Uncompensated dose as a % of bolus dose at 17cm depth (measured) (a) Cobalt-60, (b) 6MV, (c) 15MV 90
2.20 Compensated dose as a % of bolus dose for geometric cone at 17cm depth (measured) (a) Cobalt-60, (b) 6MV, (c) 15MV 91
2.21 Compensated dose as a % of bolus dose for aluminum cone at 17cm depth (measured) ((a) Cobalt-60, (b) 6MV, (c) 15MV 92
2.22 Compensated dose as a % of bolus dose for lead cone at 17cm depth (measured) (a) Cobalt-60, (b) 6MV, (c) 15MV 93
2.23 Uncompensated dose as a % of bolus dose at 21cm depth (measured) (a) Cobalt-60, (b) 6MV, (c) 15MV 94
2.24 Compensated dose as a % of bolus dose for geometric cone at 21cm depth (measured) (a) Cobalt-60, (b) 6MV, (c) 15MV 95
2.25 Compensated dose as a % of bolus dose for aluminum cone at 21cm depth (measured) ((a) Cobalt-60, (b) 6MV, (c) 15MV 96
2.26 Compensated dose as a % of bolus dose for lead cone at 21cm depth (measured) (a) Cobalt-60, (b) 6MV, (c) 15MV 97
3.01 Geometry for theoretical analysis 105

3.02 Compensated dose as a % of bolus dose for the geometric cone at 9cm depth (comparison between measurement and calculation) (a) Cobalt-60, (b) 6MV, (c) 15MV 118

3.03 Compensated dose as a % of bolus dose for the aluminum cone at 9cm depth (comparison between measurement and calculation) (a) Cobalt-60, (b) 6MV, (c) 15MV 119

3.04 Compensated dose as a % of bolus dose for the lead cone at 9cm depth (comparison between measurement and calculation) (a) Cobalt-60, (b) 6MV, (c) 15MV 120

3.05 Compensated dose as a % of bolus dose for the 7cm cone at 9cm depth (comparison between measurement and calculation) (a) Cobalt-60, (b) 6MV, (c) 15MV 121

3.06 Compensated dose as a % of bolus dose for the geometric cone at 12cm depth (comparison between measurement and calculation) (a) Cobalt-60, (b) 6MV, (c) 15MV 122

3.07 Compensated dose as a % of bolus dose for the aluminum cone at 12cm depth (comparison between measurement and calculation) (a) Cobalt-60, (b) 6MV, (c) 15MV 123

3.08 Compensated dose as a % of bolus dose for the lead cone at 12cm depth (comparison between measurement and calculation) (a) Cobalt-60, (b) 6MV, (c) 15MV 124

3.09 Compensated dose as a % of bolus dose for the 7cm cone at 12cm depth (comparison between measurement and calculation) (a) Cobalt-60, (b) 6MV, (c) 15MV 125

3.10 Compensated dose as a % of bolus dose for the geometric cone at 15cm depth (comparison between measurement and calculation) (a) Cobalt-60, (b) 6MV, (c) 15MV 126

3.11 Compensated dose as a % of bolus dose for the aluminum cone at 15cm depth (comparison between measurement and calculation) (a) Cobalt-60, (b) 6MV, (c) 15MV 127
3.12 Compensated dose as a % of bolus dose for the lead cone at 15cm depth (comparison between measurement and calculation) (a) Cobalt-60, (b) 6MV, (c) 15MV 128
3.13 Compensated dose as a % of bolus dose for the 7cm cone at 15cm depth (comparison between measurement and calculation) (a) Cobalt-60, (b) 6MV, (c) 15MV 129
3.14 Compensated dose as a % of bolus dose for the geometric cone at 17cm depth (comparison between measurement and calculation) (a) Cobalt-60, (b) 6MV, (c) 15MV 130
3.15 Compensated dose as a % of bolus dose for the aluminum cone at 17cm depth (comparison between measurement and calculation) (a) Cobalt-60, (b) 6MV, (c) 15MV 131
3.16 Compensated dose as a % of bolus dose for the lead cone at 17cm depth (comparison between measurement and calculation) (a) Cobalt-60, (b) 6MV, (c) 15MV 132
3.17 Compensated dose as a % of bolus dose for the 7cm cone at 17cm depth (comparison between measurement and calculation) (a) Cobalt-60, (b) 6MV, (c) 15MV 133
3.18 Compensated dose as a % of bolus dose for the geometric cone at 21cm depth (comparison between measurement and calculation) (a) Cobalt-60, (b) 6MV, (c) 15MV 134
3.19 Compensated dose as a % of bolus dose for the aluminum cone at 21cm depth (comparison between measurement and calculation) (a) Cobalt-60, (b) 6MV, (c) 15MV 135

3.20 Compensated dose as a % of bolus dose for the lead cone at 21cm depth (comparison between measurement and calculation) (a) Cobalt-60, (b) 6MV, (c) 15MV 136
3.21 Compensated dose as a % of bolus dose for the 7cm cone at 21cm depth (comparison between measurement and calculation) (a) Cobalt-60, (b) 6MV, (c) 15MV 137
3.22 Spectral distribution of the 6MV photon beam 145
3.23 Spectral distribution of the 15MV photon beam 146
3.24 Compensated dose as a % of bolus dose for the lead cone at 9cm depth (comparison between measurement and calculation with spectrum (a) Cobalt-60, (b) 6MV, (c) 15MV 147
3.25 Compensated dose as a % of bolus dose for the lead cone at 12cm depth (comparison between measurement and calculation with spectrum (a) Cobalt-60, (b) 6MV, (c) 15MV 148
3.26 Compensated dose as a % of bolus dose for the lead cone at 15cm depth (comparison between measurement and calculation with spectrum (a) Cobalt-60, (b) 6MV, (c) 15MV 149
3.27 Compensated dose as a % of bolus dose for the lead cone at 17cm depth (comparison between measurement and calculation with spectrum (a) Cobalt-60, (b) 6MV, (c) 15MV 150
3.28 Compensated dose as a % of bolus dose for the lead cone at 12cm depth (comparison between measurement and calculation with spectrum (a) Cobalt-60, (b) 6MV, (c) 15MV 151

4.01 Compensation with (a) a geometric compensator, (b) an optimized compensator 159
4.02 Compensated dose as a % of bolus dose for the optimized

compensator at 17cm depth with Cobalt-60 photons
(comparison between measurement and calculation) 162

4.03 Compensated dose as a % of bolus dosecomparing
geometric and optimized compensators at 17cm depth
with Cobalt-60 photons 163

4.04 Compensated dose as a % of bolus dose comparing
the geometric compensator and the 1226 cone at 9cm
depth with Cobalt-60 photons (measured) 165

4.05 Compensated dose as a % of bolus dose comparing
the geometric compensator and the 1226 cone at
12cm depth with Cobalt-60 photons (measured) 166

4.06 Compensated dose as a % of bolus dose comparing
the geometric compensator and the 1226 cone at
15cm depth with Cobalt-60 photons (measured) 167

4.07 Compensated dose as a % of bolus dose comparing
the geometric compensator and the 1226 cone at
21cm depth with Cobalt-60 photons (measured) 168

4.08 Compensated dose as a % of bolus dose for the 1226
cone at 9cm depth (comparison between measurement
and calculation) (a) 6MV, (b) 15MV 169

4.09 Compensated dose as a % of bolus dose for the 1226
cone at 12cm depth (comparison between measurement
and calculation) (a) 6MV, (b) 15MV 170

4.10 Compensated dose as a % of bolus dose for the 1226
cone at 15cm depth (comparison between measurement
and calculation) (a) 6MV, (b) 15MV 171

4.11 Compensated dose as a % of bolus dose for the 1226 cone at 17cm depth (comparison between measurement and calculation) (a) 6MV, (b) 15MV 172
4.12 Compensated dose as a % of bolus dose for the 1226 cone at 21cm depth (comparison between measurement and calculation) (a) 6MV, (b) 15MV 173
5.01 The anthropomorphic phantom - side view 178
5.02 The anthropomorphic phantom - anterior view 179
5.03 The anthropomorphic phantom with bolus 180
5.04 Location of measurement points at each layer in the anthropomorphic phantom 181
5.05 Cross sectional view of the anthropomorphic phantom showing the depths of each measurement layer 183
5.06 Percentage of bolus dose along the X-axis at layer #1 (a) Uncompensated, (b) Compensated 184
5.07 Percentage of bolus dose along the Y-axis at layer #1 (a) Uncompensated, (b) Compensated 185
5.08 Percentage of bolus dose along the X-axis at layer #2 (a) Uncompensated, (b) Compensated 186
5.09 Percentage of bolus dose along the Y-axis at layer #2 (a) Uncompensated, (b) Compensated 187
5.10 Percentage of bolus dose along the X-axis at layer #3 (a) Uncompensated, (b) Compensated 188
5.11 Percentage of bolus dose along the Y-axis at layer #3 (a) Uncompensated, (b) Compensated 189
5.12 Percentage of bolus dose along the X-axis at layer #4 (a) Uncompensated, (b) Compensated 190

5.13 Percentage of bolus dose along the Y-axis at layer #4 (a) Uncompensated, (b) Compensated 191
5.14 Percentage of bolus dose along the X-axis at layer #5 (a) Uncompensated, (b) Compensated 192
5.15 Percentage of bolus dose along the Y-axis at layer #5 (a) Uncompensated, (b) Compensated 193
5.16 Thickness profiles of the geometric and optimized compensators along the Y-axis at X = 0.0mm 197
5.17 Percentage of bolus dose at layer #1 with the optimized compensator (comparison between measurement and calculation) (a) along the X-axis, (b) along the Y-axis 198
5.18 Percentage of bolus dose at layer #2 with the optimized compensator (comparison between measurement and calculation) (a) along the X-axis, (b) along the Y-axis 199
5.19 Percentage of bolus dose at layer #3 with the optimized compensator (comparison between measurement and calculation) (a) along the X-axis, (b) along the Y-axis 200
5.20 Percentage of bolus dose at layer #4 with the optimized compensator (comparison between measurement and calculation) (a) along the X-axis, (b) along the Y-axis 201
5.21 Percentage of bolus dose at layer #5 with the optimized compensator (comparison between measurement and calculation) (a) along the X-axis, (b) along the Y-axis 202

Chapter 1

Introduction

Anyone who has been seriously engaged in scientific work of any kind realizes that over the entrance to the gates of the temple of science are written the words: Ye must have faith. It is a quality which the scientist cannot dispense with.

Max Plank

I INTRODUCTION

1.1 Rationale and Introduction to the Study

Radiotherapy stands as one of the three major modalities employed in cancer treatment today. The other forms of treatment are surgery and chemotherapy. Of those patients presently surviving five or more years after treatment for cancer, 65% survive due mainly to surgical treatment, 25% mainly due to radiation treatment, 9% are mainly due to the slow growth of their tumors, and 1% are mainly due to chemotherapy. There are also many cases when optimal treatment is achieved with a combination of two and sometimes all three of these modalities.

The successful treatment of cancer with radiation involves an attempt to achieve the highest probability of cure while at the same time realizing the lowest probability of radiation-induced complications. It is always preferable therefore, in radiotherapy involving the application of external beams, to arrange the radiation beams in such a manner as to deliver a high dose to the tumor site while at the same time delivering as low a dose to surrounding healthy tissue. It has been well documented that the high degree of tumor control desired "can only be achieved with a very high accuracy in dose delivery"[1.1]. Clinical experience has shown that as little a difference as 10% lies between a dose that will do significant damage to a tumor without damaging the surrounding healthy tissue and one that will[1.2]. The ICRU (International Commission on Radiation Units and Measurements) further concludes that "the available evidence for certain types of tumors points to

the need for an accuracy of ±5% in the delivery of an absorbed dose to a target volume if the eradication of the primary tumor is sought"[1.3].

It is therefore necessary to determine, as accurately as possible, the dose which will be delivered to various regions of the body. In order to achieve the highest degree of tumor control the dose received across the tumor volume should be uniform so as not to underdose any malignant tissue. The uniformity of the beam within the patient can be altered by a number of factors including the patient's external surface contour. In the case of highly irregular surface areas, most notably the head and neck regions, the distortion of the beam can be most acute.

One method of compensating for an irregular surface contour is to fill in the "missing tissue" with a unit density(tissue equivalent) material, called bolus. This simple procedure eliminates any distortion of the beam due to surface contour, by presenting the incident beam with a flat surface. This solution has one major drawback, which is the loss of skin sparing. Skin sparing, which is a distinct advantage of the use of high energy photon beams, is lost due to the relocation of the build up region of the beam above the patient's skin rather than below it as is the case with open field treatment. Retraction of the bolus, or tissue compensating material, away from the patient surface results in partial restoration of this desired skin sparing effect. In general, the greater the distance of retraction, the greater the degree of restoration of skin sparing. Such retracted missing tissue compensators find common use in many centers and may be constructed of near unit density materials, such as wax, or of materials of higher density, such as lead(with corresponding geometric reduction).

The retraction process not only reduces skin dose, as mentioned above, but it also alters the dose at any given depth within the body. The dose alteration is manifest as a dose reduction in comparison to that delivered under identical conditions with bolus and also the introduction of a dose nonuniformity not present with bolus. Both the dose reduction and dose nonuniformity introduced by the retraction process is due mainly to alterations in primary and first order scatter dose.

In this work both the reduction in dose and nonuniformity in dose introduced by the retraction process are investigated. These effects are modeled theoretically and the theoretical machinery thus developed is used to predict the shape of an optimized compensator which will eliminate these two effects, thus accurately reproducing the bolus dose distribution.

This study is organized into both experimental and theoretical sections. Initially the reduction and nonuniformity in dose accompanying the use of a number of retracted missing tissue compensators is examined experimentally. A theoretical model based on primary and first order scattered radiation is then developed to model the experimental arrangements examined. Finally, the theoretical model is used to determine the shape of an optimized compensator and the optimized compensator thus constructed is examined experimentally. Introductory material, necessary for completeness, is reviewed in Chapter 1.

1.2 Interaction of Radiation with Matter

1.2.1 Photon Interactions

Photons may interact with matter in a variety of ways. These interactions may be classified according to the particle with which the photon interacts and the type of interaction which takes place. These interactions are presented in Table 1.1 according to this classification. This table is adapted from Hubble[1.4]. Of these, only coherent scattering, the photoelectric effect, compton scattering, and pair and triplet production are of importance in the energy range employed in this work. The importance of the other interaction mechanisms listed in this energy range(0-15MV) is negligible. Of these other mechanisms, only the photonuclear reactions (γ,n) and (γ,p) for which the cross scetion $\sigma_{\gamma n} \alpha Z$ need mention. These consist of the absorption of an incident photon by a nucleus and the subsequent emission of a neutron or proton by the nucleus. This process is characterized by a broad peak(or "giant resonance") in its cross section centered about 24MeV for low Z nuclei and decreasing to about 12MeV for high Z nuclei. For lead, which was used in this work, the threshold energy for (γ,n) and (γ,p) are 7.4MeV and 8.0MeV respectively and the cross section peak occurs at 13.6MeV with peak width at half maximum of 3.8MeV. The value of $\sigma_{\gamma n}$ at this peak is 0.5b(0.5×10^{-24} cm^2) and as such constitutes only about 2.7% of the total attenuation cross section of lead at this energy. This photon energy occurs only as one component of the 15MV spectrum of photon energies ranging from about 0 to 15MeV with a mean energy of about 5MeV and hence the contribution to the total cross section due to this interaction may be safely ignored. The total attenuation cross section is the sum of all cross sections contributing at this

Interaction with	Type of Interaction		
	Absorption	Elastic (coherent)	Inelastic (incoherent)
Atomic electrons	Photoelectric effect	Rayleigh scattering	Compton scattering
Nucleons	Photonuclear reactions	Elastic nuclear scattering	Nuclear resonance scattering
Electric field of charged particles	Pair and Triplet production	Delbruck scattering	
Mesons	Photomeson production		

Table 1.1 Photon interactions with matter.

energy. The contributions to photon attenuation resulting from the other processes in Table 1.1 are either zero or negligible for the energies considered here(0-15MeV).

The process of coherent(or Rayleigh) scattering is depicted in Figure 1.01. Here an X-ray is incident upon an atom but does not result in the excitation or ionization of the atom. The photon is scattered by the bound electrons of the atom and the scattered photon exits without a loss of energy. The differential cross section for coherent scattering is given by

$$\frac{\partial\sigma}{\partial\Omega_{COH}} = \frac{r_o^2}{2}(1 + \cos^2(\theta))[F(q,Z)]^2 \qquad \{1.1\}$$

where $r_o = 2.81794X10^{-15}$ m(the classical electron radius) and F(q,Z) is the atomic form factor. The square of this atomic form factor gives the probability that the Z electrons of the interacting atom will receive a recoil momentum q without the absorption of energy. This process occurs mainly for low energy photons interacting with high Z atoms and the resulting scattered photons are strongly forward peaked. Thus coherent scattering serves to diverge the incident X-ray beam.

When a photon undergoes a photoelectric interaction with an atom, as shown in Figure 1.02, the photon is completely absorbed by the atom and its energy is imparted to one of the atom's bound electrons. This electron is thus ejected from the atom with an energy

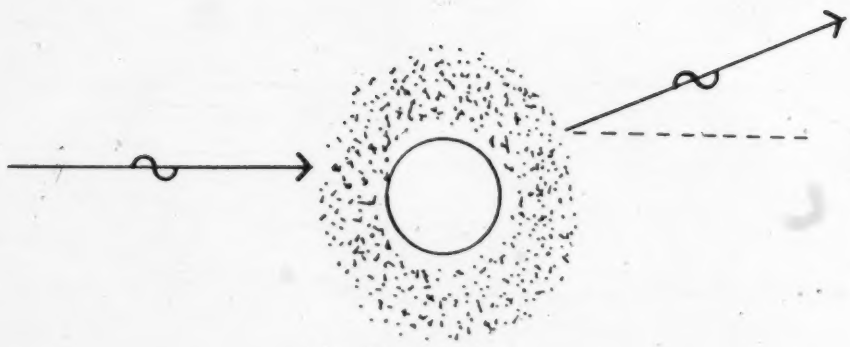

Figure 1.01 Coherent (or Rayleigh) scattering in which an incident photon is scattered without a change in energy.

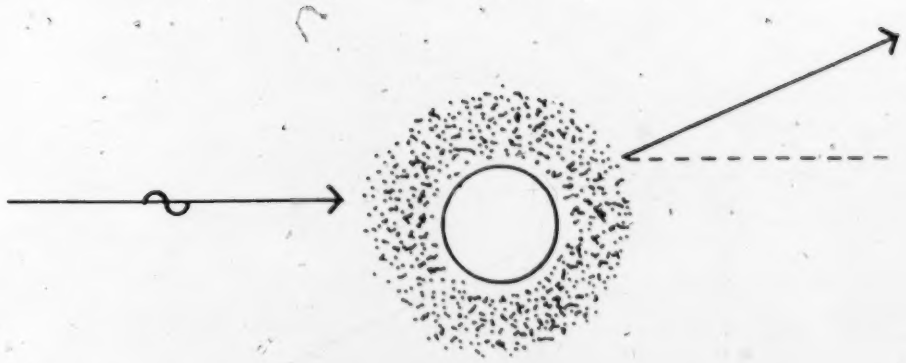

Figure 1:02 The photoelectric effect. An incident photon is absorbed by an atom resulting in the ejection of a bound electron.

$$E = h\nu - E_B \qquad \{1.2\}$$

where hν is the energy of the incident photon and E_B is the binding energy of the electron in the atom. The excited atom thus created returns to ground state via emission of fluorescent radiation and Auger electrons. Thus a photoelectric interaction can only occur if the energy of the incident photon(hν) is greater than the binding energy of the electron to be ejected. The photoelectric cross section, τ , is a decreasing function of incident photon energy with discontinuities existing at the binding energies of different electron shells as shown in Figure 1.03 [1.5]. The photoelectric cross section is also an increasing function of binding energy with approximately 80% of photoelectric interactions involving the k-shell electrons. The atomic photoelectric cross section varies approximately as

$$\tau_a \propto \frac{Z^4}{(h\nu)^3} \qquad \{1.3\}$$

for low energies, and

$$\tau_a \propto \frac{Z^5}{h\nu} \qquad \{1.4\}$$

for high energies.

Compton scattering is an inelastic interaction between an incident photon and what is considered to be a loosely bound(ie: virtually free) electron at rest in which the incident photon imparts some of its energy to the electron, resulting in a scattered photon of reduced energy, and an electron set in motion with some finite energy, as shown in Figure 1.04. To a first

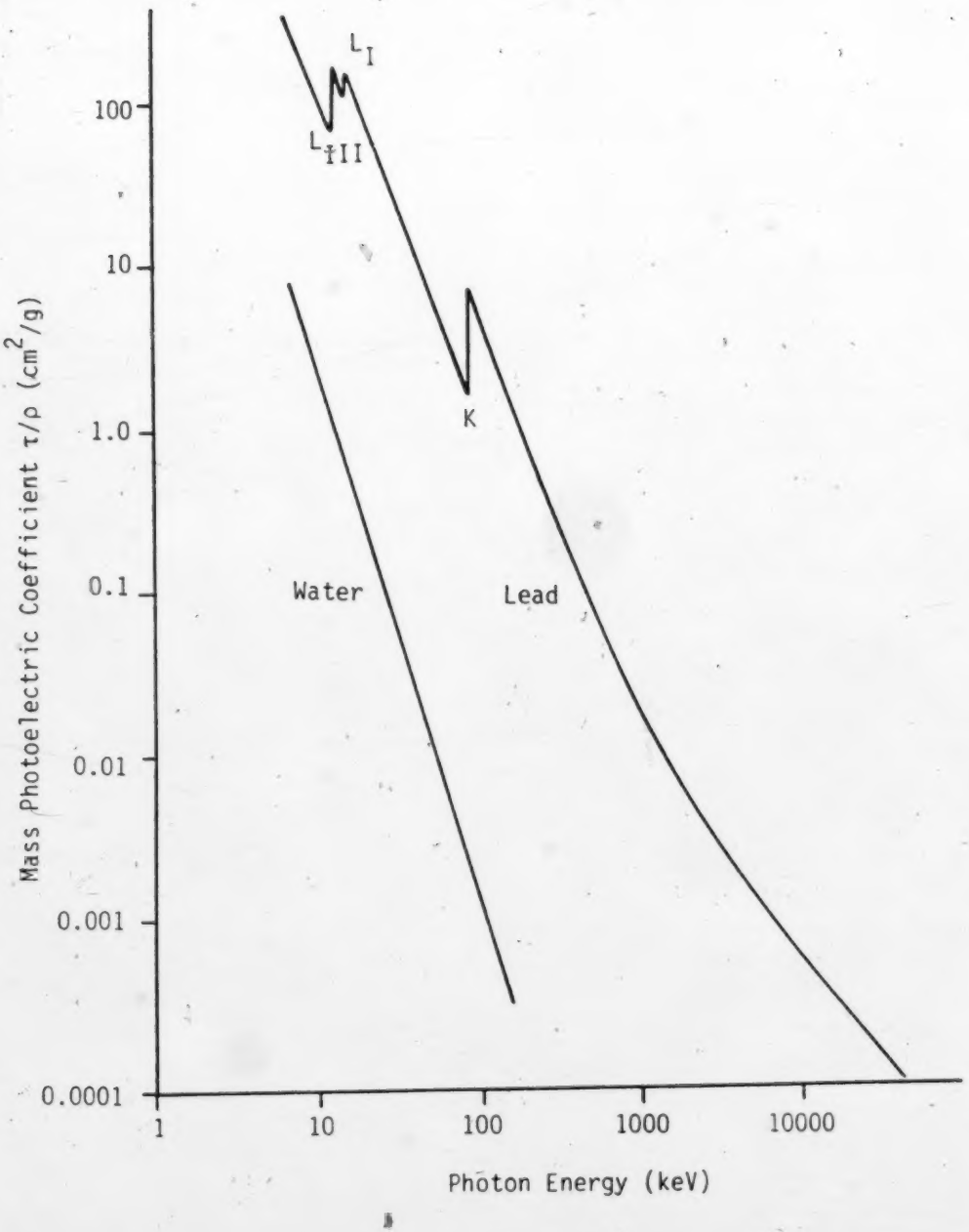

Figure 1.03 Photoelectric cross sections for water and lead showing the discontinuities at the binding energies of different electron shells.

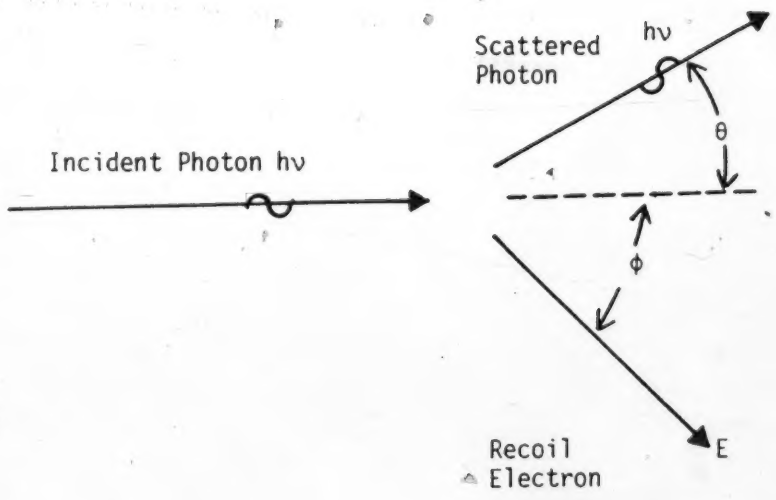

Figure 1.04 Compton scattering.

approximation the binding energy is taken to be negligible in comparison to the energy, hν, of the incident photon and the interaction is treated as being elastic. Thus the incident photon, of energy hν, is scattered through an angle θ, with energy hν′, and a recoil electron is ejected at an angle ϕ, with energy E. Applying conservation of energy and momentum to this situation yields the following relations between angle and energy for the scattered photon and recoil electron.

$$h\nu' = h\nu\left(\frac{1}{1+\alpha(1-\cos\theta)}\right) \qquad \{1.5\}$$

$$E = h\nu\left[\frac{\alpha(1-\cos\theta)}{1+\alpha(1-\cos\theta)}\right] \qquad \{1.6\}$$

where

$$\alpha = \frac{h\nu}{m_\circ c^2}$$

$m_\circ$ = rest mass of electron

and

$$\cot\phi = (1+\alpha)\tan\left(\frac{\theta}{2}\right) \qquad \{1.7\}$$

Maximum energy transfer occurs when $\theta = 180^\circ$ and $\phi = 0^\circ$. This condition yields

$$E_{max} = h\nu\frac{2\alpha}{1+2\alpha} \qquad \{1.8\}$$

$$h\nu'_{min} = h\nu \frac{1}{1+2\alpha} \qquad \{1.9\}$$

The compton electron may be scattered at any angle from 0° to 180° and the differential cross section $\sigma_e(\theta)$ giving the probability of a photon being scattered at an angle θ into the solid angle $d\Omega$ per electron is given by the Klein-Nishina cross section formula [1.6]

$$\sigma_e(\theta) = \left(\frac{d\sigma}{d\Omega}\right)_\theta = \frac{e^4}{2m_e^2c^4}\left[\frac{1}{1+\alpha(1-\cos\theta)}\right]^2\left[1+\cos^2\theta+\frac{\alpha^2(1-\cos\theta)^2}{1+\alpha(1-\cos\theta)}\right]^2 \qquad \{1.10\}$$

The angular distribution of scattered photons and recoil electrons are illustrated in Figures 1.05 [1.7] and 1.06 [1.8] respectively.

For low incident photon energies the binding of the electron must be taken into account. The momentum, q, imparted to the electron in Figure 1.04 is

$$q^2 = \frac{(h\nu)^2}{c^2} + \frac{(h\nu')^2}{c^2} - \frac{2h\nu h\nu'}{c^2}\cos\theta \qquad \{1.11\}$$

and since binding effects will be important when small amounts of momentum are imparted to the electron, the approximation $h\nu - h\nu' \cong 0$ can be made, and {1.11} becomes

$$q^2 \cong \frac{2h\nu^2}{c^2}(1-\cos\theta)$$

or $\qquad \{1.12\}$

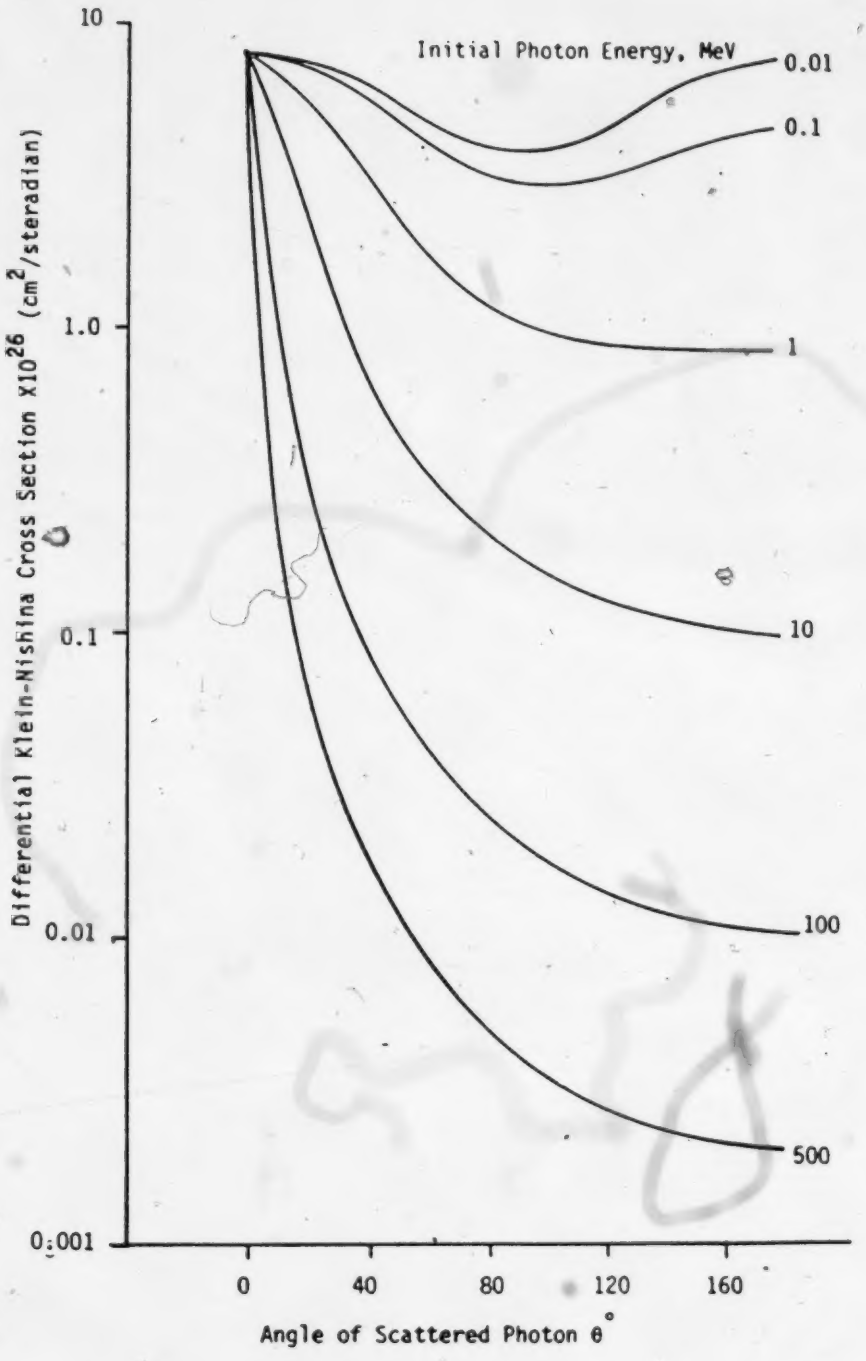

Figure 1.05 Angular distribution of compton scattered photons.

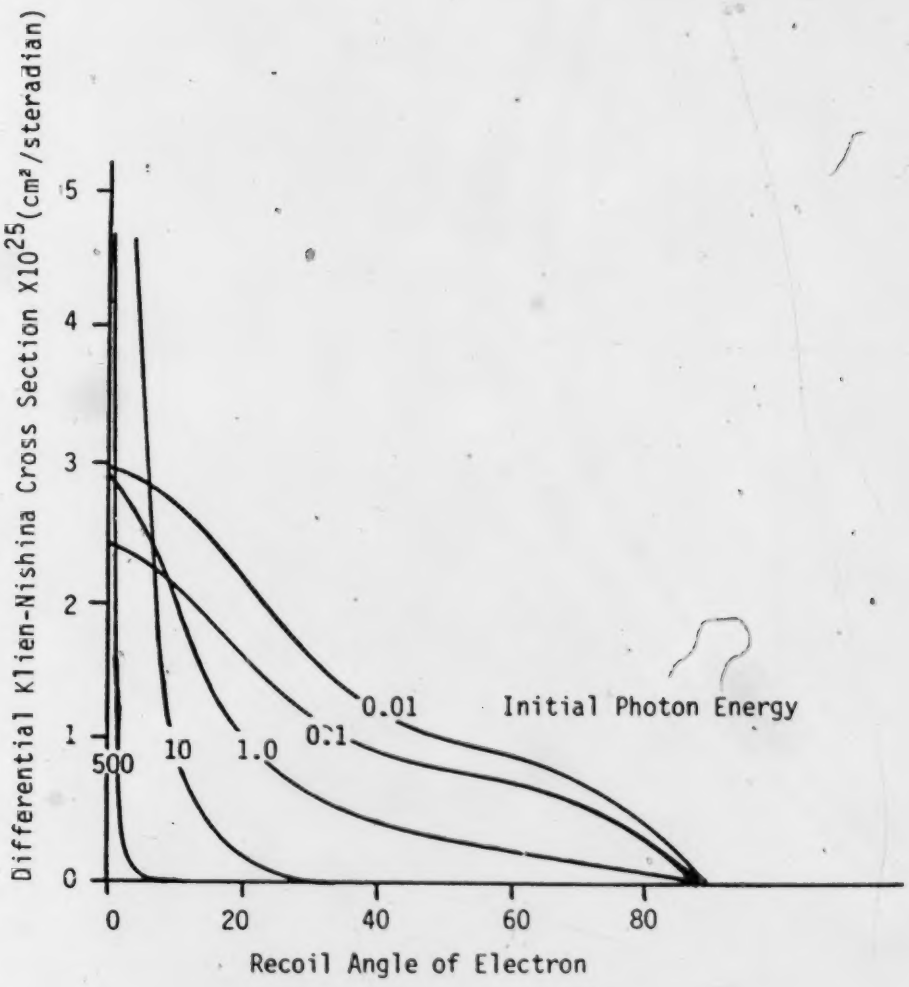

Figure 1.06 Angular distribution of compton recoil electrons.

$$q^2 \cong \frac{4(h\nu)^2}{c^2}\left[\frac{1}{2}(1-\cos\theta)\right]$$

and

$$q \cong \frac{2h\nu}{c}\sin\left(\frac{\theta}{2}\right) \qquad \{1.13\}$$

Using this approximation, Heisenberg and Bewilogua have generated a multiplicative correction factor, called the "incoherent scattering function" $S(h\nu,\theta,Z)$, for the Klein-Nishina differential cross section formula which takes into account the binding of the atomic electrons. This correction factor, $S(h\nu,\theta,Z)$, gives the probability "that any energy absorption whatsoever results when a photon of frequency ν is scattered through an angle θ and transfers a momentum $p \cong h\nu 2\sin(\theta/2)/c$ to the electrons of an atom with atomic number Z"[1.9]. Thus the modified Klein-Nishina cross section, called the incoherent scattering cross section, is given by

$$\left(\frac{d\sigma}{d\Omega}\right)_{\theta_{inc}} = S(h\nu,\theta,Z)\left(\frac{d\sigma}{d\Omega}\right)_{\theta} \qquad \{1.14\}$$

The main effect of this binding correction is to decrease the differential cross section at low incident photon energies as shown in Figure 1.07. Calculated compton energy and angular distributions along with the Klein-Nishina cross sections for incident photon energies from 10keV to 500MeV have been published in graphical form by Nelms in the NBS circular 542, 1953[1.10].

At energies greater than $2m_oc^2$, an incident photon may interact with a nucleus and be converted into an electron-positron pair. This process is referred to as pair production. The interaction of a photon with an electron to

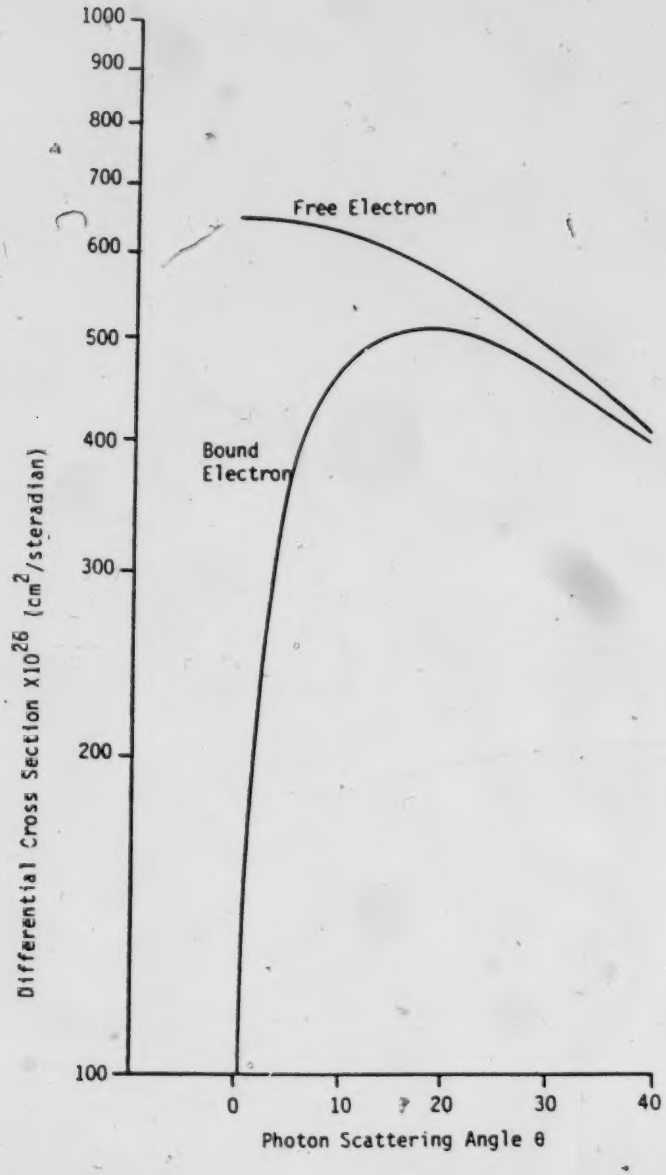

Figure 1.07 The effect of binding energy on the Klein-Nishina cross section for 300keV photons in lead.

produce an electron-positron pair is referred to as triplet production and has a threshold energy of $4m_oc^2$. The atomic cross section, π_a, for pair production is found to be roughly proportional to Z^2.

$$\pi_a \alpha Z^2 \qquad \{1.15\}$$

Values of pair and triplet production cross sections have been tabulated by Hubble in NSRDS-NBS 29[1.11].

At any given incident photon energy some or all of the above mentioned interaction processes may be taking place according to their relative probabilities. In the energy range of interest in this work(0-15MeV), all processes except coherent scattering, photoelectric effect, compton scattering, and pair and triplet production may be safely ignored. The total photon cross section at any given energy is the sum of the cross sections of each individual interaction taking place at that energy. Thus for the energy range employed in this work the total photon cross section, μ, may be expressed as

$$\mu = \sigma_{COH} + \tau + \sigma_{INC} + \pi \qquad \{1.16\}$$

The relative significance of the three processes(photoelectric, compton, and pair) which transfer energy from the X-ray beam to the attenuating medium are illustrated in Figure 1.08. From Figure 1.08 [1.12] the compton interaction is seen to be dominant over a wide spectrum of energy for media of low atomic number. The total photon cross section along with the

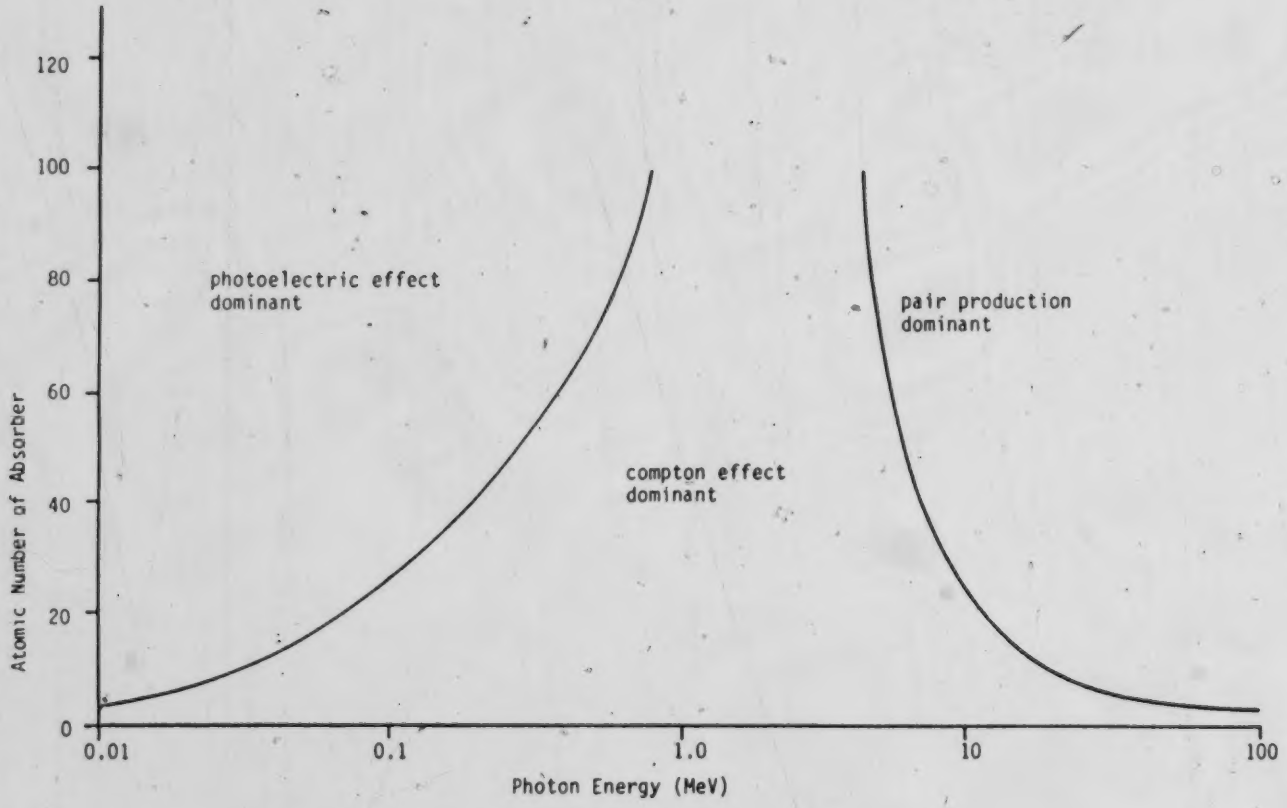

Figure 1.08 Relative importance of photon interactions.

individual interaction cross sections of which it is composed are shown in Figure 1.09 [1.13] and 1.10 [1.14] for water and lead respectively.

1.2.2 Electron Interactions

Electrons and positrons generated by the photoelectric effect, compton scattering, and pair production transfer their energy to the medium which they transit by way of collisions with the electrons and nuclei of the medium and thus undergo scattering. The main energy loss mechanism for electrons is that of electron-electron(or electron-positron) interactions, but the contribution to electron scatter from these interactions is small in comparison to the scatter resulting from electron-nucleus collisions.

The classical scattering of an electron of velocity v by a nucleus of atomic number Z is given by the Rutherford formula

$$\left(\frac{d\sigma}{d\Omega}\right)_\theta = \left(\frac{1}{4\pi\varepsilon_\circ}\right)^2 \left(\frac{Ze^2}{2m_\circ v^2}\right)^2 \frac{(1-\beta)^2}{\sin^4(\theta/2)} \qquad \{1.17\}$$

where m is the rest mass of the electron, v is the velocity of the electron, θ is the angle of scatter, and β is v/c, where c is the speed of light. This analysis does not take into account the screening of the nuclear charge nor electron spin. A more accurate cross section, in the form of an infinite series, which takes into account electron spin but not electronic screening was derived by Mott[1.15] and is accurate for low Z elements. Other cross sections have been derived which take screening into account according to different

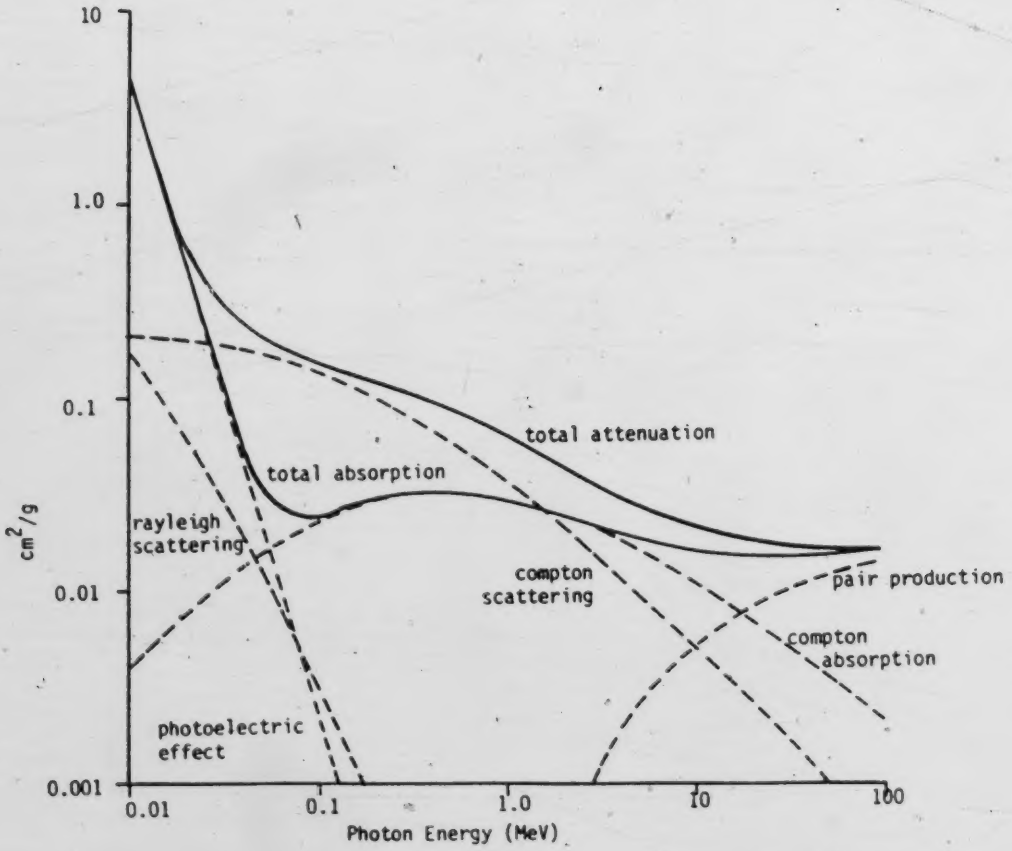

Figure 1.09 Photon interaction cross sections for water.

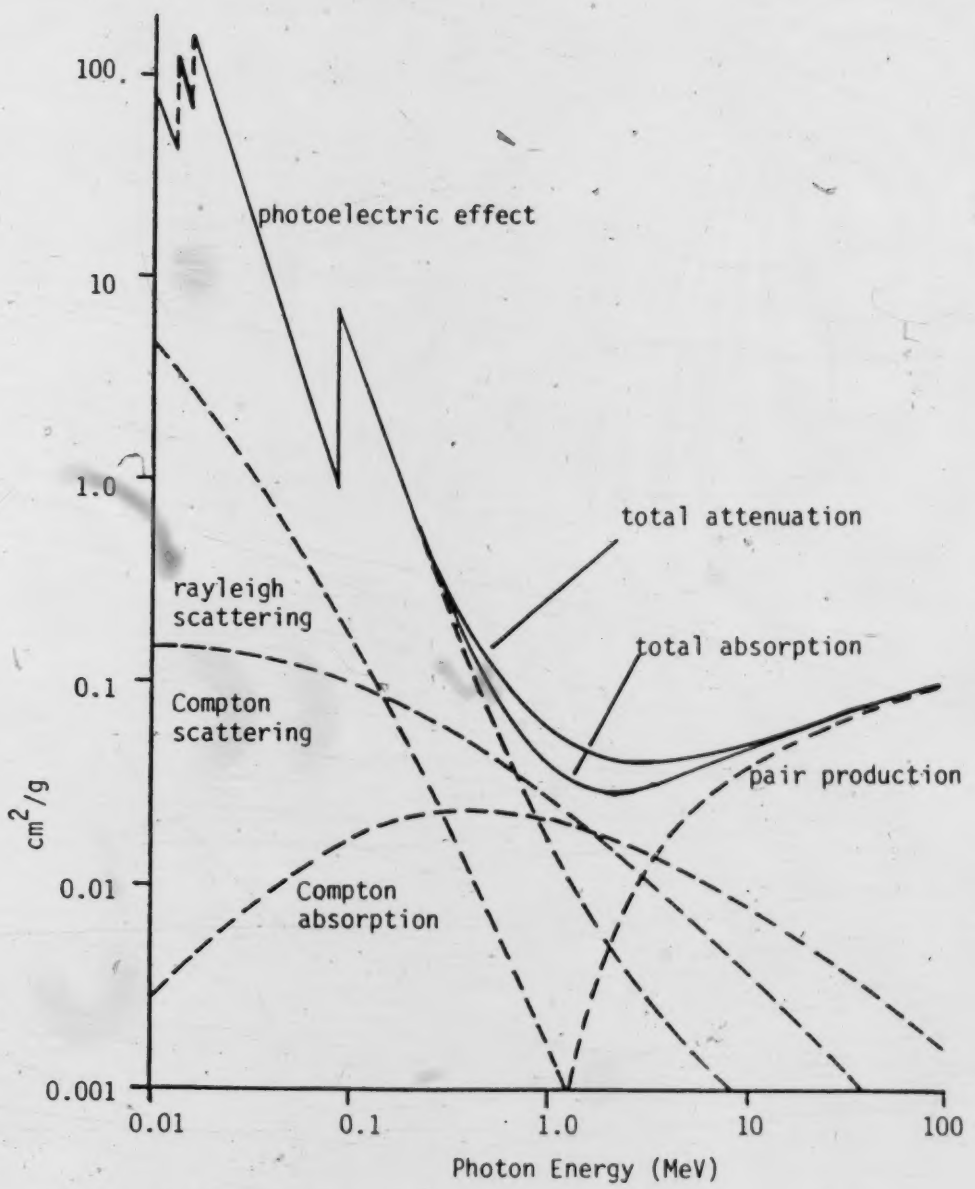

Figure 1.10 Photon interaction cross sections for lead.

considerations.The scattering due to electron-electron interactions differ from those of electron-nucleus interactions only in their dependence on Z. Electron-nucleus scattering is proportional to Z^2 while electron-electron scattering is proportional to Z.

Electrons and positrons undergo both elastic and inelastic collisions with the electrons of the medium in which they interact. The incident electrons and positrons impart a portion of their energy to the electrons of the medium in each collision process. Depending on whether the energy imparted by the incident electron or positron is greater than or less than the binding energy of the recipient electron either ionization or excitation will occur. If the binding energy is negligible compared to the energy imparted then the collision is considered to be elastic. If the binding energy is a significant portion of the energy imparted then the collision is considered to be inelastic. The electrons ejected from the atom in the elastic collisions are called δ -rays and may have energies up to half that of the incident electron and up to the entire amount of the incident positron's energy. These δ-rays impart their energy to the medium in the same manner as does the incident electron or positron. While the elastic collision has the potential for far greater energy loss by the incident electron or positron, the inelastic collision has a far greater probability of occurrence and it is by inelastic interactions that incident electrons and positrons lose the majority of their energy.

The incident electrons and positrons also undergo both elastic and inelastic collisions with the nuclei of the medium. The energy lost in an elastic interaction with a nucleus is much smaller than that lost in collisions with electrons due to the large difference in the mass of the electron/positron

and that of the nucleus. Thus in spite of the fact that elastic scattering by a nucleus is more probable than scattering by electrons(nuclear scattering being proportional to Z^2 while electronic scattering is proportional to Z) the contribution to energy loss by elastic nuclear scattering can be ignored. Inelastic scattering, on the other hand, results in significant energy loss. The collision is inelastic due to the creation of a bremsstrahlung photon in the process.

The predominance of inelastic electron-electron interactions as the collisional energy loss(to the medium) mechanism for electrons and positrons gives rise to the concept of continuous slowing down of the incident electron or positron by means of an infinite number of infinitesimal energy losses along its track. In reality the incident electron or positron undergoes a large number of small but finite energy losses along with a few large energy losses(δ-rays) along its track. In this regard an expression for the mean electron-electron collisional energy loss per unit path length dE/dx, or linear "Stopping Power" S_{col}, has been derived. Often written in terms of the mass stopping power, $(S/\rho)_{col}$, this relativistic quantum mechanical expression, originally due to Bethe[1.16], is

$$\frac{1}{\rho}\left(\frac{dE}{dx}\right)_{col} = \left(\frac{S}{\rho}\right) = \frac{2\pi e^4 N_\circ}{m_\circ v^2}\left(\frac{Z}{A}\right)$$

$$\left[\ln\left(\frac{E^2(E+2m_\circ c^2)}{2m_\circ c^2 I^2}\right) + (1-\beta^2) + \frac{1}{2} + \frac{\frac{1}{8}E^2 - (2m_\circ c^2 + m_\circ c^4)\ln 2}{(E+m_\circ c^2)^2} - \delta\right] \qquad \{1.17\}$$

where v = velocity of the electron

$\beta = v/c$

$m_\circ$ = rest mass of the electron

E = relativistic energy of the electron

I = the mean excitation energy of the medium

$N_\circ$ = Avogadro's number

δ = the density correction factor.

Values of the mean excitation energy and stopping power for the elements and a number of compounds have been tabulated by Berger and Seltzer[1.17].

The photon generated when an electron or positron undergoes an elastic collision with a nucleus is called bremsstrahlung. The differential cross section for this process is given approximately by

$$\frac{d\sigma_{rad}}{d\Omega} \cong \frac{1}{137}\left(\frac{e^2}{m_\circ c^2}\right) BZ^2 \left(\frac{E+m_\circ c^2}{E}\right)\left(\frac{1}{h\nu}\right) \qquad \{1.18\}$$

where $m_\circ$ = rest mass of the electron

$h\nu$ = energy of bremsstrahlung photon generated

E = electron relativistic energy

B = a slowly varying function of Z and E

One may define a radiative stopping power for this process as

$$\left(\frac{dE}{dx}\right)_{rad} = S_{rad} = \int_0^E \frac{d\sigma}{d\Omega} h\nu \, d(h\nu) \qquad \{1.19\}$$

and one obtains, approximately,

$$S_{rad} \alpha Z^2 E \qquad \{1.20\}$$

The approximate relative magnitudes of S_{rad} and S_{col} are given by

$$\frac{\left(\frac{S}{\rho}\right)_{rad}}{\left(\frac{S}{\rho}\right)_{col}} \cong \frac{EZ}{1600 m_o c^2} \qquad \{1.21\}$$

The total stopping power for a medium may be obtained by adding the collisional and radiative stopping powers

$$\frac{1}{\rho}\left(\frac{dE}{dx}\right)_{TOT} = \frac{1}{\rho}\left(\frac{dE}{dx}\right)_{col} + \frac{1}{\rho}\left(\frac{dE}{dx}\right)_{rad}$$

$$\left(\frac{S}{\rho}\right)_{TOT} = \left(\frac{S}{\rho}\right)_{col} + \left(\frac{S}{\rho}\right)_{rad} \qquad \{1.22\}$$

The positron loses its energy by ionization and excitation and bremsstrahlung as does an electron. Since it is an antiparticle, however, the positron will eventually be captured by an electron in the medium and will undergo annihilation with that electron. This process is more probable for low energy positrons than for high energy positrons. Annihilation with a free electron requires the creation of two photons in order to conserve momentum and their combined energy must be $\geq 2m_o c^2$.

The statistical nature of the scattering and energy loss processes dictate that there will be a distribution of depths of penetration in the medium over which the incident monoenergetic electrons will have lost all of their energy. As well there will be a distribution of energies which the electrons will possess at any given depth. This energy distribution is referred to as energy straggling and the distribution of penetration depths is referred to as range straggling. Thus there is no well defined range of electrons in a medium. It is, however, convenient to define a mean range, or continuous-slowing-down - approximation(csda) range, based on the assumption of continuous energy loss given by the total stopping power. This mean range is then

$$\frac{R}{\rho} = \int_0^{E_0} \left(\frac{\rho}{S}\right)_{TOT} dE \qquad \{1.23\}$$

1.3 Radiation Sources

1.3.1 Cobalt-60 Radiation

Photons produced by the decay of radioactive isotopes are an important source of radiation used in medicine. In 1951 high activity Cobalt-60 sources were produced in a Canadian nuclear reactor and the first radiotherapy unit, employing Cobalt-60 as its source, was constructed in Saskatchewan. Cobalt-60, with a half life of 5.26 years, is produced by neutron activation of naturally occuring Cobalt-59. The decay scheme of is shown in Figure 1.11. Cobalt-60 decays with a probability of 99.88% by beta decay with a

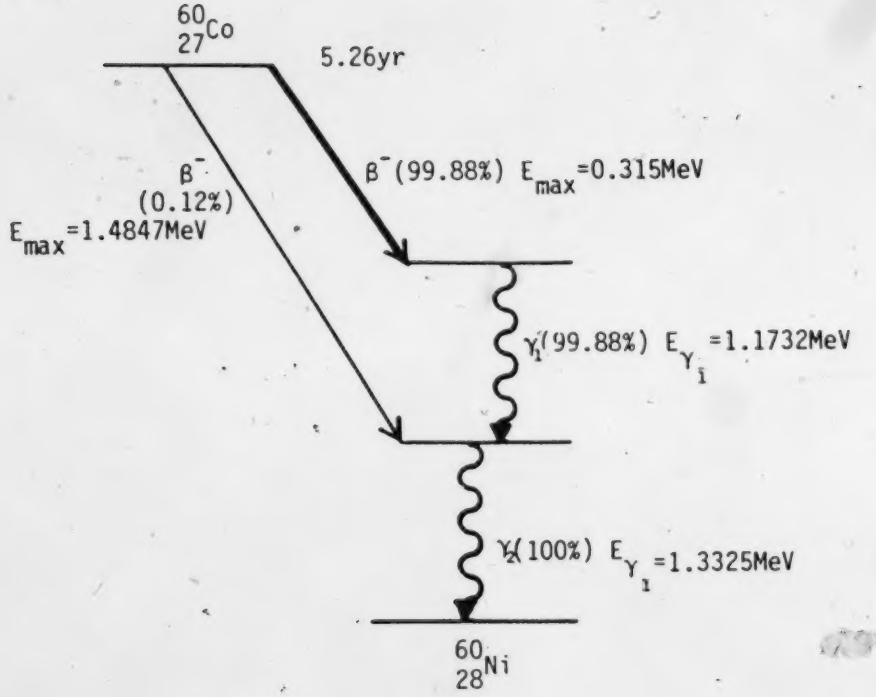

Figure 1.11 The decay scheme of Cobalt-60.

maximum energy of 0.315MeV to form an excited state of Nickel-60. This excited state of Nickel-60 decays rapidly by emission of two photons of energies 1.1732 and 1.3325MeV respectively in cascade. Cobalt-60 also decays with a probability of 0.12% by beta decay with a maximum energy of 1.4847MeV to form the lower excited state of Nickel-60 which then rapidly decays by the emission of a 1.3325MeV photon. The two photons of energies 1.1732 and 1.3325MeV, with relative intensities of 99.88 and 100 respectively, provide the radiation used in Cobalt-60 therapy and can be treated as a single photon of 1.25MeV.

The Cobalt-60 source is encapsulated in two stainless steel welded containers which are surrounded by a high Z shielding material, such as tungsten, on all sides except for the window through which the photons are to be emitted. The source is placed near the centre of a lead-filled steel container which serves as the head of the treatment device. To provide the photon beam for treatment, the source is positioned inside the head at an opening which serves as a radiation port to volumes external to the head. The beam size is determined by a set of collimators which form the end of the radiation port. The field thus produced will have an attendant penumbra due in part to the small but finite size of the source.

1.3.2 Medical Linear Accelerators

The major components of a modern linear accelerator(linac) are shown in Figure 1.12 [1.18]. In this structure microwaves are employed to accelerate electrons to high energies. The accelerated electrons are directed onto a

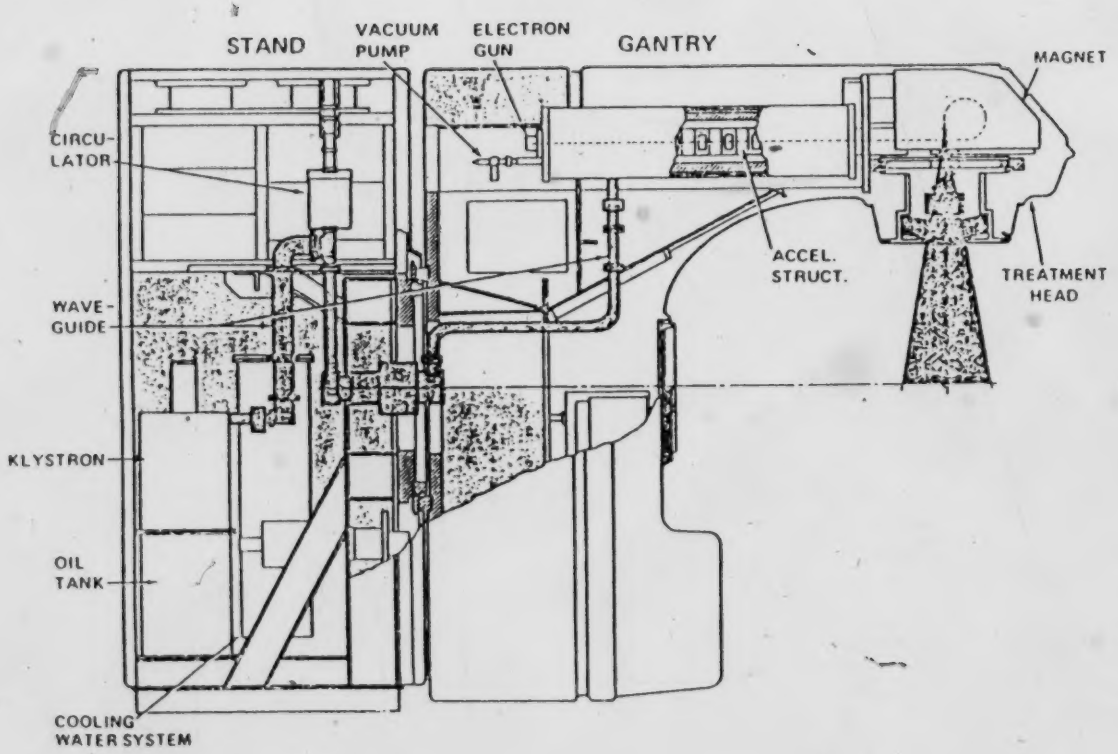

Figure 1.12 The major components of a linear accelerator.

target where they produce Bremsstrahlung photons which are used in radiotherapy.

The microwave power supply consists of either a magnetron or a klystron. Klystrons can produce higher microwave power outputs than can magnetrons and as a result magnetrons are usually found only on lower power linear accelerators. The microwave power generated by either the magnetron or klystron is transported by means of a wave guide to the accelerator structure. This acts as a microwave resonant cavity which provides the environment wherein electrons may be accelerated to high energies by means of their interaction with microwaves. The bending magnet redirects the electrons, emergent from the accelerator structure, towards the target for X-ray production. The electrons enter the treatment head where they are incident upon the target, thus producing X-rays. The rest of the treatment head contains beam modifying and monitoring devices.

The principle components of a typical treatment head are illustrated in Figure 1.13. The beam of high energy electrons produced in the accelerator structure is redirected by the bending magnet toward a high Z target, such as tungsten, thus producing bremsstrahlung photons. These bremsstrahlung photons are highly forward peaked and a flattening filter is placed in the beam to produce relatively uniform cross sectional intensity. This flattening filter tends to either harden or soften the beam as photons of energies greater than or less than about 3MeV will be attenuated to a greater extent than these photons. A low Z material is placed under the target to serve as an electron absorber which removes electrons scattered from the target.

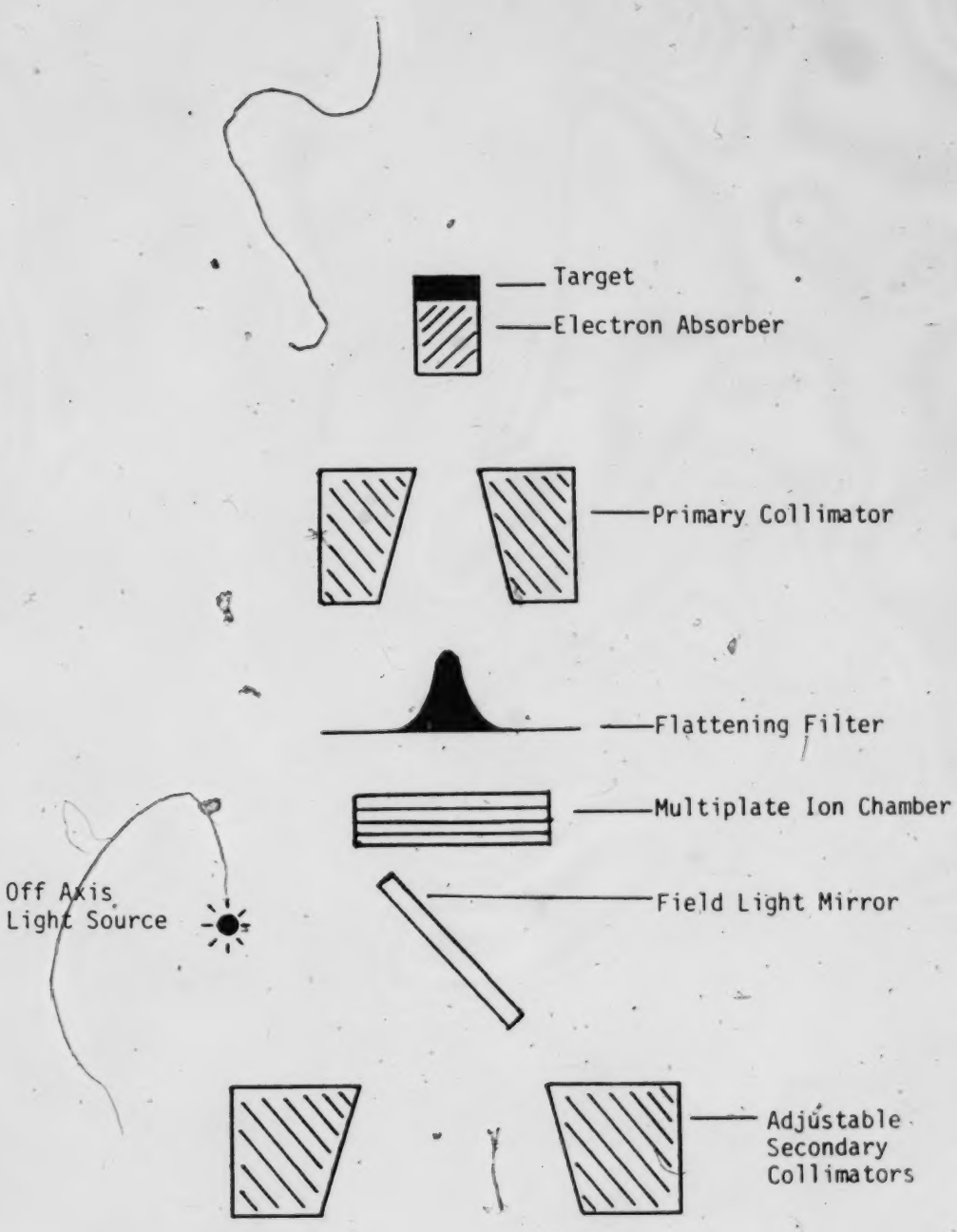

Figure 1.13 The principle components of a treatment head.

A multiplate ion chamber is also placed in the beam. This allows monitoring of the integral dose, dose rate, and field symmetry which are important parameters affecting the accurate delivery of dose to a patient. A thin field light mirror is placed in the beam as shown which allows an off axis light source to optically illuminate a surface placed in the field of the beam.

A fixed primary collimator serves to limit the maximum field size at a given distance from the source(target). The field size is further defined by an adjustable secondary collimator system. The secondary collimator position is calibrated in terms of the field defined at a fixed source to surface distance(SSD). The edge of the field is defined to be that location from the central axis of the beam where the absorbed dose in a water phantom falls to 50% of the dose along the central beam axis.

1.4 Dosimetry

1.4.1 Basic Concepts

A very important quantity in radiotherapy is the absorbed dose. It is defined as the energy absorbed per unit mass of absorbing medium.

$$\text{Absorbed dose : } D = \frac{\Delta E_{ab}}{\Delta m} \qquad [1.24]$$

The SI unit for absorbed dose is the gray(Gy) and is defined as

$$1Gy = 1J / kg \qquad \{1.25\}$$

As an X-ray photon transits a medium it interacts with matter transferring a portion of its energy to an electron or an electron-positron pair created by pair or triplet production. These charged particles in turn lose their energy as they travel outward from the point of interaction. The energy transferred to the medium at the interaction site is not necessarily equal to the energy absorbed at that point. For this reason a quantity, called kerma, has been defined as the mean energy transferred per photon to electrons(or positrons) per unit mass.

$$\text{kerma: } K = \frac{\Delta \overline{E_{tr}}}{\Delta m} \qquad \{1.26\}$$

If a beam of photons of fluence Φ is incident upon a thin slab of material of thickness Δx then the kerma will be

$$K = \Phi\left(\frac{\mu}{\rho}\right)\overline{E_{tr}} \qquad \{1.27\}$$

The word kerma is an acronym for Kinetic Energy Released in the Medium.

If one has the condition where equal amounts of energy are carried into and out of a small volume by the charged particles set in motion by photons, such that the energy absorbed by the medium in this small volume from these charged particles is equal to the energy transferred from photons to charged particles in this volume, then electronic equilibrium is said to exist in

this volume. In such regions where electronic equilibrium exists the absorbed dose is equal to the kerma and one has

$$D = K = \Phi\left(\frac{\mu}{\rho}\right)\overline{E_{tr}} \qquad \{1.28\}$$

If a fraction f of the energy transferred by a photon is reradiated as bremsstrahlung then one may define the mean energy absorbed by the medium per photon as

$$\overline{E_{ab}} = (1-f)\,\overline{E_{tr}} \qquad \{1.29\}$$

and {1.28} becomes

$$D = K = \Phi\left(\frac{\mu}{\rho}\right)\overline{E_{ab}} \qquad \{1.30\}$$

1.4.2 Ionization Based Dosimetry

1.4.2.1 Standard Air Chamber

Ionization based dosimetry involves the calculation of the absorbed dose in a volume based on the measurement of the ionization produced by radiation in that volume. The primary ionization based dosimeter is called a standard air chamber. In a standard air chamber, as shown in Figure 1.14, a narrow X-ray beam passes through the centre of the device. A large

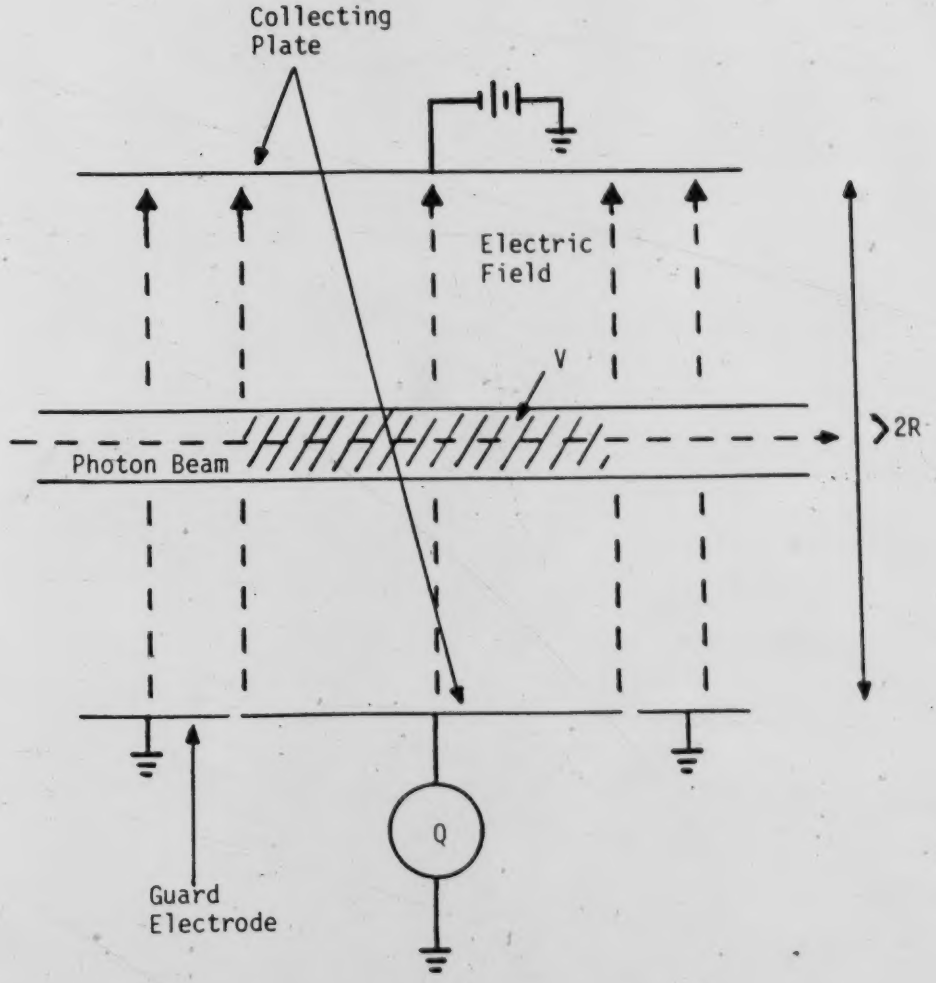

Figure 1.14 Schematic representation of a standard air chamber.

potential difference is maintained across the upper and lower collection plates and serves to remove ions produced in the volume V and also reduce recombination of these ions, such that they may be collected by these plates. Guard electrodes on either side of the lower collection plate minimize edge effects associated with the collection field. The upper and lower collection plates are separated by a distance greater than twice the range of any secondary electrons generated in order that only ions produced by the secondary electrons will be collected. The dimensions of the chamber required for the existence of electronic equilibrium are such that photon attenuation becomes significant for photon energies above 3MeV and hence standard air chambers are not employed for energies above 3MeV, and are typically limited to energies not above 0.5MeV.

Assuming complete collection of all ions produced, one may define a quantity X, called exposure, as the amount of charge dQ per unit mass, generated in mass dm

$$X = \frac{dQ}{dm} \qquad \{1.31\}$$

when all of the secondary electrons generated by photons in mass dm of air have been brought to rest. The unit of exposure is the roentgen, R, and is defined as

$$1\ R = 2.58 \times 10^{-4}\ C / kg\ \text{of air} \qquad \{1.32\}$$

It is found experimentally that the average energy required to produce a single ionization in a gas is constant over a large range of gas pressures and electron energies and hence one may determine the absorbed dose at a point from the exposure measured at that point. For air the average energy, W, required to produce one ionization is

$$W = 33.85 \text{ eV per ion pair} = 33.85 \text{ J/Coulomb} \quad \{1.33\}$$

Thus the absorbed dose in air is

$$D_{air} = W_{air}\left(\frac{Q_{air}}{m_{air}}\right) = W_{air}X_{air} \quad \{1.34\}$$

where the mass of the air is determined from a knowledge of the density of air in the measuring volume V.

1.4.2.2 Practical Ion Chambers

Standard air chambers are used for calibration in standards labs while much smaller "air-wall" ion chambers are used for routine radiation measurements. Such an air-wall ion chamber consists of a small air filled cavity containing a central electrode and bounded by an outer electrode. Surrounding the cavity is a wall of material with X-ray absorption and scattering properties very similar to that of air but of a much higher density. The high density of the wall allows electronic equilibrium to be established

around the cavity in much smaller dimensions than that of the standard air chamber. Special compositions of plastic usually serve as the wall material.

By careful choice of parameters, the "air-wall" chamber can be constructed such that its response to photon energies is very close to that of the standard air chamber. One may thus calibrate an air-wall chamber according to a standard air chamber to produce an exposure calibration factor $N_X(E)$. This calibration factor may then be used to determine the exposure X measured by the air-wall chamber in terms of the charge q collected by the chamber electrodes.

$$X = N_X(E)\, f(q) \qquad \{1.35\}$$

where E is the energy of the photons being measured and f(q) represents the meter reading of the device which measures the charge collected. Build-up caps may be added to the outside of the air-wall to extend the use of the chamber to higher energies.

1.4.2.3 Solid State Detectors

The basic underlying principle of semiconductor detectors is the same as that of ionization chambers: the production of the equivalent of ion pairs by radiation transiting the material of the detector. A simplified semiconductor detector consists of a block of semiconductor material across which exists an electric potential. This potential may arise from conditions within the semiconductor itself or be applied externally. An externally applied potential

may also be used to enhance the internally arising potential of the semiconductor. By means of this potential the ionization produced in the semiconductor is converted into an electrical signal which may be amplified and analyzed by suitable electronic equipment. Of available semiconductor materials, silicon is the predominant material used in charged particle detection, while germanium is the predominant material of ion-drifted detectors, which are employed in X-ray spectroscopy.

1.4.2.4 Thermoluminescent Dosimetry (TLD)

A thermoluminescent material is one in which many of the electrons, or their hole counterparts, which are produced by the passage of ionizing radiation through the material, while at a normal operating temperature, become trapped at lattice imperfection sites(traps) in the material. A thermoluminescent material suitable for dosimetry purposes is one in which the probability that these trapped electrons or holes will remain trapped is high if the material remains at or below the specific operating temperature, but, upon raising the temperature of the material the probability of electron or hole escape increases. Those electrons or holes which escape their lattice traps return to stable energy states in the lattice by emission of visible light. This emitted light may be measured and can be plotted as a function of the temperature of the material. The resulting "glow curve" will exhibit one or more peaks which correspond to the different energies of the traps in the lattice. By means of suitable calibration the absorbed dose of the material may then be determined as a function of the total light emitted in part or all of

the glow curve, or the relative height of one or more of the particular peaks in the curve.

1.5 General Introduction and Review of Previous Work on Compensators

When radiation is used for therapeutic purposes it is most often desirable to deliver a high and homogeneous dose to a specific volume(such as a tumor volume) in the body while at the same time delivering as low a dose as possible to surrounding volumes. In cases where these surrounding volumes include organs of high sensitivity to radiation this is of extreme importance. The response of tissue in the target(high dose) volume is dependent upon the absorbed dose distribution realized in that volume. It has been shown by Brahme that "high tumor control rates can only be achieved with a very high accuracy in dose delivery"...."An absolutely necessary prerequisite for precise radiation therapy.... is therefore a high accuracy in the delivery of absorbed dose to the target volume"[1.19]. As a natural consequence of the requirement for accuracy is the need for dose uniformity in the target volume so that the degree of tumor control achieved in a high dose region of the volume is not negated by inadequate control realized in a low dose region. Indeed, when "normal tissue complications are a problem complete tumor control cannot be achieved without severe complications unless the dosimetric uncertainties are very small. Uniform and precise dose delivery is therefore one of the cornerstones of accurate radiation therapy"[1.19]. Brahme further concludes that for good tumor

control to be achieved, dose variations over the target volume should be less than 5 percent and in some cases as small as 3 percent.

One factor which contributes to a non-uniform dose distribution at depth in a patient or phantom is a non-flat, or irregular surface topology. The distortion in the dose distribution resulting from a non-flat patient surface contour can be quite acute in regions of high surface irregularity such as the head and neck, where treatment of the lower head, the neck, and the upper thorax may be given. A very simple method of eliminating the dose distortion arising from patient surface topology consists of filling in the "missing tissue" in the air gaps with a tissue like material(called bolus) as illustrated in Figure 1.15. The bolus material presents a flat surface normal to the incident radiation beam and thus the dose heterogeneity due to irregular surface topology is eliminated.

The use of bolus to eliminate the distortions in absorbed dose due to irregular patient surface topology is both simple and elegant, but suffers from a major drawback when used in high energy photon radiotherapy treatment. This drawback is the loss of skin sparing: the delivery of a low dose to the outer layers of skin relative to the high dose delivered to deeper lying volumes. This skin sparing effect has been shown to be clinically desirable[1.20] in most cases, indeed the clinical benefits of this skin sparing effect are "undesirable only when the region to be treated includes the skin or superficial tissue"[1.21].

This effect may be seen by considering an X-ray beam incident normal to the flat surface of a homogeneous phantom as shown in Figure 1.16. A plot

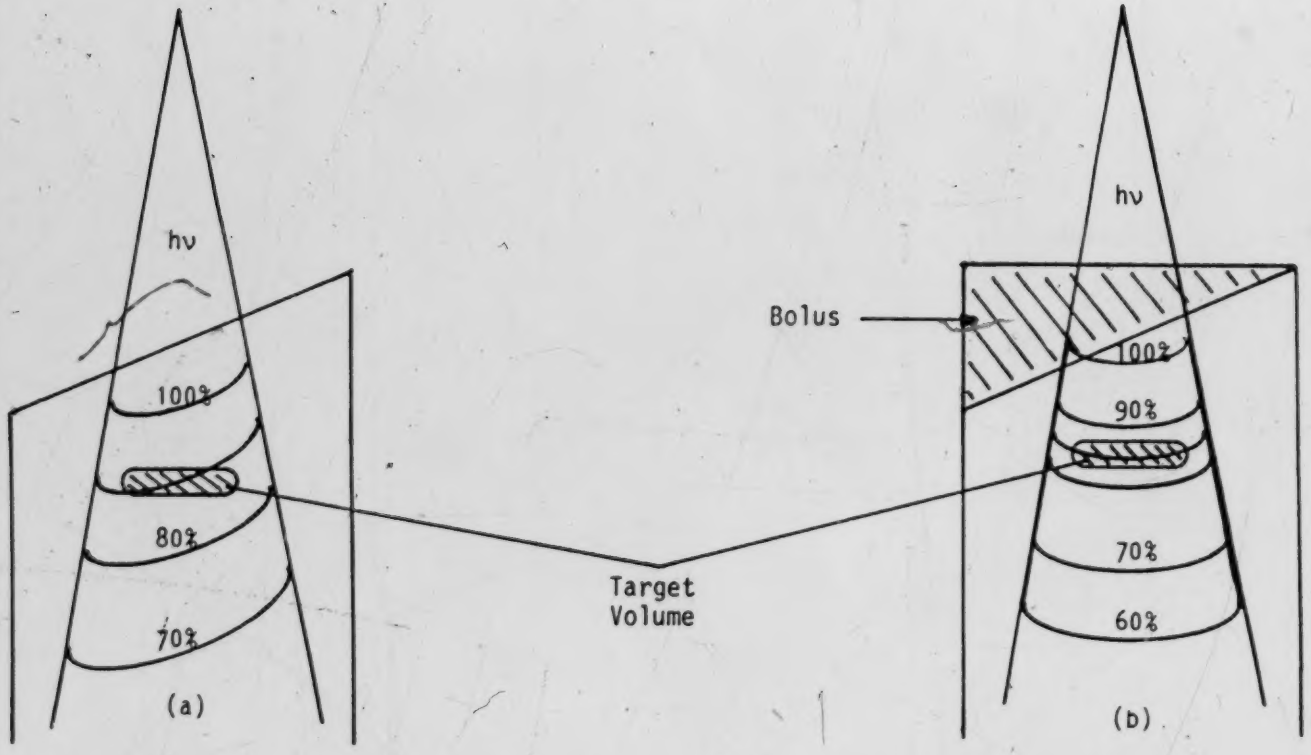

Figure 1.15 The effect of bolus on isodose curves. (a) Isodose curves without bolus. (b) Isodose curves with bolus on the phantom surface.

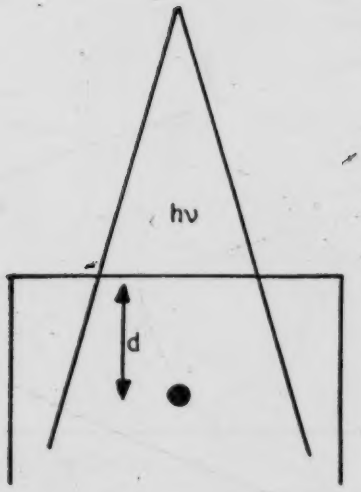

Figure 1.16 An X-ray beam incident normal to the surface of a homogeneous phantom.

of absorbed dose as a function of depth along the central beam axis under these conditions is shown in Figure 1.17. Such plots are characterized by a dose which initially increases rapidly from a low(but finite) value at zero depth to a maximum at a particular depth and subsequently decreases in an almost exponential manner as depth is increased further. The depth at which the maximum dose occurs is referred to as d_{max}. The region between the phantom surface and d_{max} is referred to as the "build up" region as it corresponds to the region in which the absorbed dose is building up to its maximum value at d_{max}. The existence of this build up region results in the skin sparing effect as the outer lying volumes of skin are spared from receiving a high dose and is of distinct advantage when high energy photons are used to treat tumors underlying the skin surface.

The use of bolus to overcome the distortions introduced by patient surface contour results in the loss of the skin sparing effect, as the build up region now occurs within the bolus material rather than under the skin surface. As a result a much higher surface dose is delivered to the patient's outer skin than without the use of bolus.

Partial restoration of the skin sparing effect may be achieved by retraction of the bolus away from the patient surface in the direction of the beam. Such retracted bolus is referred to as a retracted missing tissue compensator. The restoration of partial skin sparing associated with compensator retraction is the result of the introduction of an air gap between the compensator and patient surface. This air gap reestablishes the existence of a build up region below the patient's skin thus reintroducing the skin sparing effect. The restoration of skin sparing is only partial, due to a surface dose resulting

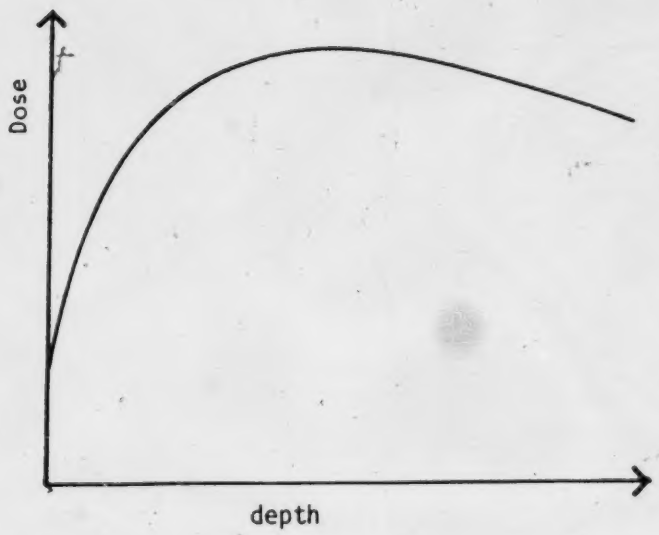

Figure 1.17 A plot of dose as a function of depth for the geometry of Figure 1.16.

from scattered electrons and low energy photons originating from within the compensator. Since the fluence of scattered electrons and photons from the compensator incident on the patient surface decreases with increasing retraction distance, the degree to which skin sparing is restored increases as retraction distance is increased.

While the retraction of the compensator produces a desired reduction in skin surface dose it also introduces a complication in determination of dose at depths below the patient's surface. The complication introduced is as follows: the dose at any given depth is altered by the retraction process from that which would be observed with the use of bolus. The alteration produced varies in a complex manner according to a large number of variables including retraction distance and measurement depth. As will be seen in the work presented here, dose nonuniformity can also be introduced at depth by the retraction process if compensators are not designed correctly.

The use of tissue compensators was first proposed in 1959 by Ellis[1.22] and since that time numerous papers have appeared on the subject. Tissue compensators have been used to compensate for irregular patient surface contour[1.23, 1.24, 1.25, 1.26], variations in scatter and SSD for large fields[1.27], oblique incidence of the beam[1.28], and internal body heterogeneities [1.29, 1.30]. Compensators have been used to correct for one or more of these effects at one time.

The alteration in dose at depth introduced by compensator retraction is due to change of scattered radiation. It is fairly simple to design a compensator to correct for missing primary attenuation resulting from surface

topology and internal heterogeneities, but compensation for deviations in scattered radiation is a much more difficult task. The dose at a given point in the body resulting from scattered radiation is dependent, in a complicated fashion, upon a number of factors: including the primary photon spectrum; the densities of the different materials in the body; the depth and position of the point in the body; and the size of the beam. Construction of a compensator to provide correct compensation at all points in the body is thus an impossibility. The need to take into account scatter in the design of compensators has long been recognized and many papers have appeared with regard to this matter. To date the contribution to dose due to scatter has been dealt with in terms of empirically determined effective attenuation coefficients and thickness ratios. These effective attenuation coefficients and thickness ratios are measured with either square or circular fields using flat slabs of attenuator material. In order to apply these parameters to a real situation they must be measured over a wide range of experimental geometries, as their magnitude is dependent upon an number of experimental factors including attenuator thickness, distance of measurement point from the central beam axis, and measurement depth. In particular the value of the effective attenuation coefficient to be used "decreases drastically as field size increases"[1.31]. The case is well summed up by Leung et al as they conclude that the effective attenuation coefficient "is dependent on the experimental setup and thus the simulation of treatment conditions for its measurement is very important"[1.32]. In any case such parameters indicate the average amount of scatter for these fields from idealized(flat) compensator geometries but they do not take into account the varying scatter conditions which exist in an irregular geometry.

Varying degrees of compensation have been reported experimentally. These range from satisfactory compensation where "the compensated profile is uniform within ±3.5% over the entire field"[1.33] to unsatisfactory compensation where "the ratio of the dose at mid-axilla to that at the center is worse with compensation than without"[1.34]. Compensation at a particular depth creates errors at other depths which, in some cases, can be substantial. Wilks and Casebow have shown that for a Cobalt-60 beam with a field size of 12X12cm^2 at 100cm SSD, correct compensation at a depth of 5cm below a water phantom surface results in errors of up to 3% for depths up to 8cm and errors of up to 10% for depths up to 15cm[1.35].

A number of materials have been used in the construction of compensators including wax, acrylic, gypsum and various metals. Of these, lead seems to be the most popular material. The vertical dimensions of a compensator constructed of a non-unit density material must be scaled appropriately according to the ratio of that material's linear attenuation coefficient to that of tissue.

Three main techniques are employed in the design and fabrication of tissue compensators: (i) fabrication based on a particular method of surface topography measurement; (ii) fabrication based on the dose distribution obtained upon irradiating a film by passing the beam through the patient; (iii) and fabrication based on the density distribution information of the body obtained by methods of CT scanning. Surface measurement techniques were the first to be employed and of these methods a mechanical rod box was the first to be used to map the surface topography of the area to be irradiated[1.36, 1.37, 1.38]. A modified version of this technique is presently

employed at the Cross Cancer Institute. Non-mechanical surface measuring techniques have been developed using photogrammetry[1.39, 1.40, 1.41, 1.42, 1.43, 1.44]. These techniques determine the surface contour from photographs taken of the patient at several angles. Such surface measurement techniques suffer from two drawbacks. First, such techniques, due to their very nature, do not yield information regarding internal tissue inhomogeneities, and secondly, the surface contour of a patient may change under treatment conditions, eg. such as if a patient is turned over for anterior and posterior parallel opposed fields. In such a case body parts display a tendency to migrate downward in each position thus shifting the surface topography.

The design of compensators from portal films is extensively reported in the literature[1.45, 1.46, 1.47, 1.48, 1.49]. In this technique port films are scanned to determine the density encountered by each primary ray path through the volume to be irradiated. These densities are then used to compensate midline doses for parallel opposed fields. The limitation of such a technique is the inability to distinguish the positions of varying density along any single ray path.

Finally, compensator design based on density distribution information provided by CT scans is potentially the most accurate method due to the large volume of information that CT scans are capable of providing. These possibilities have been explored by a few authors[1.50, 1.51] but this technique suffers from the drawbacks of high cost and the limited availability of CT scanners and CT scan time.

As true or correct compensation is achieved at only one depth(due primarily to scattering) errors in compensation will occur for all other depths in any particular arrangement. These errors have been investigated for wax compensators by Jackson[1.52] who has concluded that "large retraction distances, while reducing skin contamination, may lead to serious depth dose errors unless the wax is thin....If the error is thought to be excessive it may be reduced by the choice of a smaller retracting distance, though at the expense of increased skin dose. The technique is evidently most suitable for small fields where adequate skin protection can be achieved with a small retracting distance and the consequent depth dose errors are also small. With large fields it may be possible to compromise between skin dose and depth dose errors by reducing the retraction distance, but in certain instances it may well be concluded, especially if the wax is thick, that the errors are unacceptable"[1.52].

Until recently the majority of published work on compensators had been carried out for Cobalt-60 energies while very little has been reported concerning higher energies. Jackson[1.52] has examined both Cobalt-60 and 4MV energies and in the past few years more work with higher energies has been reported[1.53, 1.54, 1.55, 1.56, 1.57] but as recently as 1985 Huang et al states that "published quantitative information about scattered photons from beam-modifying filters is lacking"[1.58].

The magnitude of the modification of the dose at a specific point in a phantom, which results from the introduction of a compensator into the beam between the source and phantom, is dependent upon a number of factors. The work of Jackson[1.52] with flat slab geometries has been extended by

the author[1.59] to higher energy photon beams and high atomic number compensator materials. The results of this investigation revealed this dose modification to be a complicated function of retraction distance, field size, depth of target volume, compensator thickness, compensator material, and energy of the incident X-ray beam. The potential for significant errors in delivered dose has been amply demonstrated in the case of these idealized flat slab geometries and such results suggest that even greater errors could occur with a more clinically relevant surface geometry.

As a preliminary investigation of a clinically relevant geometry, an anthropomorphic phantom, along with its corresponding retracted missing tissue compensator of the type which would find use in actual clinical treatment in this institution, was constructed. This phantom, shown in Figures 1.18 and 1.19, was constructed of layers of wax, with its surface contour defined by the immobilization shell of a patient who received treatment in the supraclavicular region. Channels were carved into the wax at the layer boundaries to allow for the placement of p-type measurement diodes. A wax retracted missing tissue compensator was constructed for this phantom using the methods employed in the construction of compensators for actual clinical use. Specifically, those methods required the replacement of missing attenuation along primary ray paths in accordance with patient surface geometry. The phantom was irradiated with 6MV photons both in the compensated and uncompensated configurations.

Representative of the results obtained are those for layers 4 and 7(Figures 1.20 and 1.21), which are 8.5cm and 14cm respectively below the 100cm SSD point marked on the phantom(Figure 1.18). The points of

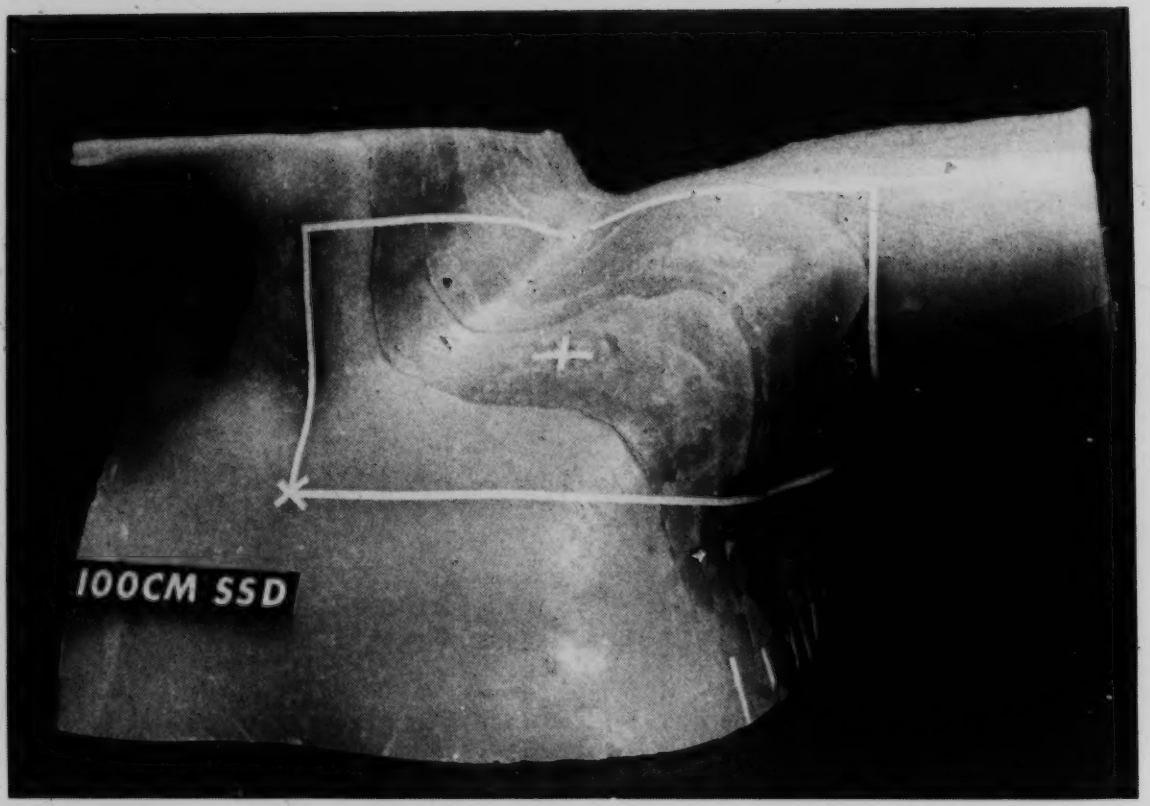

Figure 1.18 Anterior view of the anthropomorphic phantom.

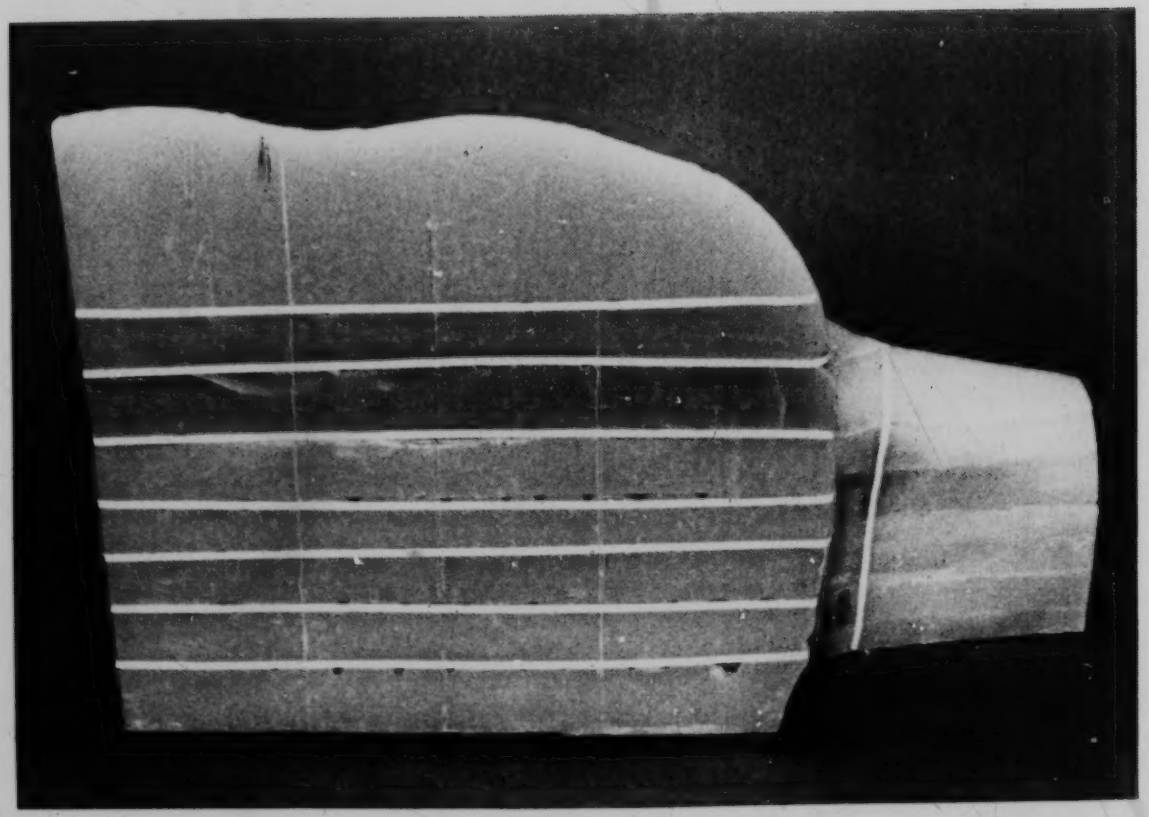

Figure 1.19 Cross-sectional view of the anthropomorphic phantom revealing plains of measurement.

Point	Compensated (% of *2)	Uncompensated (% of *2)
1	107%	105%
2	100%	100%
3	113%	127%
4	104%	103%
5	110%	128%
6	116%	118%
7	110%	109%
8	100%	106%
9	115%	118%
10	109%	114%
mean	108.4% ± 5.7%	112.7 ± 9.8%

Figure 1.20 Measurements at layer #4 located 8.5cm below 100cm SSD.

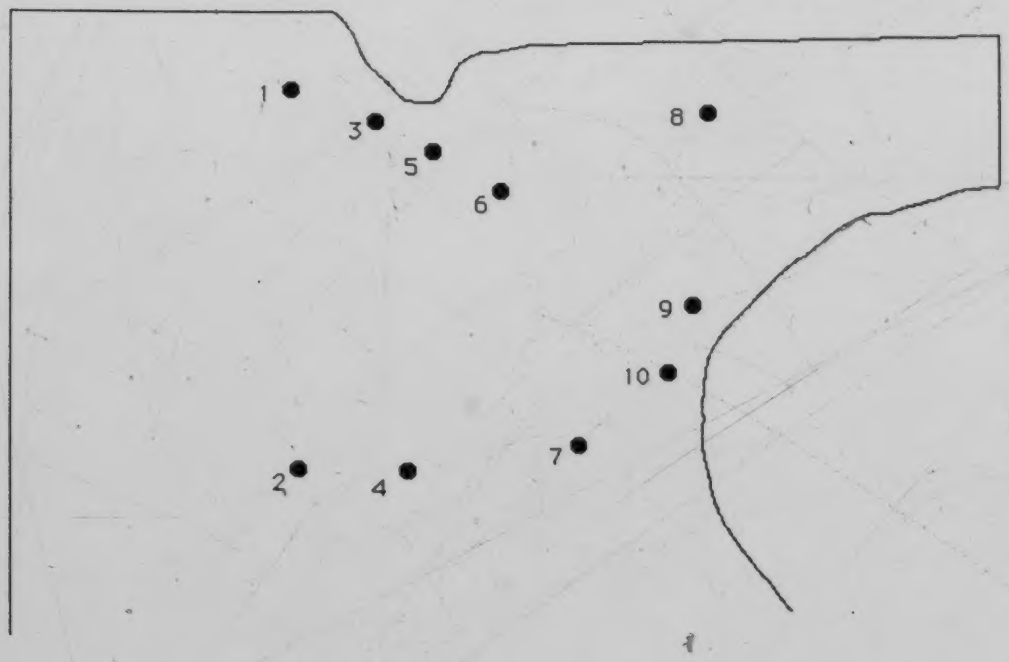

Point #	Compensated (% of #2)	Uncompensated (% of #2)
1	113%	109%
2	100%	100%
3	124%	135%
4	117%	141%
5	107%	106%
6	126%	129%
7	107%	110%
8	113%	124%
9	115%	120%
10	118%	116%
mean	114.7% ± 8.3%	119.6 ± 13.5%

Figure 1.21 Measurements at layer #7 located 14cm below 100cm SSD.

measurement are indicated by the numbered dots. All measurements are normalized with respect to point #2 for the purpose of comparison.

As expected, the uncompensated irradiation produced a large variation in measured dose across each measurement plane. Plane #4 exhibited a standard deviation of 9.8% in dose with individual deviations as large as 28%. The standard deviation in dose for plane #7 was 13.5% with individual variations as large as 41% observed.

With the introduction of a retracted missing tissue compensator into the beam one would ideally expect to measure relatively flat dose distributions at each layer boundary, corresponding to those obtained in a homogeneous phantom having a flat surface. The standard deviation in measured dose observed in the case of compensated irradiation is indeed reduced from that in the uncompensated irradiation to 5.7% and 8.3% for layers 4 and 7 respectively, but individual dose deviations of as much as 16% and 26% for layers 4 and 7 respectively are still seen. The use of a compensator designed to compensate for missing primary attenuation only(hereafter referred to as a geometric compensator) is thus seen to improve dose uniformity over that obtained with uncompensated irradiation, but the performance achieved is clearly seen to be less than optimum.

The results obtained with this anthropomorphic geometry clearly demonstrate the need for improvement in tissue compensator design. The mathematical complexity of such an anthropomorphic geometry is, however, not readily amenable to analytical analysis. Therefore, in order to study further the dose distribution resulting from the use of a retracted missing

tissue compensator, the conical geometry described in the sections following was constructed.

Chapter 2

Experimental Results with Conical Compensators

When you can measure what you are speaking about and express it in numbers, you know something about it; but when you cannot measure it, when you cannot express it in numbers, your knowledge is of a meager and unsatisfactory kind; it may be the beginning of knowledge, but you have scarcely, in your thoughts, advanced to the stage of science, what ever the matter be.

William Thomson
Lord Kelvin

II EXPERIMENTAL RESULTS WITH CONICAL COMPENSATORS

2.1 Experimental Parameters

The results of the flat slab investigations previously discussed have proven instructive with regard to the dose perturbation associated with retracted tissue compensators. By the very nature of the problem which compensators are intended to overcome(ie. irregular surface contours), flat slab geometries can, however, hardly be said to be realistic end points in the investigation. Stepping immediately to a fully anthropomorphic geometry is, however, unwise as the level of complexity introduced by such a surface topology serves only to increase the difficulty of both the experimental and theoretical analysis. As an intermediate between these two extremes the conical geometry depicted in Figures 2.01 and 2.02 was chosen for investigation. This geometry combines mathematical simplicity with similarity to the more tortuous anatomical regions, such as the head and neck and supraclavicular regions, where retracted tissue compensators are often employed.

As shown in Figure 2.02 the experimental arrangement of the conical geometry consists of three main components. The contour for which compensation is required is created by a thin conical shell of plexiglass which serves to define a conical surface depression in a water tank. The latter, open at the top, serves as the phantom. The electron density of water is 3.343×10^{23} el cm^{-3}. Cones machined from polystyrene, Aluminum, and lead serve as retracted compensators for the surface depression created by

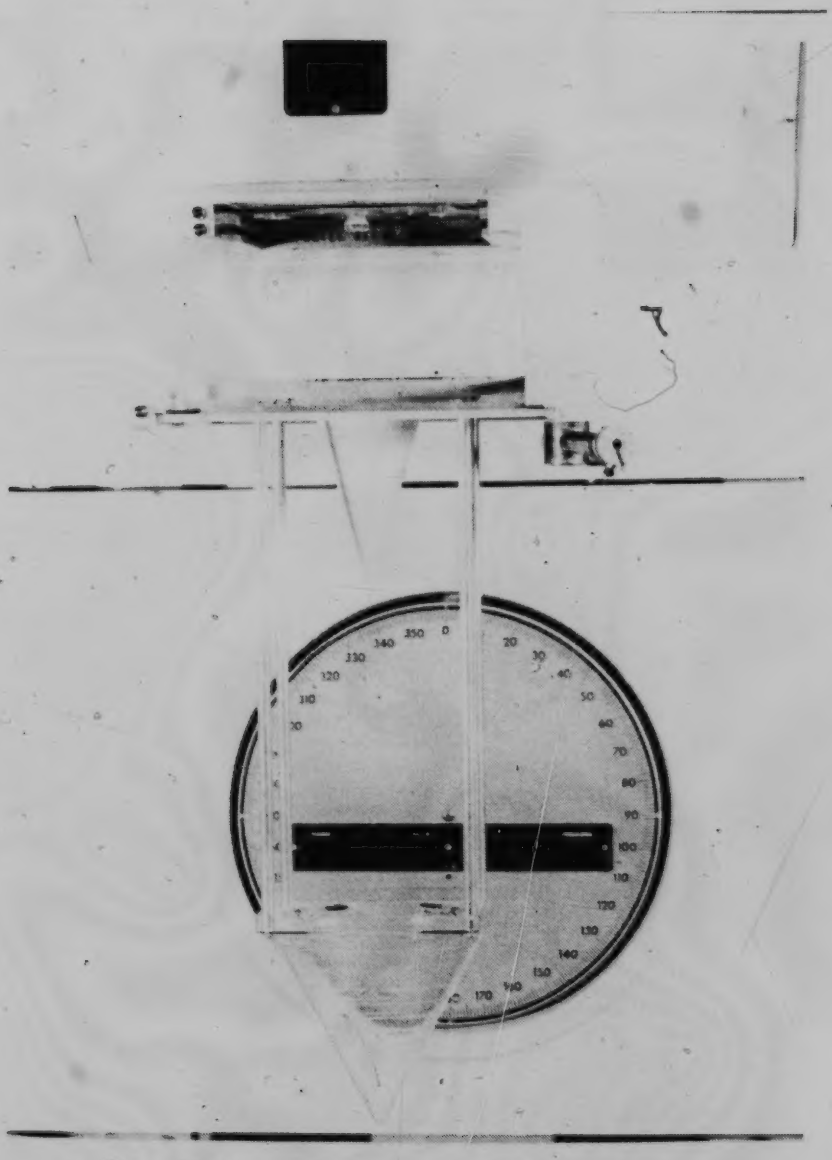

Figure 2.01 The conical geometry showing its main compone..ts

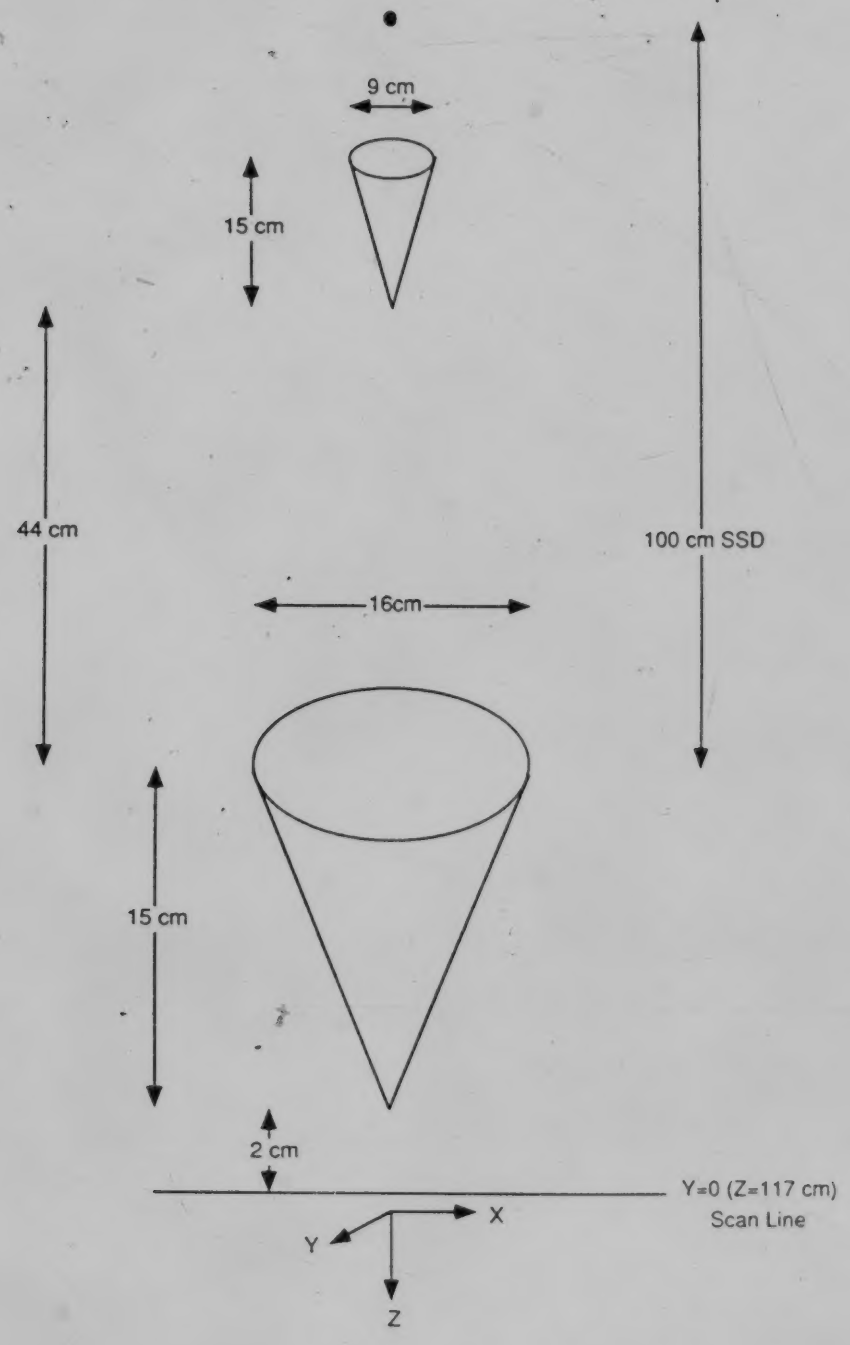

Figure 2.02 Diagramatic representation of the conical geometry.

the conical plexiglass shell. The material used in compensator construction is an approximately tissue equivalent opaque white polystyrene which has an electron density of $3.50X10^{23}$ el cm^{-3} and a mass density of 1.08 g cm^{-3}. The polystyrene used is derived from clear polystyrene$(C_8H_8)_n$ by the addition of a fine particulate filler of titanium dioxide(TiO_2) (3.7% by weight) which improves the tissue equivalence of polystyrene for low energy photons($E(\gamma) < 0.1$ MeV) and high energy photons($E(\gamma) > 10$ MeV)[2.1]. The aluminum and lead used in compensator construction have electron densities of $7.832X10^{23}$ el cm^{-3} and $2.707X10^{24}$ el cm^{-3} and mass densities of 2.699 g cm^{-3} and 11.36 g cm^{-3} respectively.

Both the thin conical shell and the retracted conical compensators were held in place by a rigid support mechanism which ensured good geometric alignment. The physical dimensions of this arrangement are shown in Figure 2.02. The axis of both the compensator cone and surface depression cone are aligned with the central beam axis. The surface depression cone has a depth at apex of 15.0 ± 0.1 cm and a diameter at base of 16.0 ± 0.1 cm. The polystyrene compensator cone was designed as a geometric compensator to provide the same attenuation along primary ray paths as would exist with bolus, and thus compensates only for the missing primary attenuation introduced by the surface depression cone. This is the design philosophy underlying the vast majority of retracted missing tissue compensators. Such compensators are constructed by geometrically reducing the missing bolus in the lateral dimensions as required by beam divergence. For this reason compensators which are constructed according to this design shall be referred to as geometric compensators throughout this work. This geometric polystyrene compensator has a height at apex of 15.0 ± 0.1 cm and a

diameter at base of 9.0±0.1 cm in accordance with beam divergence. Using an effective photon energy of 1.25MeV for Cobalt-60 photons, 2MeV for 6MV photons, and 5MeV for 15MV photons, then at Cobalt-60 $\mu = 0.0639\ cm^{-1}$ for polystyrene and $\mu = 0.0633\ cm^{-1}$ for water, while at 15MV $\mu = 0.0302\ cm^{-1}$ for polystyrene and $\mu = 0.0303\ cm^{-1}$ for water. Thus over the range of energies employed in this investigation(Cobalt-60 to 15MV) the attenuation along the maximum primary path length(15cm) in both the geometric polystyrene compensator cone and the cone of missing water does not differ appreciably and this polystyrene cone acts as a geometric compensator at each of the three primary photon energies used.

The attenuation properties of both aluminum and lead make it impossible to construct a single cone of either material which will act as a geometric compensator over the energy range used. The sizes of the aluminum and lead cones were thus chosen to yield geometric compensation at the single energy corresponding to Cobalt-60 photons. The aluminum cone has a height at apex of 6.4±0.1 cm and the lead cone has a height at apex of 1.44±0.1 cm. Both aluminum and lead cones have a diameter at base of 9.0±0.1 cm.

Based on considerations of primary attenuation only, compensation with the geometric polystyrene cone should yield a dose distribution which deviates from the bolus dose distribution by not more than +0.90% at Cobalt-60, +0.36% at 6MV, and -0.19% at 15MV. Similarly the aluminum cone compensated dose distribution should not deviate from the bolus dose distribution by more than -0.12% at Cobalt-60, +0.70% at 6MV, and +3.54% at 15MV. Deviation from bolus dose with the lead cone compensator should

not exceed +0.04% at Cobalt-60 and +0.01% at 6MV. At 15MV, however, the lead cone dose distribution based on primary attenuation along the maximum primary ray path is expected to deviate from the bolus dose distribution by as much as 21%.

A second polystyrene compensator cone, which yielded incorrect compensation, was also employed mainly for later comparisons between theory and experiment. This incorrect cone has a height at apex of 15.0±0.1 cm and a diameter at base of 7.0±0.1 cm.

Measurements were taken by scanning a p-type diode along the X-axis(Y=0) at 5 different depths below the water phantom surface. The depths of measurement are 9.0, 12.0, 15.0, 17.0, and 21.0 cm below the water surface. The bolus configuration was achieved by removing the compensator from the beam and filling the surface cone with water to the level of the water outside the cone.

In order to demonstrate the dose perturbation resulting from the uncompensated conical surface depression, measurements were also taken with the compensator removed from the beam and the surface cone unfilled. Since the aim of employing retracted missing tissue compensators is the restoration of the bolus dose distribution which would result from the use of bolus, compensator performance is judged by comparison with bolus dose. Therefore, measurements obtained in both the compensated and uncompensated configurations are expressed as a percentage of the measurements in the bolus arrangement. The beam field size was set at 16X16 cm^2 at 100cm SSD throughout.

Experimental uncertainties in the relative dose measurements are inherently difficult to ascertain a priori. Therefore uncertainties in all dose measurements were determined by making each measurement a number of times and determining the standard deviation of these measurements. The standard deviations thus determined were found to be consistent over a large number of determinations performed on different days. Propagation of error was determined using the formulas for limit error. All length measurements were performed to an accuracy of ± 1mm or better, and this is taken as the error in such measurements unless stated otherwise.

2.1.2 Radiation Sources

2.1.2.1 Cobalt-60

The source of the Cobalt-60 X-rays employed in this work is an AECL Theratron 780 Cobalt 60 teletherapy unit with an SAD(source-to-axis-distance) of 80cm. The Cobalt-60 source is exposed by means of a source drawer which is operated by compressed air. The actual source employed is a 1.75cm diameter standard source which had an activity of 7934 curies of Cobalt-60 and provided an exposure rate of 131.7 roentgens per minute at one meter when measured September 25, 1987.

2.1.2.2 6MV

The source of the 6MV X-rays employed in this work is a 6MV Siemens Mevatron 67 medical linear accelerator with an SAD of 100cm. This accelerator uses a standing wave system which provides an electron beam of 3mm diameter with energies up to 6MeV. This electron beam is bent through 270° to strike a tungsten target and the X-ray field produced is flattened by a brass flattening filter. The primary collimator provides a maximum field size of 35X35 cm^2 at the isocentre. With an electron beam energy of 6MeV the X-rays produced form a spectrum with ranges in energy from a few keV up to 6MeV and is thus referred to as a 6MV X-ray beam. The energy of the 6MV beam is defined as providing a depth dose of (67±2)% when measured at 10cm depth in water for a 10X10 cm^2 field defined at the water surface at 100cm SSD. The depth of maximum dose is 1.5±0.2 cm as measured in water for a 10X10 cm^2 field at 100cm SSD. The effective energy of the 6MV beam is approximately 2MeV.

The waveguide is powered by a 2MW(peak) magnetron operating at a frequency of 2.998GHz. The waveguide operates in a pulsed mode and delivers a constant 200 cGy per minute.

2.1.2.3 15MV

The source of 15MV X-rays employed in this work is a 15MV Siemens Mevatron XX medical linear accelerator with an SAD of 100cm. This accelerator employs a standing wave waveguide which provides an electron

beam of less than 3mm diameter with energies up to 18MeV. This electron beam is deflected through 270° to strike a tungsten target and the X-ray field produced is flattened by a stainless steel flattening filter. The primary collimator provides a maximum field size of 40X40 cm^2 at 100cm from the target(100cm SSD). This accelerator provides an X-ray beam of 15MV X-rays which is comprised of a spectrum of X-rays ranging in energy from a few keV up to 15MeV. The energy of the 15MV beam is defined as providing a depth dose of (77±2)% when measured at 10cm depth in water for a 10X10 cm^2 field defined at the water surface at 100cm SSD. The depth of maximum dose is 3.0±0.2 cm as measured in water for a 10X10 cm^2 field at 100cm SSD. The effective energy of the 15MV beam is approximately 5MeV.

The waveguide is powered by a 7MW(peak) klystron operating at a frequency of 2.998GHz. The waveguide operates in a pulsed mode and delivers a constant dose rate of 300cGy per minute.

2.1.3 DOSIMETRY DEVICES

All measurements, unless otherwise stated, within the water phantom were carried out with the right angle p-type measurement diode depicted in Figure 2.03. Doping of the p-type silicon in the p-region is about $1.5X10^{15}$ boron atoms cm^{-3} while in the n-region is is about 10^{18} phosphorous atoms cm^{-3}. The silicon crystal itself measures 2.5X2.5X0.4 mm^3 with an effective ionization measurement volume of 0.3mm^3. The centre of the effective measurement volume is approximately 0.5mm below the outer diode

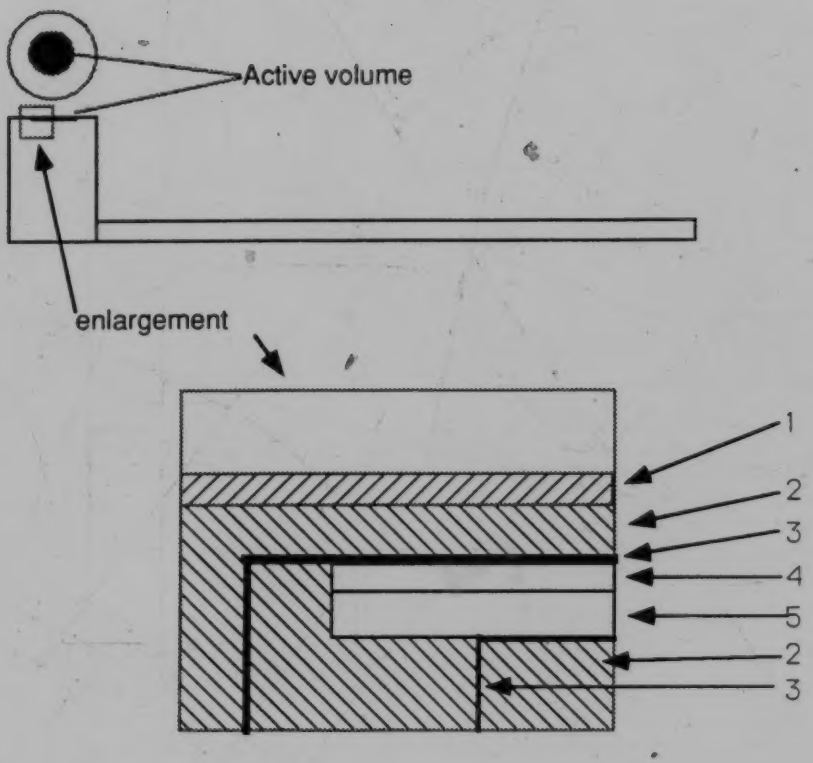

(1) water resistant paint
(2) epoxy resin
(3) aluminum foil for electrical connection
(4) ionization volume
(5) silicon crystal

Figure 2.3 Design of the p-type right angle silicon detector.

surface. Important physical characteristics of this diode are listed in Table 2.1 [2.2].

This p-type diode was operated in short circuit mode(zero bias) in conjunction with either a DPD-5 electrometer or an RFA-7 electrometer. Numerous cross checks demonstrated no appreciable difference in readings between the two electrometers.

When diodes are employed in radiation measurement the question of energy dependence on the part of the diode with respect to an ion chamber inevitably arises. The manufactures specifications on the right angle diode used here indicate just such an energy dependence at energies below 0.3MeV. According to the data supplied by the manufacturer(Figure 2.04) [2.3] this energy dependence is, however, insignificant over the energy range involved in this work.

As this energy dependence is most evident at low energies the response of the measurement diode was compared with that of an ion chamber for photon beams with maximum energies ranging from 75keV to 250keV. The ion chamber employed in this set of measurements was a Capintec PR - 06c air equivalent plastic Farmer Replacement ionization chamber with an effective volume of 0.6ml. The chamber has an inner diameter of 7mm and a length of 22mm and an air equivalent plastic wall of 50mg cm^{-2} thickness. This ion chamber was used in conjunction with a Capintec Model 192 Digital exposure meter which supplied a collection voltage of 300 volts to the probe. The results are shown in Figure 2.05. Diode response is expressed as a percent ratio of the ion chamber reading and is normalized to 100% for

Atomic number	14
Density	$2.3X10^{3}$ kg m^{-3}
Ionization volume	0.3 mm^{3}
p doping	$1.5X10^{15}$ boron atoms cm^{-3}
n doping	10^{18}phosphorus atoms cm^{-3}
Resistivity	10 ohm cm^{-1}
Capacitance	10 pF
W	3.6 eV
Mobility (electrons)	103 cm^{2} $V^{-1}s^{-1}$
Life time (electrons)	$5X10^{-6}$ s
Diffusion length	$9X10^{-8}$ m
Depletion layer	$5X10^{-6}$ m
Conductivity	10^{-8} (ohm) $^{-1}$
Radiation sensitivity	220 nC Gy^{-1}
Measuring point	0.4-0.6 mm below surface

Table 2.1 Important physical characteristics of the semiconductor detector.

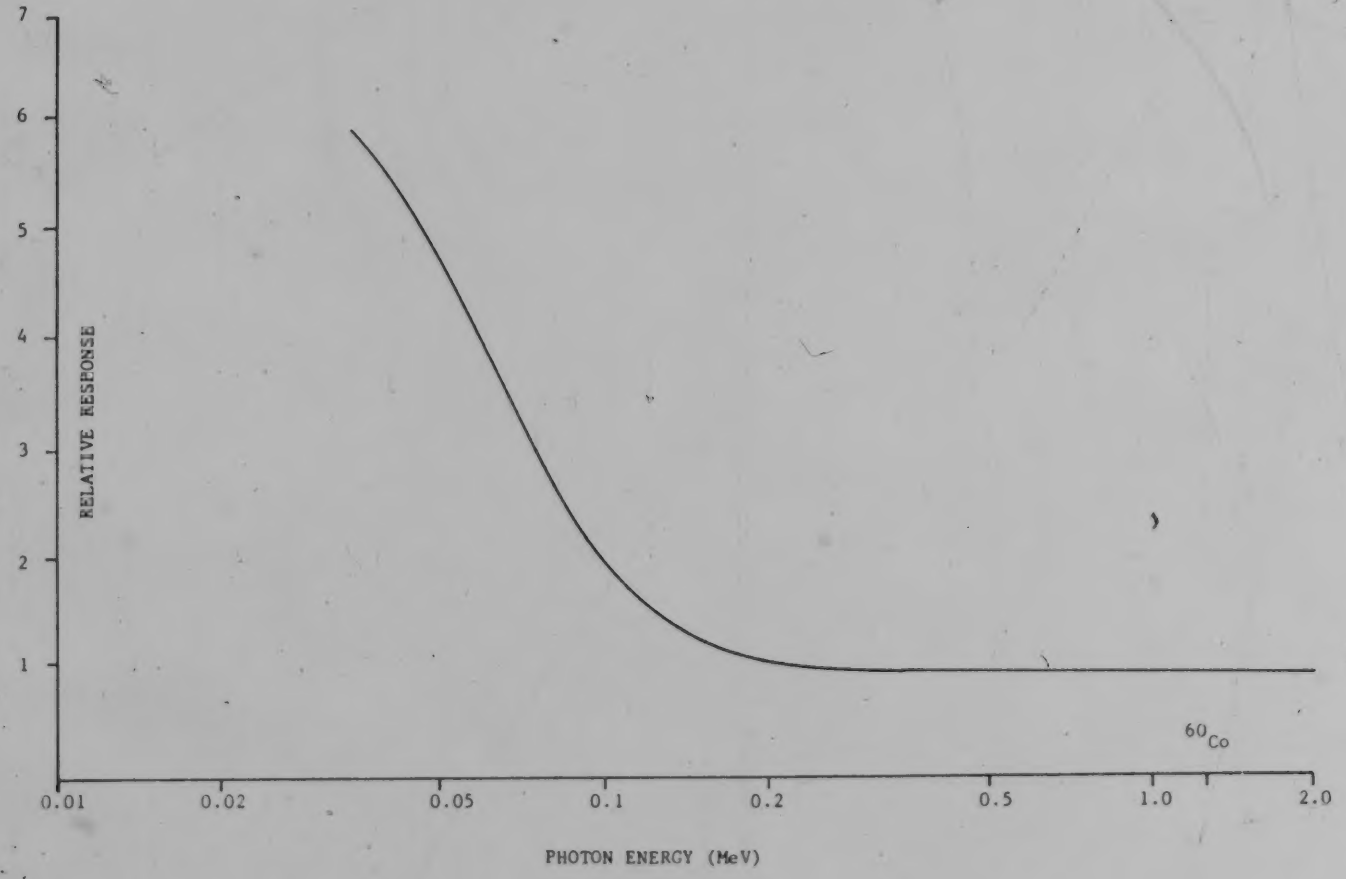

Figure 2.04 Energy response of the right angle semiconductor detector.

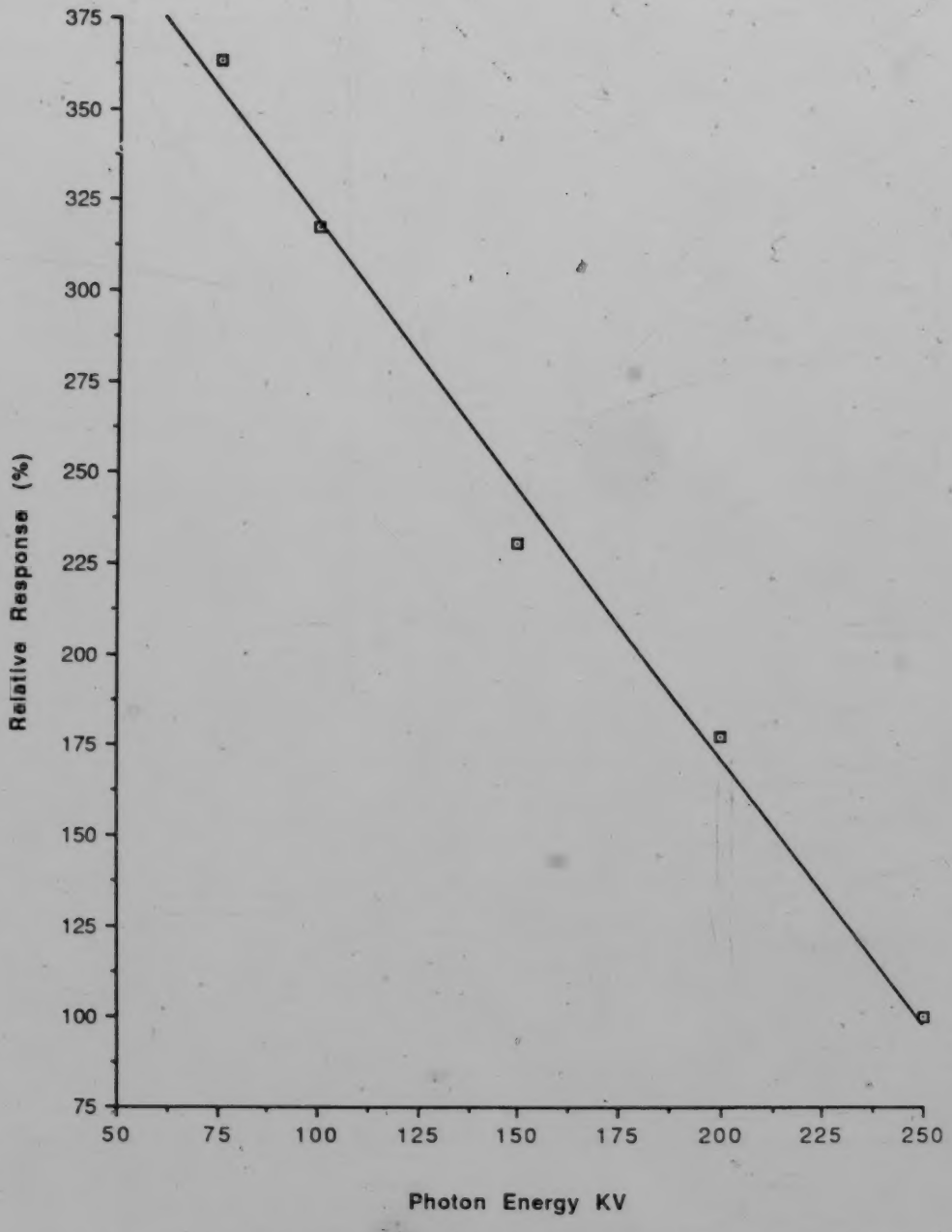

Figure 2.05 Diode response versus ion chamber response at low photon energies (measured).

photons with peak energy of 250 keV. As Figure 2.05 clearly shows, there is a marked energy dependence of the diode with respect to the ion chamber at these low energies.

The equivalent energies of these photon beams range from about 25keV to about 85keV for the photon beams with maximum energies of 75keV and 250keV respectively, and thus are well below the lowest primary photon energy used in this investigation. In order to determine the presence of any energy dependence at higher energies relevant to this investigation, a scan was made in water with both the measurement diode and a small submersible ion chamber with Cobalt-60 photons. The field size, as defined at the water surface, was 16X16cm^2 at 100cm SSD.This scan was made at a depth of 17cm below the flat surface of water in a water tank. The ion chamber used for these measurements is a PTW N23333 Farmer Type ionization chamber with an effective volume of 0.1ml. The chamber has a diameter of 3.5mm and a length of 12.0mm and an acrylic/dag wall of 0.053g cm^{-2} thickness This ion chamber was operated at a collection voltage of 300 volts in conjunction with the RFA electrometer.

The scan(diode vs ion chamber) is presented in Figure 2.06. In Figure 2.06 both the ion chamber and diode readings are normalized to 100% at mid scan which corresponds to the central axis of the beam. Over the entire field, including the penumbral regions, the diode and ion chamber responses are equal within experimental error. The manufacturers specifications are thus verified and the diode is seen to provide the same response(within experimental error) as does the ion chamber for photon

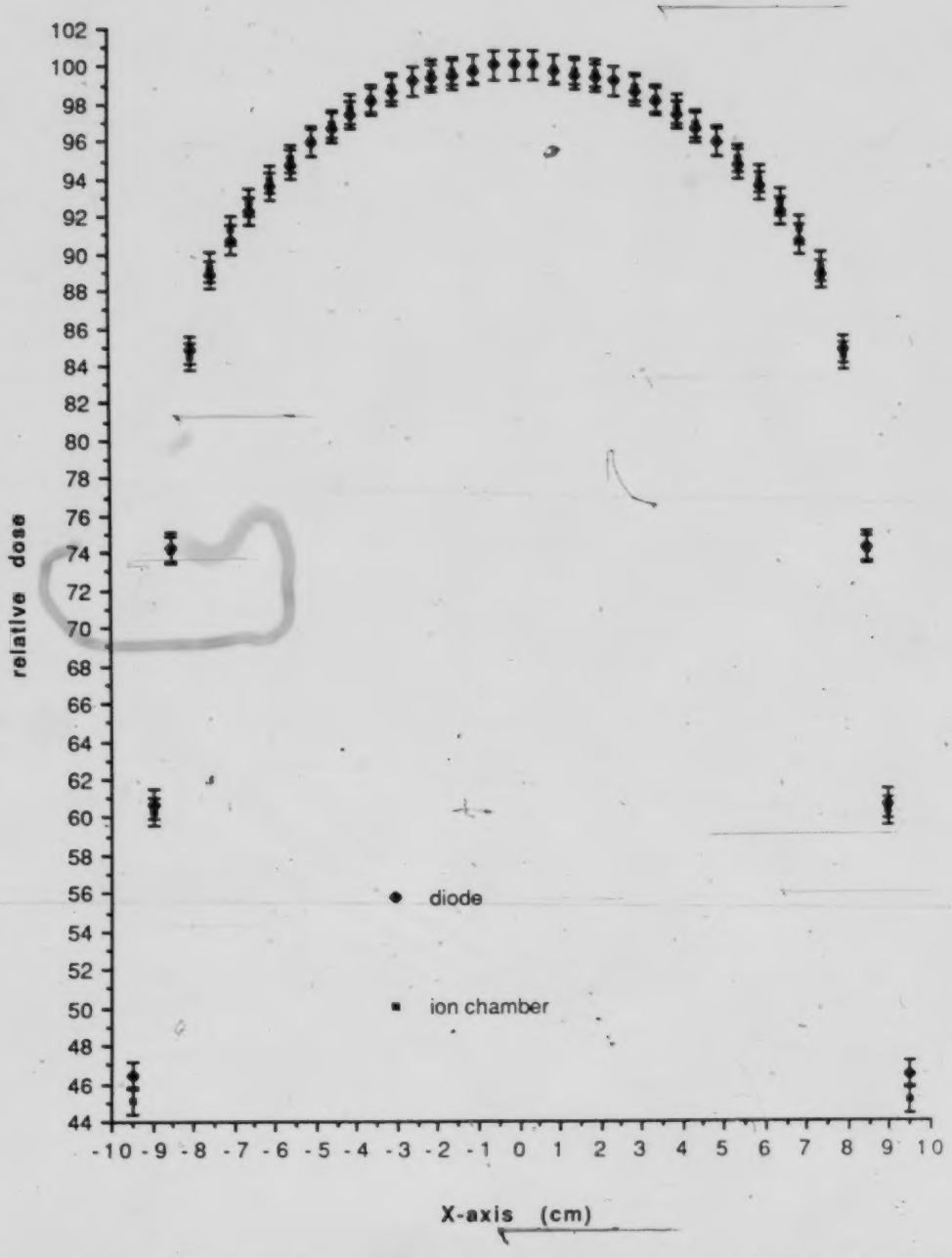

Figure 2.06 Diode response versus ion chamber response across the field with Cobalt-60 photons at 17cm depth (measured).

energies relevant to this work. The diode is preferred over the ion chamber for use in the water tank for its ease of use and greater spatial resolution.

2.2 Experimental Results

In order to test the performance of geometric compensators, three such compensators,each of a different material and designed for use with Cobalt-60 photons, were examined. Of these three, only the polystyrene cone qualifies as a geometric compensator at all three photon energies employed. The dose distributions produced by the aluminum and lead cones at 6MV and 15MV were used to examine the result of compensators constructed according to primary attenuation considerations only for compensator materials of densities greater than unity. Also examined was the dose distribution produced in the uncompensated configuration for all three energies and all depths. As the polystyrene compensator cone provides geometric compensation at all energies investigated it is referred to throughout in the graphs as the "geometric cone".

These distributions, expressed as a percentage of the bolus dose distribution, are presented in Figures 2.07 through 2.26.

2.3. Analysis and discussion of Results

The perturbations (or changes from bolus dose) in dose at depth introduced by the uncompensated surface depression cone and the degree of compensation for this perturbation provided by the polystyrene, aluminum,

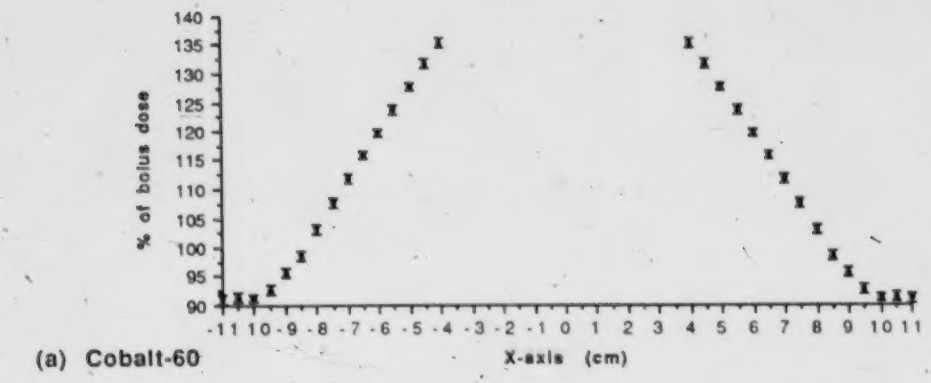

(a) Cobalt-60

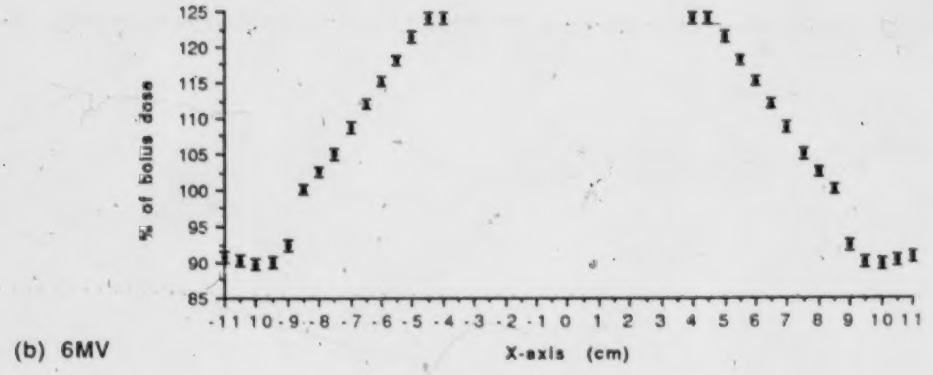

(b) 6MV

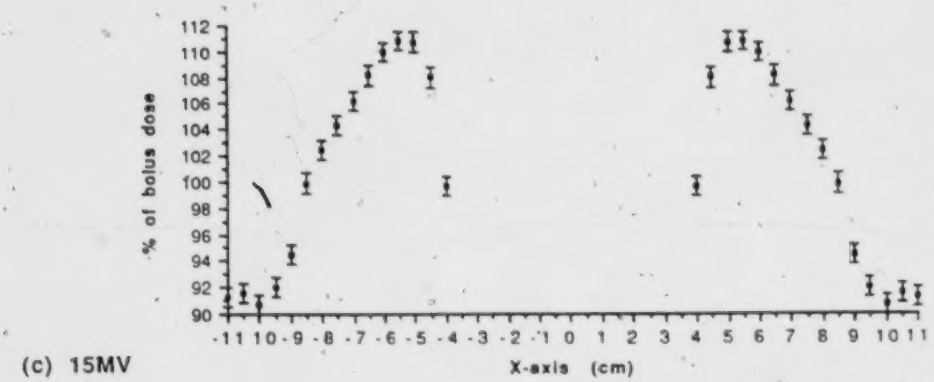

(c) 15MV

Figure 2.07 Uncompensated dose as a % of bolus dose at 9cm depth (measured) (a) Cobalt-60, (b) 6MV, (c) 15MV.

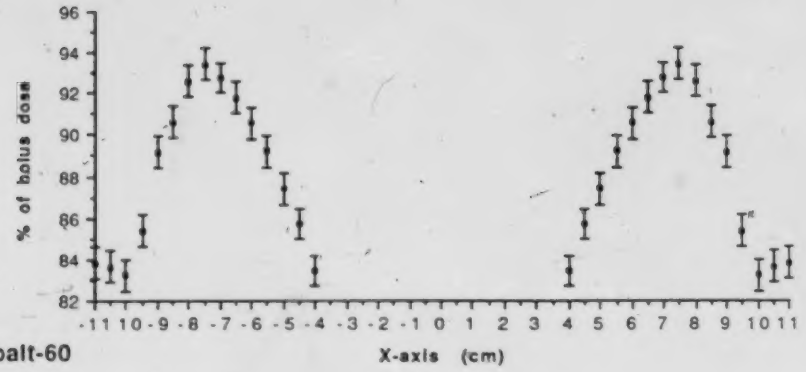

(a) Cobalt-60

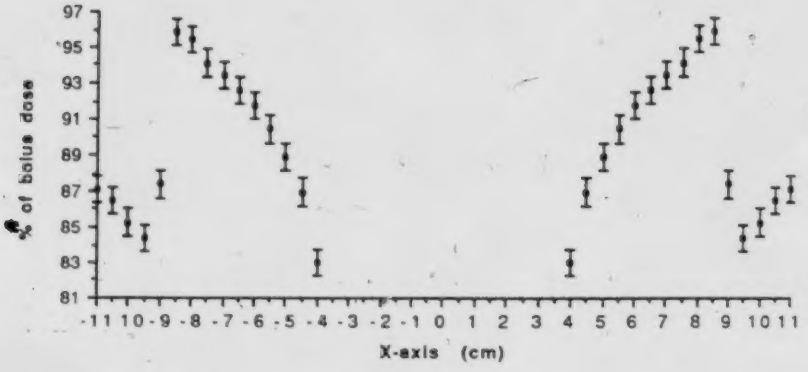

(b) 6MV

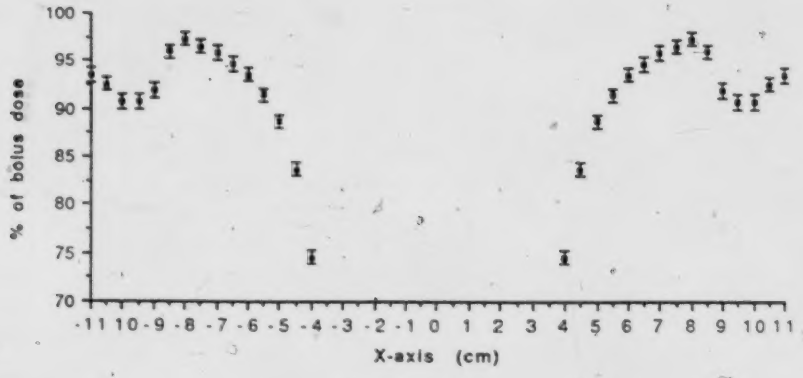

(c) 15MV

Figure 2.08 Compensated dose as a % of bolus dose for the geometric cone at 9cm depth (measured) (a) Cobalt-60, (b) 6MV, (c) 15MV.

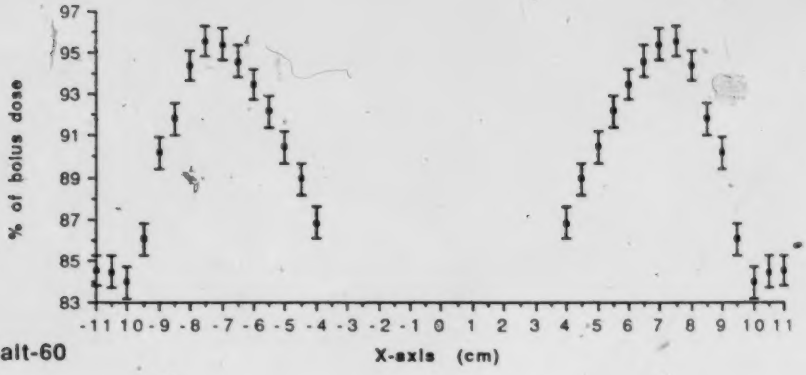

(a) Cobalt-60

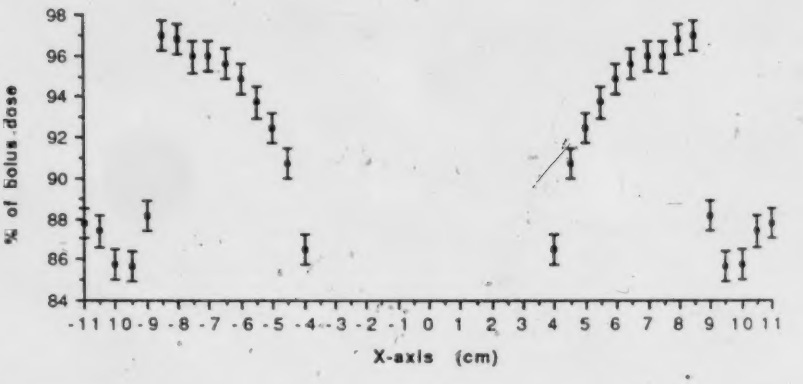

(b) 6MV

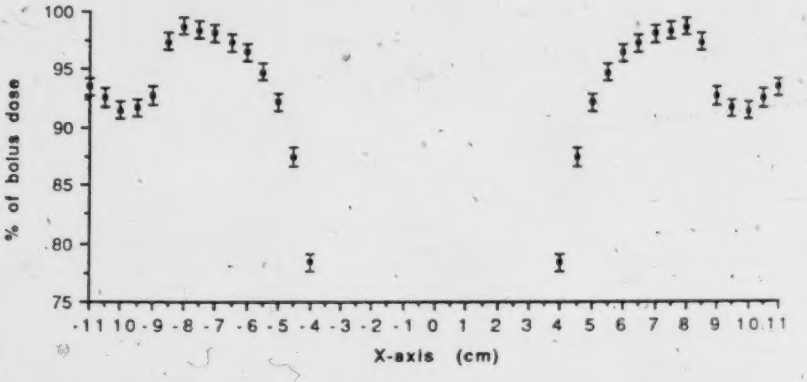

(c) 15MV

Figure 2.09 Compensated dose as a % of bolus dose for the aluminum cone at 9cm depth (measured) (a) Cobalt-60, (b) 6MV, (c) 15MV.

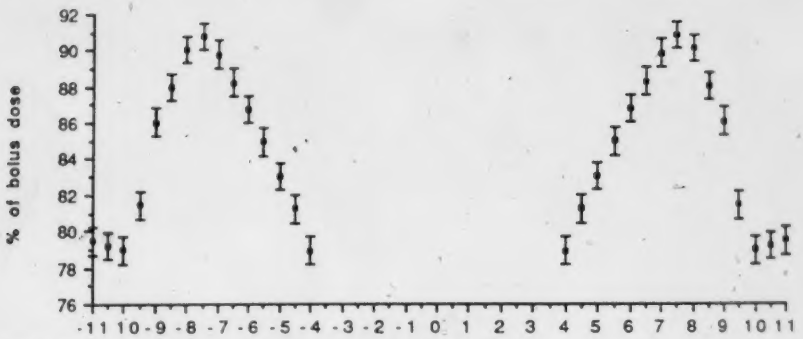

(a) Cobalt-60

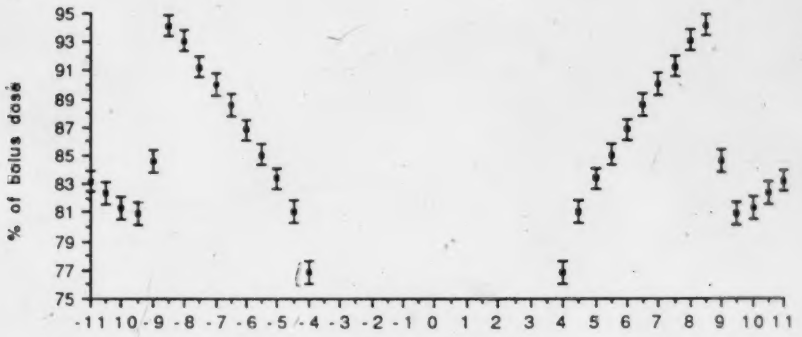

(b) 6MV

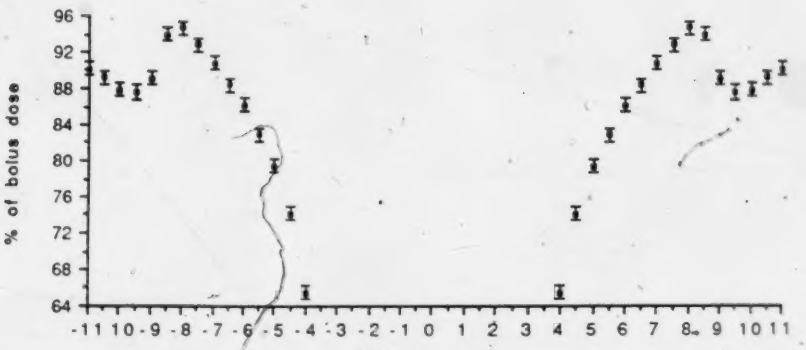

(c) 15MV

Figure 2.10 Compensated dose as a % of bolus dose for the lead cone at 9cm depth (measured) (a) Cobalt-60, (b) 6MV, (c) 15MV.

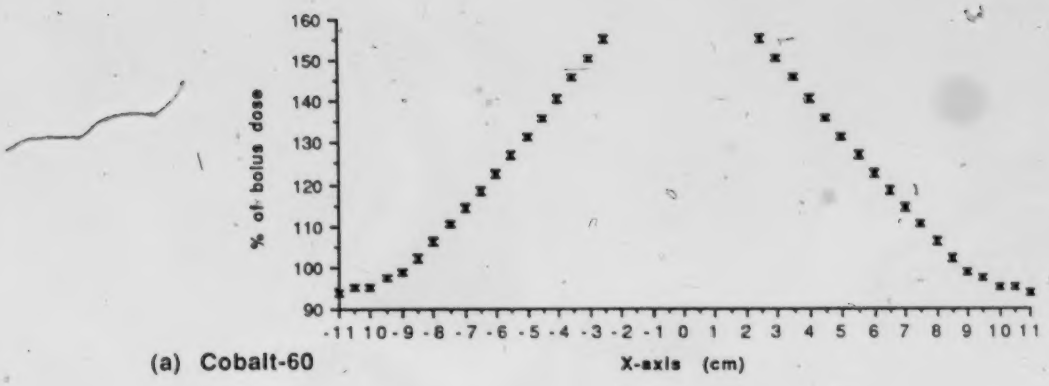

(a) Cobalt-60

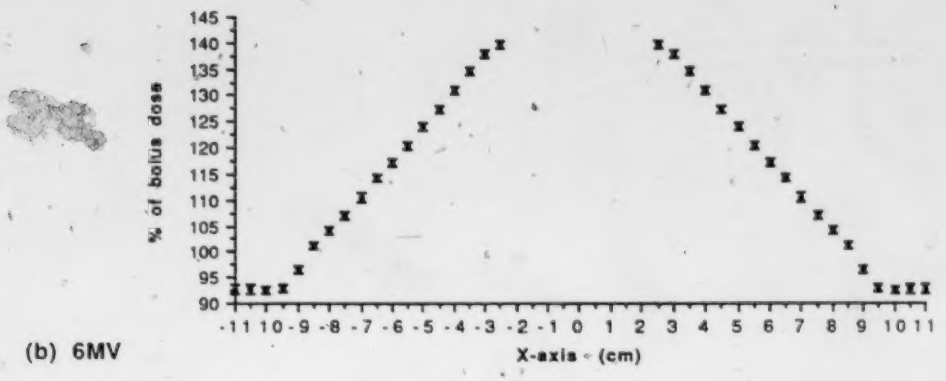

(b) 6MV

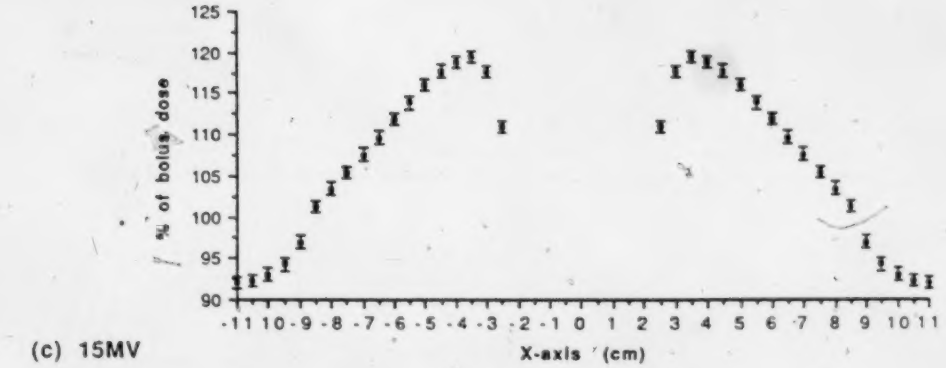

(c) 15MV

Figure 2.11 Uncompensated dose as a % of bolus dose at 12cm depth (measured) (a) Cobalt-60, (b) 6MV, (c) 15MV.

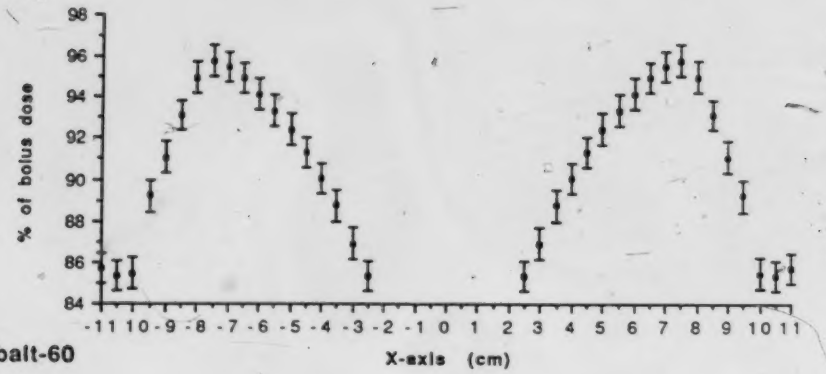

(a) Cobalt-60

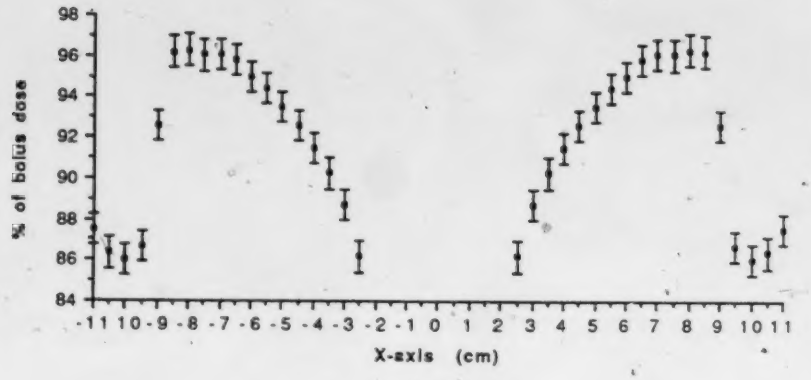

(b) 6MV

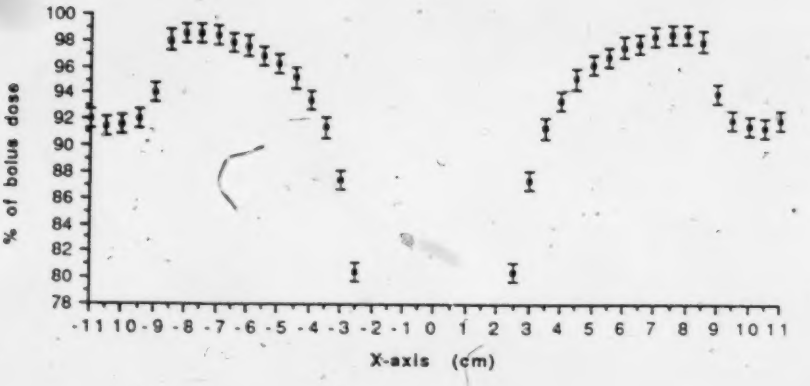

(c) 15MV

Figure 2.12 Compensated dose as a % of bolus dose for the geometric cone at 12cm depth (measured) (a) Cobalt-60, (b) 6MV, (c) 15MV.

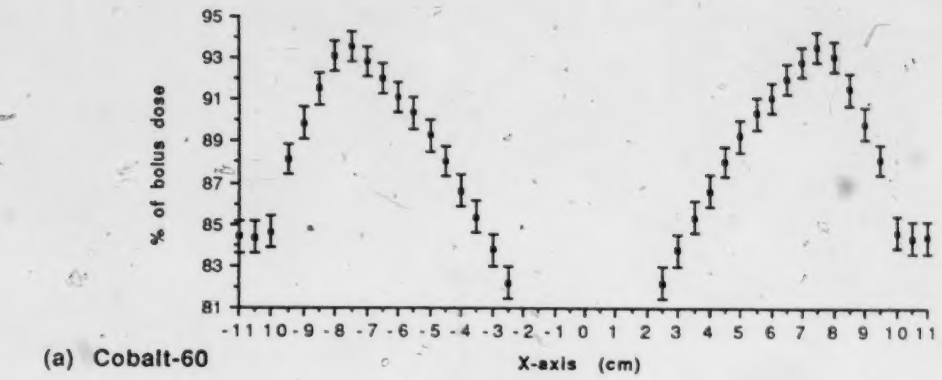

(a) Cobalt-60

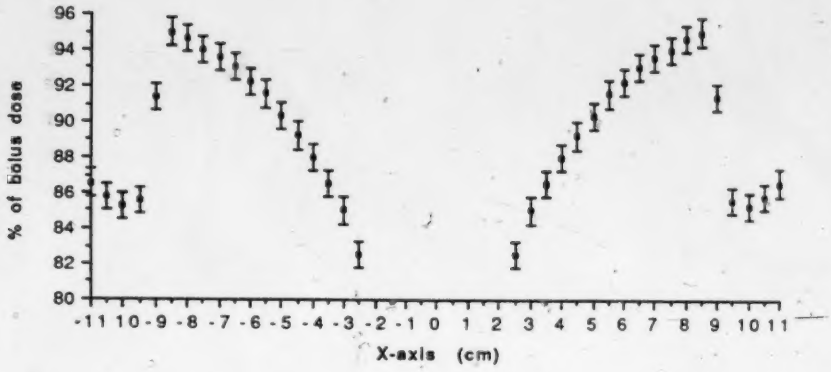

(b) 6MV

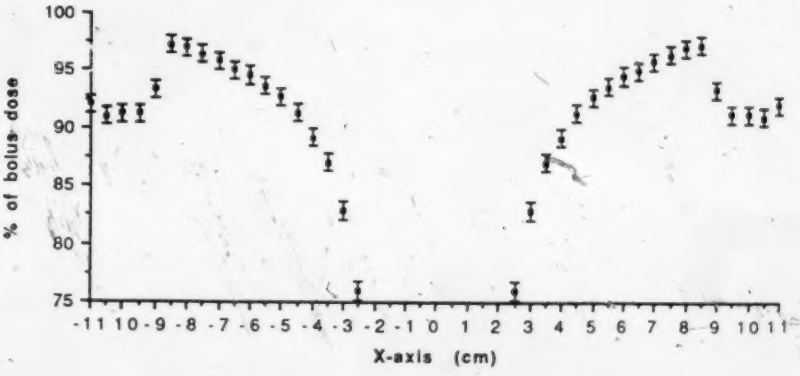

(c) 15MV

Figure 2.13 Compensated dose as a % of bolus dose for the aluminum cone at 12cm depth (measured) (a) Cobalt-60, (b) 6MV, (c) 15MV.

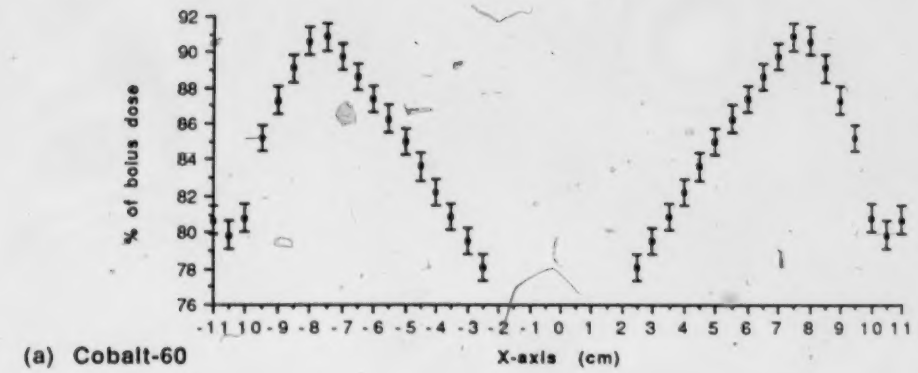

(a) Cobalt-60

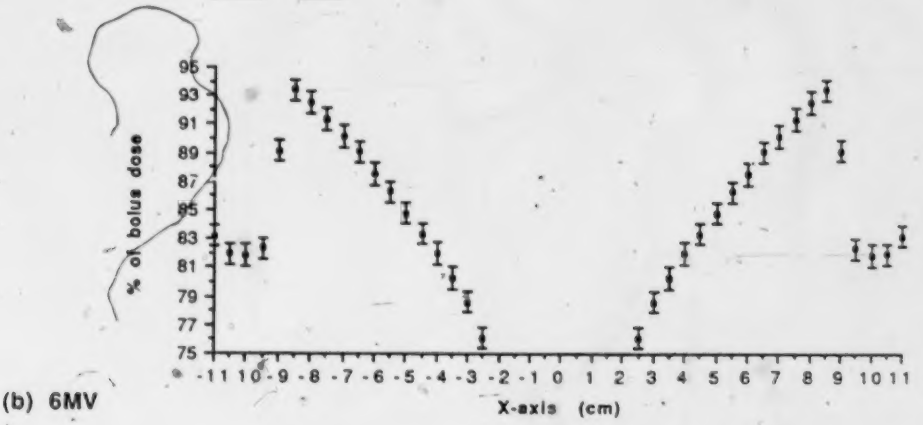

(b) 6MV

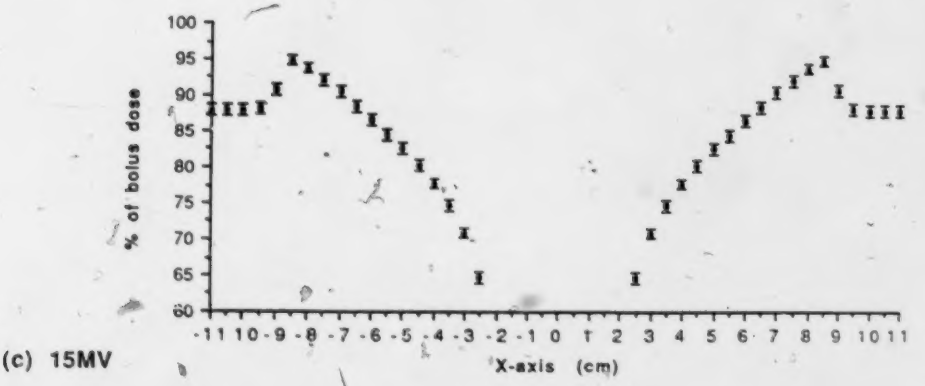

(c) 15MV

Figure 2.14 Compensated dose as a % of bolus dose for the lead cone at 12cm depth (measured) (a) Cobalt-60, (b) 6MV, (c) 15MV.

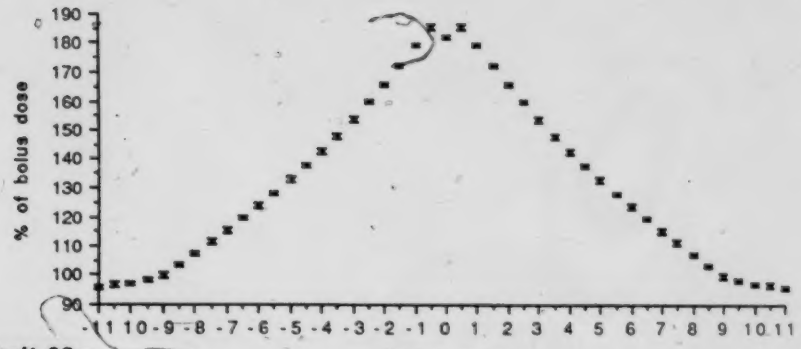

(a) Cobalt-60

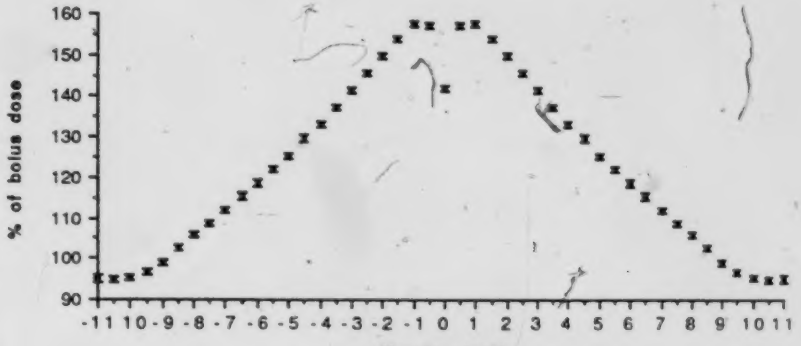

(b) 6MV

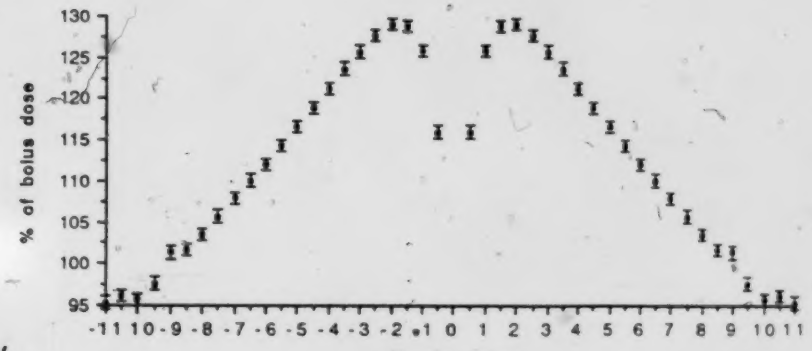

(c) 15MV

Figure 2.15 Uncompensated dose as a % of bolus dose at 15cm depth (measured) (a) Cobalt-60, (b) 6MV, (c) 15MV.

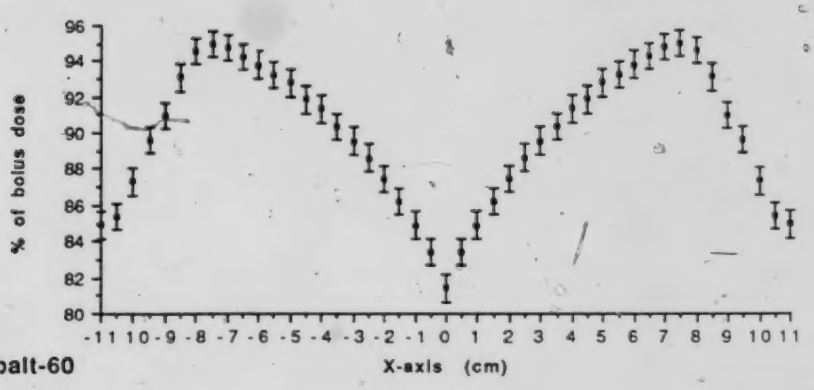

(a) Cobalt-60

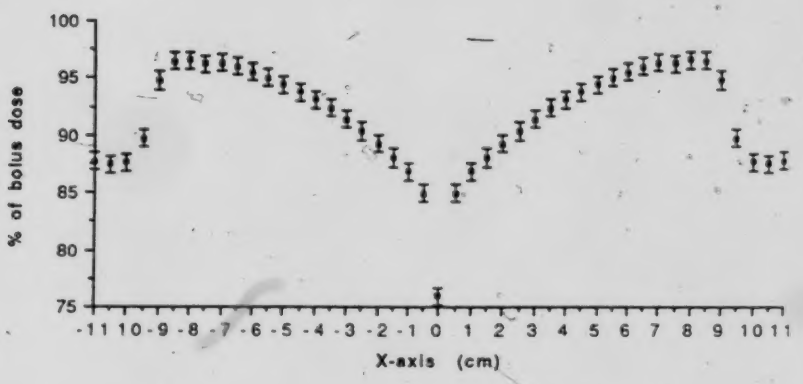

(b) 6MV

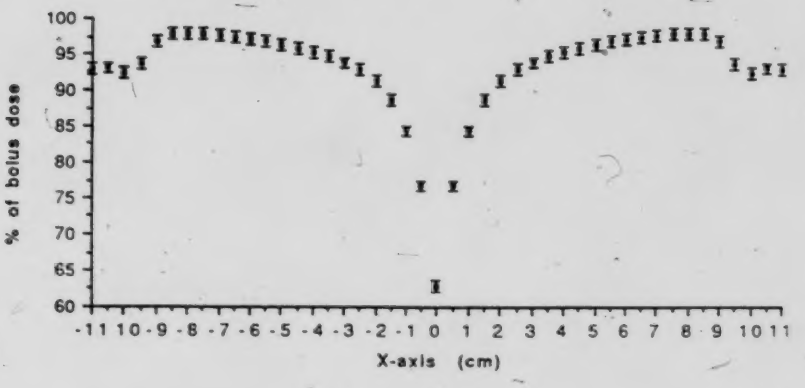

(c) 15MV

Figure 2.16 Compensated dose as a % of bolus dose for the geometric cone at 15cm depth (measured) (a) Cobalt-60, (b) 6MV, (c) 15MV.

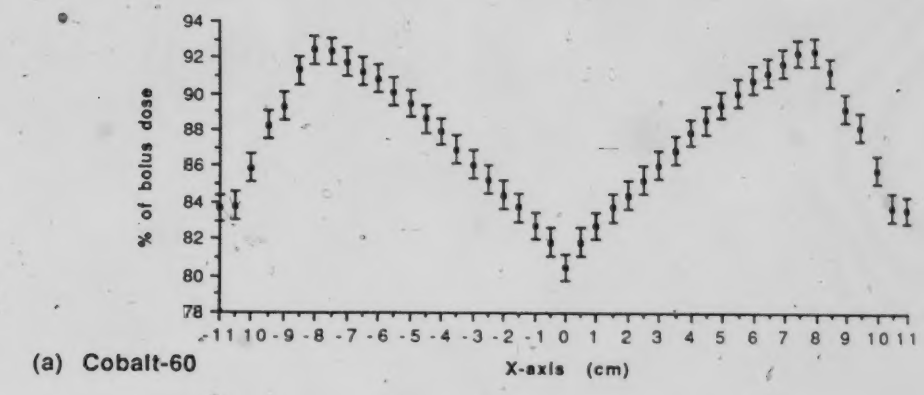

(a) Cobalt-60

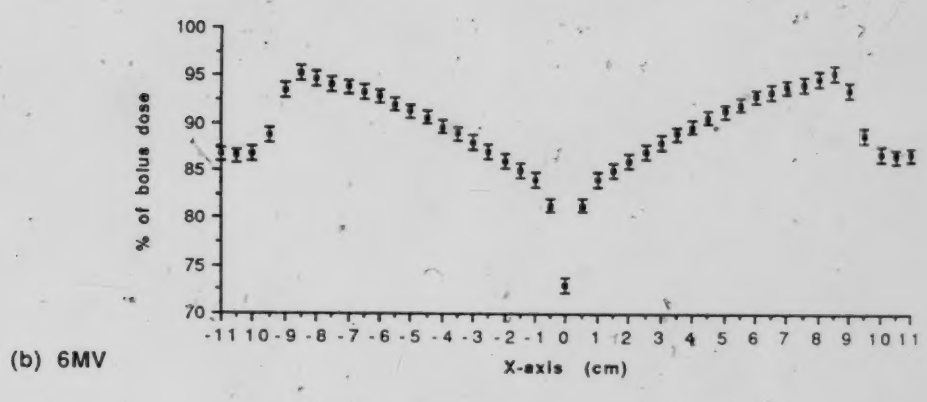

(b) 6MV

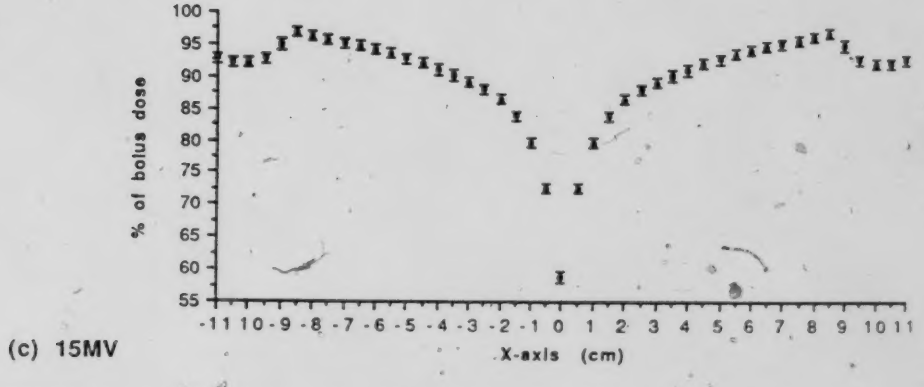

(c) 15MV

Figure 2.17 Compensated dose as a % of bolus dose for the aluminum cone at 15cm depth (measured) (a) Cobalt-60, (b) 6MV, (c) 15MV.

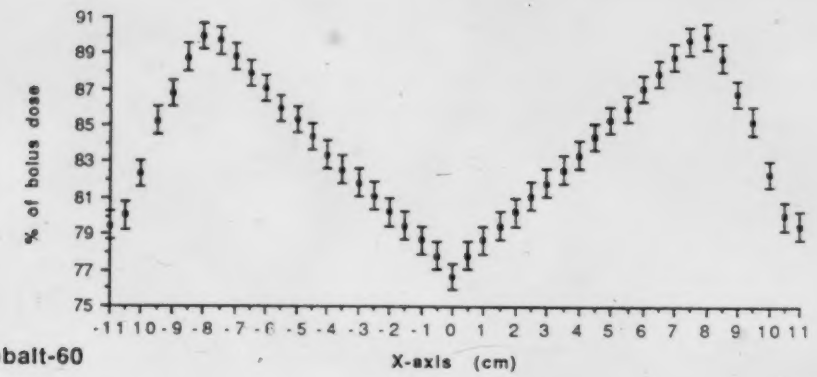

(a) Cobalt-60

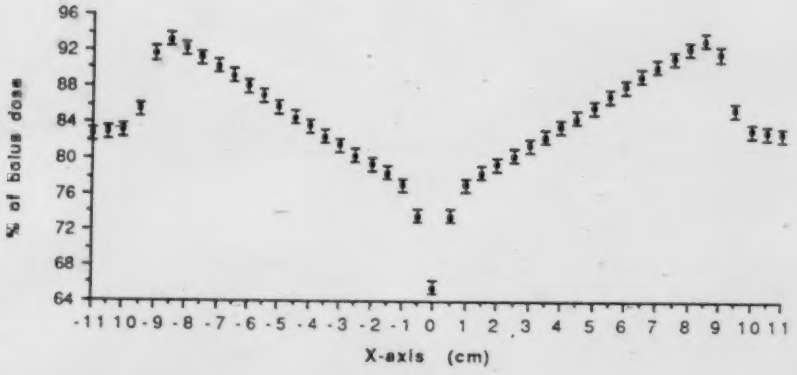

(b) 6MV

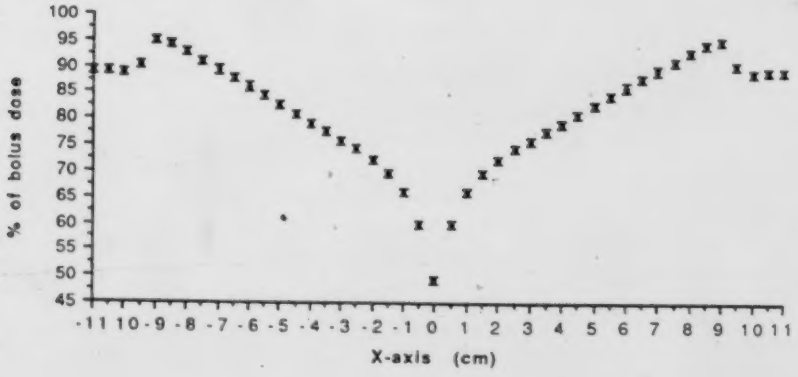

(c) 15MV

Figure 2.18 Compensated dose as a % of bolus dose for the lead cone at 15cm depth (measured) (a) Cobalt-60, (b) 6MV, (c) 15MV.

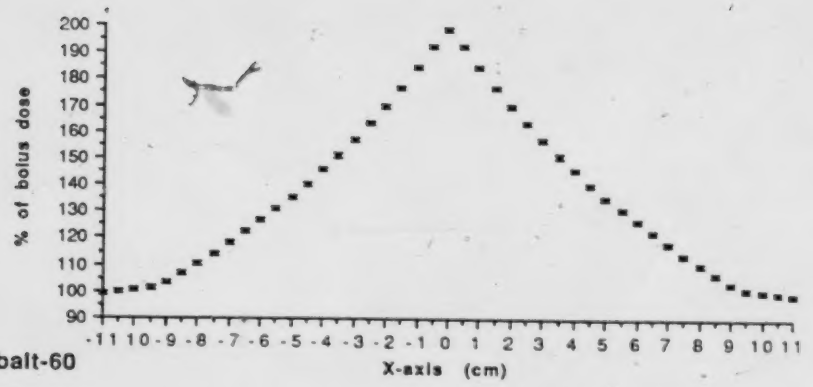

(a) Cobalt-60

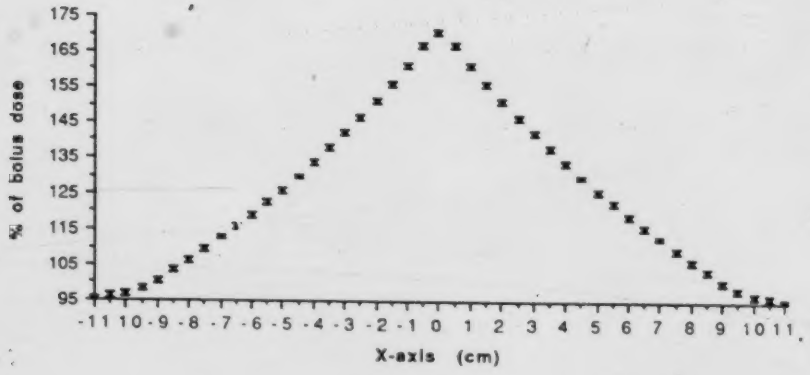

(b) 6MV

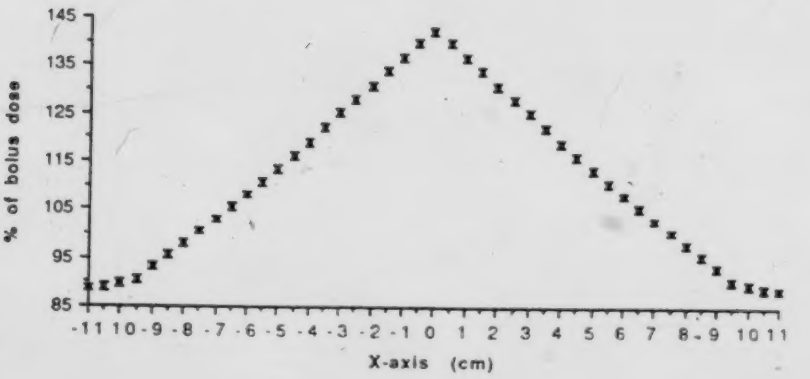

(c) 15MV

Figure 2.19 Uncompensated dose as a % of bolus dose at 17cm depth (measured) (a) Cobalt-60, (b) 6MV, (c) 15MV.

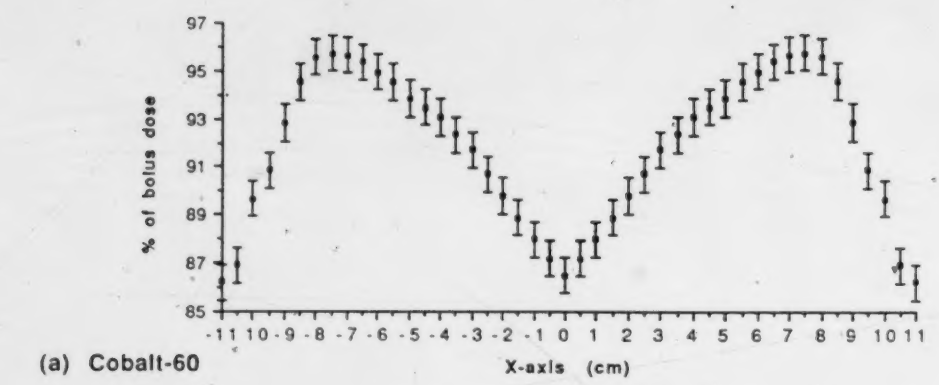

(a) Cobalt-60

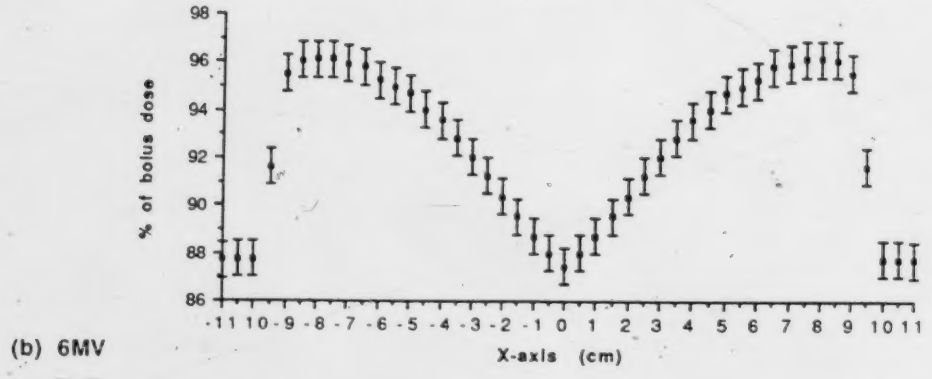

(b) 6MV

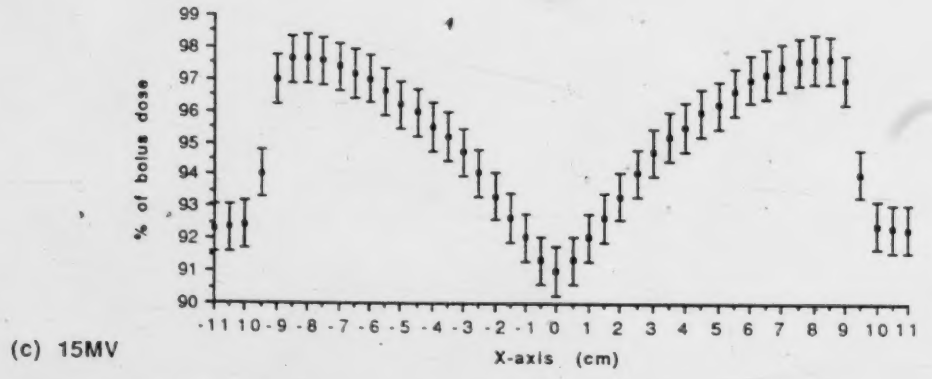

(c) 15MV

Figure 2.20 Compensated dose as a % of bolus dose for the geometric cone at 17cm depth (measured) (a) Cobalt-60, (b) 6MV, (c) 15MV.

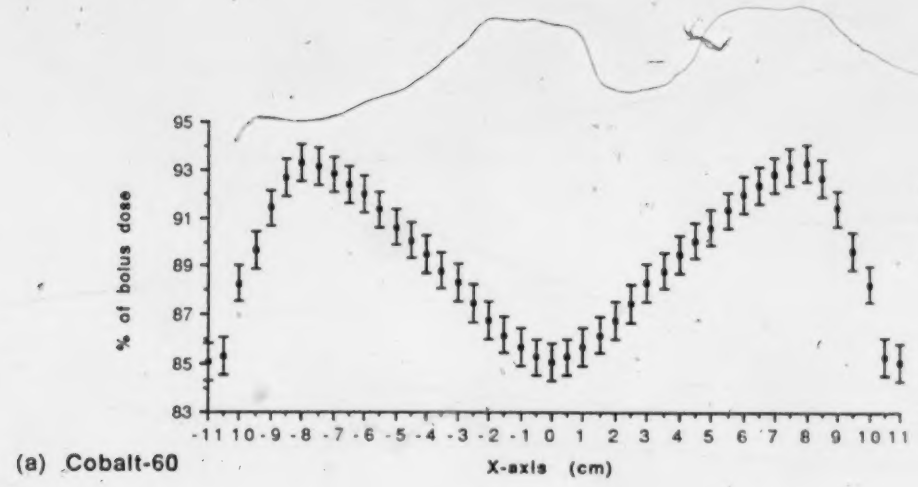

(a) Cobalt-60

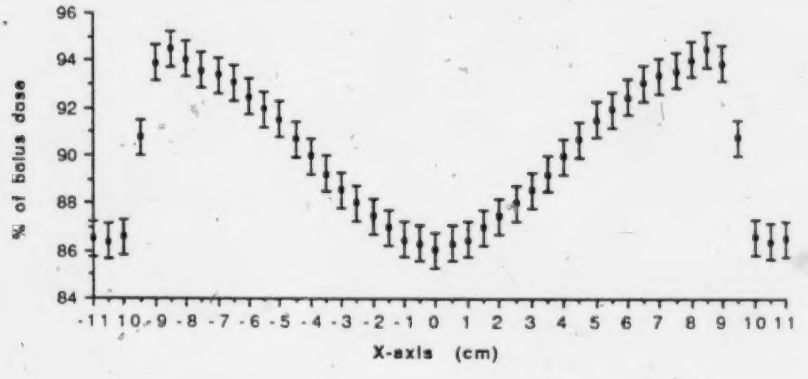

(b) 6MV

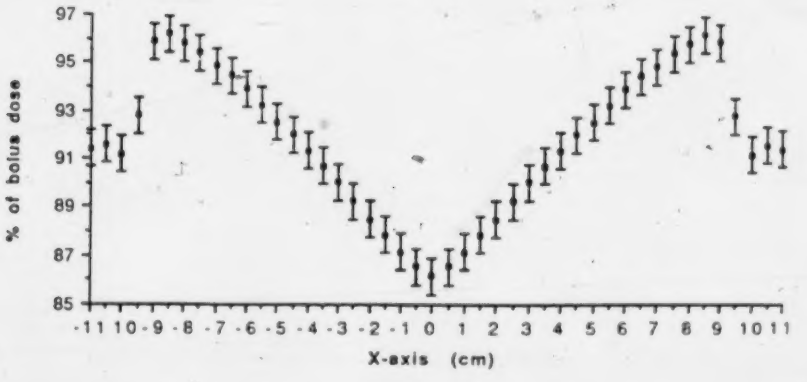

(c) 15MV

Figure 2.21 Compensated dose as a % of bolus dose for the aluminum cone at 17cm depth (measured) (a) Cobalt-60, (b) 6MV, (c) 15MV.

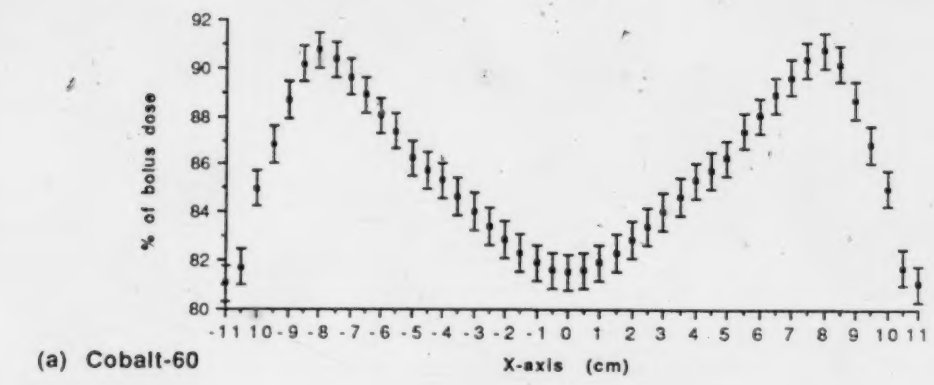

(a) Cobalt-60

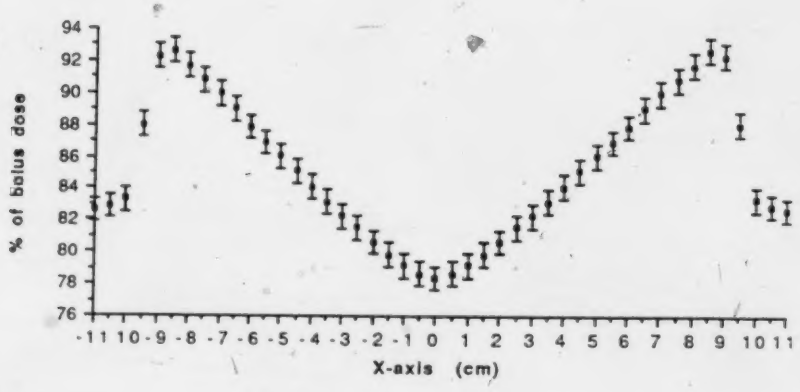

(b) 6MV

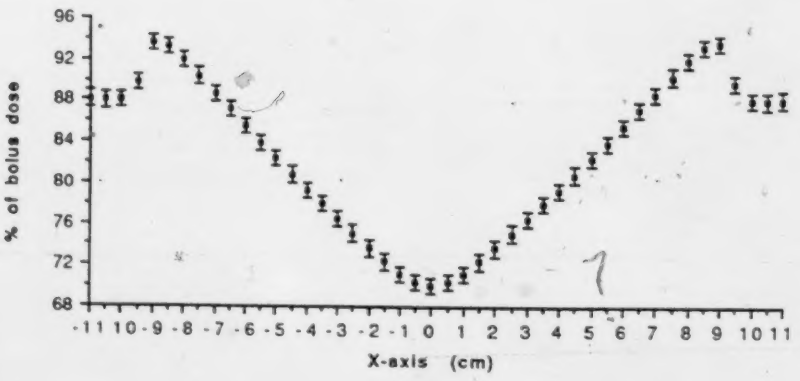

(c) 15MV

Figure 2.22 Compensated dose as a % of bolus dose for the lead cone at 17cm depth (measured) (a) Cobalt-60, (b) 6MV, (c) 15MV.

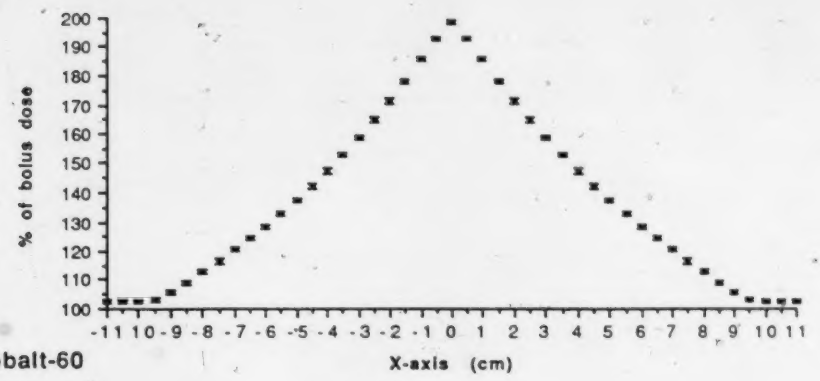

(a) Cobalt-60

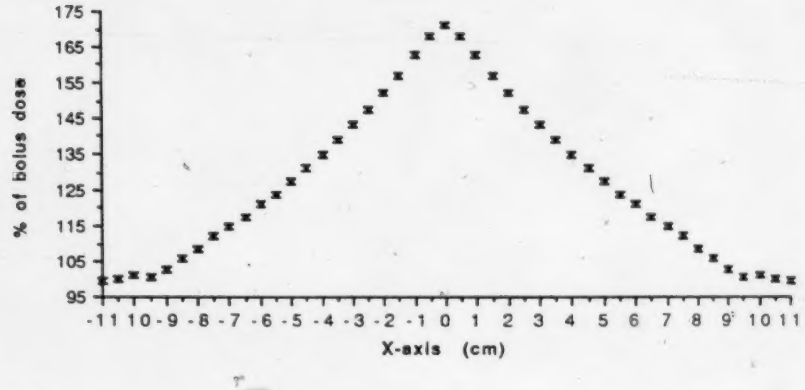

(b) 6MV

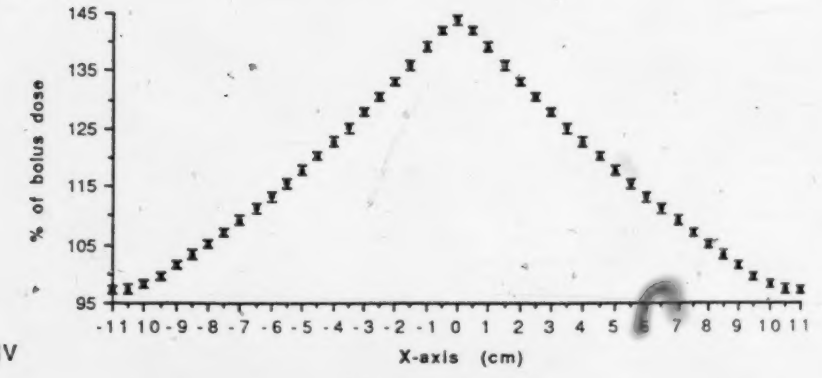

(c) 15MV

Figure 2.23 Uncompensated dose as a % of bolus dose at 21cm depth (measured) (a) Cobalt-60, (b) 6MV, (c) 15MV.

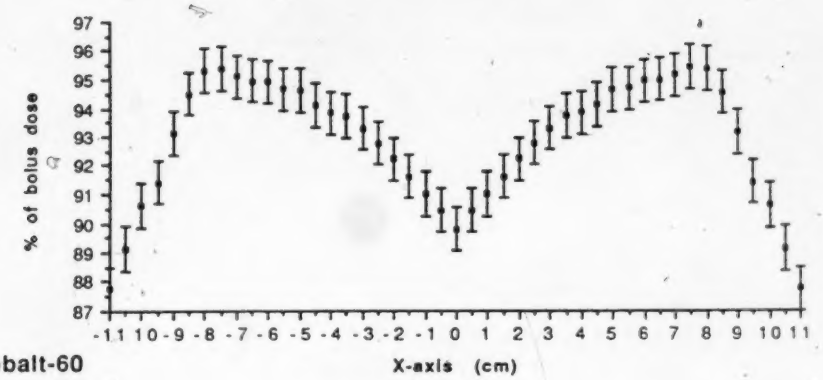

(a) Cobalt-60

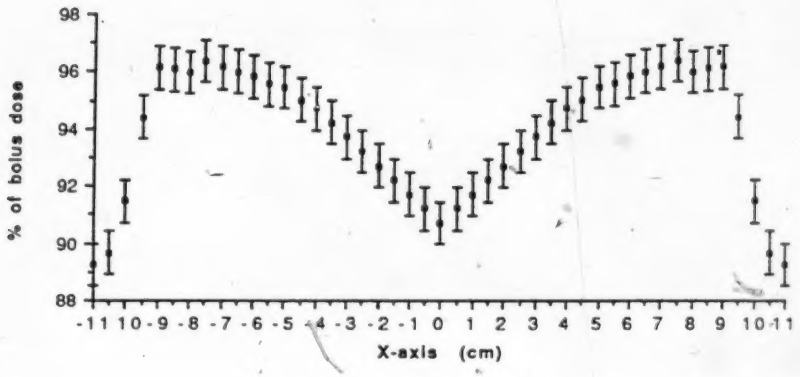

(b) 6MV

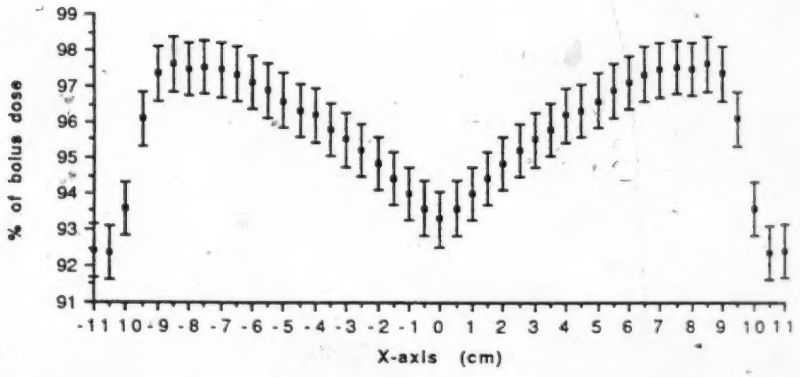

(c) 15MV

Figure 2.24 Compensated dose as a % of bolus dose for the geometric cone at 21cm depth (measured) (a) Cobalt-60, (b) 6MV, (c) 15MV.

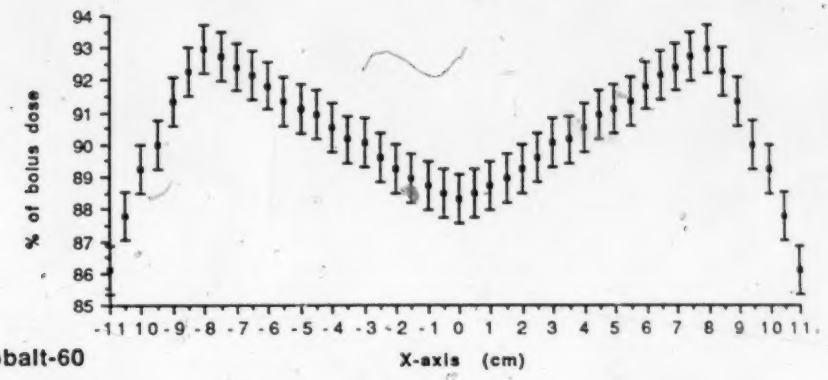

(a) Cobalt-60

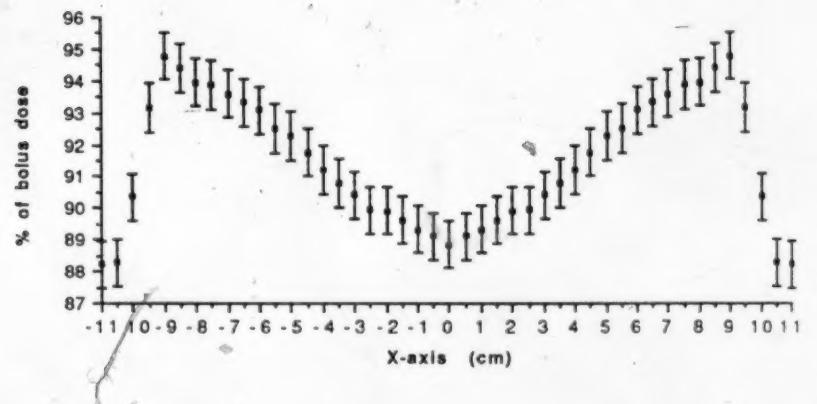

(b) 6MV

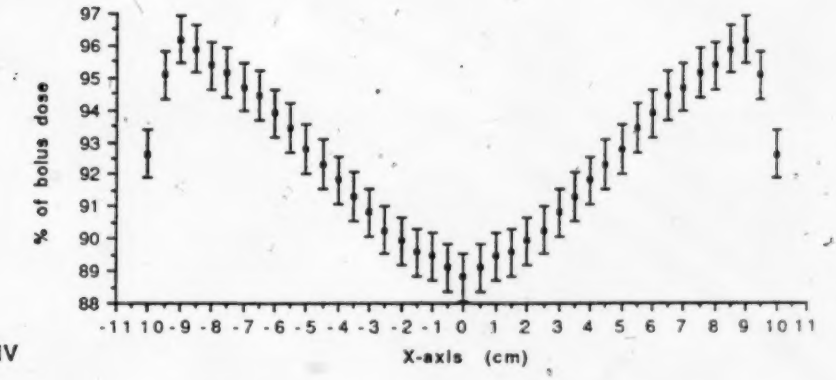

(c) 15MV

Figure 2.25 Compensated dose as a % of bolus dose for the aluminum cone at 21cm depth (measured) (a) Cobalt-60, (b) 6MV, (c) 15MV.

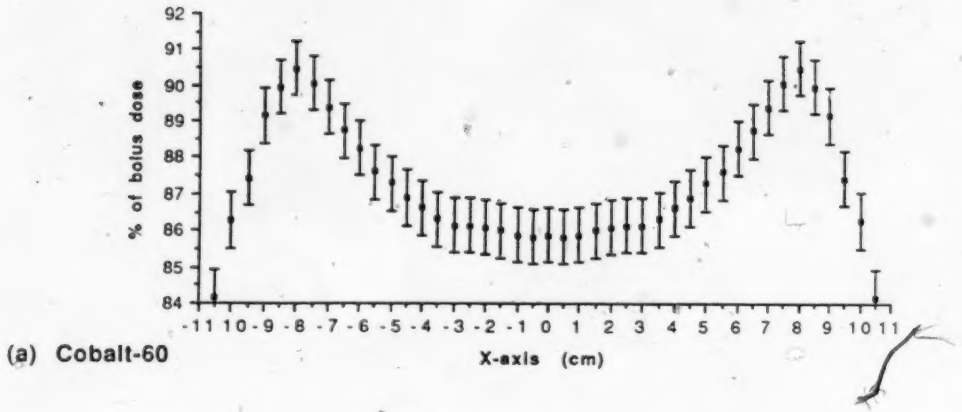

(a) Cobalt-60

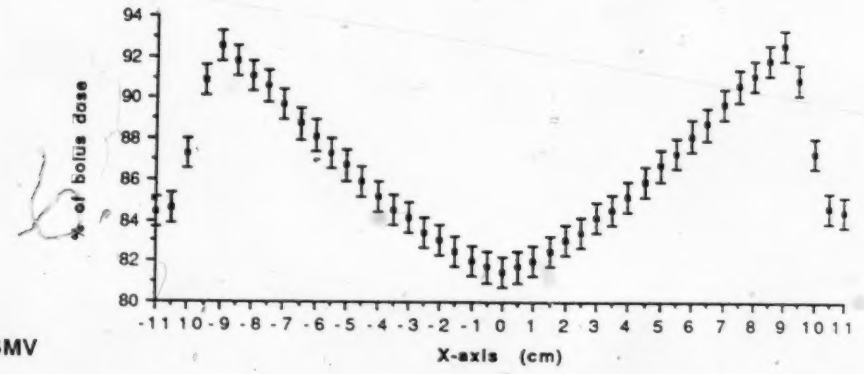

(b) 6MV

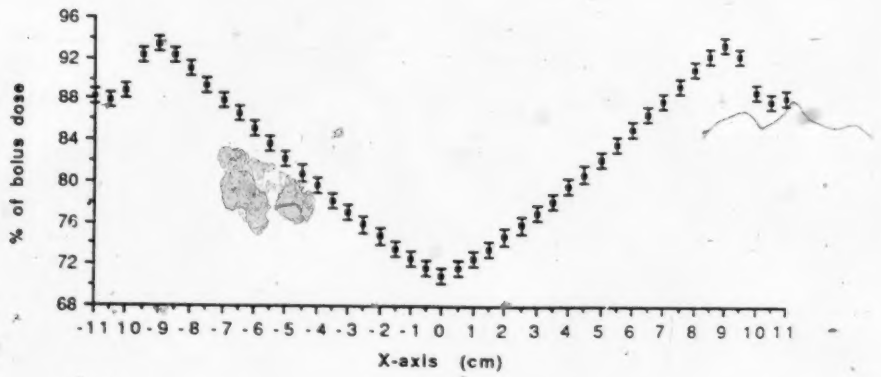

(c) 15MV

Figure 2.26 Compensated dose as a % of bolus dose for the lead cone at 21cm depth (measured) (a) Cobalt-60, (b) 6MV, (c) 15MV.

and lead compensator cones are revealed for the five different depths for each photon energy in Figures 2.07 through 2.26. While the degree of perturbation and subsequent degree of compensation varies from one situation to another, the following general observations apply:

a) Uncompensated dose distributions

i) Large perturbations from bolus dose are introduced at all depths and energies by the surface depression cone.

ii) Departures from bolus dose introduced by the surface cone are greatest for Cobalt-60, least for 15MV, and intermediate for 6MV photons at a given depth and location along the line of measurement. At the centre of the field at 17cm depth with Cobalt-60 photons the uncompensated dose is 100% greater than the bolus dose, while at the same location with 15MV photons the uncompensated dose is 40% greater than bolus dose. 6MV photons yield an uncompensated dose of about 71% greater than the bolus dose at this same location.

b) Compensated dose distributions

i) Dramatic reductions in the differences from bolus dose at all depths and all energies are achieved with the use of each of the three compensators. At the field centre, at 17cm depth, with Cobalt-60 photons the +100% uncompensated perturbation is reduced to -13.5% with the polystyrene geometric cone while at the same location, with 15MV photons, the +40% uncompensated perturbation is reduced to -9% with the same compensator.

ii) Ideally, the use of a compensator should yield graphs at a particular depth which present flat lines at 100%, ie: a situation

in which the compensator accurately restores the bolus dose distribution at all points at that depth. The measurements taken in the compensated configurations show clearly that at no depth or energy is ideal compensation achieved with any of the compensators used. In all cases the compensated dose is less than the bolus dose across the entire field of measurement.

iii) In all cases the degree of restoration of bolus dose achieved by these compensators is non-uniform across the entire field of measurement. For Cobalt-60 photons at 17cm depth the compensated dose varies from a minimum of 4% below bolus dose near the field edges to a maximum of 13.5% below bolus dose at the centre of the field. For 15MV photons at the same depth with the same compensator the compensated dose varies from a minimum of 2% below bolus dose near the field edges to a maximum of 9% below bolus dose at the centre of the field.

iv) In all cases the maximum departure from bolus dose observed for compensated irradiation is greater than that predicted on the basis of primary attenuation considerations only. These maximum departures(both experimental and predicted) are listed in Table 2.2 for ease of comparison.

v) In all cases the observed compensated dose distributions are inadequate and demonstrate the need for improved tissue compensator design.

vi) The greatest degree of restoration of bolus dose with geometric compensators is achieved with polystyrene, the least is achieved with lead, and intermediate restoration is achieved

Compensator	Depth (cm)	Primary Photon Energy					
		Cobalt-60		6MV		15MV	
		predicted	measured	predicted	measured	predicted	measured
Geometric Polystyrene	9	+0.9%	13.0%	+0.4%	13.5%	0.2%	21.5%
	12	+0.9%	15.0%	+0.4%	14.0%	0.2%	19.5%
	15	+0.9%	19.0%	+0.4%	24.0%	0.2%	37.0%
	17	+0.9%	13.5%	+0.4%	12.5%	0.2%	9.0%
	21	+0.9%	10.0%	+0.4%	9.5%	0.2%	6.5%
Aluminum	9	0.1%	16.5%	+0.7%	17.0%	+3.5%	25.5%
	12	0.1%	18.0%	+0.7%	17.5%	+3.5%	24.0%
	15	0.1%	19.5%	+0.7%	27.0%	+3.5%	41.0%
	17	0.1%	15.0%	+0.7%	14.0%	+3.5%	14.0%
	21	0.1%	11.5%	+0.7%	11.0%	+3.5%	11.0%
Lead	9	+0.04%	21.0%	+0.01%	23.0%	21.0%	34.5%
	12	+0.04%	22.0%	+0.01%	24.0%	21.0%	35.5%
	15	+0.04%	23.5%	+0.01%	35.0%	21.0%	51.0%
	17	+0.04%	18.5%	+0.01%	22.0%	21.0%	30.0%
	21	+0.04%	14.0%	+0.01%	18.5%	21.0%	29.0%

Table 2.2 Maximum departure from bolus dose in the conical geometry. Comparison between that predicted on the basis of replacement of missing primary attenuation only and that observed experimentally.

with aluminum. Thus if geometric compensators are to be employed clinically, as they often are, then the use of near unit density materials for their construction is recommended and the use of higher density materials is not recommended. In particular, the use of lead is to be avoided.

Chapter 3

Theoretical Analysis

For hypothesis ought ... to explain the properties of things and not attempt to predetermine them except in so far as they can be an aid to experiments.

Isaac Newton

III THEORETICAL ANALYSIS

3.1 Rationale and Introduction

The first step towards the rigorous design of improved tissue compensators is the development of analytic machinery which will accurately model the experimental results already obtained. Such a theoretical model should not be restricted in its applicability to a limited set of special cases but rather have as wide a scope as possible. In order to achieve this the analysis should make minimum use of ad hoc measured "effective" coefficients and functions. When pressed for a rigorous explanation of a physical phenomenon it is most desirable to produce an argument based on the fundamental physical laws which are applicable to that situation. Thus this model should maximize its use of the fundamental physical laws governing the interactions of radiation with matter such as are relevant to the scope of applicability contemplated. Inherent to any theoretical analysis of a physical situation is a set of assumptions or simplifications which serve either as starting points for the analysis or constraints upon the derivations involved. They serve the purposes of simplifying the calculations involved and keeping clear the focus upon the concepts of primary importance. These assumptions and simplifications should be clearly stated whenever and wherever they are invoked.

In an arrangement employing a retracted tissue compensator the dose to any point in a phantom may be divided into three components: (1) the dose

due to primary radiation, (2) the dose due to scattered radiation originating from within the phantom, (3) and the dose due to scattered radiation originating from within the compensator. Of these three, the dose due to primary radiation is most often the predominant component. The experimental results shown in Chapter 2 with compensators designed to account only for missing primary attenuation would seem to bear out such an assumption as they indeed yield a good first approximation to the complete restoration of the desired bolus dose distribution. However, the obvious deficiencies in the observed results clearly demonstrate that scattered radiation originating in both the phantom and compensator must therefore be taken into account if the degree of optimization achieved is to be further improved.

3.2 THE ANALYTIC MODEL

The total dose D, at a point P in a phantom, such as is shown in Figure 3.01, can be decomposed as

$$D = \sum_{ij} D_{ij} \qquad \begin{matrix} i=0,1,2\cdots \\ j=0,1,2\cdots \end{matrix} \qquad \{3.01\}$$

where D_{ij} is the component of dose at P due to photons which have scattered "i" times in the phantom and "j" times in the compensator prior to interacting at P.

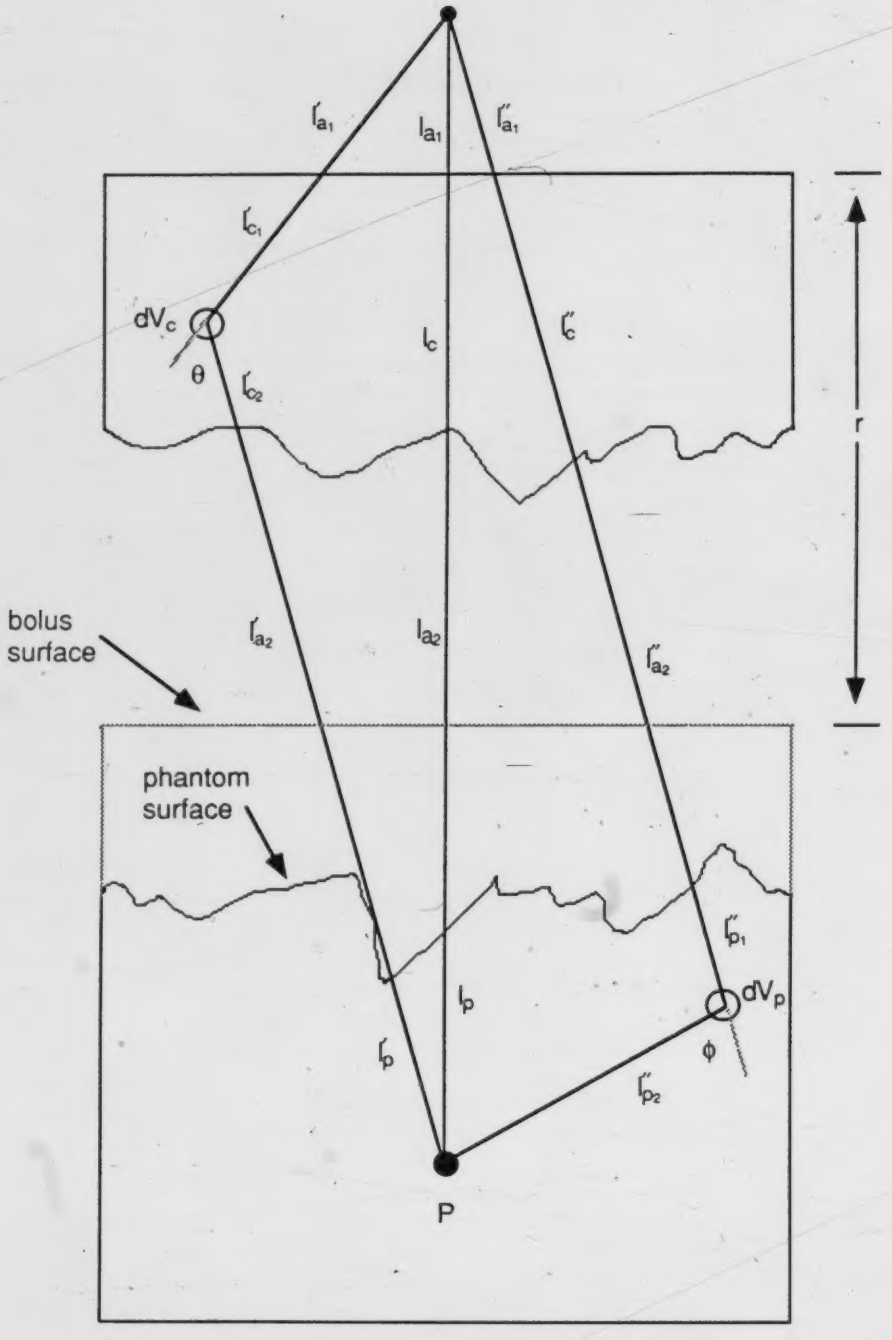

3.01 Geometry for theoretical analysis

For Cobalt-60 radiation at a depth of 10cm in water with a 10cm radius field, 93% of the total dose is accounted for by the dose due to primary and singly scattered radiation[3.1]. Calculation of dose due to scatter of higher than first order, while possible (Monte Carlo calculations), rapidly becomes intractable both in terms of complexity and calculation time. One is thus lead to attempt an analysis based on zero and first order scatter only and this is the first assumption made in this analytical model. Then equation 3.1 reduces to

$$D = D_{00} + D_{10} + D_{01} \qquad \{3.2\}$$

or, for the sake of clarity

$$D = D_0 + D_p + D_c \qquad \{3.3\}$$

where D_0 = dose due to primary radiation, D_p = dose due to first order scatter originating within the phantom, and D_c = dose due to first order scatter originating within the compensator.

The decay of Cobalt-60 produces photons which may be regarded as monoenergetic with an energy of 1.25MeV. It is well known that the photon output from a Cobalt-60 treatment unit consists of more than the primary decay photons. A low energy contamination component arising from scatter both from within the source itself and from the collimator system is also present. This scatter component has been measured by Scrimger and Cormack[3.2] and can be characterized by 250keV photons which contribute

approximately 10% of the intensity of the primary output of such a unit. For the purposes of analysis this contamination component will be ignored and the output from the Cobalt-60 teletherapy unit used in this work will be considered as consisting of monoenergetic photons of energy 1.25MeV.

As was mentioned previously, the photon output of a linac consists of a spectrum of energies ranging from some minimum value up to a specific maximum value, with the beam produced being characterized according to this maximum photon energy. A contamination component arising from scatter produced by the collimation system and other devices in the treatment head of the accelerator is also present. While such a beam is far from monoenergetic, there exist photons of a single energy which possess the same linear attenuation characteristics in water as does this beam. This single energy is referred to as the equivalent energy of the spectrum beam. For a 6MV photon beam the equivalent energy is 2MeV and for a 15MV beam the equivalent energy is 5MeV. In order to simplify the analysis the beams produced by the 6MV and 15MV accelerators used in this work will be treated as if they consist of monoenergetic photons of energies 2MeV and 5MeV respectively.

With the above assumption, consider the case in which the compensator-phantom arrangement shown in Figure 3.01 is irradiated with monoenergetic photons of energy E_0(MeV). If electronic equilibrium exists at point P, the dose due to primary photons at P is

$$D_0(r) = \Phi_0\, e^{-\mu_a(E_0)[l_{a_1}+l_{a_2}]}\, e^{-\mu_c(E_0)l_c}\, e^{-\mu_p(E_0)l_p} \left(\frac{\mu_{en}}{\rho}\right)_{E_0} \left(\frac{E_0}{dA}\right) \left(\frac{dA}{[l_{a_1}+l_{a_2}+l_c+l_p]^2}\right) \quad \{3.4\}$$

where Φ_0 = photon number per unit solid angle(photons sr^{-1}); $\mu_a(E_0)$, $\mu_c(E_0)$, $\mu_p(E_0)$ = linear attenuation coefficients(cm^{-1}) at photon energy E_0 for air, compensator material, and phantom material respectively; $l_{a_1}+l_{a_2}$ = the total primary path length through air(cm); l_c and l_p = primary path lengths through compensator and phantom respectively(cm); $(\mu_{en}/\rho)_{E_0}$ = mass energy absorption coefficient at E_0 for the phantom material(cm^2/g); r=compensator retraction distance(cm); and dA =infinitesimal area element at P(cm^2).

As discussed in Chapter 1, the only interactions of photons with matter which need to be considered in this work(due to the energy range of primary photons employed) are coherent scattering, photoelectric effect, Compton scattering, and pair and triplet production. The cross sections for these interactions in the four materials(water, polystyrene, aluminum, and lead) used in this study are shown in Tables 3.1 and 3.2. At the primary photon energy of 1.25MeV the compton interaction cross section is orders of magnitude greater than the other interaction cross sections for water, polystyrene, and aluminum. One thus need only consider the Compton interaction as a scattering mechanism for polystyrene, water, and aluminum at this energy. In lead at 1.25MeV the compton interaction cross section is almost 3000 times greater than the pair production cross section and thus one may safely ignore pair production in lead at this energy. Coherent scattering in lead at this energy is some 26 times less likely than compton

Material	Interaction Cross Section (barns)			
	σ_{COH}	σ_{INC}	τ_{photo}	π_{pair}
Water	0.00098	1.365	0.00009	0.00018
Polystyrene	0.00046	1.061	——	0.00009
Aluminum	0.0041	2.456	0.0007	0.0003
Lead	0.5875	15.40	3.987	0.0055

Table 3.1 Interaction cross sections for the materials water, polystyrene, aluminum, and lead at photon energy of 1.25MeV

Material	Interaction Cross Section (barns)			
	σ_{COH}	σ_{INC}	τ_{photo}	π_{pair}
Water	0.00009	0.600	——	0.06558
Polystyrene	——	0.4663	——	0.03876
Aluminum	0.0003	1.080	0.0001	0.1918
Lead	0.0373	6.805	0.4096	7.288

Table 3.2 Interaction cross sections for the materials water, polystyrene, aluminum, and lead at photon anergy of 5.0MeV

scattering and one may also safely ignore coherent scattering in lead at this energy. Compton scattering is, however, less than 4 times as likely as photoelectric interactions in lead at 1.25MeV. A 1MeV electron produced by a photoelectric interaction has a range of less than 1mm in lead and less than 4.5 mm in water and can thus be safely ignored for the measurement depths involved in this study. A 1.25 MeV incident photon compton scattered through 40° has an energy of 800 keV and has an attenuation coefficient in lead of 0.0872 $cm^2\ g^{-1}$. A K shell characteristic photon with an energy of 88keV resulting from a photoelectric interaction has an attenuation coefficient which is more than 20 times greater than the above 800keV compton scattered photon and thus characteristic radiation resulting from photoelectric interactions in lead may be safely ignored.

At a photon energy of 5MeV the coherent and photoelectric cross sections are again insignificant in comparison with the compton cross sections for water, polystyrene, and aluminum. The compton cross sections for water and polystyrene are approximately 10 times as great as that for pair production. The maximum energy of either the positron or electron created in pair production by a 5MeV photon is approximately 4MeV. Electrons and positrons with an energy of 5MeV have a range in both water and polystyrene of about 2.5cm and hence their contribution to the dose at the depths under consideration in this work may be safely ignored. The energy distribution between positrons and electrons created in pair production is, to a fairly good first approximation equal [3.3]. This, combined with the rather tortuous path of electrons(and positrons) having these initial energies, make it reasonable to assume that Bremsstrahlung photons created by these pair

electrons and positrons will have an isotropic angular distribution. The Bremsstrahlung yield for a 4MeV electron in water or polystyrene is approximately 0.0149 and hence a 4MeV electron in either material will radiate approximately 60keV of its energy away in the form of Bremsstrahlung photons. A 5MeV incident photon compton scattered through 40° has an energy of approximately 1.5MeV which has an attenuation coefficient in water of 0.0575 $cm^2\ g^{-1}$. A Bremsstrahlung photon of 60keV has an attenuation coefficient of 0.2046 $cm^2\ g^{-1}$ in water. These factors combined would suggest that the dose due to Bremsstrahlung photons associated with pair production in water and polystyrene may be safely ignored at 5MeV. Examination of Table 3.2 shows that similar arguments may be made for disregarding pair production in aluminum at 5MeV.

For lead, with 5MeV incident photons, the coherent cross section is more than 180 times smaller than the compton cross section and coherent scattering may be safely ignored. The photoelectric cross section for lead at this energy is more than 16 times smaller than the compton cross section and, following arguments similar to those made above for 1.25MeV incident photons, the contribution due to the photoelectric effect may also be safely disregarded at 5MeV in lead. The pair production cross section in lead at 5MeV is, however, greater than that of the compton cross section. Following arguments similar to those presented for water and polystyrene one may also safely disregard the dose directly due to electrons and positrons created by the pair production process. The Bremsstrahlung yield in lead is considerably higher than that in water for electrons(positrons) at any given

electron(positron) energy and one may not be justified in disregarding the dose due to Bremsstrahlung photons generated in lead by pair production electrons and positrons. For the sake of simplifying calculations the Bremsstrahlung dose due to pair production in lead with 15MV photons will be disregarded, the validity(or lack thereof) of this assumption will be born out by comparison between theory and measurement.

Following the above arguements, the assumption will be made that only Compton scattering need be considered. The dose $dD_c(r)$ at P due to single scattering from volume element dV_c in the compensator is then

$$dD_c(r) = \Phi_0 \frac{dA}{[l'_{a_1}+l'_{c_1}]^2} e^{-\mu_a(E_0)l'_{a_1}} e^{-\mu_c(E_0)l'_{c_1}} \left(\frac{\partial\sigma}{\partial\Omega}\right)_\theta \rho_{ec}\, dl_{vc} \frac{dA}{[l'_{c_2}+l'_{a_2}+l'_p]^2} \quad \{3.5\}$$

$$X \quad e^{-\mu_c(E_1)l'_{c_2}} e^{-\mu_a(E_1)l'_{a_2}} e^{-\mu_p(E_1)l'_p} \left(\frac{\mu_{en}}{\rho}\right)_{E_1} \frac{E_1}{dA}$$

where electronic equilibrium is again assumed at point P and $\partial\sigma/\partial\Omega_\theta$ = the differential Compton scattering cross-section($cm^2\ e^{-1} sr^{-1}$); ρ_{ec}= electron density of compensator medium($e\ cm^{-3}$);dl_{vc}= linear dimension(cm) along l'_{c_1} of compensator scattering volume element dV_c ; and E_1= energy of single scattered photons at angle θ from.dV_c (MeV).

Similarly, the dose $dD_p(r)$ at P due to single scattering from volume element dV_p in the phantom is

$$dD_p(r) = \Phi_0 \frac{dA}{\left[l''_{a_1}+l''_c+l''_{a_2}+l''_{p_1}\right]^2} e^{-\mu_a(E_0)\left(l''_{a_1}+l''_{a_2}\right)} e^{-\mu_c(E_0)l''_c} e^{-\mu_p(E_0)l''_{p_1}} \left(\frac{\partial\sigma}{\partial\Omega}\right)_\phi \rho_{ep}\, dl_{vp}$$

$$\frac{dA}{\left[l''_{p_2}\right]^2} e^{-\mu_p(E_2)l''_{p_2}} \left(\frac{\mu_{en}}{\rho}\right)_{E_2} \frac{E_2}{dA} \qquad \{3.6\}$$

where ρ_{ep}= electron density of phantom material(e cm^{-3}), dl_{vp}= linear dimension(cm) along l''_{p_1} of phantom scattering volume element dV_p ; and E_2= energy of single scattered photon at angle ϕ from phantom volume dV_p(MeV).

The total first scatter dose to point P is then

$$D(r) = D_0(r) + \int_{V_c} dD_c(r) + \int_{V_p} dD_p(r) = D_0(r) + D_c(r) + D_p(r) \,. \qquad \{3.7\}$$

where V_c and V_p are the volumes of the compensator and phantom respectively.

The ratio R(r) of the dose in the retracted compensator geometry to that with bolus at point P is thus

$$R(r) = \frac{D(r)}{D(r=0)} \qquad \{3.8\}$$

3.3 Analytic Results

A computer program was written to evaluate numerically the integrals of equation 3.7. This program was in turn used to calculate R(r) for the experimental geometries detailed in Chapter 2. This program, called CONE, was written in Fortran-77 to run on the VMS operating system of a VAX 11/780 computer. In this program both the phantom and compensator volumes are divided up into interaction volume elements, or voxels, of size 0.5X0.5X0.5 cm^3. The centre of each voxel serves as the interaction site of that volume element. That is to say that for the purpose of simplification each interaction occurring within the volume element, whether it be scattering or dose deposition, is regarded as occurring at the centre of that voxel as if at the moment of interaction the entire mass of the volume element were suddenly collapsed into an infinitesimal sphere at the centre of the voxel. In reality, photons incident upon such a finite voxel from an external point source would have differing interaction path lengths through the mass and the scattered photons produced in this volume element and directed towards another voxel would possess a spectrum of scattering angles and energies. This "trick" of regarding interactions in a small but nevertheless finite volume as interactions at a point greatly simplifies calculations as questions of differing interaction path lengths in the volume, differing scattering angles and energies, and orientation of the volume element with regard to both the external point source of incident photons and the volume to which scattered photons are directed are circumvented. The degree of agreement achieved between measurement and calculation would seem to justify this as a reasonable simplification.

Voxels eligible for scattering and, in the phantom, deposition of both primary and scattered dose are determined by the size of the field and the geometry of the physical setup. The intensity of the X-ray beams used experimentally is not constant over the entire area of the beam. In an attempt to model this as well as the penumbral regions of the beam, scans of the beams were made in air with a diode. These measurements were made for field sizes of 5X5, 10X10, 15X15, 20X20,and 25X25 cm^2 at 100cm SSD for each beam quality. The intensity profiles measured along each axis in the plane normal to the central axis of the beam are modeled by Fermi functions of the form

$$\Phi(x) = \frac{\Phi_\circ}{1+ \exp\left(\frac{\left|x-\frac{fsx}{2}\right|}{a_x}\right)} \qquad \{3.9\}$$

where $\Phi_\circ$ = photon number per unit solid angle along the central beam axis (x=0, y=0) sr^{-1}; x = the distance(cm) along the X-axis at 100cm SSD; fsx = field size in the $\hat{x}$ direction(cm); and a_x = a parameter chosen to give the best fit between {3.9} and the experimental in air intensity profile along the X-axis for each particular field size(cm).

The photon number per unit solid angle at any point (x,y) on a plane normal to the beam at 100cm SSD is taken to be the product of two such Fermi functions

$$\Phi(x,y) = \frac{\Phi_\circ}{1+\exp\left(\left|\frac{x-\frac{fsx}{2}}{a_x}\right|\right)} \frac{\Phi_\circ}{1+\exp\left(\left|\frac{y-\frac{fsy}{2}}{a_y}\right|\right)}$$

{3.10}

where fsy = field size in the $\hat{y}$ direction(cm), and a_y = a parameter chosen to give the best fit between the last term in {3.10} and the experimental in air intensity profile along the Y-axis at a particular field size.

Field sizes intermediate between the ones measured are estimated by linear interpolation of the parameters a_x and a_y (between the values determined to give the best fit at the field sizes measured).

Using this analytical model and its implementation in the program CONE, calculations of compensated dose as a percentage of bolus dose were performed for the experimental geometries detailed in Chapter 2. The incorrect polystyrene compensator cone described in Chapter 2 was also modeled in order to further test the accuracy of this method of analysis. The results of these calculations are presented in comparison with the measured results for each geometry in Figures 3.02 through 3.21. The nomenclature throughout these figures for the geometric polystyrene compensator and the aluminum and lead compensators is the same as that employed in Chapter 2. The incorrect polystyrene cone is referred to throughout in the graphs as the "7cm cone".

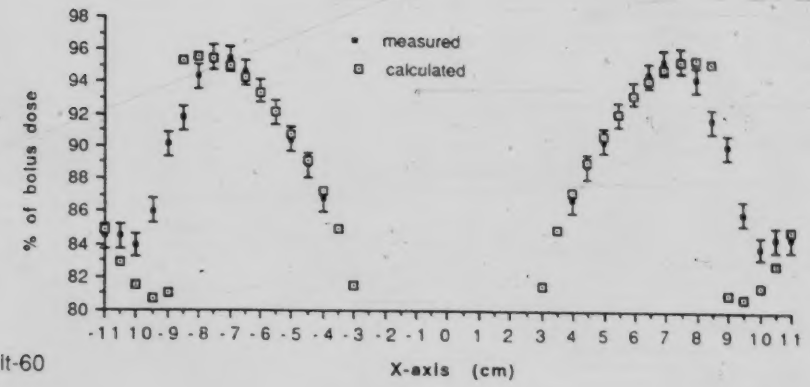

(a) Cobalt-60

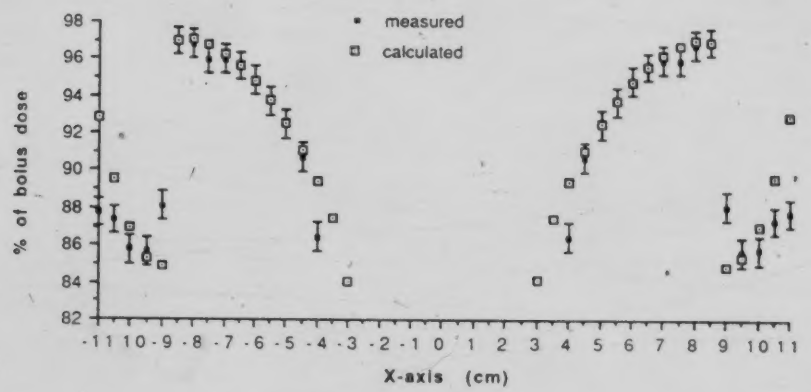

(b) 6MV

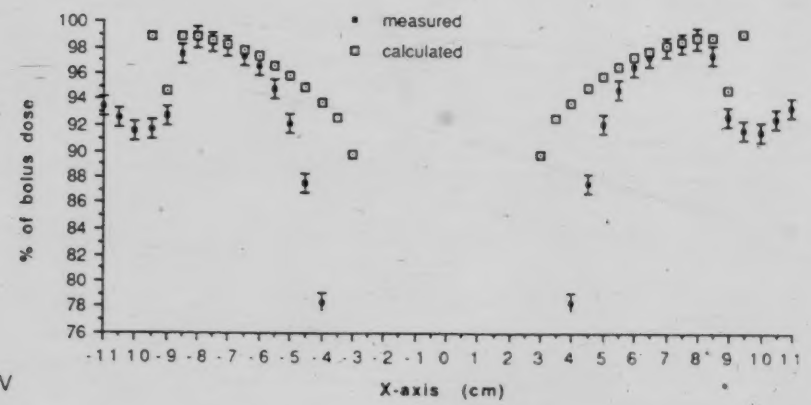

(c) 15MV

Figure 3.02 Compensated dose as a % of bolus dose for the geometric cone at 9cm depth (comparison between measurement and calculation) (a) Cobalt-60, (b) 6MV, (c) 15MV.

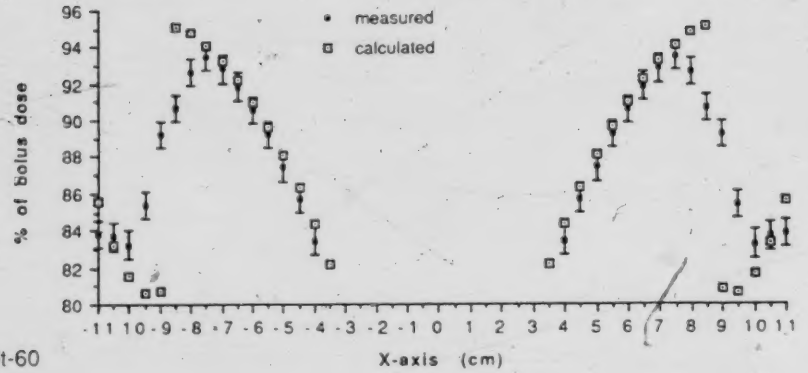

(a) Cobalt-60

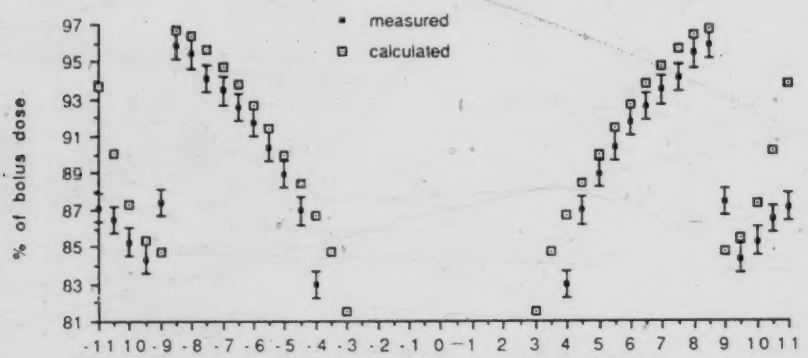

(b) 6MV

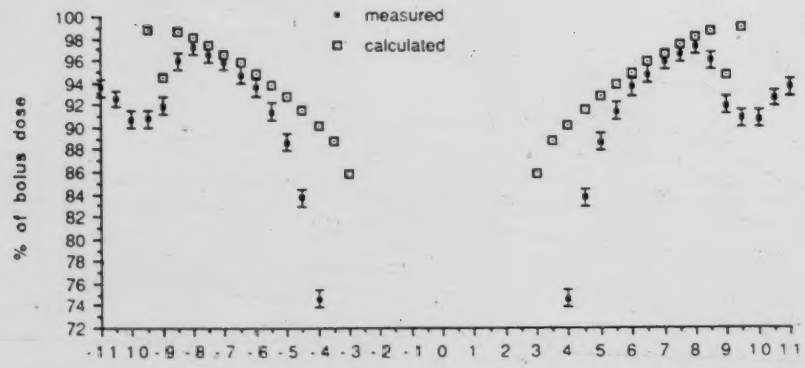

(c) 15MV

Figure 3.03 Compensated dose as a % of bolus dose for the aluminum cone at 9cm depth (comparison between measurement and calculation) (a) Cobalt-60, (b) 6MV, (c) 15MV.

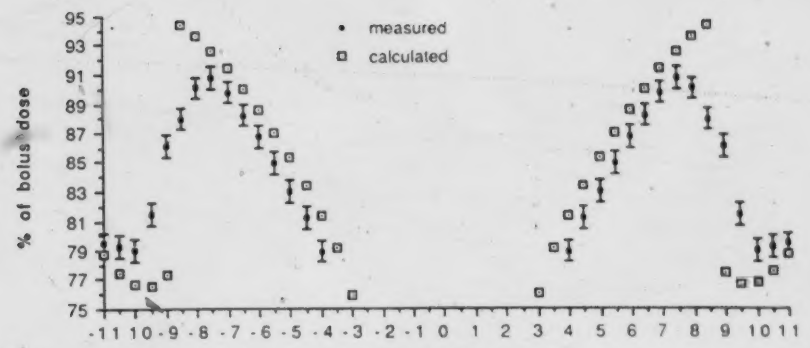

(a) Cobalt-60

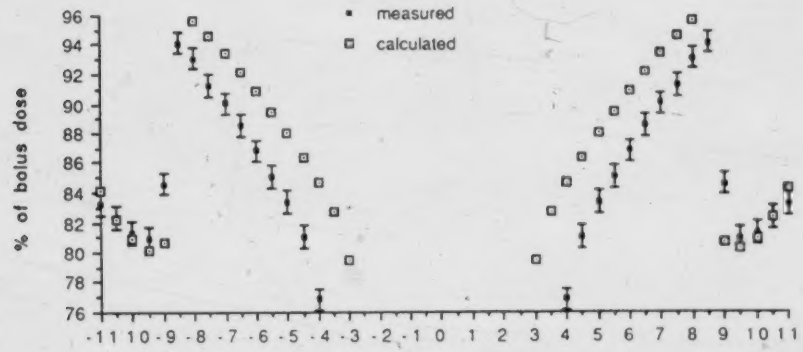

(b) 6MV

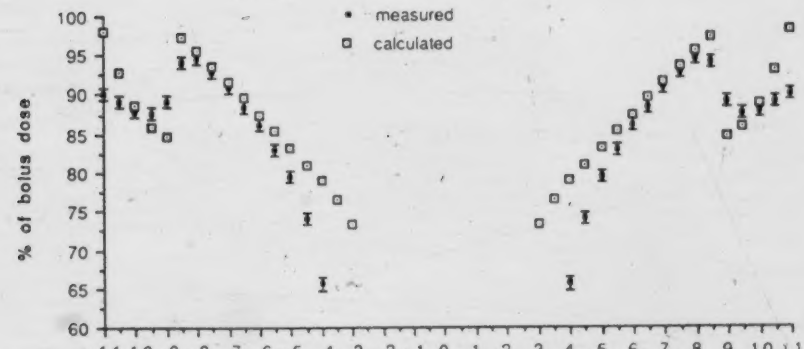

(c) 15MV

Figure 3.04 Compensated dose as a % of bolus dose for the lead cone at 9cm depth (comparison between measurement and calculation. (a) Cobalt-60, (b) 6MV, (c) 15MV.

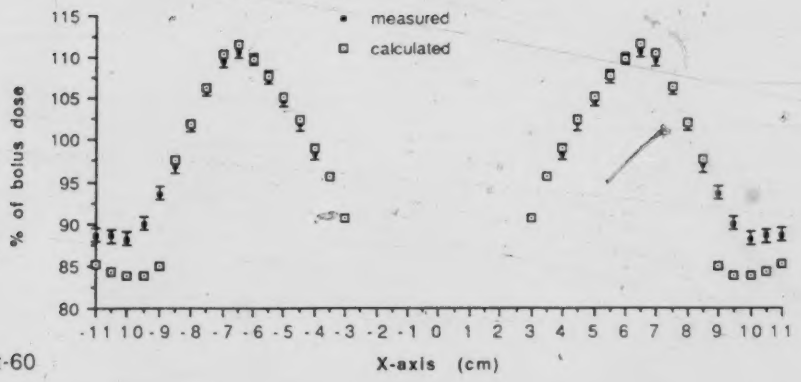

(a) Cobalt-60

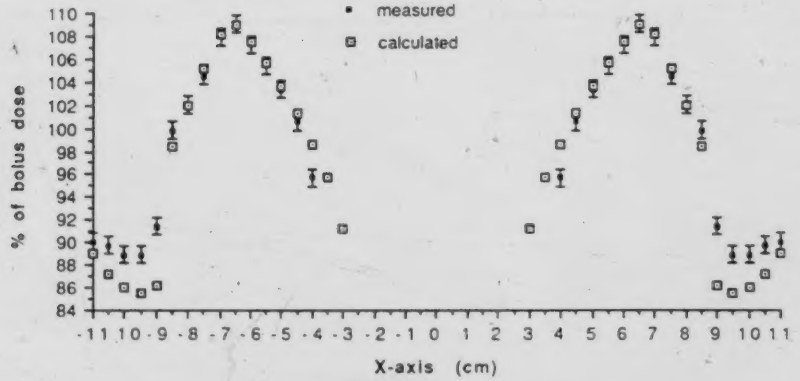

(b) 6MV

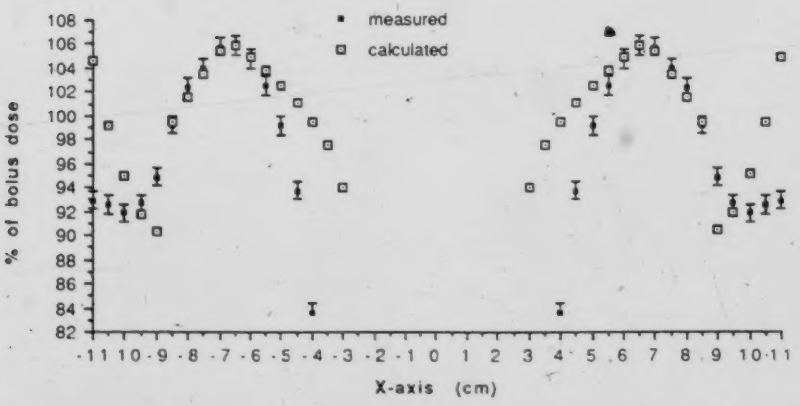

(c) 15MV

Figure 3.05 Compensated dose as a % of bolus dose for the 7cm cone at 9cm depth (comparison between measurement and calculation) (a) Cobalt-60, (b) 6MV, (c) 15MV.

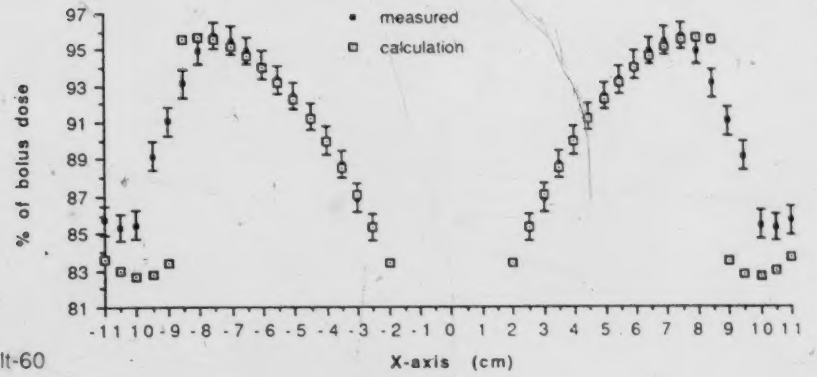

(a) Cobalt-60

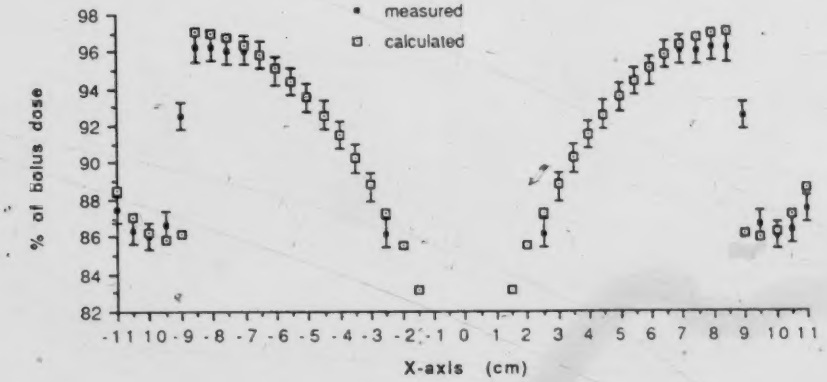

(b) 6MV

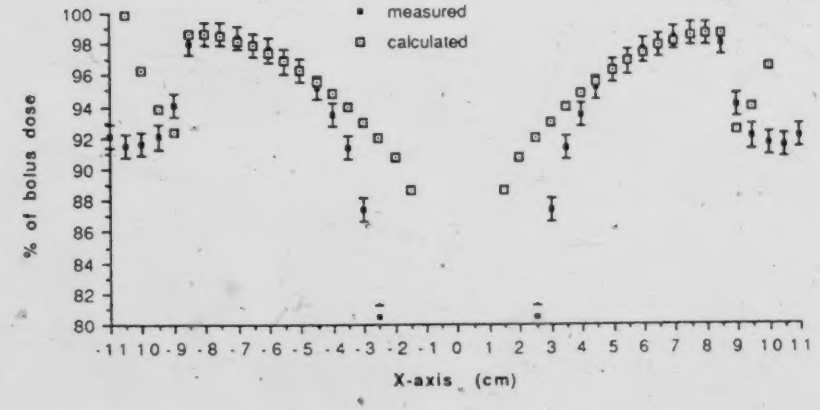

(c) 15MV

Figure 3.06 Compensated dose as a % of bolus dose for the geometric cone at 12cm depth (comparison between measurement and calculation) (a) Cobalt-60, (b) 6MV, (c) 15MV.

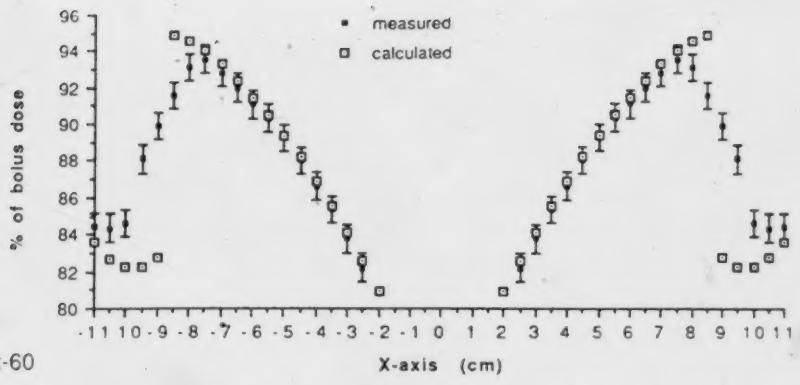

(a) Cobalt-60

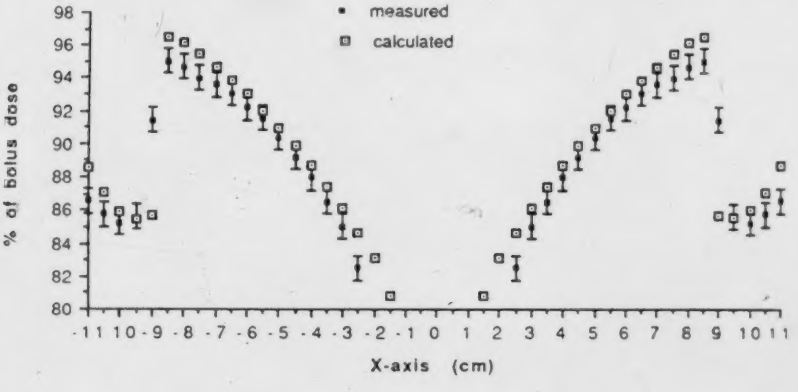

(b) 6MV

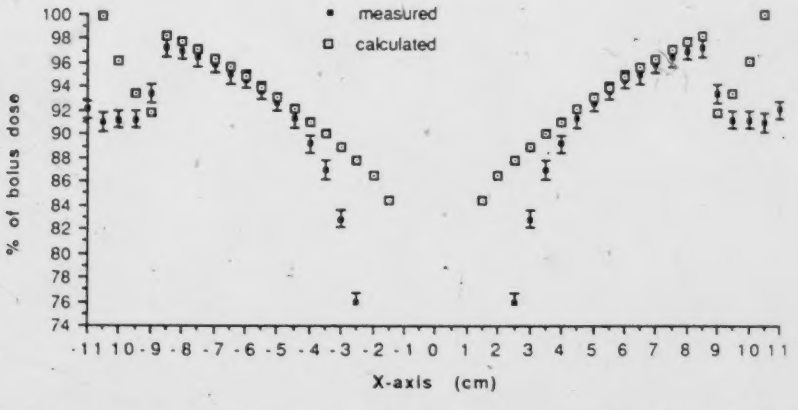

(c) 15MV

Figure 3.07 Compensated dose as a % of bolus dose for the aluminum cone at 12cm depth (comparison between measurement and calculation) (a) Cobalt-60, (b) 6MV, (c) 15MV.

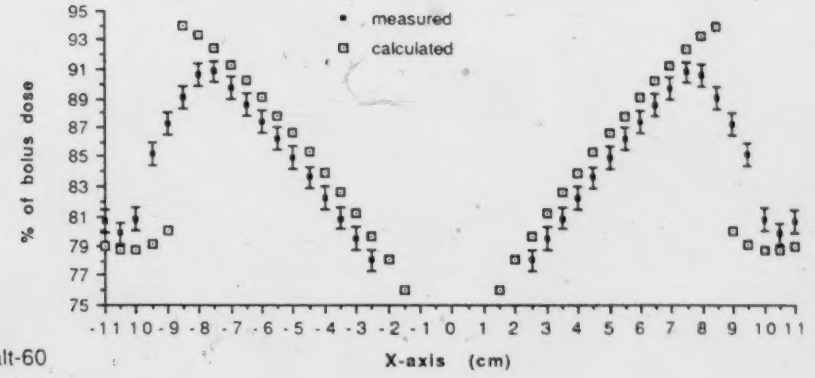

(a) Cobalt-60

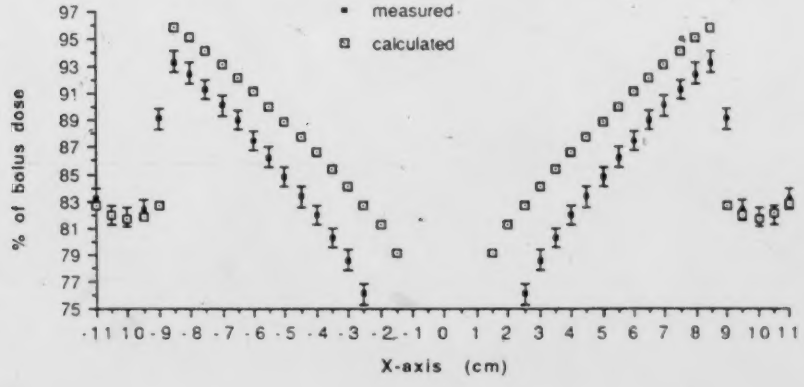

(b) 6MV

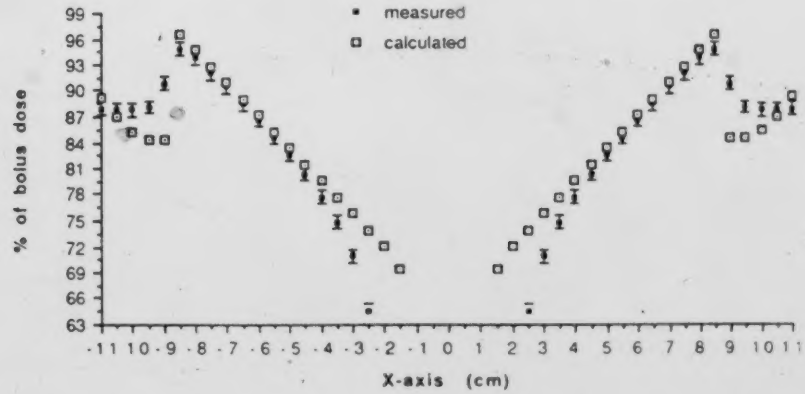

(c) 15MV

Figure 3.08 Compensated dose as a % of bolus dose for the lead cone at 12cm depth (comparison between measurement and calculation. (a) Cobalt-60, (b) 6MV, (c) 15MV.

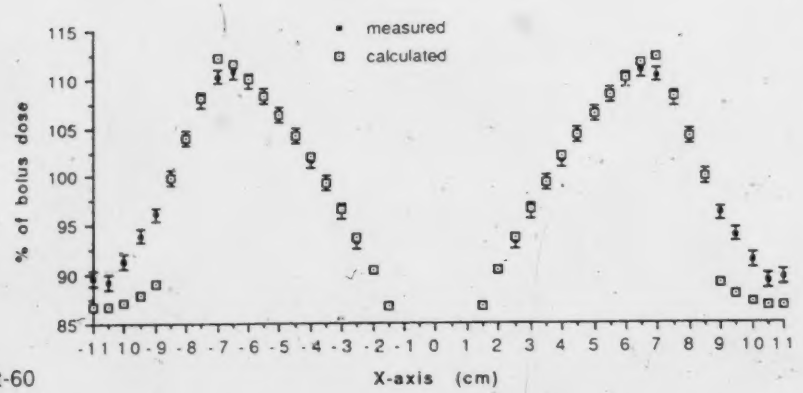

(a) Cobalt-60

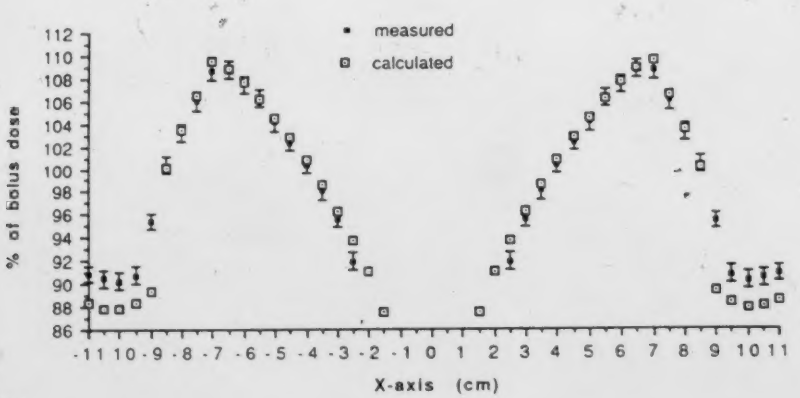

(b) 6MV

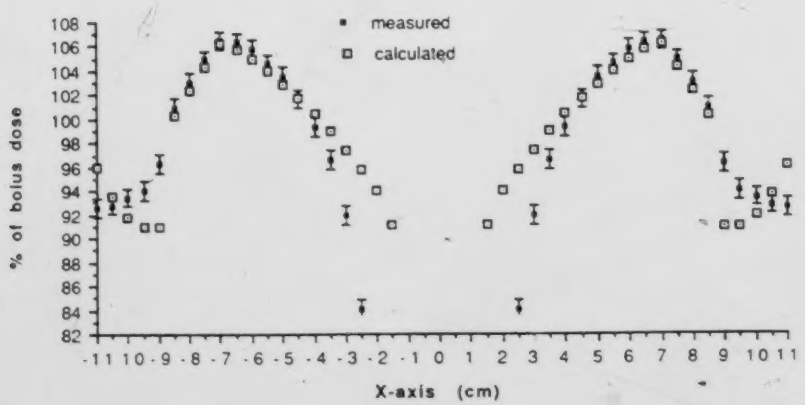

(c) 15MV

Figure 3.09 Compensated dose as a % of bolus dose for the 7cm cone at 12cm depth (comparison between measurement and calculation) (a) Cobalt-60, (b) 6MV, (c) 15MV.

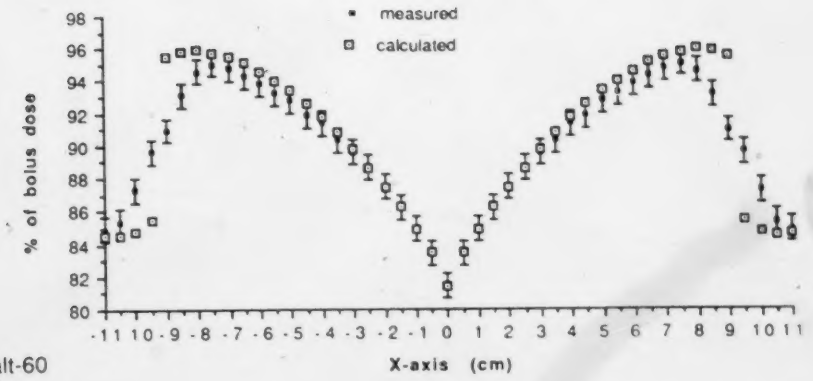

(a) Cobalt-60

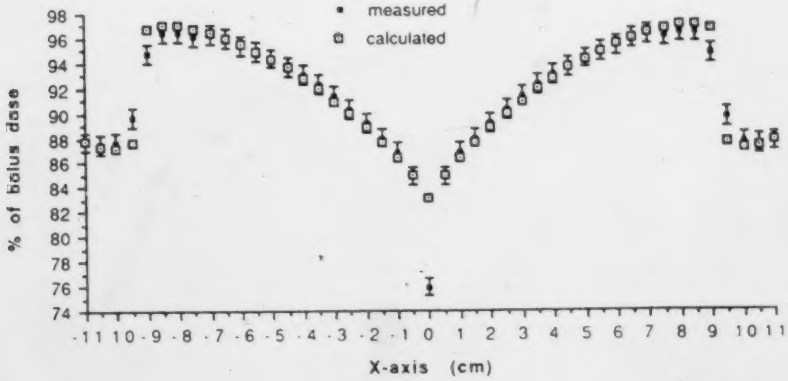

(b) 6MV

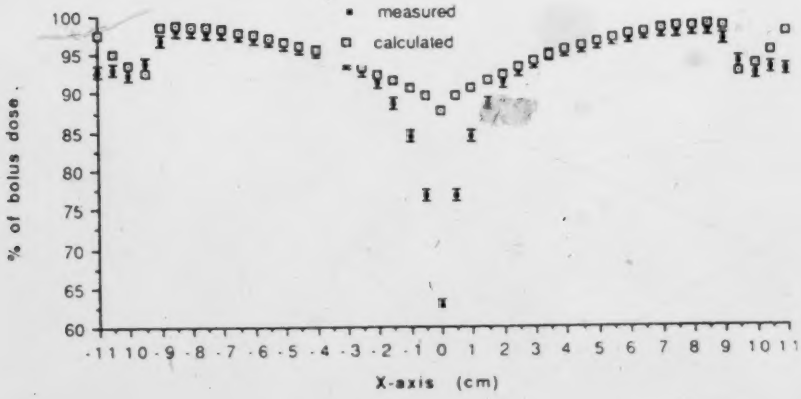

(c) 15MV

Figure 3.10 Compensated dose as a % of bolus dose for the geometric cone at 15cm depth (comparison between measurement and calculation) (a) Cobalt-60, (b) 6MV, (c) 15MV.

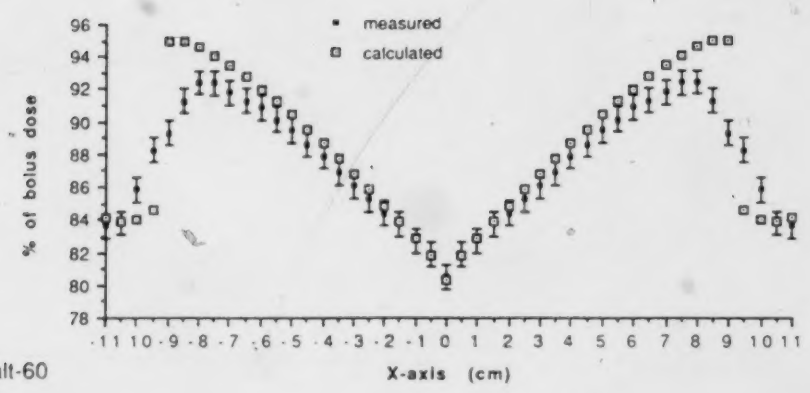

(a) Cobalt-60

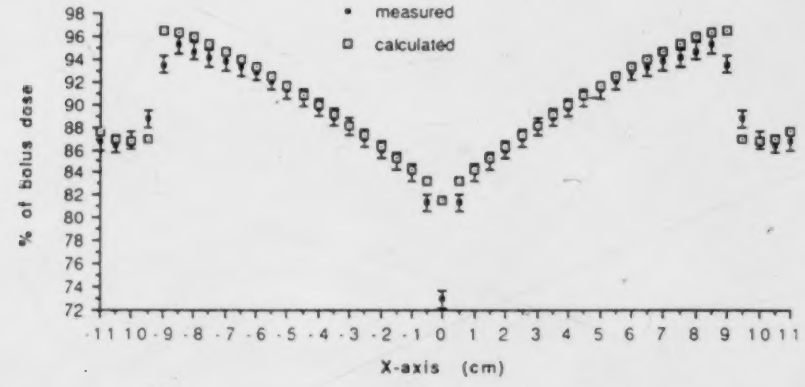

(b) 6MV

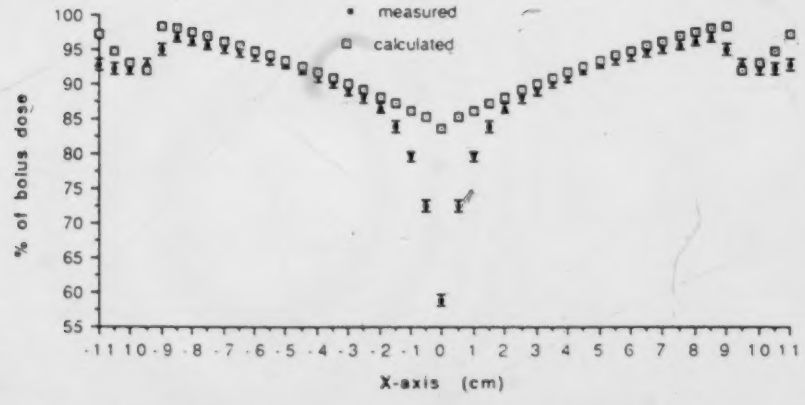

(c) 15MV

Figure 3.11 Compensated dose as a % of bolus dose for the aluminum cone at 15cm depth (comparison between measurement and calculation) (a) Cobalt-60, (b) 6MV, (c) 15MV.

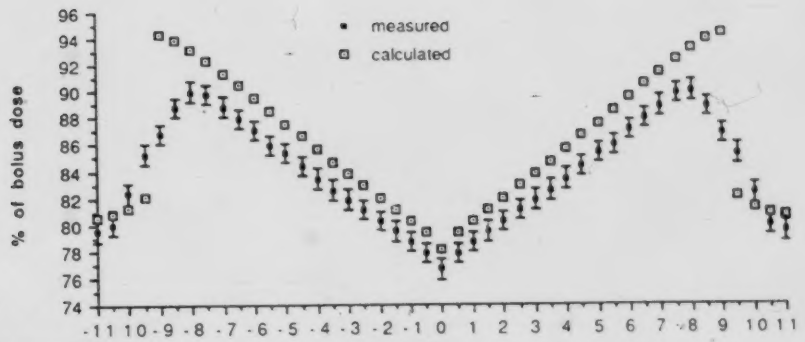

(a) Cobalt-60

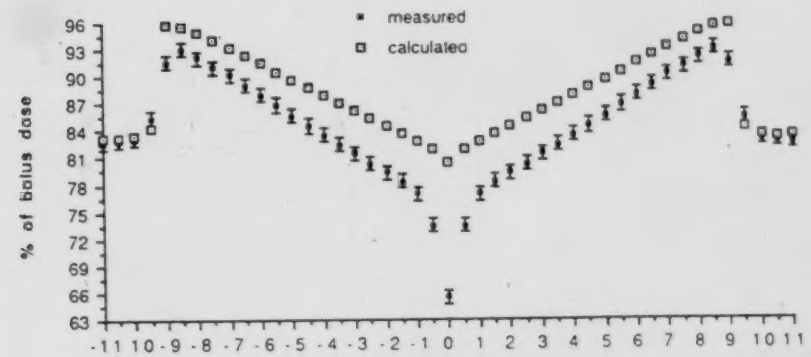

(b) 6MV

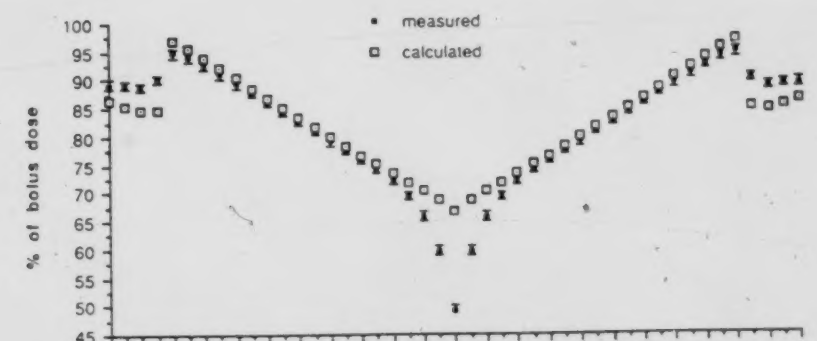

(c) 15MV

Figure 3.12 Compensated dose as a % of bolus dose for the lead cone at 15cm depth (comparison between measurement and calculation. (a) Cobalt-60, (b) 6MV, (c) 15MV.

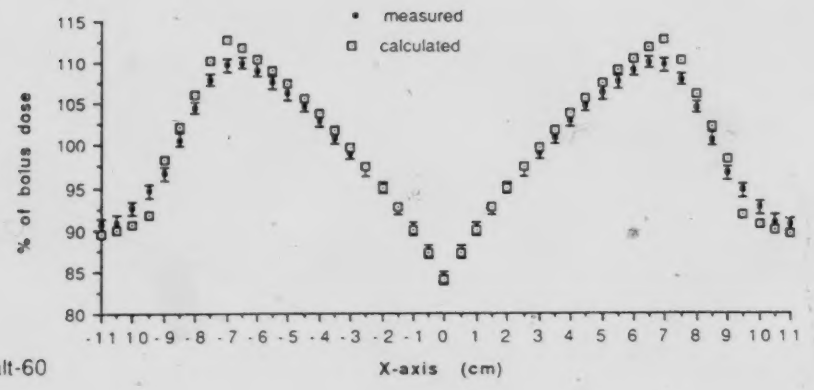

(a) Cobalt-60

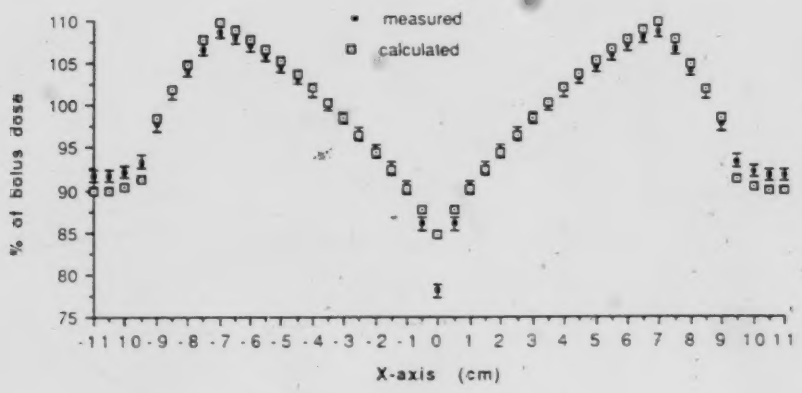

(b) 6MV

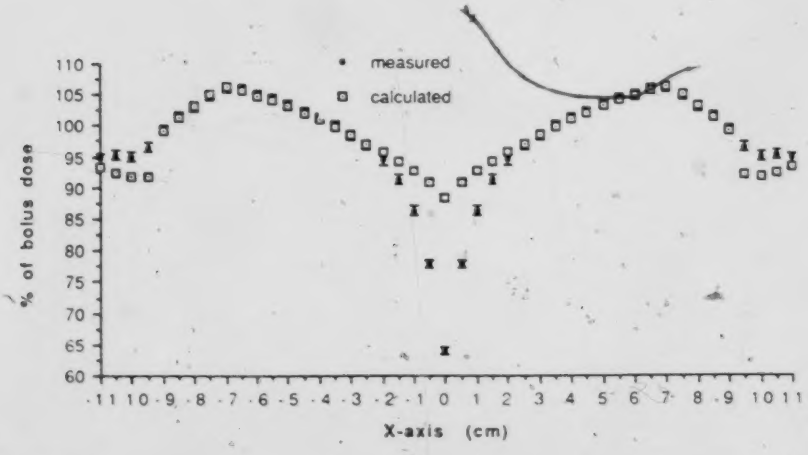

(c) 15MV

Figure 3.13 Compensated dose as a % of bolus dose for the 7cm cone at 15cm depth (comparison between measurement and calculation) (a) Cobalt-60, (b) 6MV, (c) 15MV.

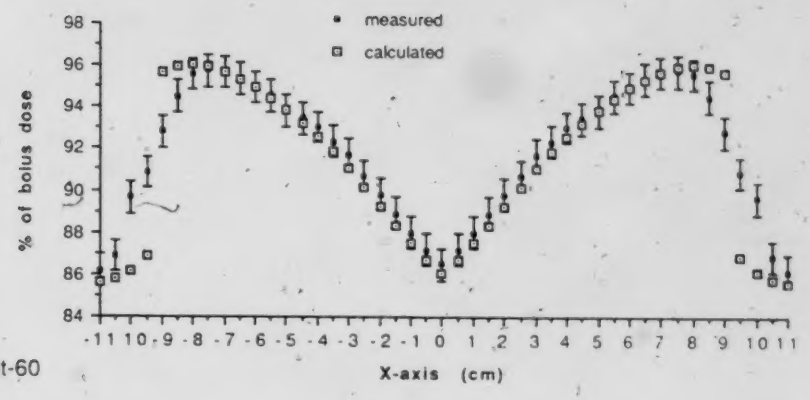

(a) Cobalt-60

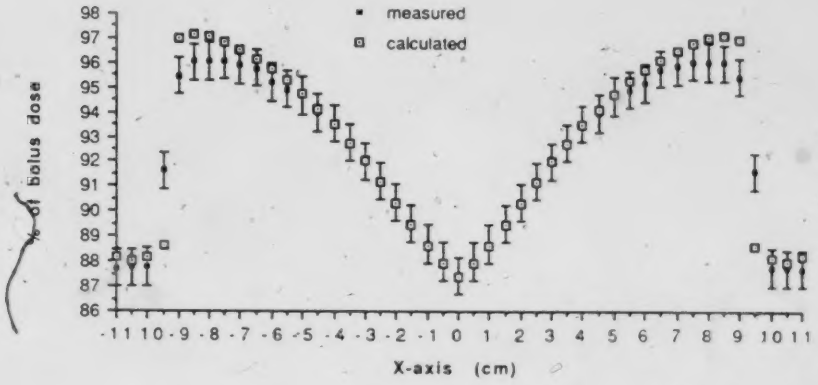

(b) 6MV

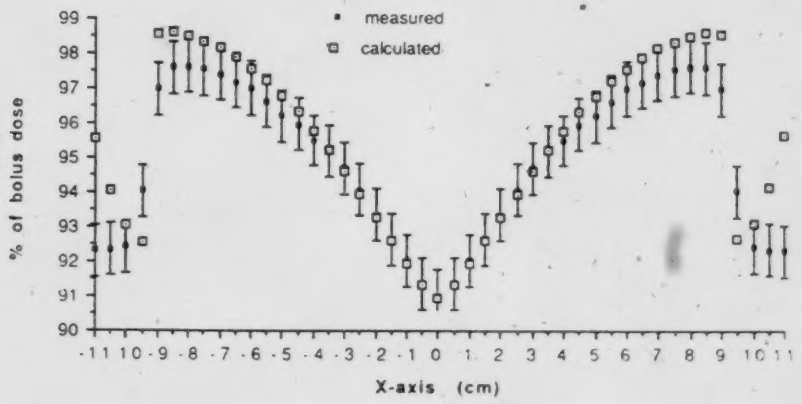

(c) 15MV

Figure 3.14 Compensated dose as a % of bolus dose for the geometric cone at 17cm depth (comparison between measurement and calculation) (a) Cobalt-60, (b) 6MV, (c) 15MV.

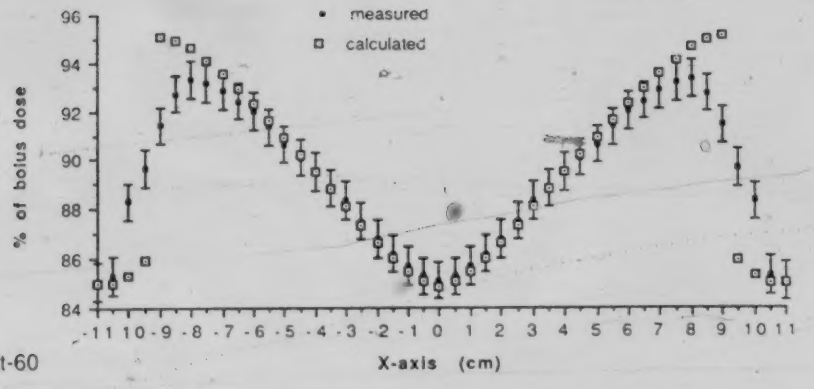

(a) Cobalt-60

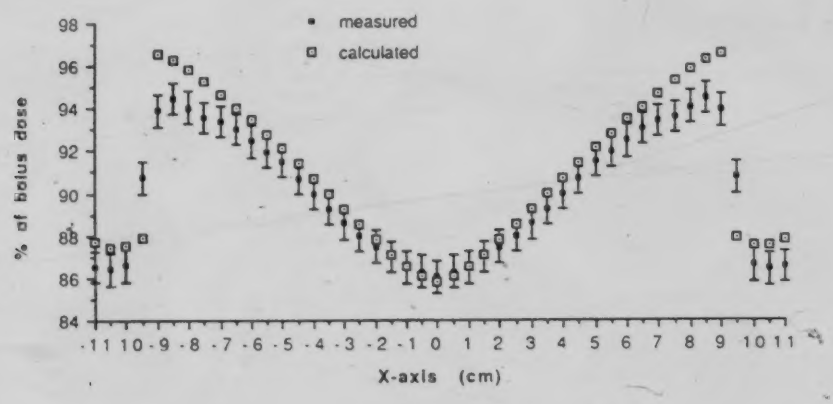

(b) 6MV

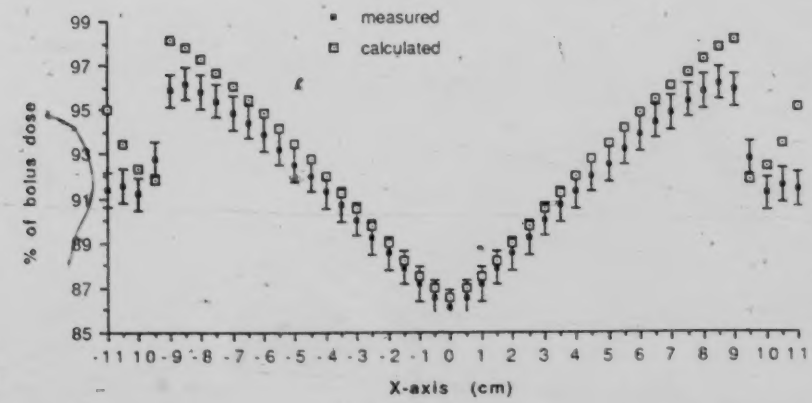

(c) 15MV

Figure 3.15 Compensated dose as a % of bolus dose for the aluminum cone at 17cm depth (comparison between measurement and calculation) (a) Cobalt-60, (b) 6MV, (c) 15MV.

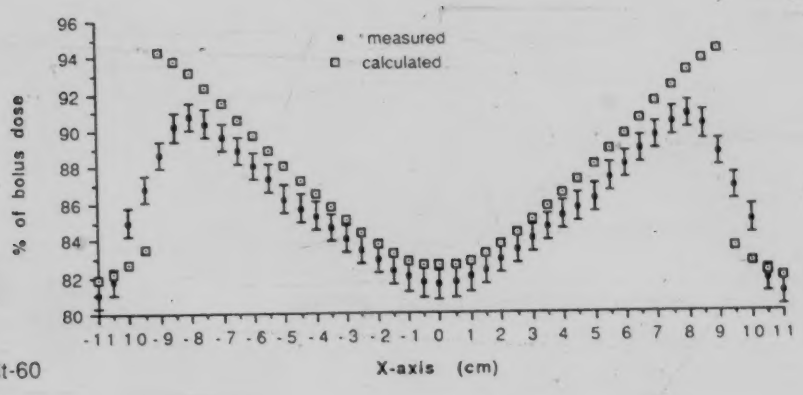

(a) Cobalt-60

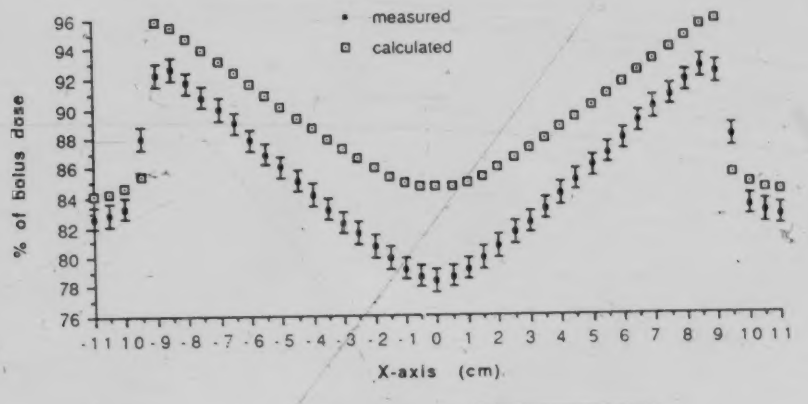

(b) 6MV

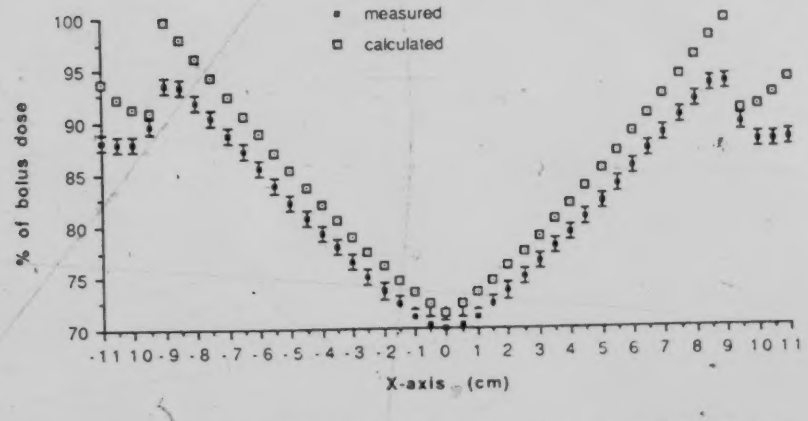

(c) 15MV

Figure 3.16 Compensated dose as a % of bolus dose for the lead cone at 17cm depth (comparison between measurement and calculation. (a) Cobalt-60, (b) 6MV, (c) 15MV.

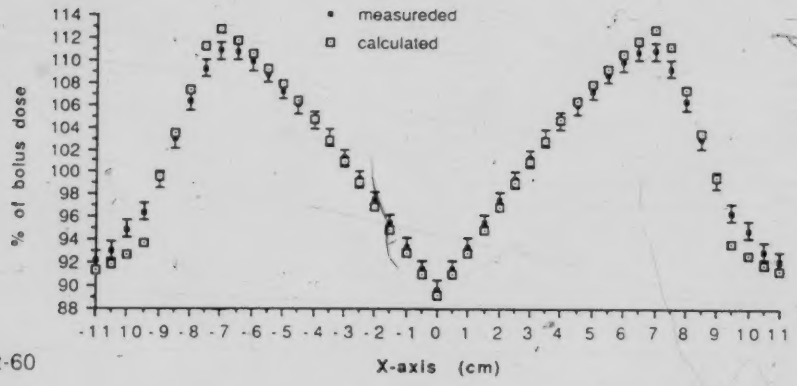

(a) Cobalt-60

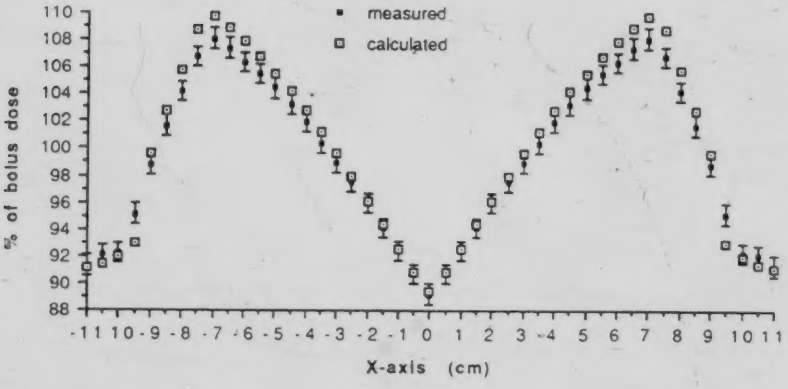

(b) 6MV

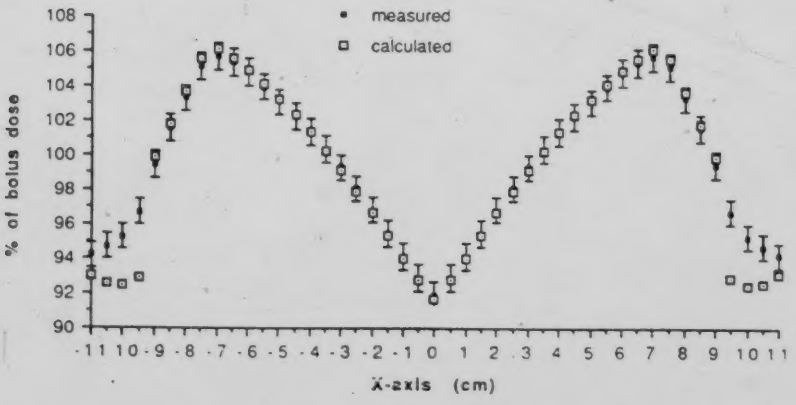

(c) 15MV

Figure 3.17 Compensated dose as a % of bolus dose for the 7cm cone at 17cm depth (comparison between measurement and calculation) (a) Cobalt-60, (b) 6MV, (c) 15MV.

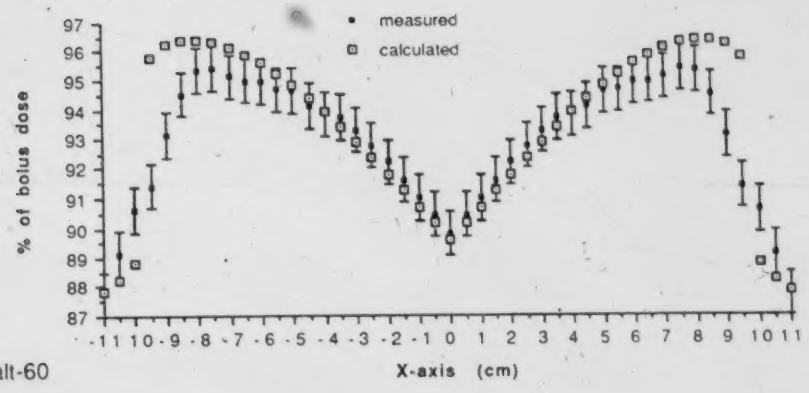

(a) Cobalt-60

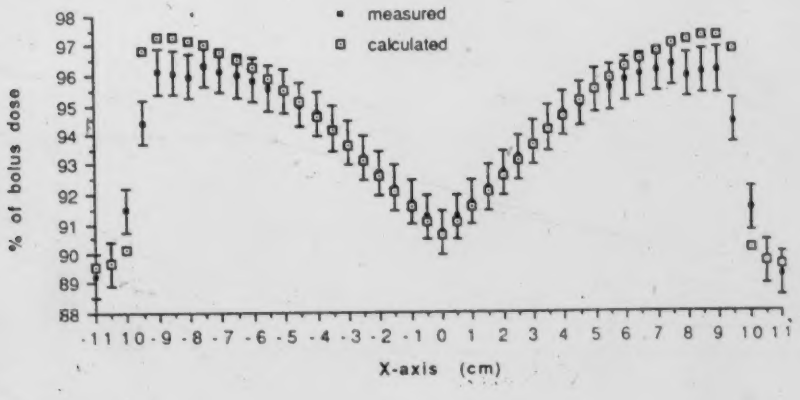

(b) 6MV

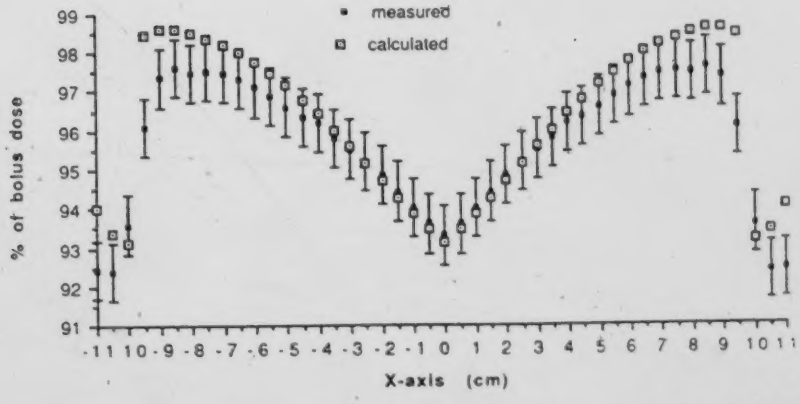

(c) 15MV

Figure 3.18 Compensated dose as a % of bolus dose for the geometric cone at 21cm depth (comparison between measurement and calculation) (a) Cobalt-60, (b) 6MV, (c) 15MV.

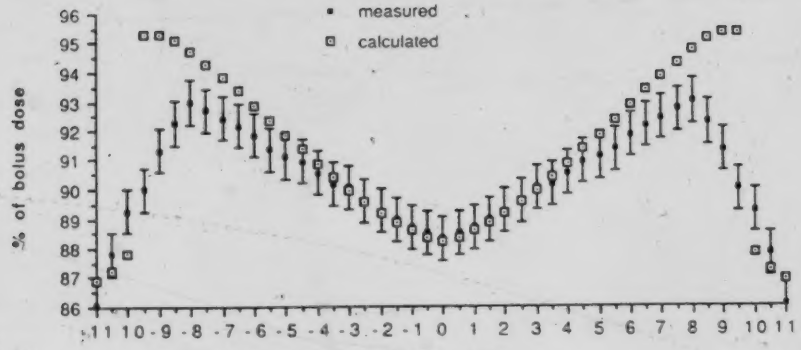

(a) Cobalt-60

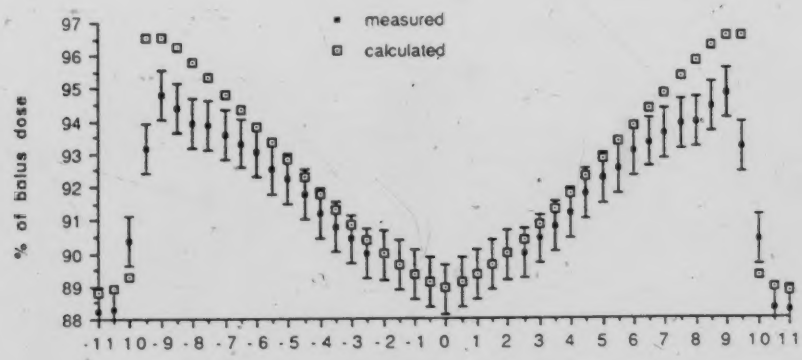

(b) 6MV

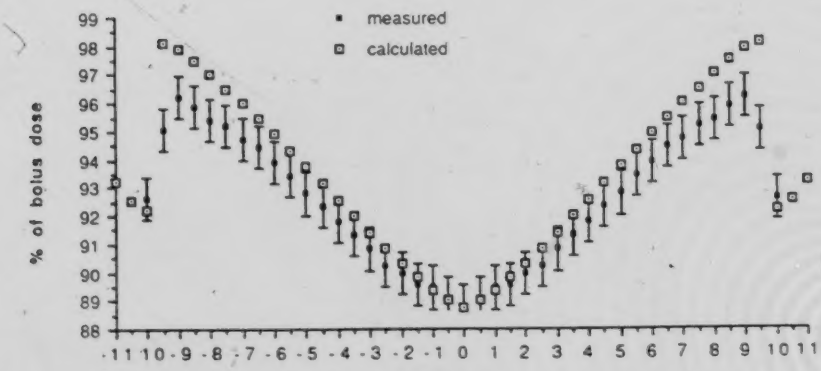

(c) 15MV

Figure 3.19 Compensated dose as a % of bolus dose for the aluminum cone at 21cm depth (comparison between measurement and calculation) (a) Cobalt-60, (b) 6MV, (c) 15MV.

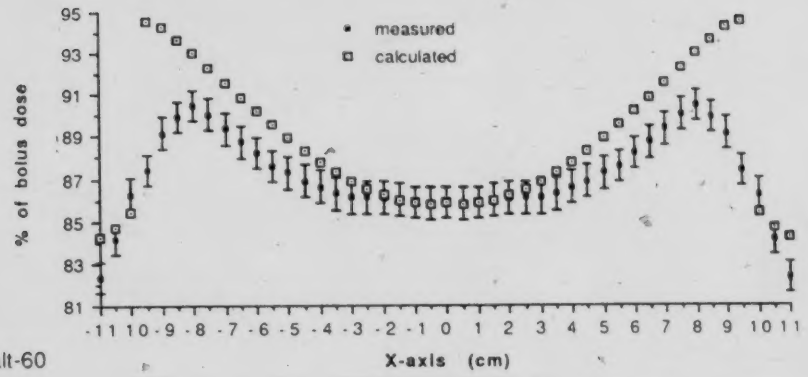

(a) Cobalt-60

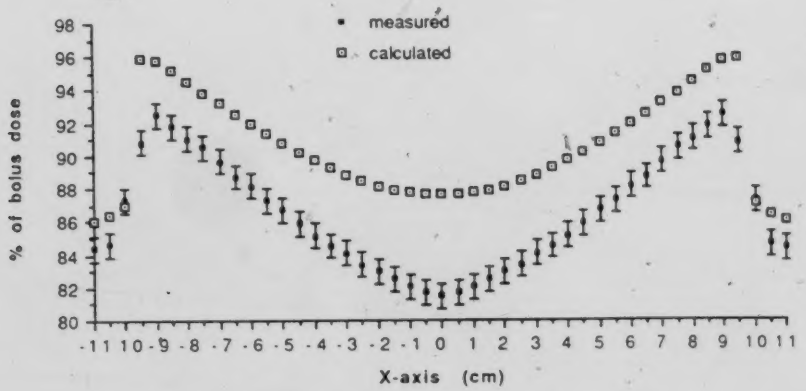

(b) 6MV

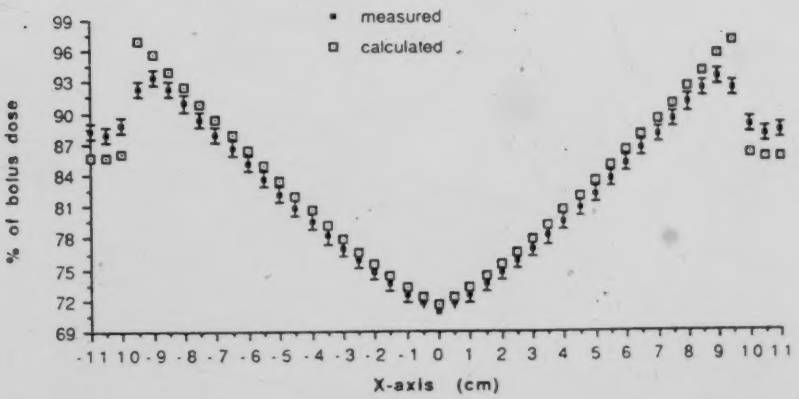

(c) 15MV

Figure 3.20 Compensated dose as a % of bolus dose for the lead cone at 21cm depth (comparison between measurement and calculation: (a) Cobalt-60, (b) 6MV, (c) 15MV.

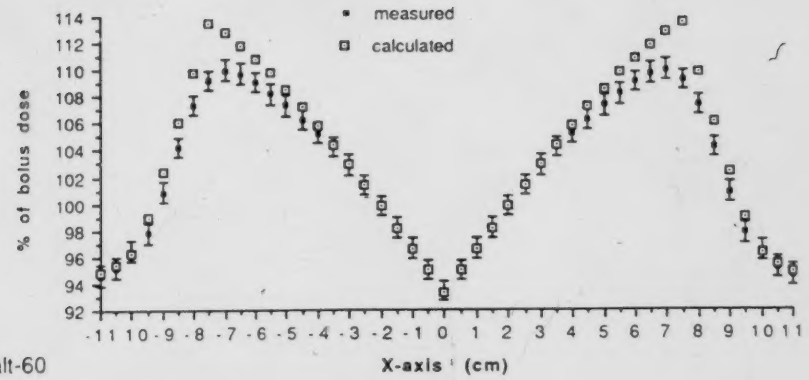

(a) Cobalt-60

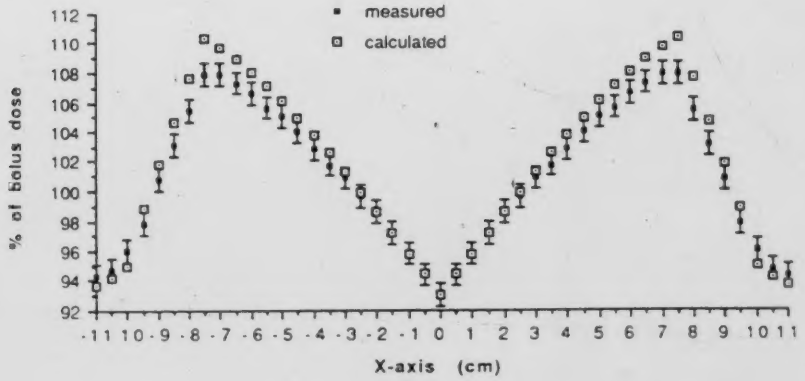

(b) 6MV

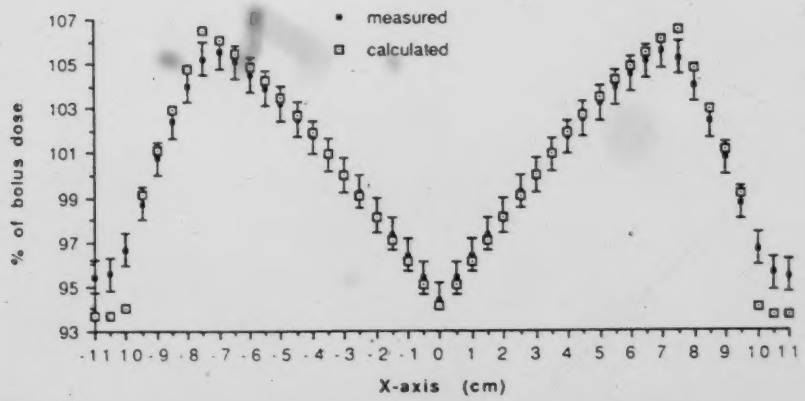

(c) 15MV

Figure 3.21 Compensated dose as a % of bolus dose for the 7cm cone at 21cm depth (comparison between measurement and calculation) (a) Cobalt-60, (b) 6MV, (c) 15MV.

3.4 Analysis and Discussion of Results

The degree of agreement between theory and experiment is different for each situation, but the following general observations apply:

1) Polystyrene geometric compensator

   a) Cobalt-60

      i) at all depths theory agrees with experiment within experimental error except within and beyond the penumbral regions of the beam. In these regions electronic equilibrium does not exist.

   b) 6MV

      i) at depths of 17cm and 21cm theory agrees with experiment within experimental error except within and beyond the penumbral regions of the beam.

      ii) at depths of 9cm, 12cm, and 15cm the same observations as detailed for 17cm and 21cm depths apply, with the following exceptions:

      - at 15cm depth there is a large disagreement between theory and experiment at the point directly below the surface cone tip(x=0). Here theory overpredicts experiment by more than 7%.
      - at 9cm and 12cm depths theory overpredicts experiment near the surface cone edges. At 12cm depth the overprediction is just over 1% while at 9cm the overprediction is almost 3%.
      - these overpredictions occur in the regions near the surface cone where electronic equilibrium dose not exist.

c) 15MV

i) at depths of 17cm and 21cm theory agrees with experiment within experimental error except within and beyond the penumbral regions of the beam. In these regions electronic equilibrium does not exist.

ii) at depths of 9cm, 12cm, and 15cm the same observations as detailed for depths of 17cm and 21cm apply with the following exception: in regions nearest the surface cone disagreement is observed as theory overpredicts experiment. These regions of disagreement coincide with regions where electronic equilibrium does not exist.

2) Incorrect polystyrene compensator

a) Cobalt-60

i) at all depths theory agrees with experiment within experimental error except near the field edges, within and beyond the penumbral regions. The disagreement seen near the field edges is in all cases manifested as an overprediction by theory.

b) 6MV

i) at 17cm and 21cm depths theory agrees with experiment within experimental error except near the field edges,and within and beyond the penumbral regions.

ii) at depths of 9cm, 12cm, and 15cm the same observations as detailed for depths of 17cm and 21cm apply with the following exception: in regions nearest the surface cone disagreement is observed as theory overpredicts experiment. These regions of

disagreement coincide with regions where electronic equilibrium does not exist.

3) Aluminum cone

a) Cobalt-60

i) at depths of 9cm, 12cm, and 17cm theory agrees with experiment within experimental error except within and beyond the penumbral regions of the beam. In these regions electronic equilibrium does not exist.

ii) at depths of 15cm and 21cm the same observations detailed for 9cm,12cm, and 17cm apply, with the following exception: at these two depths(15cm and 21cm) disagreement between theory and experiment is observed near the field edges as well. This disagreement is manifest as an overprediction by theory.

b) 6MV

i) at depths of 17cm and 21cm theory agrees with experiment within experimental error except near, within, and beyond the penumbral regions of the beam. Disagreement for regions near the field edges is manifest as an overprediction by theory.

ii) at depths of 12cm and 15cm the observations detailed for 17cm and 21cm depths apply, with the following exception: in regions nearest the surface cone disagreement is observed as theory overpredicts experiment. These regions coincide with regions where electronic equilibrium does not exist.

iii) at 9cm depth agreement between theory and experiment is not observed over the entire field of measurement. This disagreement is manifest for all regions except the penumbral regions as an over

prediction by theory as compared to experiment. This overprediction is greatest for those regions nearest the surface cone and also those regions beyond the penumbral regions of the beam where, in both cases, electronic equilibrium does not exist.

c) 15MV

i) at depths of 17cm and 21cm theory agrees with experiment within experimental error except near, within, and beyond the penumbral regions of the beam. Disagreement for regions near the field edges is manifest as an overprediction by theory.

ii) at depths of 12cm and 15cm the observations detailed for 17cm and 21cm depths apply, with the following exception: in regions nearest the surface cone disagreement is observed as theory overpredicts experiment. These regions coincide with regions where electronic equilibrium dose not exist.

iii) at 9cm depth agreement between theory and experiment exists at only a few points near the field edge. At all other points theory overpredicts experiment. The degree of disagreement is greatest for those regions nearest the surface cone and also those beyond the penumbral regions of the beam where, in both cases, electronic equilibrium dose not exist.

4) Lead cone

a) Cobalt-60

i) at all depths except 21cm disagreement between theory and experiment is seen over the entire field of measurement except for points beyond the penumbral regions of the beam at 15cm and 17cm depths. For all regions within the primary(inside the field

edges) and penumbral regions of the beam this disagreement is manifest as an overprediction by theory.

ii) at 21cm depth the same observations detailed for 9, 12, 15, and 17cm depths apply, with the following exception: near the centre of the scan(-3cm to +3cm) agreement between theory and experiment exists.

iii) at all depths the degree of overprediction by theory is greatest within the penumbral regions of the beam.

b) 6MV

i) at all depths for all points within the primary and penumbral regions of the beam disagreement between theory and experiment exists. This disagreement is manifest as an overprediction by theory as compared to experiment.

c) 15MV

i) at 21cm depth agreement exists between theory and experiment only over a small region (-2.5cm to +2.5cm) near the central beam axis. At all other points within the primary and penumbral regions of the beam theory overpredicts measurement.

ii) at 17cm depth disagreement between theory and measurement is observed over the entire field of measurement. At all points theory overpredicts experiment.

iii) at 12cm and 15cm depths agreement between theory and experiment exists within experimental error for a number of points within the primary region of the beam. Disagreement is observed within regions near, within, and beyond the penumbral regions of the beam. Disagreement is also seen for points nearest the

surface cone. The disagreement between theory and experiment for points nearest the surface cone and near the field edge is manifest as overprediction by theory. The region nearest the surface cone coincides with a region in which electronic equilibrium does not exist.

iv) at 9cm depth agreement exists at only a few points near the field edge. Disagreement within the primary region of the beam is manifest by overprediction by theory. The degree of overprediction in this region is greatest for points nearest the surface cone where electronic equilibrium does not exist.

The general disagreement between theory and experiment observed with the lead compensator cone is, in part, due to the assumption of monoenergetic primary photons used in the theoretical model presented. The total attenuation for both water and lead are presented in Figures 1.9 and 1.10 respectively. The assumption of a monoenergetic primary photon beam used in the theoretical model is due to the fact that for water and other tissue equivalent materials the linear attenuation properties of the linac spectrum photon beams can be reproduced by monoenergetic photon beams of an appropriate "effective" energy. For Cobalt-60 photon beams the low energy contaminant component previously discussed was disregarded for the purposes of simplification in order to preserve the monoenergetic beam assumptions of the model. Observations of the total attenuation for water and lead presented in Figures 1.9 and 1.10 clearly show that the total attenuation for lead varies in a manner quite different from that of water. This being the case then, one should expect a monoenergetic photon beam to

possess a different "effective energy" in lead than in water or other near unit density material like polystyrene.

In an attempt to more accurately model the lead compensator geometries the continuous spectrums of the 6MV and 15MV photon beams were modeled by a discrete number of spectral energies. The spectral distributions of the 6MV and 15MV photon beams used in this work have been determined by Mackie[3.4] and are presented in Figures 3.22 and 3.23 respectively. The 6MV beam was represented by the five spectral energies: 1MeV, 2MeV, 3MeV, 4MeV, and 5MeV with relative weights of 0.3730, 0.2516, 0.1842, 0.1261, and 0.06566 respectively. The 15MV beam was approximated by the seven spectral energies: 1MeV, 3MeV, 5MeV, 7MeV, 9MeV, 11MeV, and 13MeV with relative weights of 0.2410, 0.1880, 0.1566, 0.13735, 0.1181, 0.0988, and 0.0650 respectively. The Cobalt-60 beam was modeled by a beam with two spectral components of energies 1.25MeV and 250keV with relative weights of 0.95 and 0.05 respectively. The results obtained for the lead compensator cone geometries using these spectral component beams are presented in Figures 3.24 thru 3.28.

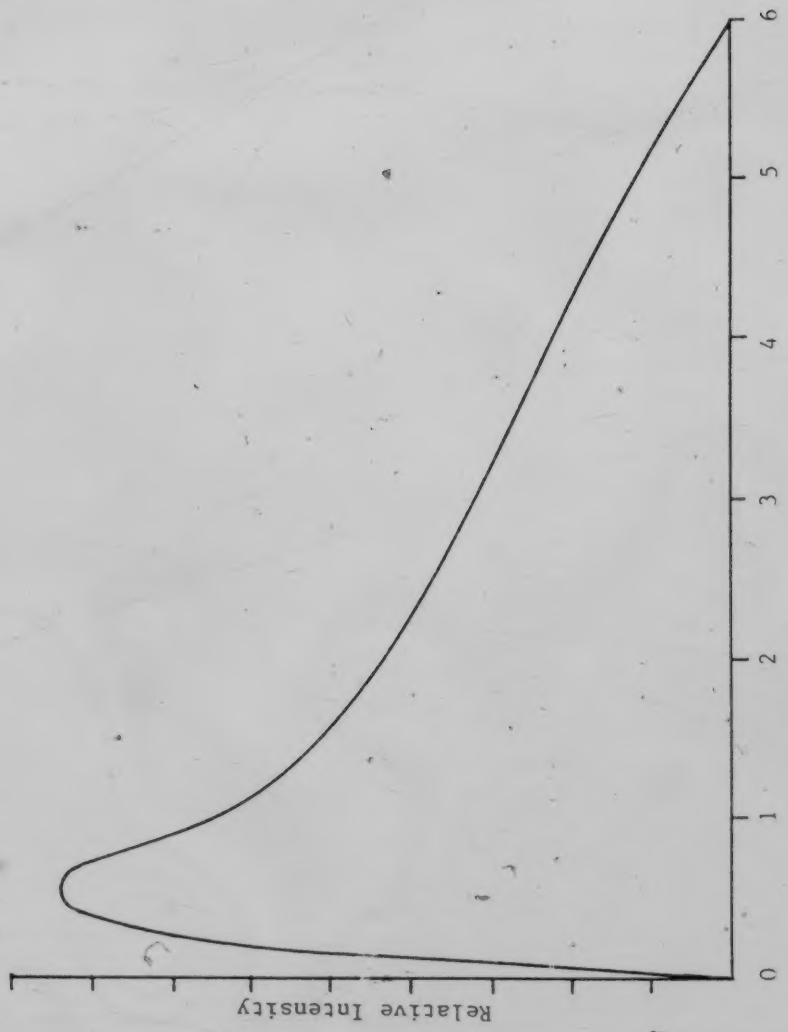

Figure 3.22 Spectral distribution of the 6MV photon beam.

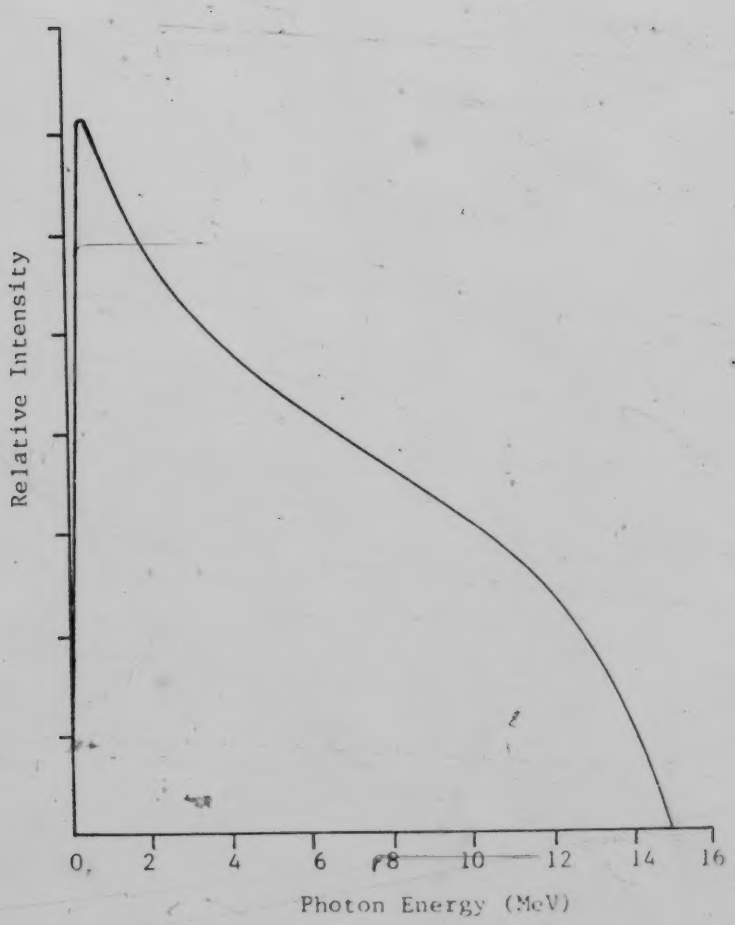

Figure 3.23 Spectral distribution of the 15MV photon beam.

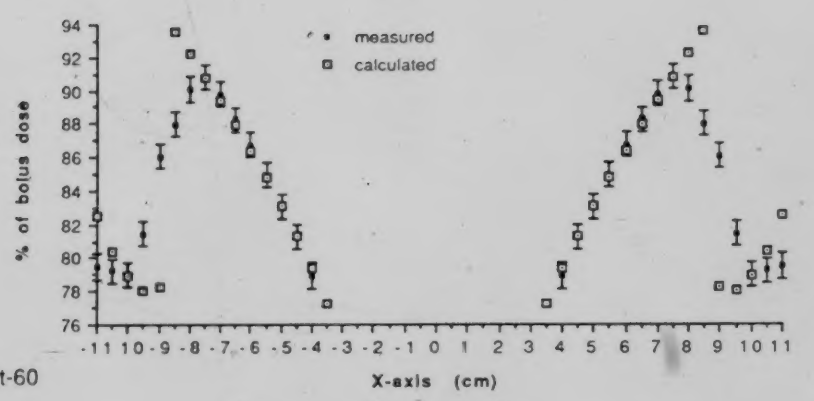

(a) Cobalt-60

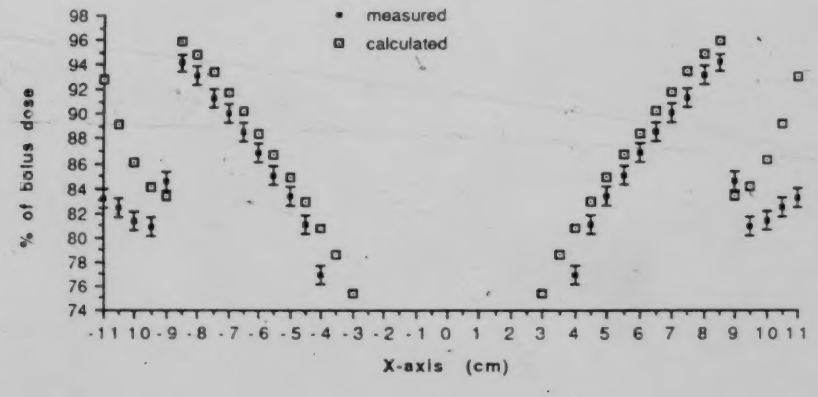

(b) 6MV

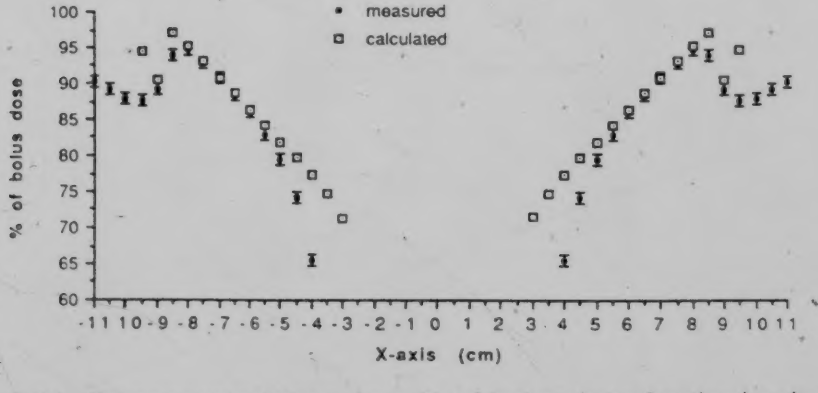

(c) 15MV

Figure 3.24 Compensated dose as a % of bolus dose for the lead cone at 9cm depth (comparison between measurement and calculation with spectrum (a) Cobalt-60, (b) 6MV, (c) 15MV.

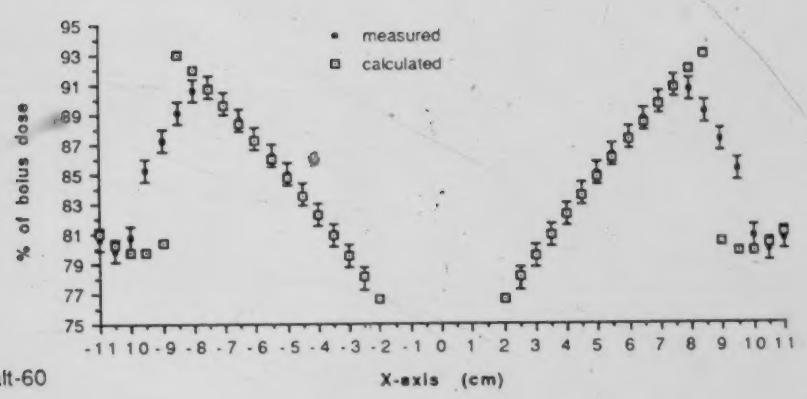

(a) Cobalt-60

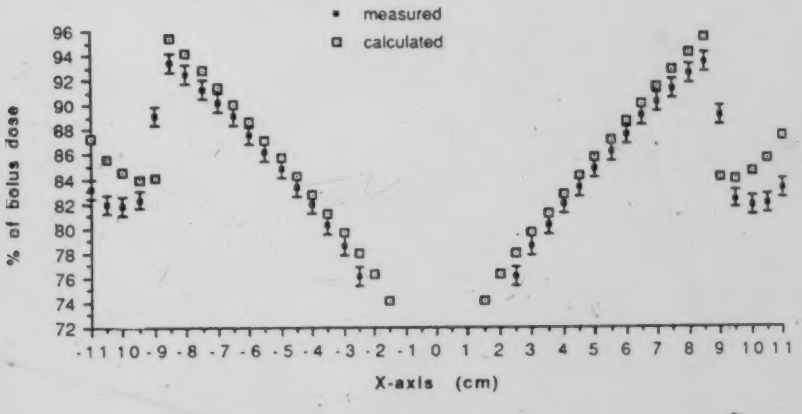

(c) 6MV

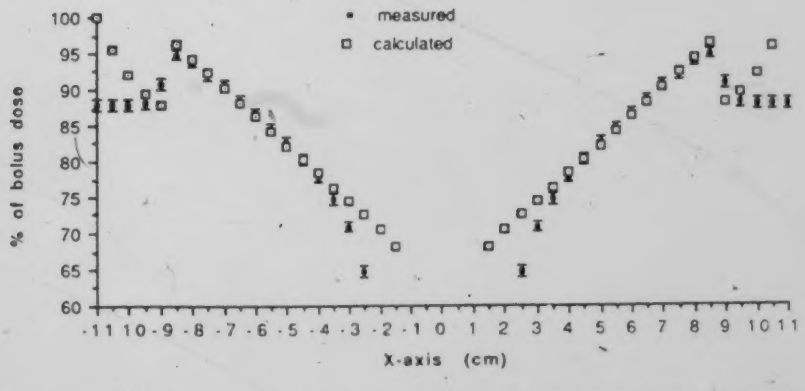

(c) 15MV

Figure 3.25 Compensated dose as a % of bolus dose for the lead cone at 12cm depth (comparison between measurement and calculation with spectrum (a) Cobalt-60, (b) 6MV, (c) 15MV.

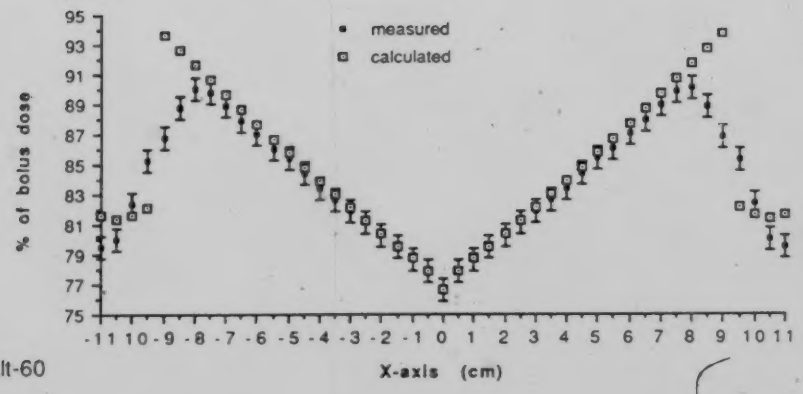

(a) Cobalt-60

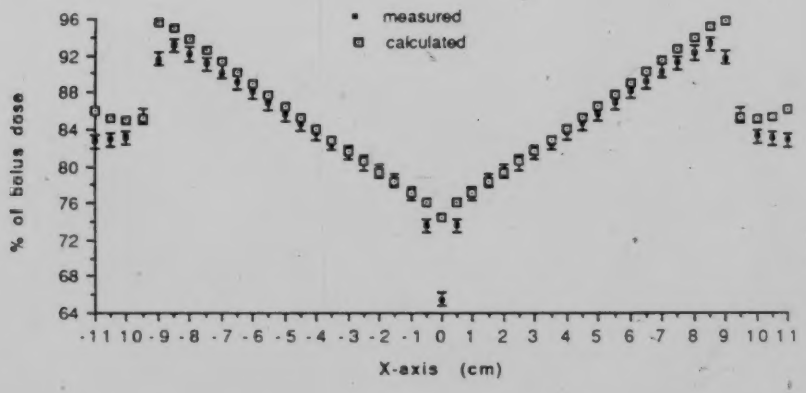

(b) 6MV

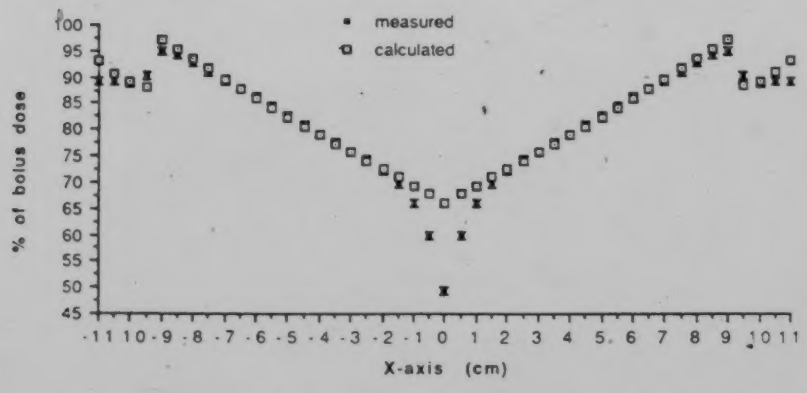

(c) 15MV

Figure 3.26 Compensated dose as a % of bolus dose for the lead cone at 15cm depth (comparison between measurement and calculation with spectrum (a) Cobalt-60, (b) 6MV, (c) 15MV.

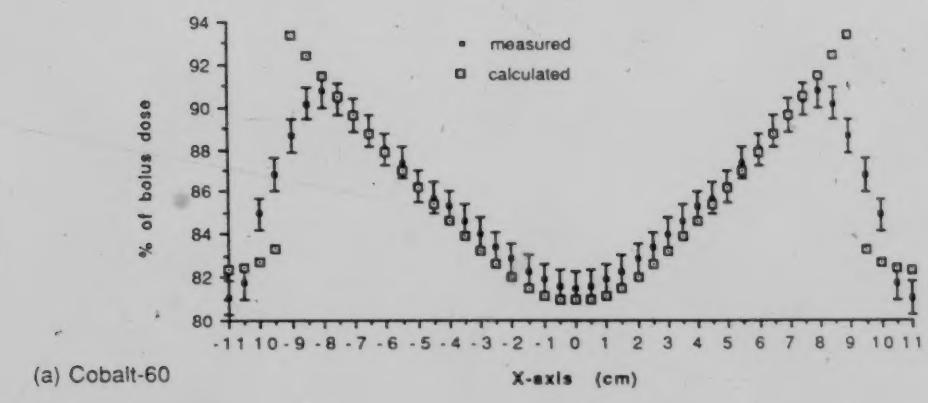

(a) Cobalt-60

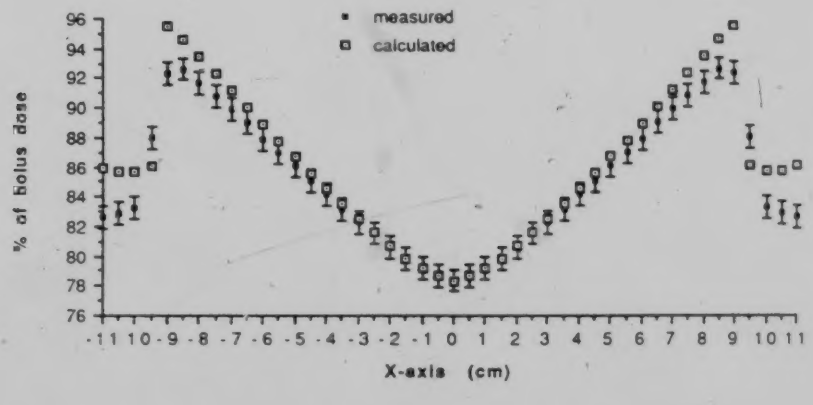

(b) 6MV

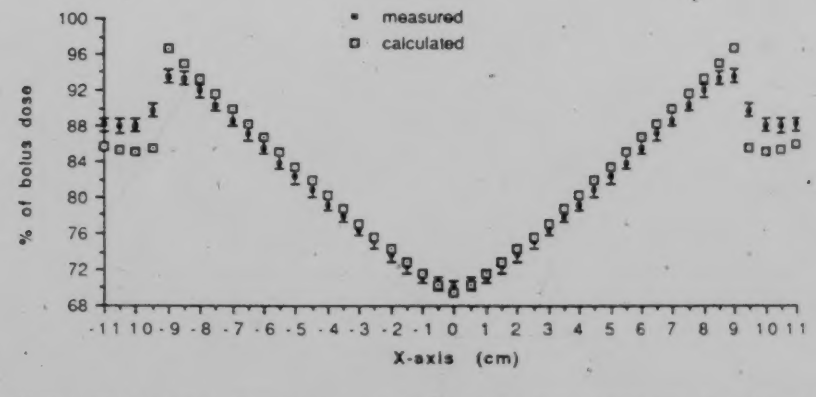

(c) 15MV

Figure 3.27 Compensated dose as a % of bolus dose for the lead cone at 17cm depth (comparison between measurement and calculation with spectrum (a) Cobalt-60, (b) 6MV, (c) 15MV.

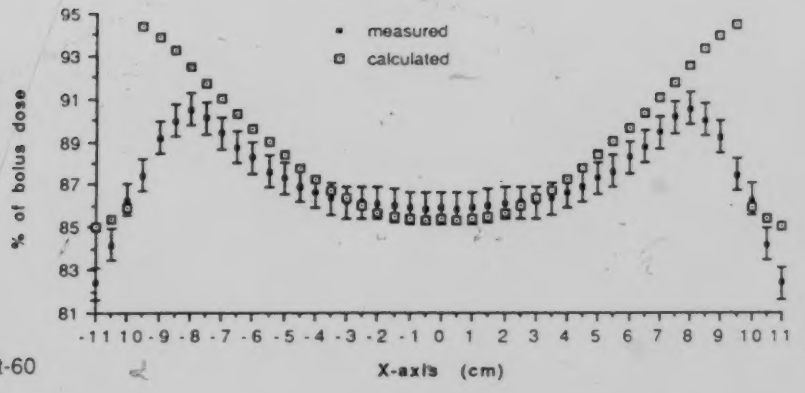

(a) Cobalt-60

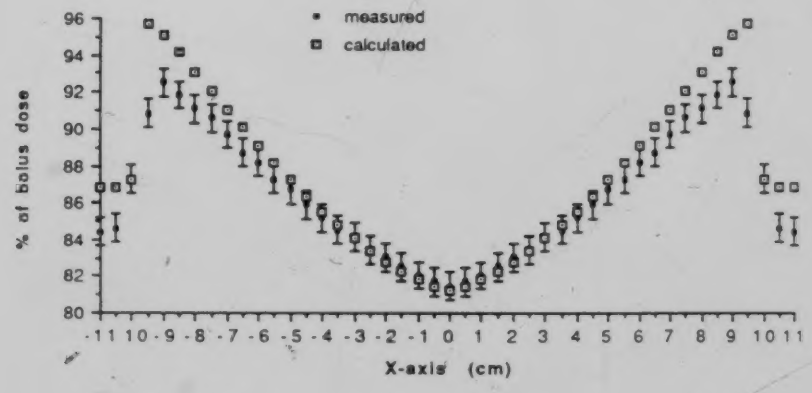

(b) 6MV

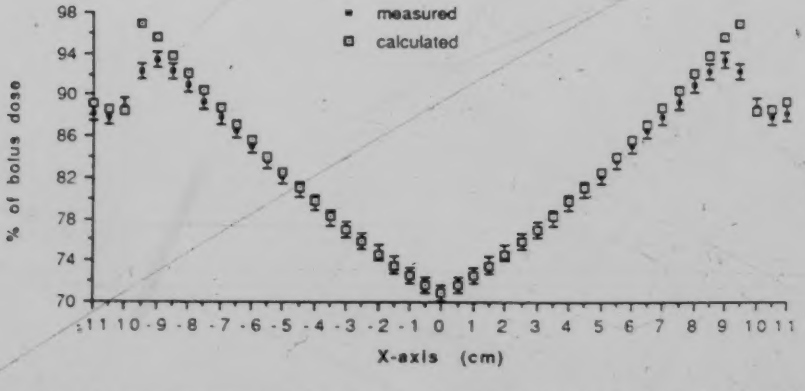

(c) 15MV

Figure 3.28 Compensated dose as a % of bolus dose for the lead cone at 21cm depth (comparison between measurement and calculation with spectrum (a) Cobalt-60, (b) 6MV, (c) 15MV.

As with the calculations involving monoenergetic beams, the degree of agreement between theory and experiment evidenced by the spectrum calculations is different for each situation, but the following general observations apply

a) Cobalt-60

i) at all depths the degree of agreement between theory and experiment is improved over that achieved with the monoenergetic calculations.

ii) at 21cm depth the improvement achieved with the spectrum calculations is marginal. The region of agreement is extended from the -2.5 to +2.5cm region with the monoenergetic calculations to a -4.0 to +4.0 region with the spectrum calculations.

b) 6MV

i) at all depths the degree of agreement between theory and experiment is improved over that achieved with the monoenergetic calculations.

ii) although improved, at depths of 9cm and 12cm agreement within experimental error is not achieved at any point over the entire field of measurement. Disagreement is greatest within those regions nearest to the surface cone where electronic equilibrium dose not exist.

iii) at 15cm depth agreement is achieved over a limited portion of the field. Agreement is not achieved within regions nearest the surface cone, near the field edges, and within and beyond the penumbral regions of the beam. Theory again overpredicts for regions near the

field edge and nearest the surface cone where electronic equilibrium does not exist.

iv) at 17cm and 21cm depths agreement is achieved except for regions near the field edge and within and beyond the penumbral regions. Theory overpredicts near the field edges.

c) 15MV

i) at all depths the degree of agreement between theory and experiment is improved over that achieved with the monoenergetic calculations.

ii) at 9cm, 12cm, and 15cm depths agreement within experimental error is achieved except within regions nearest the surface cone and within and beyond the penumbral regions of the beam.

iii) at 17cm and 21cm depths agreement exists between theory and experiment except for regions near the field edges and within and beyond the penumbral regions of the beam. Theory overpredicts near the field edges.

Collectively these graphs, Figures 3.02 through 3.21 and 3.24 through 3.28 reveal both the strengths and weaknesses of the theoretical approach taken to model the experimental geometries examined. With the exception of the lead cone geometries, the monoenergetic primary photon model achieved agreement, within experimental error, over large portions of the field of measurement for a wide range of depths and energies. Regions where theory fails to achieve agreement are those near the field edges, within and beyond the penumbral regions, and near the surface cone in regions where electronic equilibrium does not exist.

Failure to achieve agreement in regions beyond the penumbra is not of great importance since even though the relative disagreement between theory and experiment can be substantial, the absolute dose in this region is minimal and thus the absolute disagreement is also small.

Disagreement between theory and experiment in the penumbral regions and regions nearest the surface cone where electronic equilibrium does not exist are to be expected and arise from the assumption of electronic equilibrium implicit in the theoretical model. This is born out by the observation that the disagreement observed in these regions is always manifest as an overprediction by theory. This serves as a major limitation of the theoretical approach and can only be overcome by the inclusion of electron transport into the model.

The overpredictions observed near the field edges for some geometries are most likely due to the way in which the penumbral characteristics of the primary photon beams were represented. As discussed earlier, the intensity profile of the primary beam was determined from experimental in-air measurements of the beam intensity. These greatly reduce the contribution of scattered radiation to the measurement(in comparison to that which would be observed in an in water measurement) but does not eliminate scatter completely as scatter generated from the surrounding air and the collimators is always present. This scatter contribution is not critical near the centre of the beam but leads to an overestimation of the primary beam intensity within the penumbral region. This overprediction results from the fact that in reality the primary and scatter dose gradients differ greatly in this region as the

scatter contribution is increasing relative to that of the primary. This produces a broadening of the penumbral region and a subsequent artificially high primary intensity prediction in this region. The increased primary in the penumbral regions, in the calculation predicts a greater scatter contribution to adjacent volumes, resulting in overpredictions near the field edges. The field size used in this experiment was intermediate to those employed to determine the above intensity profiles and hence the field characteristics for this field were determined according to the method of interpolation already discussed. This may also have contributed to the overpredictions seen near the field edges.

It has been shown that the mean energy of an X-ray beam produced by a linac is not constant across the entire area of the field[3.5]. In particular, it decreases as the distance from the central axis is increased. The results of Mohan, et al [3.5] would suggest that near the field edges in these experiments the mean energy of the 6MV beam has decreased by ≈ 5% and the mean energy of the 15MV beam has decreased by ≈ 10%. Examination of the linear attenuation properties of polystyrene, aluminum, and lead shows that such an energy degradation with increasing distance form the central beam axis would result in increased attenuation along ray paths directed toward the field edges. This effect would also result in an overprediction on the part of theory near the field edges as the fields used in the model were monoenergetic.

The results obtained with the lead compensator geometries demonstrate the limitations of the monoenergetic primary photon beam assumption when

lead(and presumably other high Z materials) are used in compensator construction. A greater degree of agreement is achieved by resorting to a polyenergetic beam approach but the degree of improvement achieved is less than desirable. This may indicate the need to take into account the contribution due to Bremsstrahlung photons generated in the lead compensators.

In general, the degree of agreement between the theoretical predictions made in this thesis and experiment is quite good, considering the number of simplifying assumptions incorporated into the theoretical model. Inclusion of second order scattering, photon interactions other than compton scattering, and electron transport would undoubtedly increase the accuracy of the model presented but the potential gain would seem unwarranted in view of the level of the added complexity which would be introduced. Agreement between theory and experiment is seen to be greatest with polystyrene compensators, poorest with lead compensators, and intermediate with aluminum compensators. From this observation one might conclude that the theoretical approach used here best describes compensators constructed from near unit density materials. This, combined with the observation concerning lead geometric compensators expressed at the end of Chapter 2, would suggest that lead is the least desirable material for compensator construction.

Chapter 4

Optimized Compensators

But the years of anxious searching in the dark, with their intense longing, their alterations of confidence and exhaustion, and the final emergence into the light - only those who have experienced it can understand that.

Einstein

IV OPTIMIZED COMPENSATORS

4.1 Theoretical Considerations

The results obtained in Chapter 3 with the theoretical model demonstrate the utility of this approach based on consideration of only zero and first order scatter. With the good agreement obtained between theory and experiment using polystyrene compensators, it is natural to extend the theoretical model to predict the shape of an optimized compensator which will accurately restore the desired bolus dose distribution.

As a starting point consider equation 3.3, for the dose at point P within a phantom, rewritten as

$$D = D_0 e^{-\mu_c(E_0) l_c} + D_p + D_c \qquad \{4.1\}$$

where D_0 is now the primary dose at P with no compensator in the beam, and l_c=primary path length through the compensator with surface z=f(x,y) as shown in Figure 4.01. With the optimized compensator of Figure 4.01 equation 4.1 becomes

$$D' = D_0 e^{-\mu_c(E_0) l'_c} + D'_p + D'_c \qquad \{4.2\}$$

where l'_c=the primary path length through the optimized compensator with surface z=g(x,y).

Dividing {4.1} by {4.2} one obtains

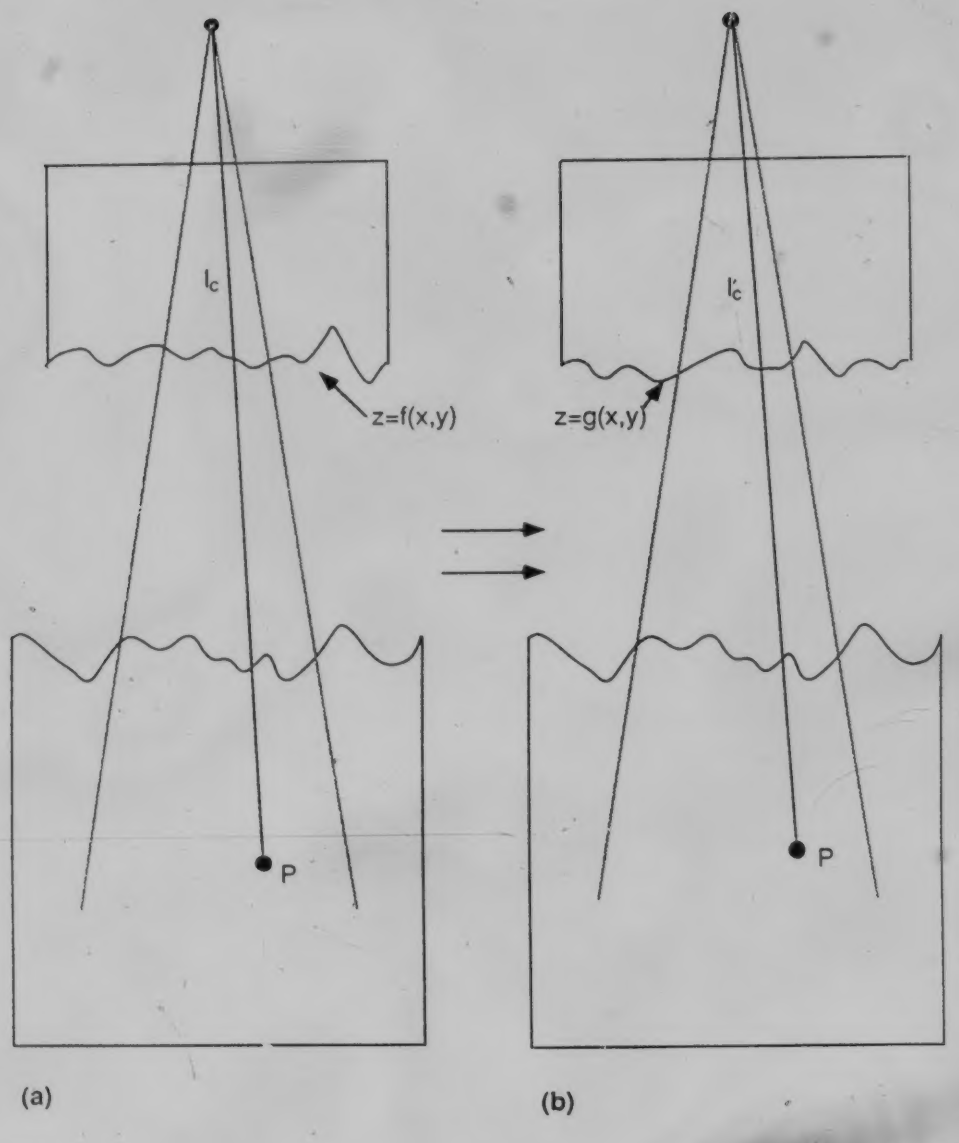

Figure 4.01 Compensation with (a) a geometric compensator, (b) an optimized compensator.

$$\frac{D}{D'} = \frac{D_0\, e^{-\mu_c(E_0) l_c}}{D_0\, e^{-\mu_c(E_0) l_c'} + D_p' + D_c'} + \frac{D_p}{D_0\, e^{-\mu_c(E_0) l_c'} + D_p' + D_c'} + \frac{D_c}{D_0\, e^{-\mu_c(E_0) l_c'} + D_p' + D_c'} \qquad \{4.3\}$$

Assuming that the predominant change in dose at P in going from the original compensator z=f(x,y) to the optimized compensator z=g(x,y) is that due to the change in primary dose, and that in both cases the primary component is predominant, one may drop the last 2 terms of equation 4.3 and write it to first order as

$$\frac{D}{D'} \cong \frac{D_0\, e^{-\mu_c(E_0) l_c}}{D_0\, e^{-\mu_c(E_0) l_c'}} \qquad \{4.4\}$$

Equation 4.4 may be also written as

$$R(r) \cong \frac{D_0\, e^{-\mu_c(E_0) l_c}}{D_0\, e^{-\mu_c(E_0) l_c'}} \cong e^{-\mu_c(E_0)\, \Delta l_c} \qquad \{4.5\}$$

where $l_c' = l_c + \Delta l_c$, since D' = bolus dose. Thus to first order

$$\Delta l_c \cong - \frac{1}{\mu_c(E_0)} \ln(R(r)) \qquad \{4.6\}$$

Equation 4.6 may be applied iteratively to define the desired optimizing compensator surface z=g(x,y) .

4.2 Results and Analysis

Using this approach, it was determined, after two iterations, that a polystyrene compensator cone of 12.26cm height and 8.9cm diameter would produce a dose distribution very close to the desired bolus dose distribution at a depth of 17cm with Cobalt-60 photons. Figure 4.02 shows both the theoretically predicted and experimentally measured dose distribution produced by this optimized compensator. Excellent agreement is seen to exist between theory and experiment and the desired bolus dose distribution is reproduced to within experimental error over 85% of the field area. Agreement to within ± 1.7% is achieved over the entire area of the field except within penumbral regions. The degree of improvement obtained with this optimized compensator is further seen in Figure 4.03 in which the experimental results obtained with this optimized compensator are compared with the experimental results obtained with the geometric polystyrene compensator at this depth. For the latter arrangement the maximum deviation from bolus dose at 17cm depth with Cobalt-60 photons is -13.5% and occurs directly below the tip of the surface cone while the minimum deviation from bolus dose is about -4% and occurs at the field edge. In the optimized compensator geometry the maximum deviation from bolus dose seen with the geometric compensator directly beneath the surface cone tip is reduced to zero and the minimum deviation from bolus dose at the field edges is reduced to -1.5%. The overall improvement in restoration of bolus dose achieved with the optimized compensator is dramatic as Figure 4.03 clearly shows.

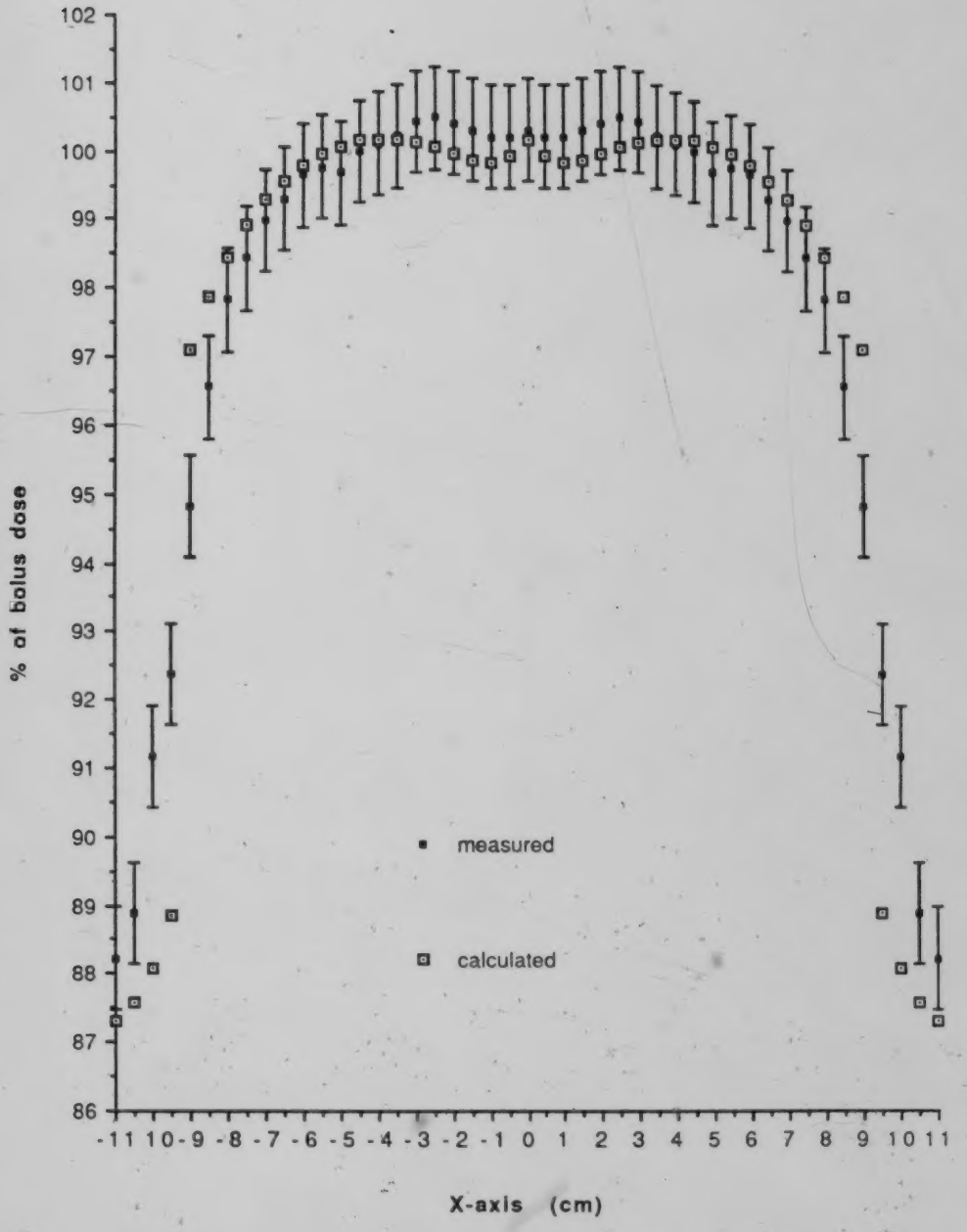

Figure 4.02 Compensated dose as a % of bolus dose for the optimized compensator at 17cm depth with Ccbalt-60 photons (comparison between measurement and calculation).

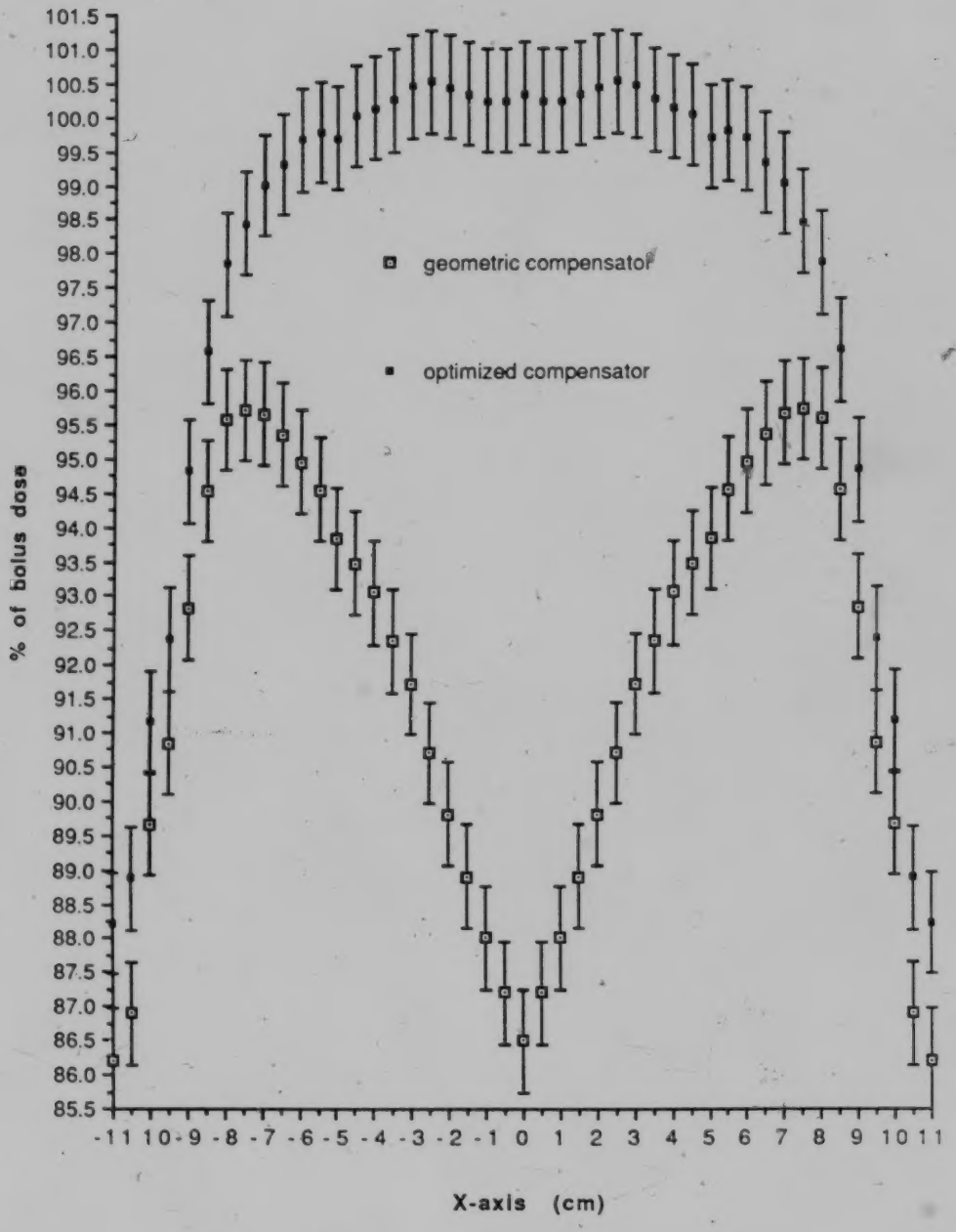

Figure 4.03 Compensated dose as a % of bolus dose comparing geometric and optimized compensators at 17cm depth with Cobalt-60 photons.

Although this optimized compensator is designed for 17cm depth with Cobalt-60 photons, it is of interest to investigate the degree of compensation provided at other depths with Cobalt-60 photons. To this end, the dose distributions obtained with this optimized compensator at depths of 9, 12, 15, and 21cm are compared to the dose distributions obtained with the geometric polystyrene compensator at these same depths with Cobalt-60 photons in Figures 4.04 thru 4.07. At 9cm depth the maximum deviation from bolus dose within the primary field, which occurs near the surface cone is reduced from -13% with the geometric compensator to -6.5% with the optimized compensator. The minimum deviation from bolus dose at this depth occurs at the field edge and is reduced from -4.5% with the geometric compensator to -2.0% with the optimized compensator. This dramatic improvement in the restoration of bolus dose achieved with the use of the optimized compensator occurs at all depths with Cobalt-60 photons. The improvements achieved are clearly evident in Figures 4.04 through 4.07.

Although the compensator which is designed to provide optimum compensation at 17cm depth with Cobalt-60 photons is not the correct geometry to provide optimum compensation at other energies, it can be employed to further test the predictive power of the theoretical model presented here. In the discussion and figures to follow, this compensator will, for the sake of brevity, be referred to as the 1226 cone. Using this 1226 cone with 6MV and 15MV photon beams at all experimental depths, the theoretical and experimental dose distributions presented in Figures 4.08 through 4.12 were obtained. Figures 4.11(a) and 4.11(b) show the results obtained with 6MV and 15MV photons at 17cm depth respectively.

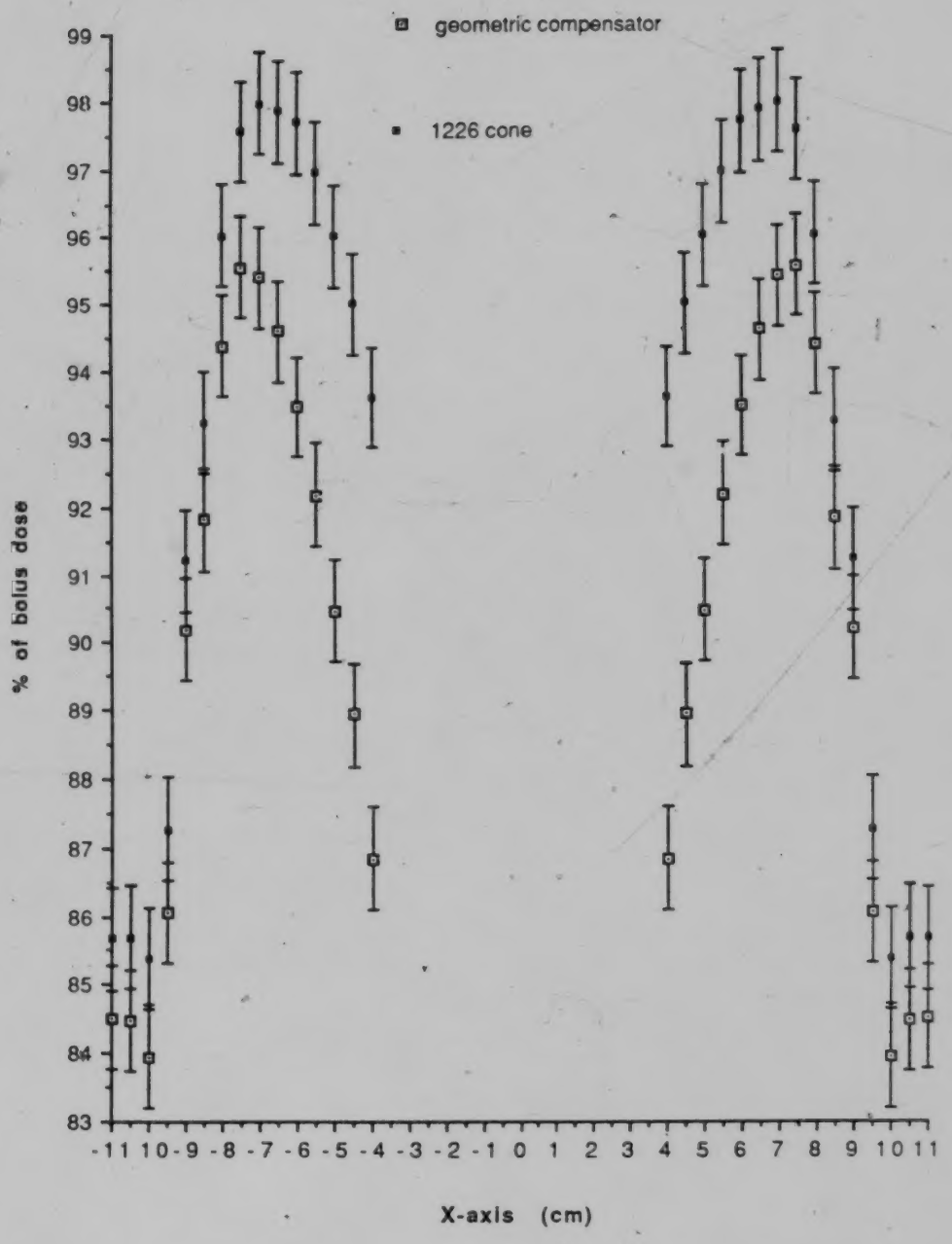

Figure 4.04 Compensated dose as a % of bolus dose comparing the geometric compensator and the 1226 cone at 9cm depth with Cobalt-60 photons (measured).

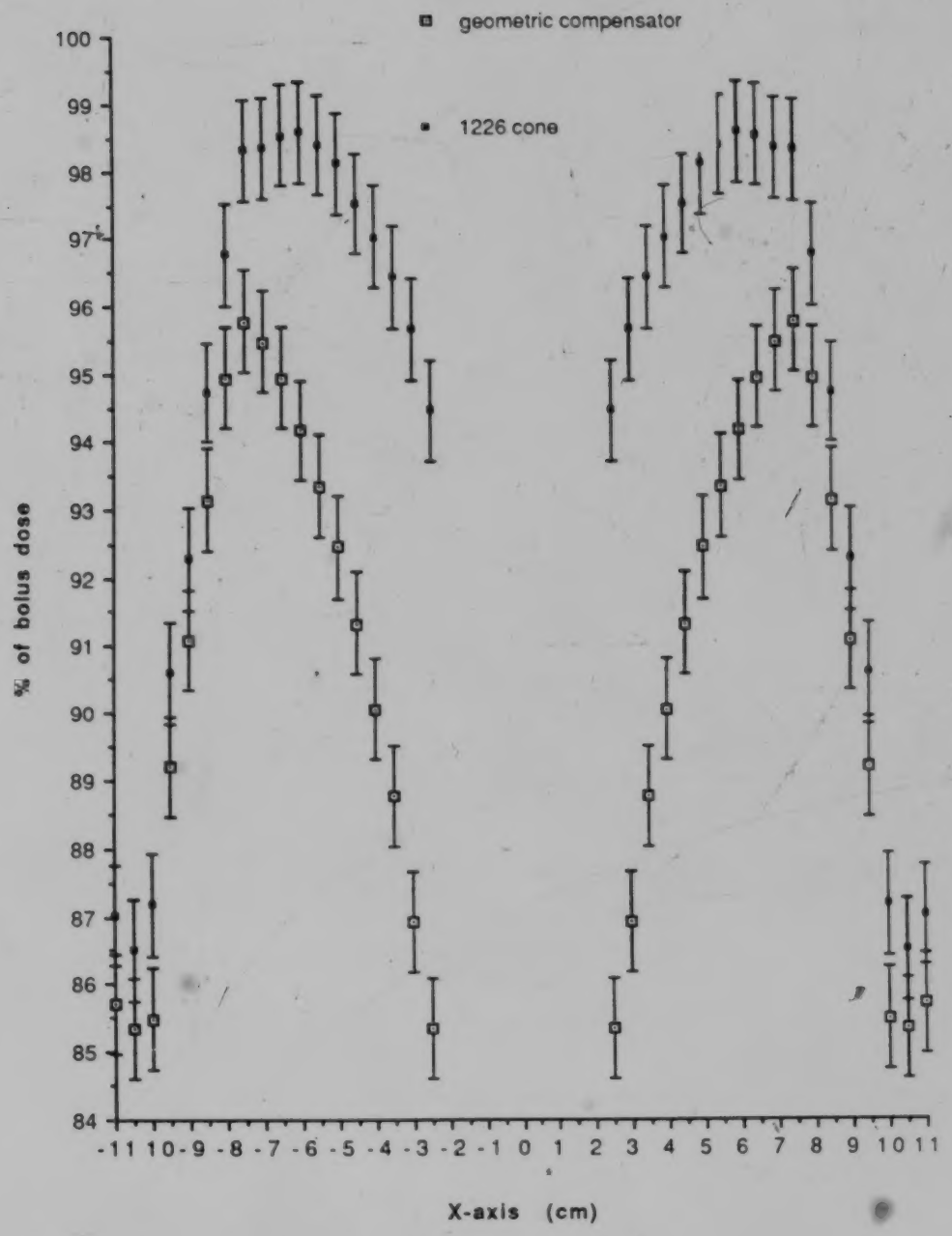

Figure 4.05 Compensated dose as a % of bolus dose comparing the geometric compensator and the 1226 cone at 12cm depth with Cobalt-60 photons (measured).

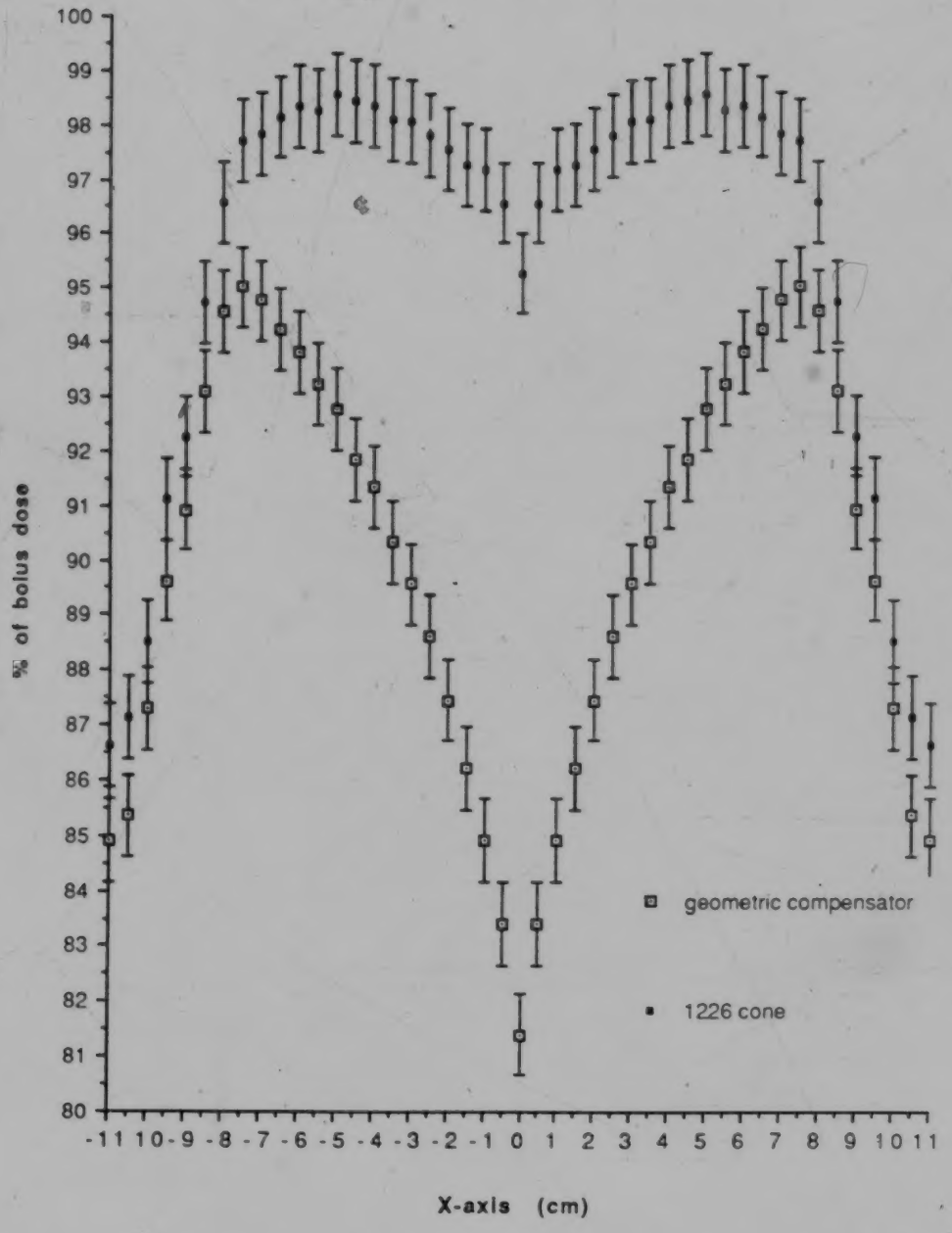

Figure 4.06 Compensated dose as a % of bolus dose comparing the geometric compensator and the 1226 cone at 15cm depth with Cobalt-60 photons (measured).

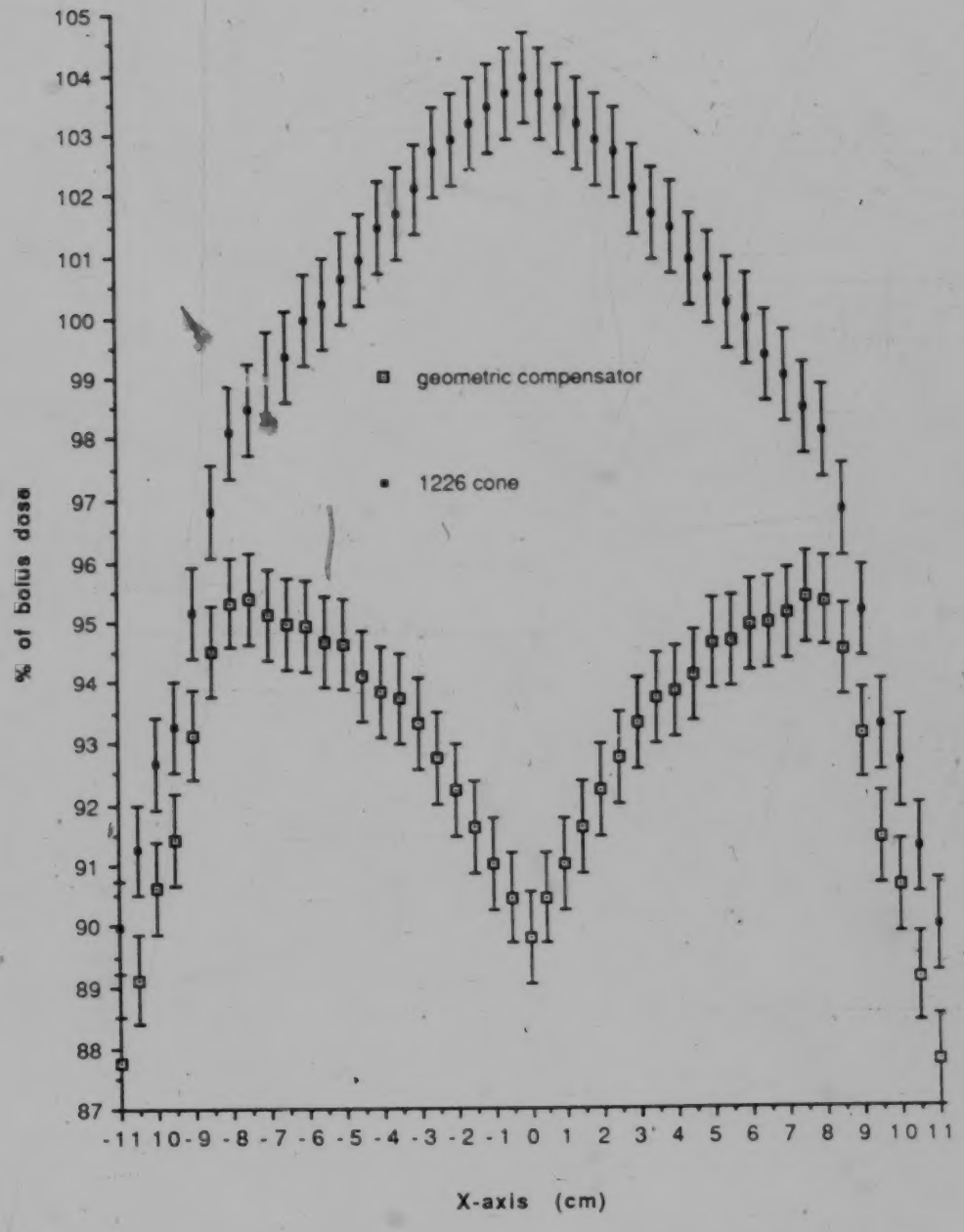

Figure 4.07 Compensated dose as a % of bolus dose comparing the geometric compensator and the 1226 cone at 21cm depth with Cobalt-60 photons (measured).

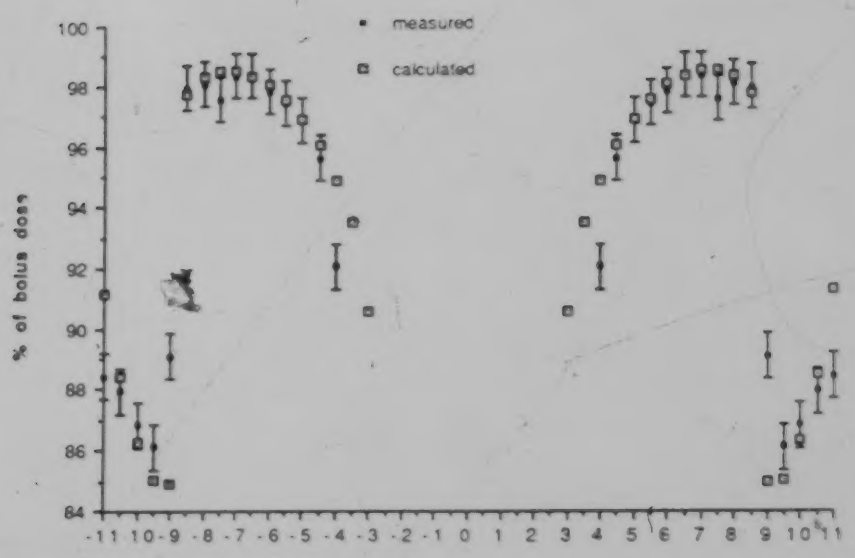

(a) 6MV

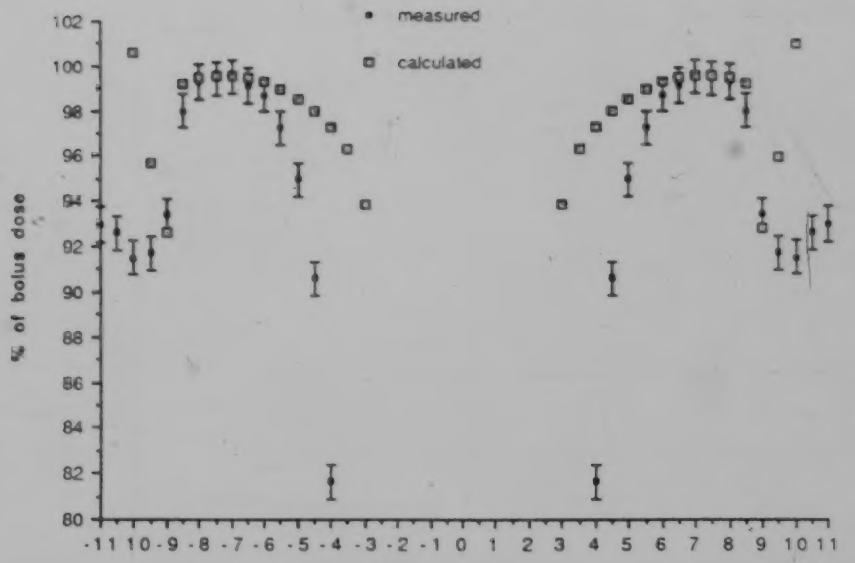

(b) 15MV

Figure 4.08 Compensated dose as a % of bolus dose for the 1226 cone at 9cm depth (comparison between measurement and calculation) (a) 6MV, (b) 15MV.

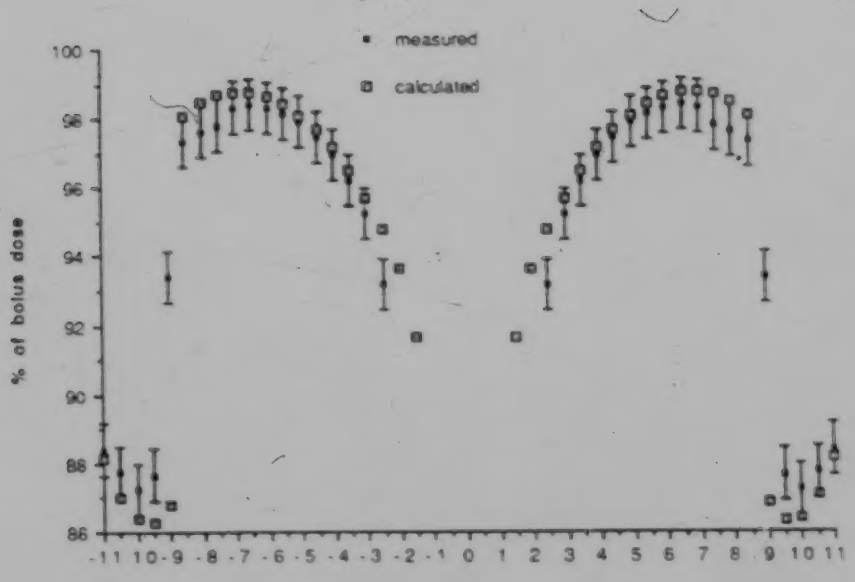

(a) 6MV

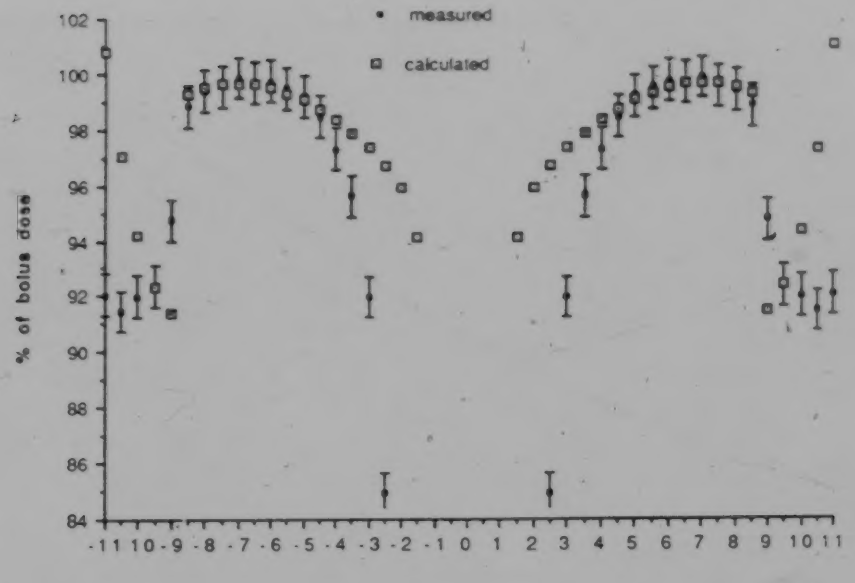

(b) 15MV

Figure 4.09 Compensated dose as a % of bolus dose for the 1226 cone at 12cm depth (comparison between measurement and calculation) (a) 6MV, (b) 15MV.

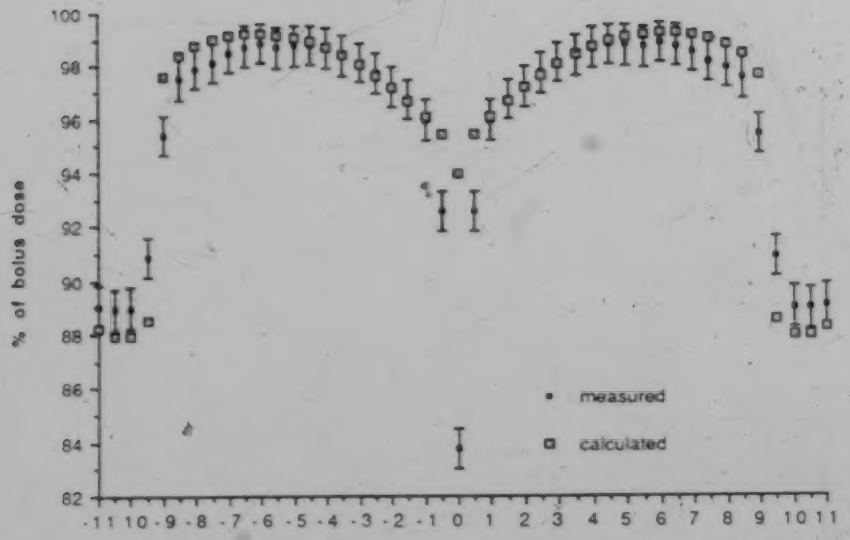

(a) 6MV

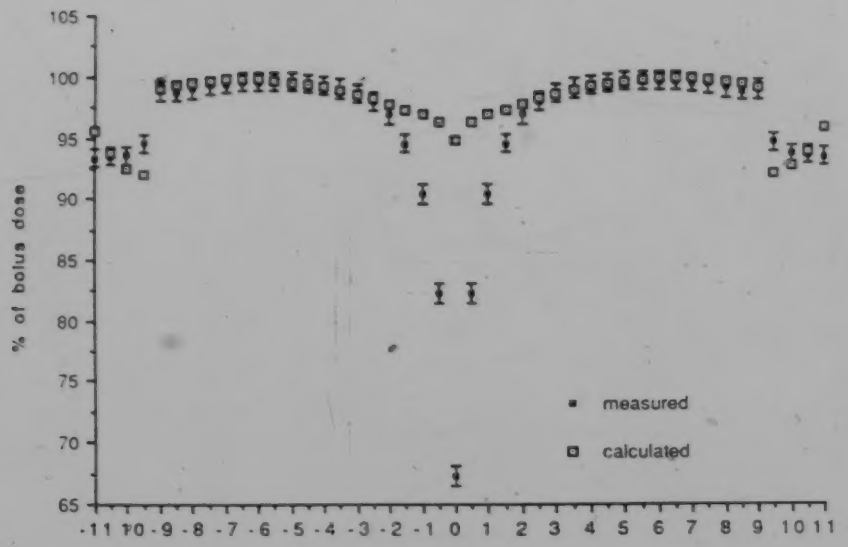

(b) 15MV

Figure 4.10 Compensated dose as a % of bolus dose for the 1226 cone at 15cm depth (comparison between measurement and calculation) (a) 6MV, (b) 15MV.

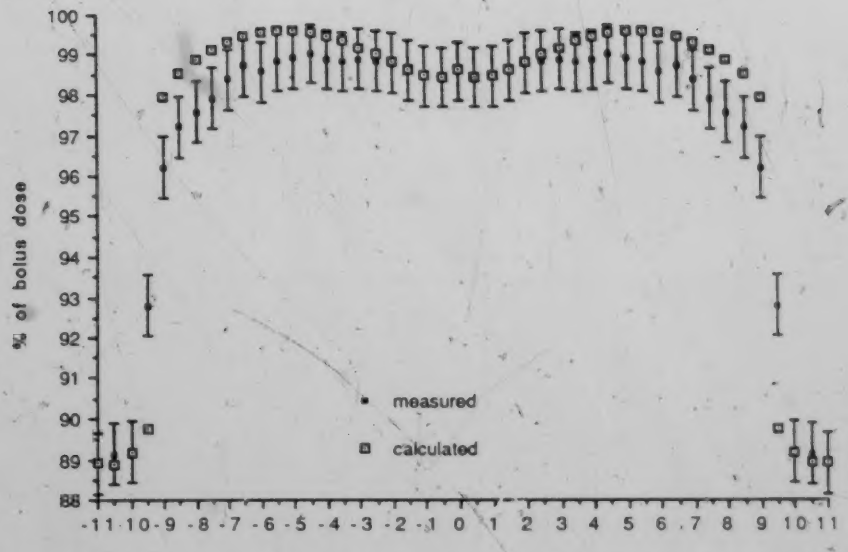

(a) 6MV

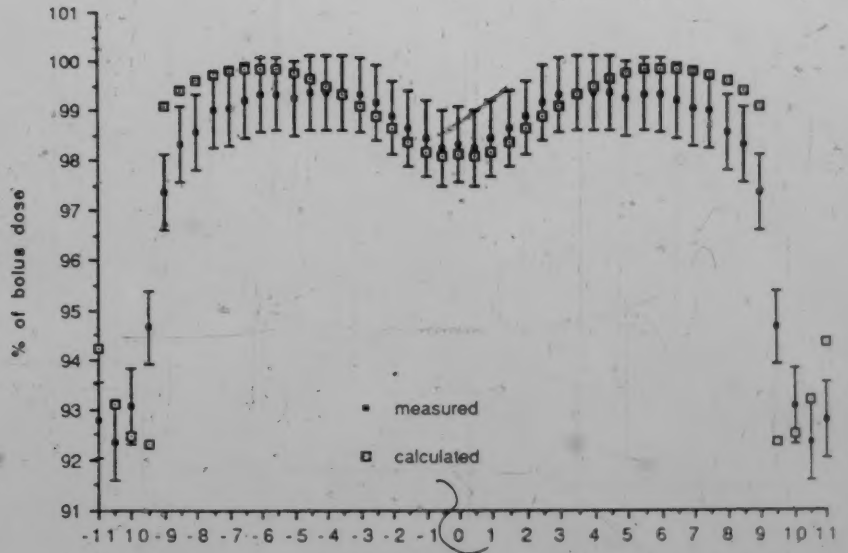

(b) 15MV

Figure 4.11 Compensated dose as a % of bolus dose for the 1226 cone at 17cm depth (comparison between measurement and calculation) (a) 6MV, (b) 15MV.

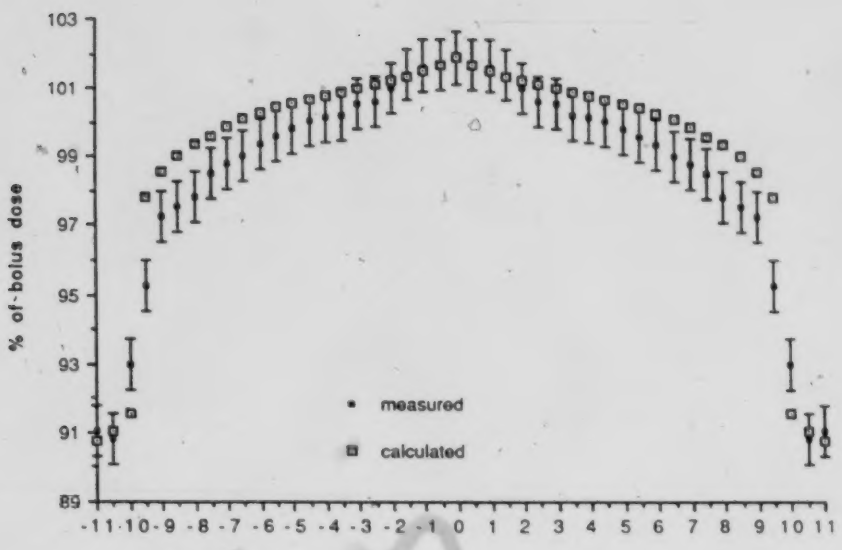

(a) 6MV

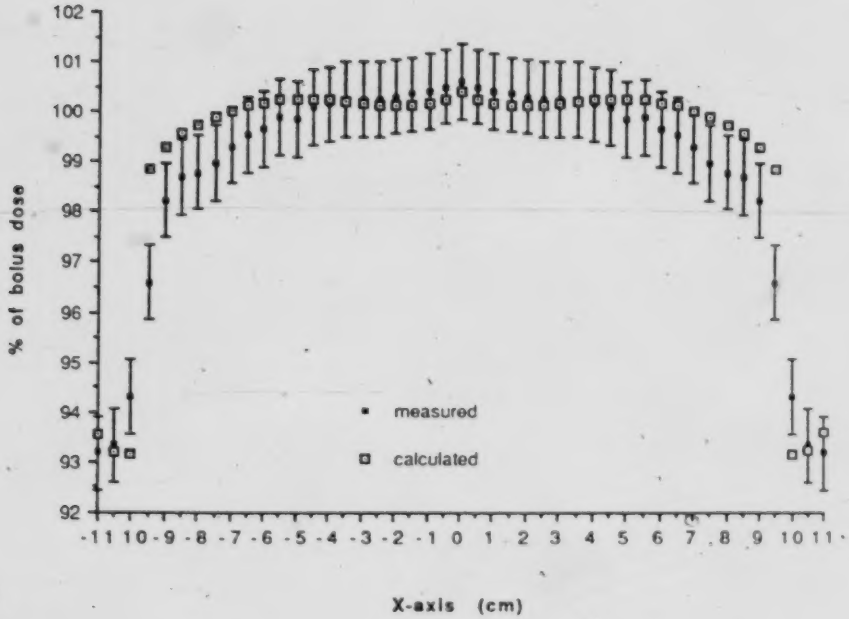

(b) 15MV

Figure 4.12 Compensated dose as a % of bolus dose for the 1226 cone at 21cm depth (comparison between measurement and calculation) (a) 6MV, (b) 15MV.

Agreement between theory and experiment(within experimental error) is seen to exist over 60% of the primary field at both 6MV and 15MV. As in the case with Cobalt-60, the discrepancies between theory and experiment are greatest near the field edges. Within the field edges(primary field) the maximum absolute discrepancies seen for these two geometries are no greater than 1.5% at 6MV and 1% at 15MV.

As was seen in the comparisons presented in Chapter 3, discrepancies exist nearest the surface cone at depths of 9cm, 12cm, and 15cm for both energies. These discrepancies are manifest as overpredictions by theory in accordance with the inability of the theoretical model to correctly handle situations in which electronic disequilibrium exists. Discrepancies are also seen at all depths for both energies within and beyond the penumbral regions of the beam.

Overall, the extent of agreement between theory and measurement seen in Figures 4.08 through 4.12 is very good. The maximum absolute disagreement between theory and experiment within the primary field is found nearest the field edges and even in the worst cases is less than 2%. These results add further weight to the evidence provided in Chapter two of the validity of the theoretical model to both accurately model experimental compensator geometries, and to predict the shape of a compensator which will provide optimum compensation at a designated depth and improved compensation at all other depths.

This data(both theoretical and experimental) also reveals a most interesting volume effect, which has been observed by others. Examination

of Figures 4.03 through 4.07(and 4.08 through 4.12) reveals that the accurate restoration of bolus dose at a designated depth provided through use of an optimized compensator results in volumes above this designated depth being undercompensated while volumes beneath the designated depth are overcompensated. This volume effect which is produced through use of an optimized compensator may be of important clinical relevance. In any case this volume effect does not negate the dramatic improvements produced at all depths through the use of an optimized compensator.

Chapter 5

An Anthropomorphic Geometry

As far as the laws of mathematics refer to reality, they are not certain; and as far as they are certain, they do not refer to reality.

Einstein

V An Anthropomorphic Geometry

5.1 Experimental Parameters

In actual clinical use compensators are required to deal with the irregular surface of real patients. To investigate the applicability of the analytic machinery developed in Chapters 3 and 4 to a clinically relevant geometry an anthropomorphic phantom of the neck region was constructed. This anthropomorphic phantom, shown in Figures 5.01 and 5.02, was constructed of horizontal layers of paraffin wax. The surface contour of this phantom was defined by an immobilization shell specific to the head and neck region. Paraffin was also used to create the bolus geometry shown in Figure 5.03.

Paraffin ($C_{36}H_{74}$), which has a mass density of 0.905 g cm^{-3} and an electron density of $3.806X10^{23}$ e cm^{-3}, was chosen for its near unit density, its ease of use in construction, and its availability in pure form. Both the phantom and its corresponding bolus were constructed by pouring molten paraffin into appropriate molds and allowing it to solidify. A wax geometric missing tissue compensator was also constructed for this geometry using a rod box of the type first described by Watkins[5.1].

Dosimetry was provided by TLD in the form of Lithium Fluoride chips. Small holes were carved along the axes at each layer boundary in the phantom to accommodate these dosimeters. The location of the points of measurement are indicated in Figure 5.04. The phantom was irradiated with

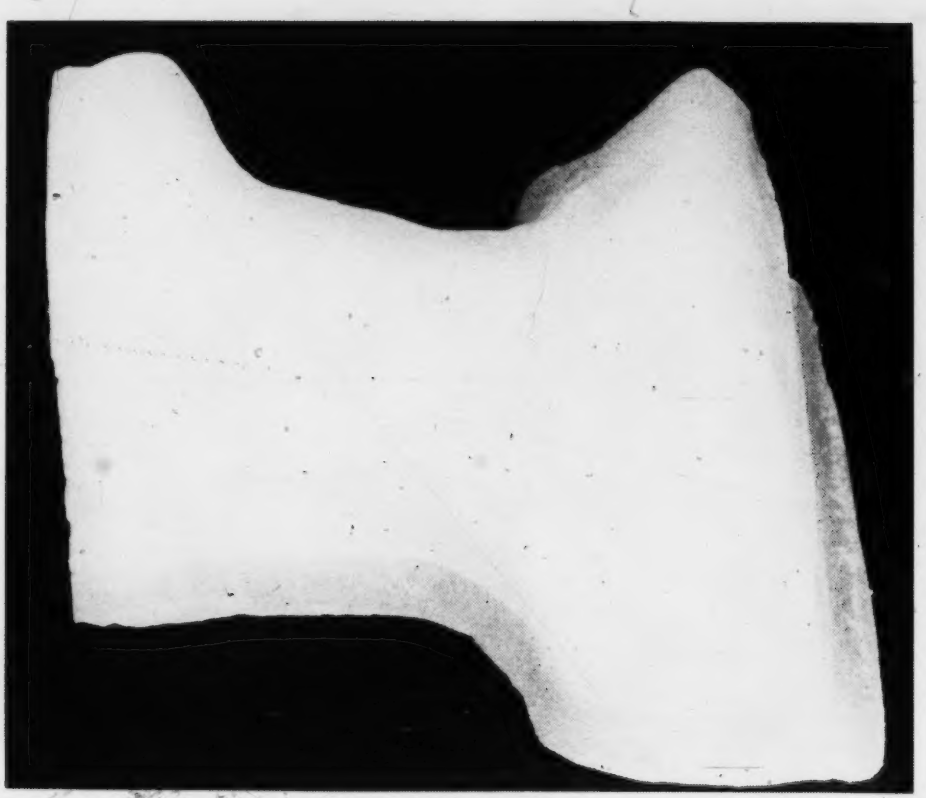

Figure 5.01 The anthropomorphic phantom - side view.

Figure 5.02 The anthropomorphic phantom - anterior view.

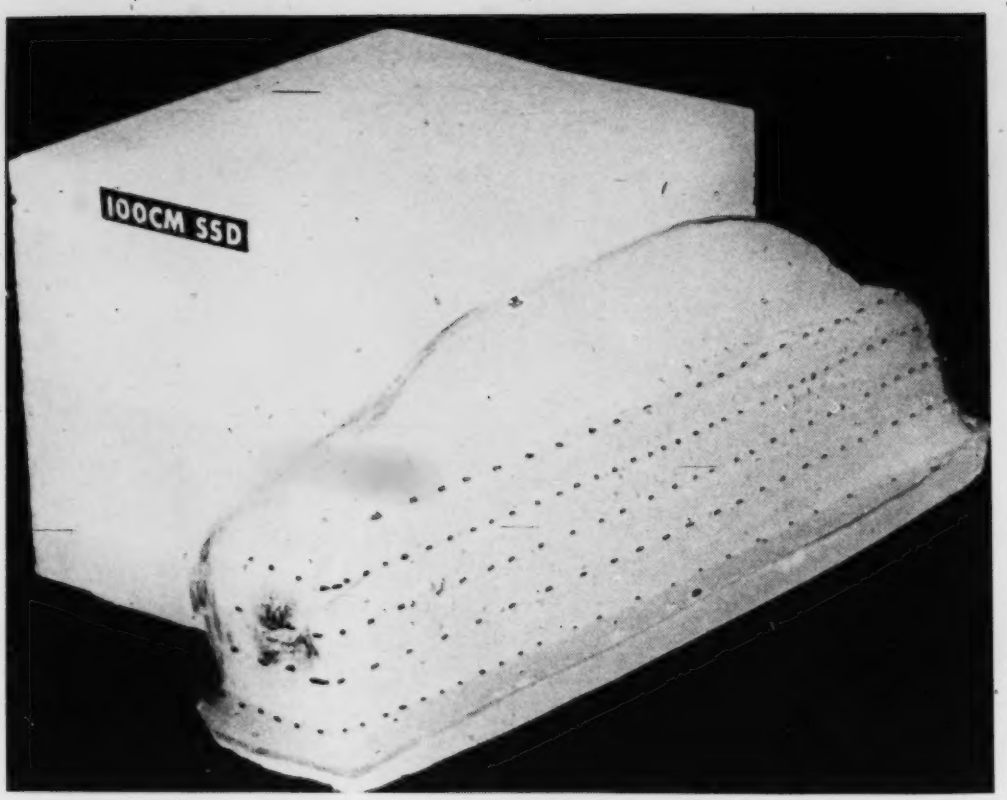

Figure 5.03 The anthropomorphic phantom with bolus.

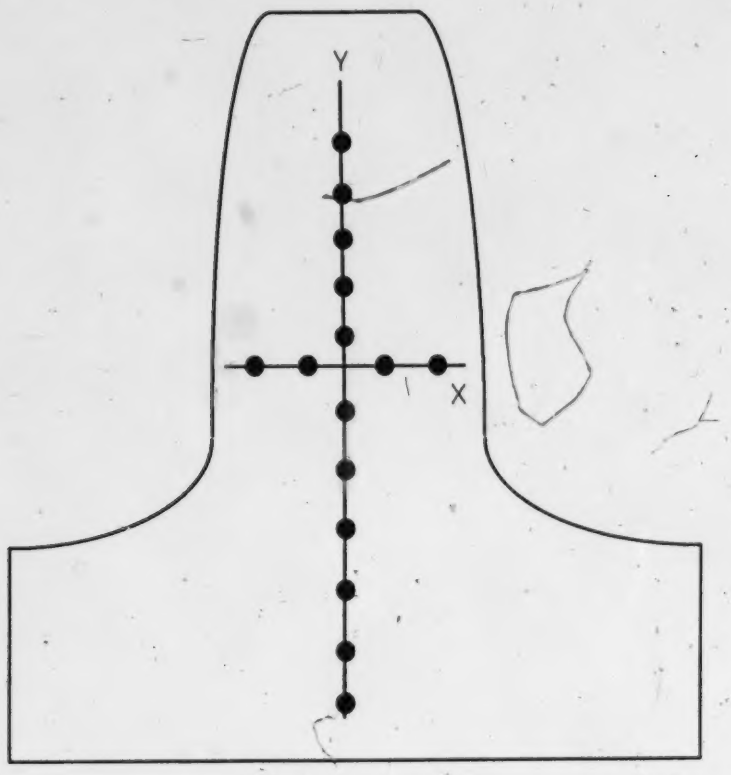

Figure 5.04 Location of the measurement points at each layer in the anthropomorphic phantom.

6MV photons both in the compensated, uncompensated, and bolus configurations with the central beam axis normal to the horizontal layers.

The highest point on the phantom, corresponding to the chin, was set at 100cm SSD which served to define the bolus surface. The depth of each measurement layer is indicated in the principal axis cross section of the phantom-bolus arrangement shown in Figure 5.05. As was the case in the conical geometry, uncertainties in all dose measurements were determined by making each measurement a number of times and determining the standard deviation of these measurements. Propagation of error was determined according to the formulas for limit error.

5.2 Experimental Results

Measurements obtained at each layer boundary in both the uncompensated and compensated configurations are expressed as a percentage of bolus dose and are presented in Figures 5.06 through 5.15.

Figures 5.06 through 5.15 reveal large deviations from bolus dose in the uncompensated dose distributions. Maximum deviations from bolus dose are seen to range from +16% to +28% without compensation. All compensated dose measurements are less than those with bolus; with the deviation varying from point to point at each layer. At no point of measurement is the desired bolus dose restored. At some points the absolute deviation from bolus dose is in fact greater with compensation than without.

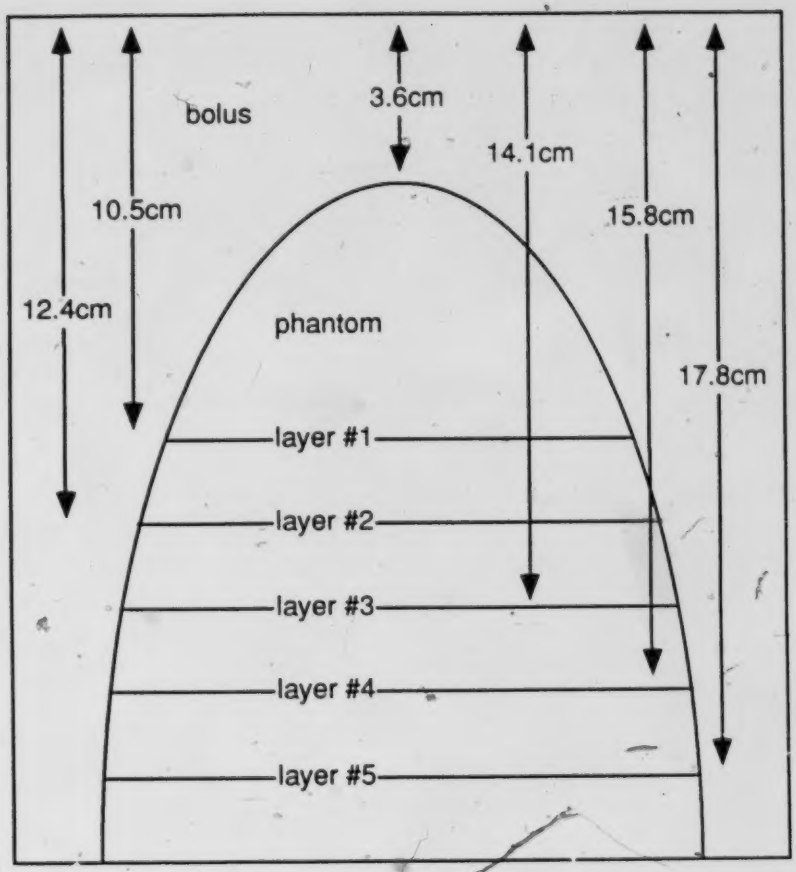

Figure 5.05 Cross sectional view of the anthropomorphic phantom-bolus configuration.

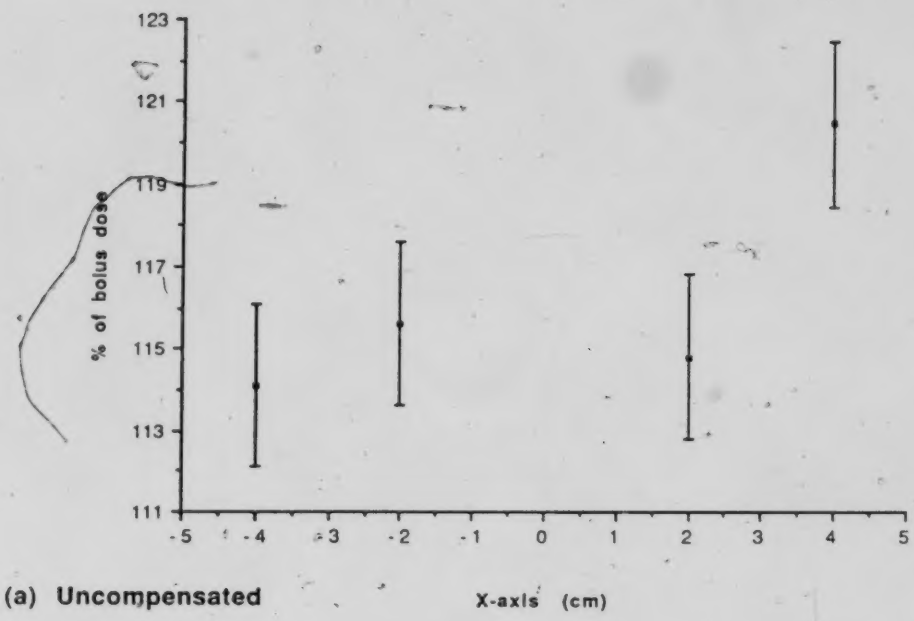

(a) Uncompensated

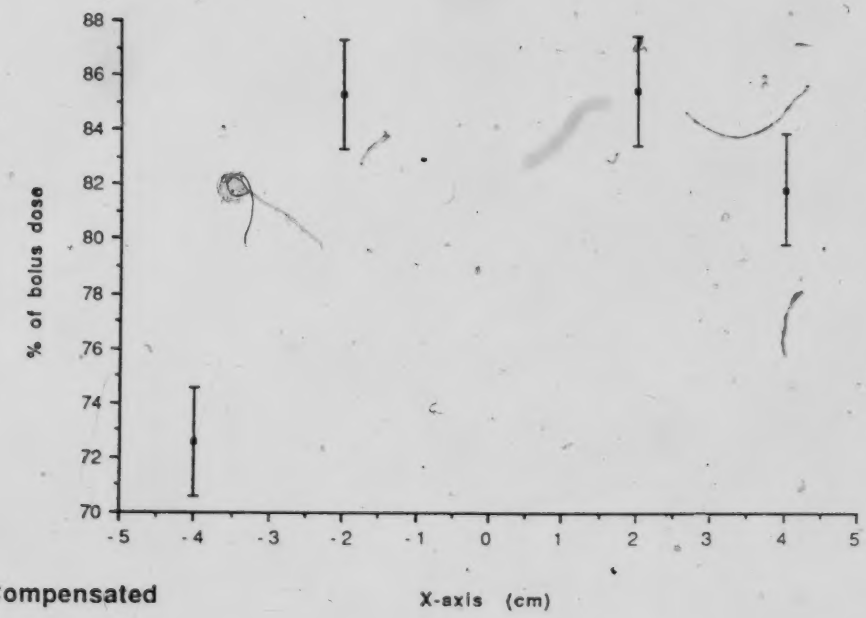

(b) Compensated

Figure 5.06 Percentage of bolus dose along the X-axis at layer #1 (a) Uncompensated, (b) Compensated.

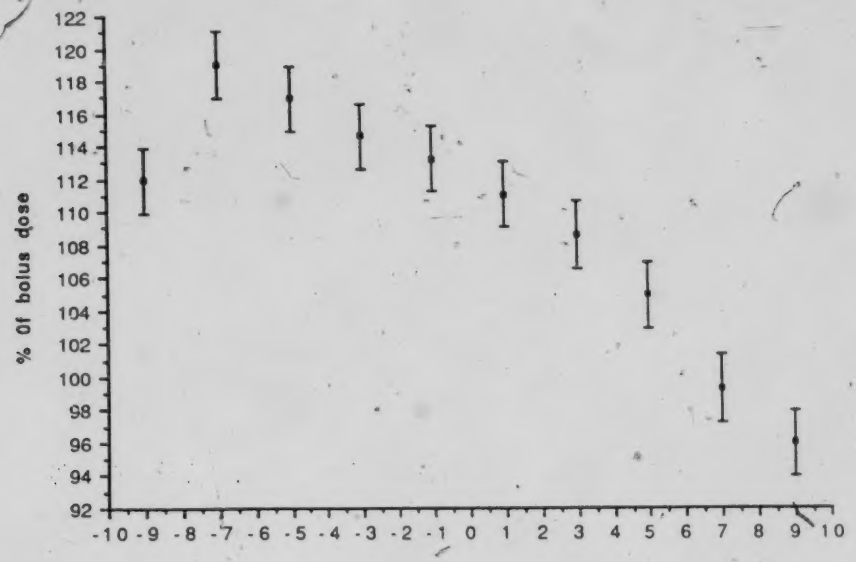

(a) Uncompensated

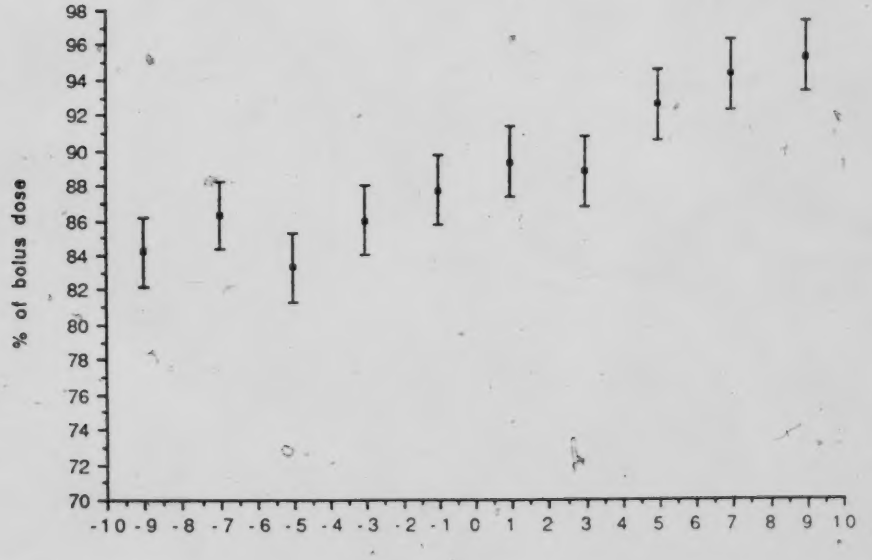

(b) Compensated

Figure 5.07 Percentage of bolus dose along the Y-axis at layer #1 (a) Uncompensated, (b) Compensated.

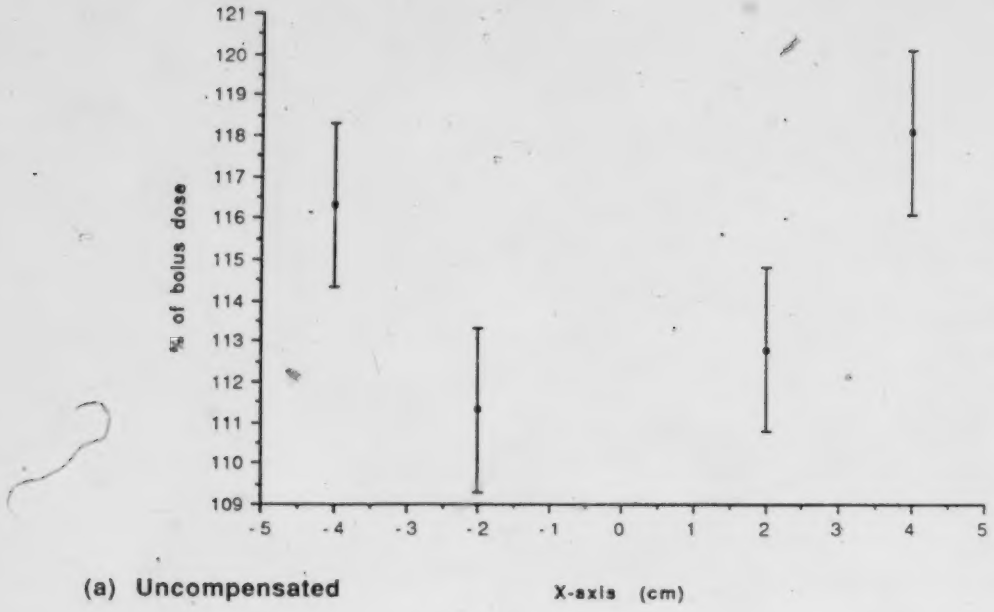

(a) Uncompensated

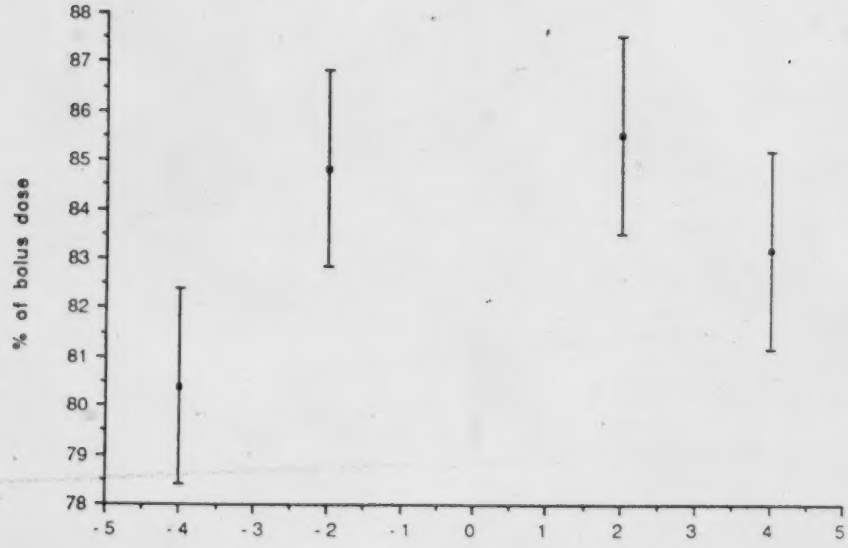

(b) Compensated

Figure 5.08 Percentage of bolus dose along the X-axis at layer #2 (a) Uncompensated, (b) Compensated.

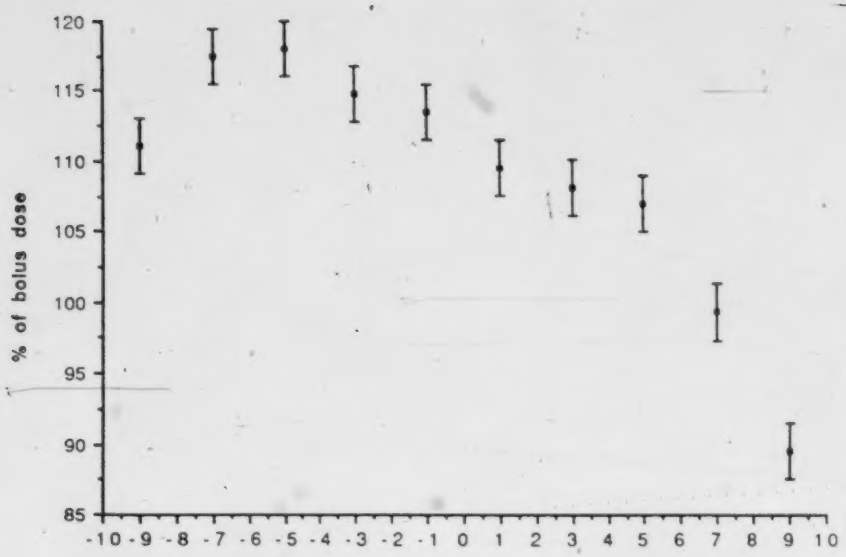

(a) Compensated

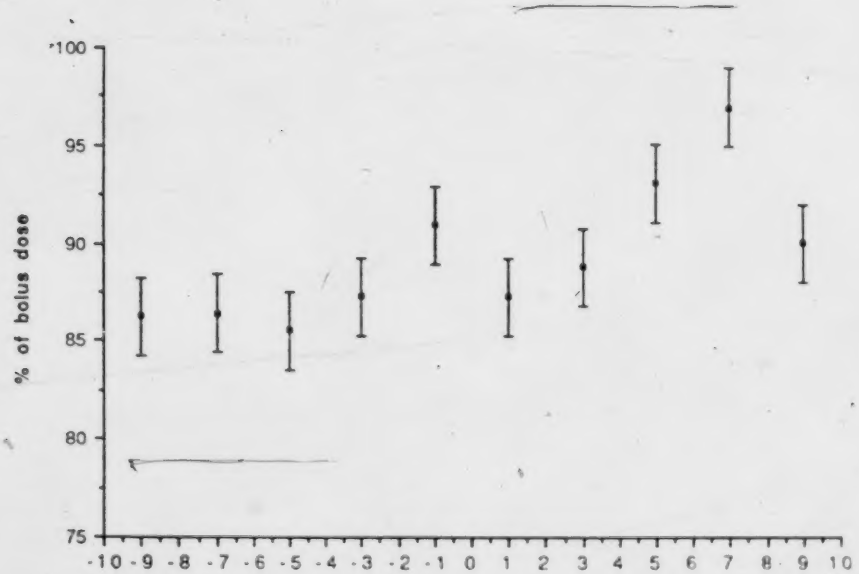

(b) Compensated

Figure 5.09 Percentage of bolus dose along the Y-axis at layer #2 (a) Uncompensated, (b) Compensated.

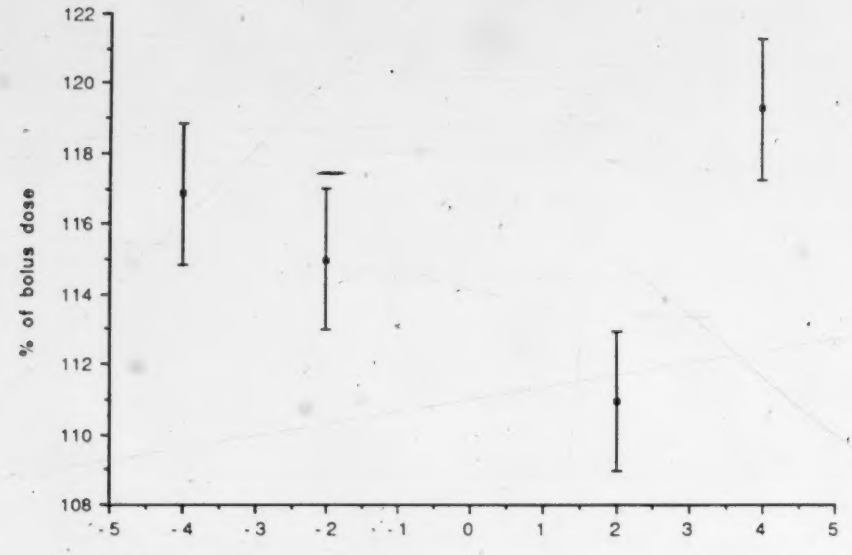

(a) Uncompensated

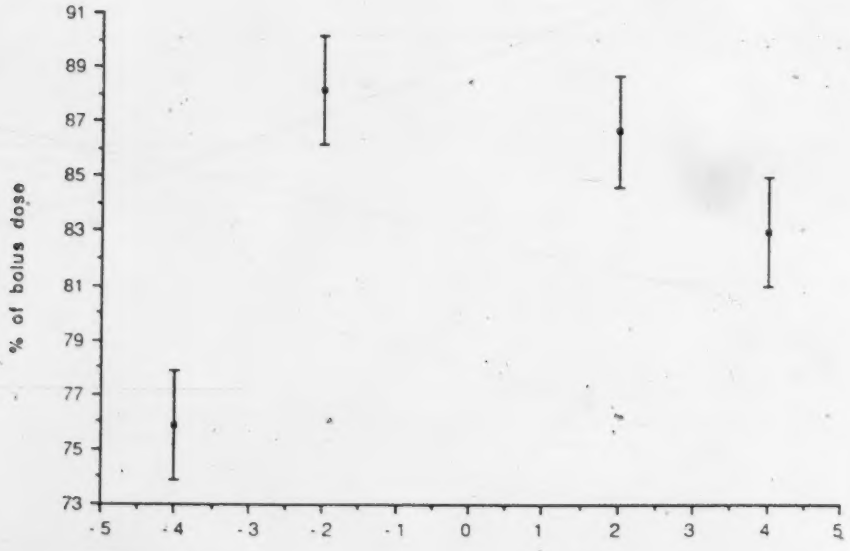

(b) Compensated

Figure 5.10 Percentage of bolus dose along the X-axis at layer #3 (a) Uncompensated, (b) Compensated.

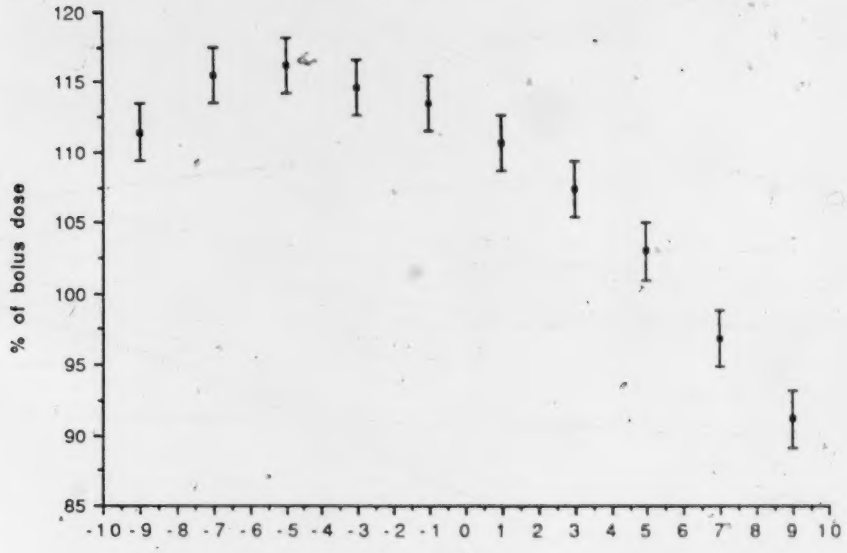

(a) Uncompensated

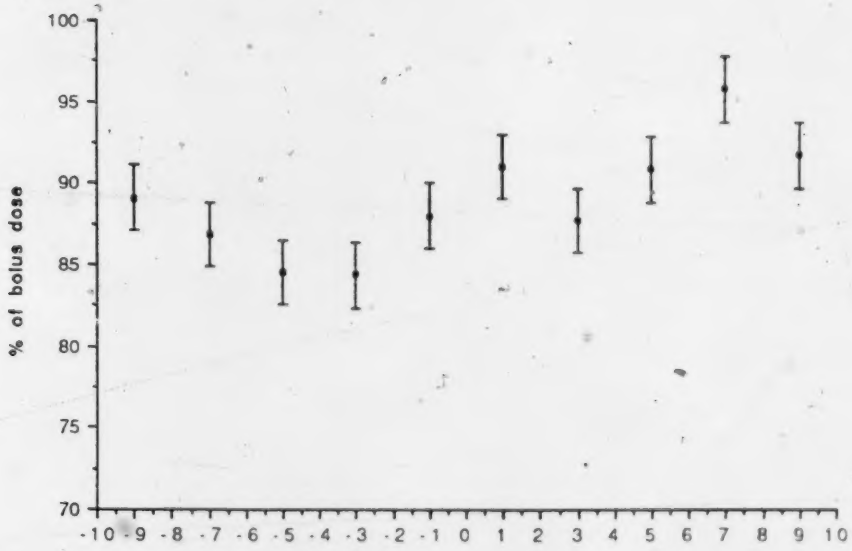

(b) Compensated

Figure 5.11 Percentage of bolus dose along the Y-axis at layer #3 (a) Uncompensated, (b) Compensated.

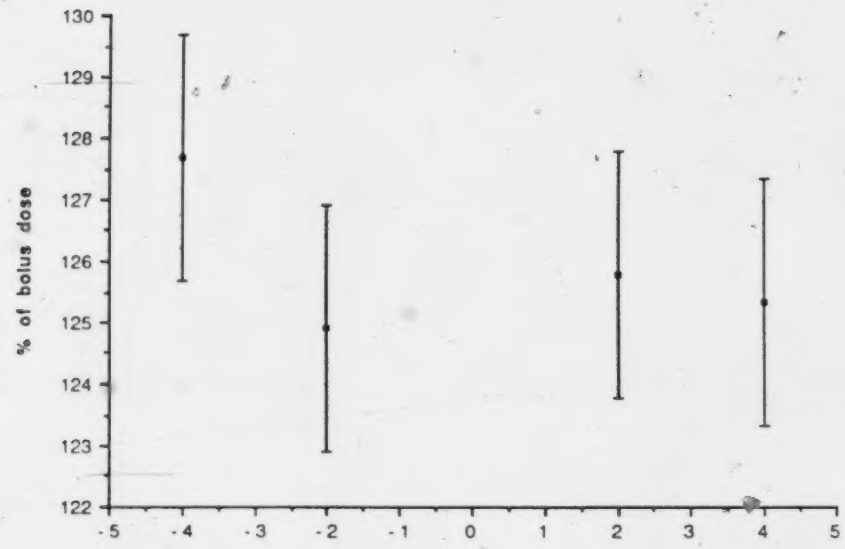

(a) Uncompensated

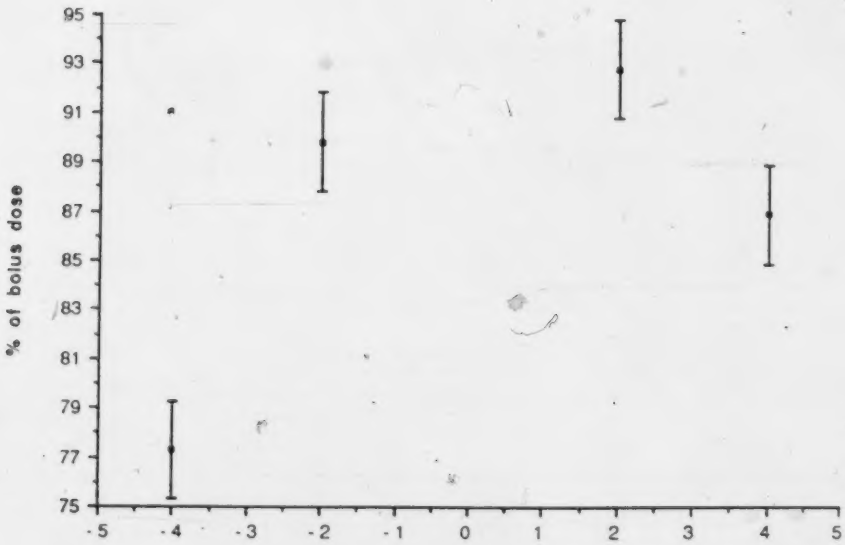

(b) Compensated

Figure 5.12 Percentage of bolus dose along the X-axis at layer #4 (a) Uncompensated, (b) Compensated.

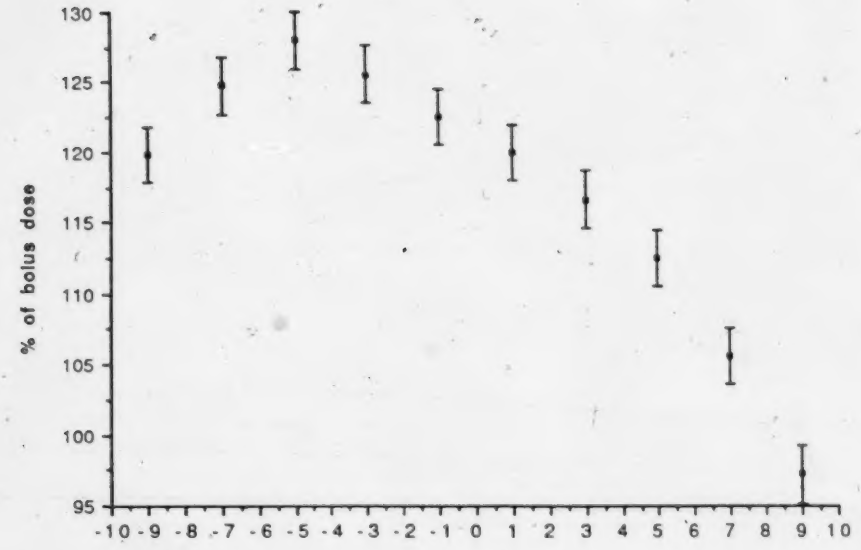

(a) Uncompensated

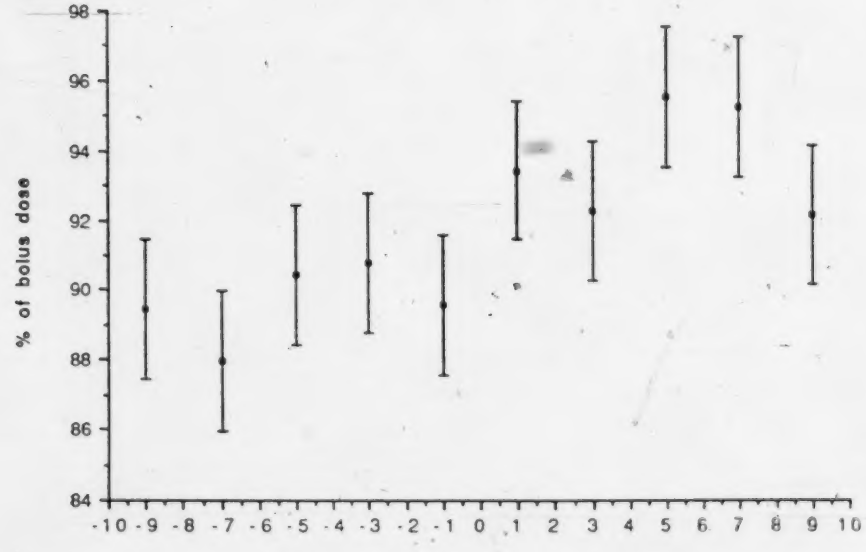

(b) Compensated

Figure 5.13 Percentage of bolus dose along the Y-axis at layer #4 (a) Uncompensated, (b) Compensated.

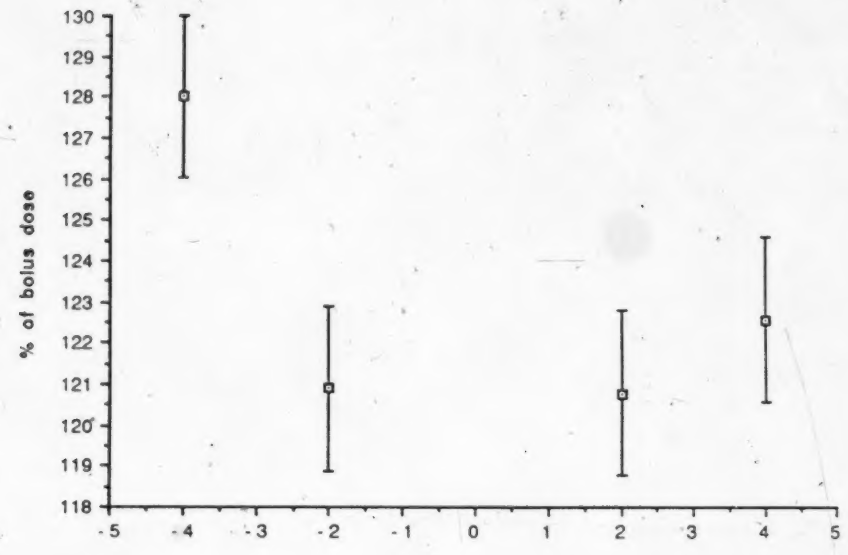

(a) Uncompensated

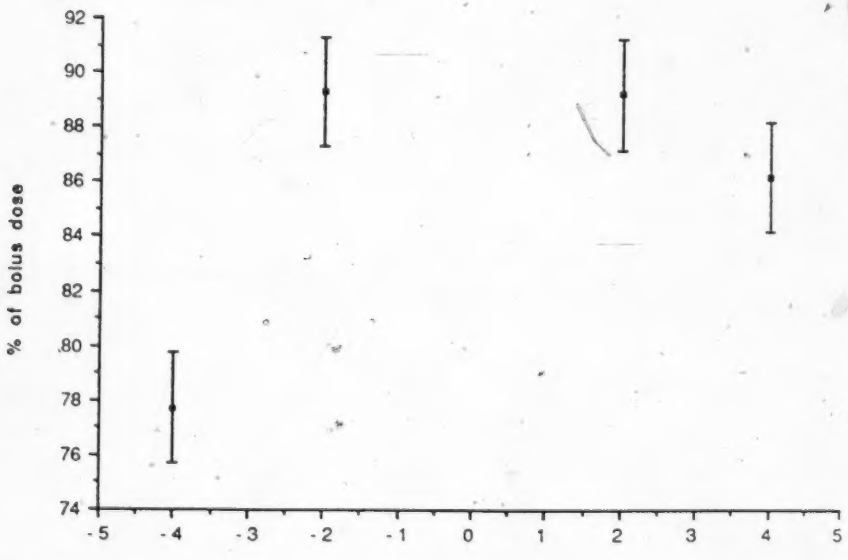

(b) Compensated

Figure 5.14 Percentage of bolus dose along the X-axis at layer #5 (a) Uncompensated, (b) Compensated.

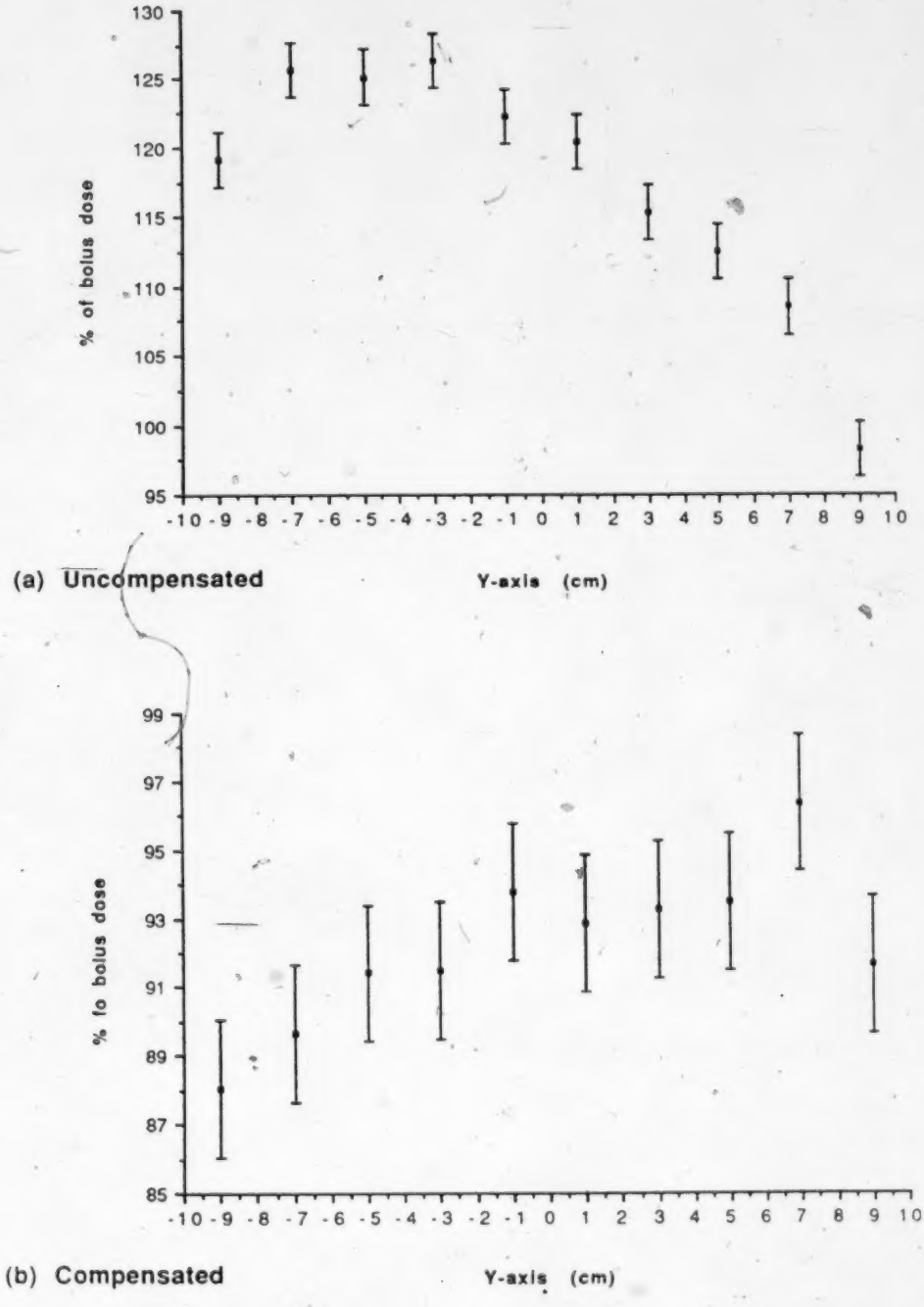

Figure 5.15 Percentage of bolus dose along the Y-axis at layer #5 (a) Uncompensated, (b) Compensated.

The mean deviations from bolus dose along the axes at each layer are presented in Table 5.1. Signed deviations indicate that all values were either greater than (+) or less than (-) bolus dose while unsigned values are absolute deviations as measurements both greater than and less than bolus dose were recorded along that axis. Along the X-axis the mean deviation from bolus dose is smaller with compensation for layers 4 and 5 while for layers 1,2, and 3 the mean deviation is larger with compensation than without. Examination of Figures 5.06 through 5.15 and Table 5.1 clearly indicates that the degree of compensation achieved with a geometric compensator specific to this geometry leaves much to be desired and the need for improvement is obvious.

5.3 Optimized Compensation

The theoretical approach developed in Chapter 3 has shown its ability to accurately model the dose distributions experimentally observed for a mathematically describable geometry. In Chapter 4 the theoretical model was used to predict the shape of a compensator which would provide optimum compensation for the mathematical geometry of Chapter 3. The accuracy of this prediction was experimentally verified.

To test the model's clinical usefulness the geometry routines of the program CONE were rewritten to handle irregular surfaces. The new program created, called IRREG, was applied to this anthropomorphic phantom and, as in the case with the conical geometry, after two iterations, produced a predicted shape for a compensator which would restore the bolus dose distribution at layer 3. Thickness profiles along the Y-axis for

Configuration	Layer #1		Layer #2		Layer #3		Layer #4		Layer #5	
	Axis		Axis		Axis		Axis		Axis	
	X	Y	X	Y	X	Y	X	Y	X	Y
Uncompensated	+16.3	10.6	+14.6	11.1	+15.5	10.4	+28.9	17.8	+23.2	17.4
Compensated	-18.5	-11.6	-16.5	-10.8	-16.4	-11.0	-13.3	-8.4	-14.3	-7.9

Table 5.1 Mean deviation (percentage) from bolus dose in the uncompensated and compensated configurations.

both the geometric and optimized compensators are shown in Figure 5.16 for purposes of comparison. As can be seen from Figure 5.16, no simple relationship exists between the geometric and optimized geometries. This optimized compensator was constructed of paraffin wax. The experimental results obtained with this optimized compensator are presented, in comparison with theoretically predictions, in Figures 5.17 through 5.21.

At layer 3 the optimized compensator accurately restores the desired bolus dose distribution within experimental error (±2%)over 70% of the field area.Restoration to within 3.5% is achieved over the entire area of the field with theory and experiment agreeing within experimental error at all points of measurement. At the other depths, below and above layer 3, agreement within experimental error is seen to exist between theory and experiment except for a few points within and beyond the penumbral regions of the beam. Again, it is seen that depths above the plane of optimization receive doses lower than with bolus while depths below the optimization depth receive doses greater than with bolus. This effect is a desirable as it acts counter to the natural increased attenuation of the beam with increasing depth and thus enhances the dose uniformity achieved in a volume surrounding the plane of optimization. Comparison with the results obtained using the geometric compensator specific to this geometry clearly demonstrates the utility of this approach to the design of effective tissue compensators which achieve the goals for which they were originally intended.

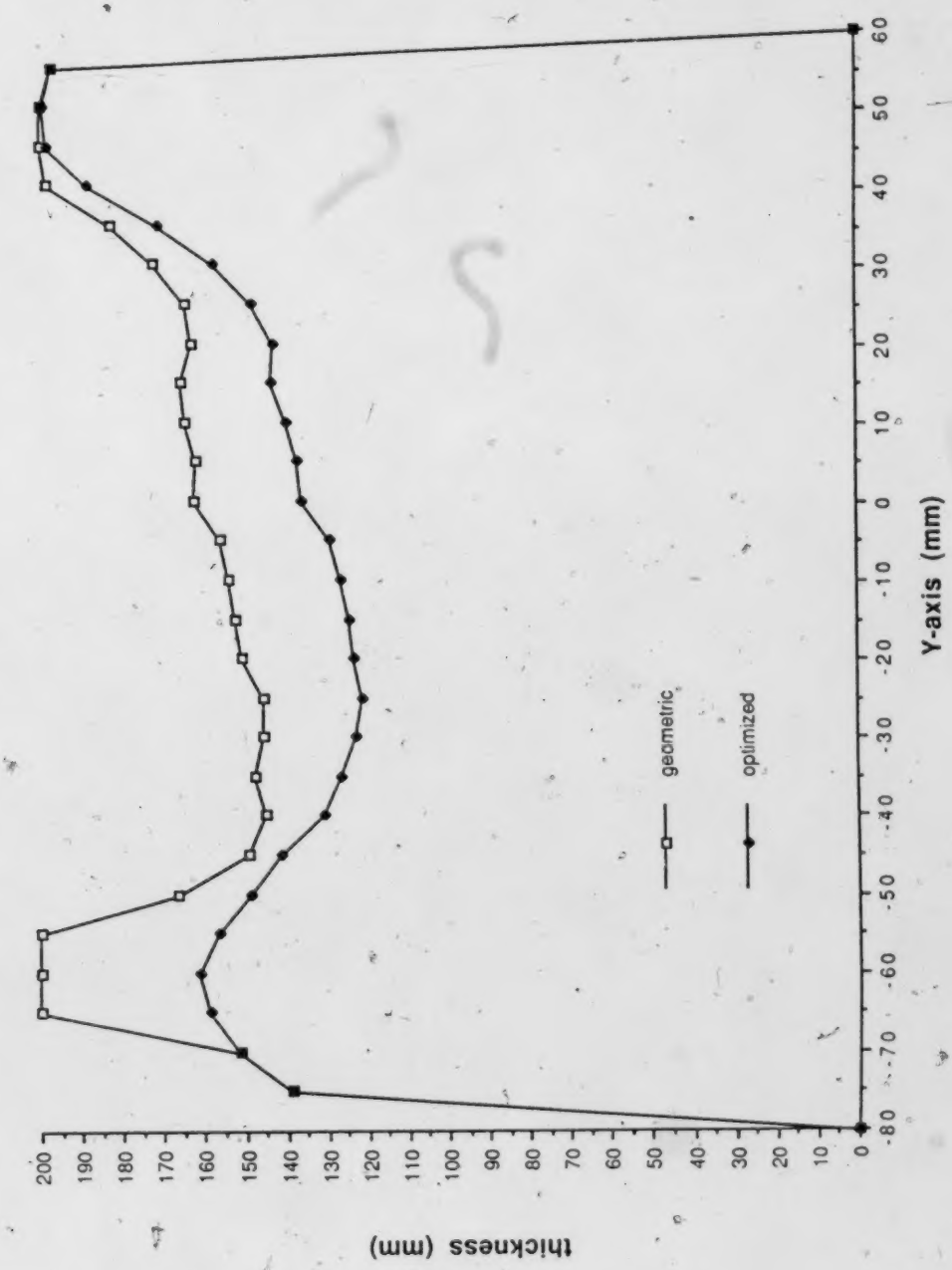

Figure 5.16 Thickness profiles of the geometric and optimized compensators along the Y-axis at X = 0.0mm

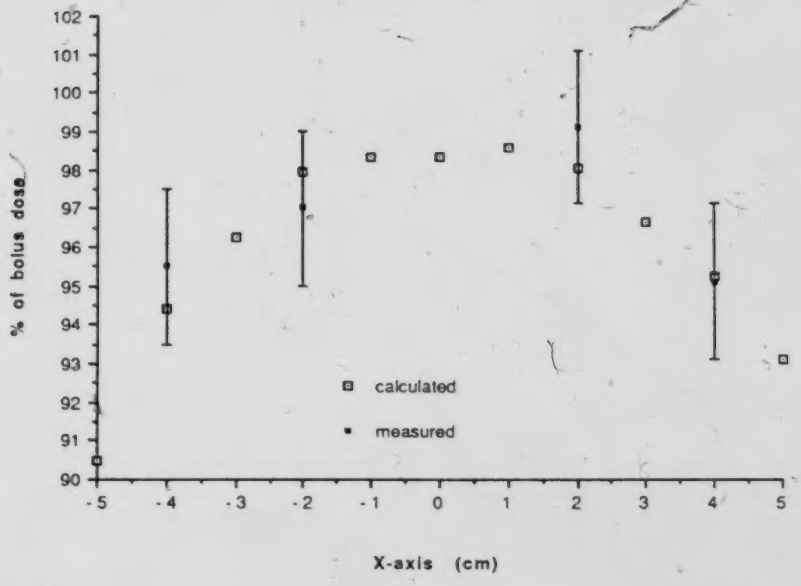

(a)

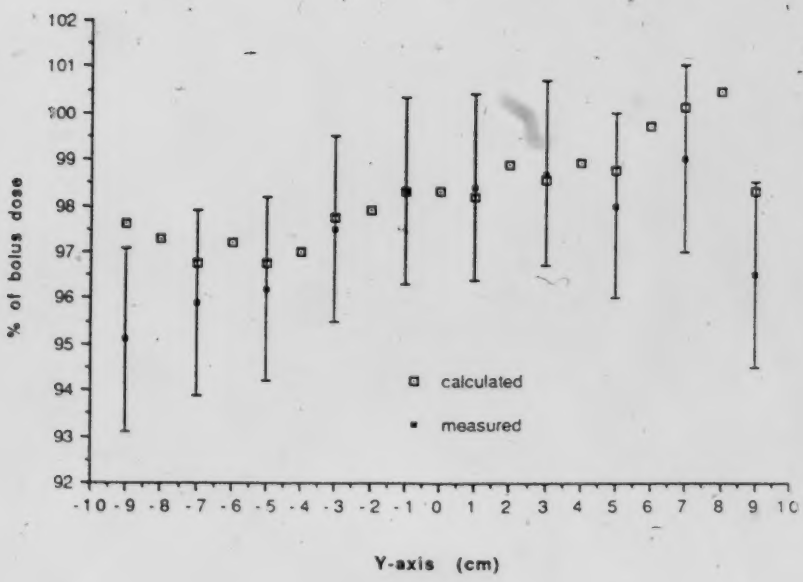

(b)

Figure 5.17 Percentage of bolus dose at layer #1 with the optimized compensator (comparison between measurement and calculation) (a) along the X-axis, (b) along the Y-axis.

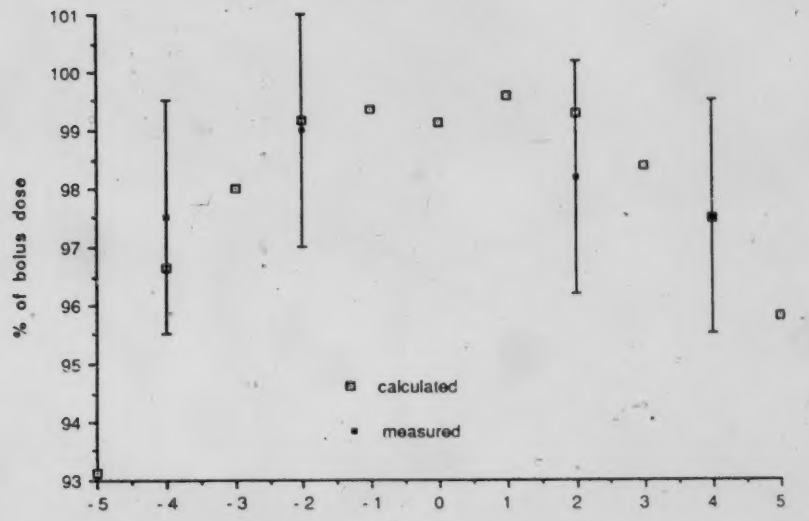

(a)

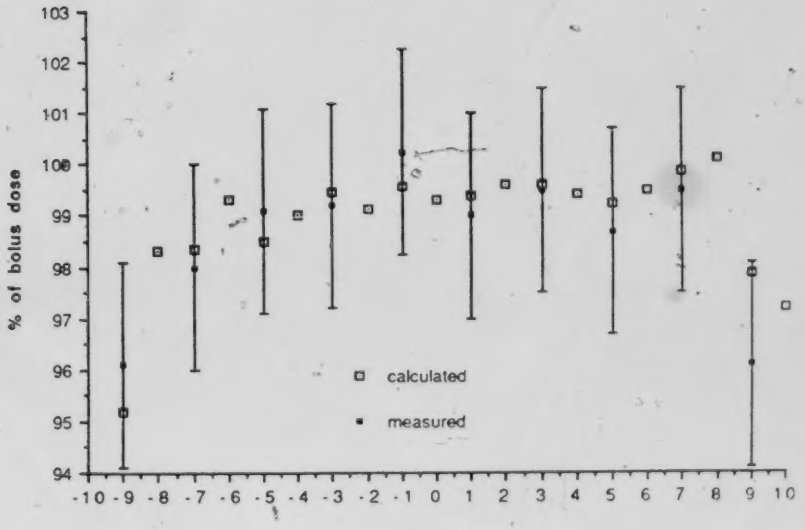

(b)

Figure 5.18 Percentage of bolus dose at layer #2 with the optimized compensator (comparison between measurement and calculation) (a) along the X-axis, (b) along the Y-axis.

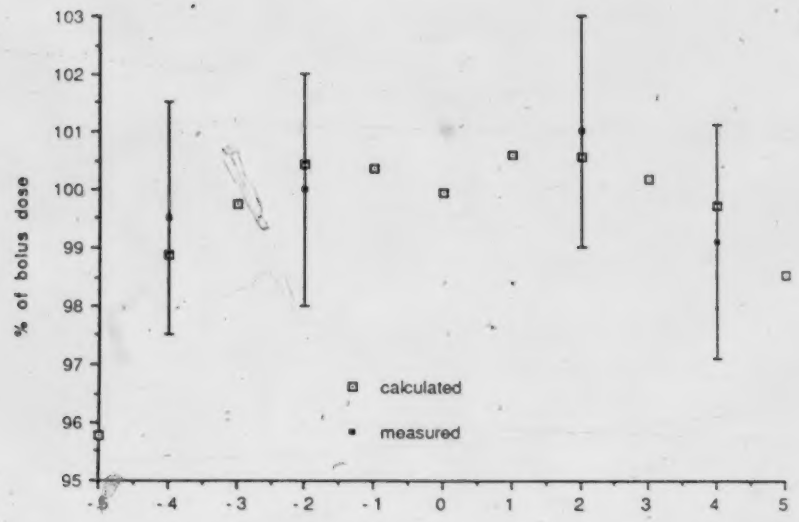

(a)

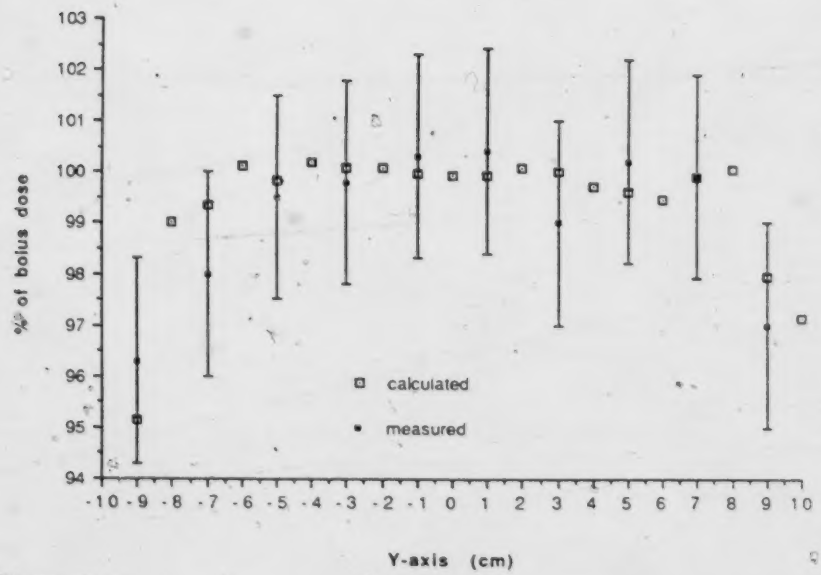

(b)

Figure 5.19 Percentage of bolus dose at layer #3 with the optimized compensator (comparison between measurement and calculation) (a) along the X-axis, (b) along the Y-axis.

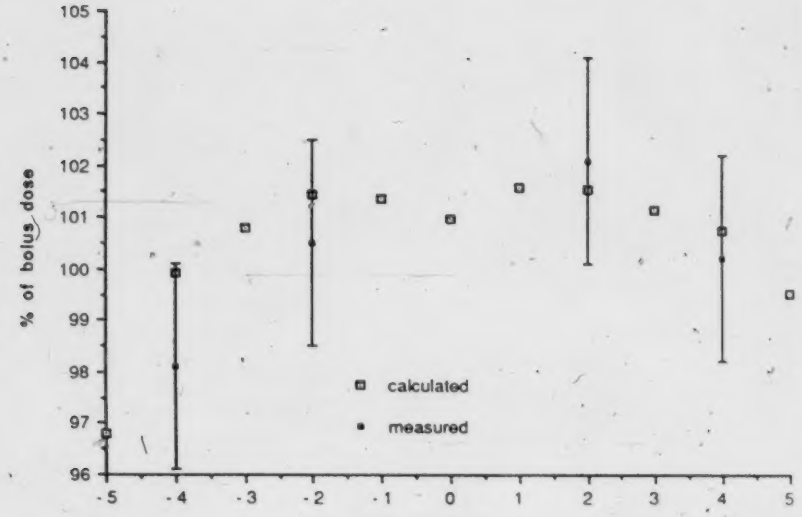

(a)

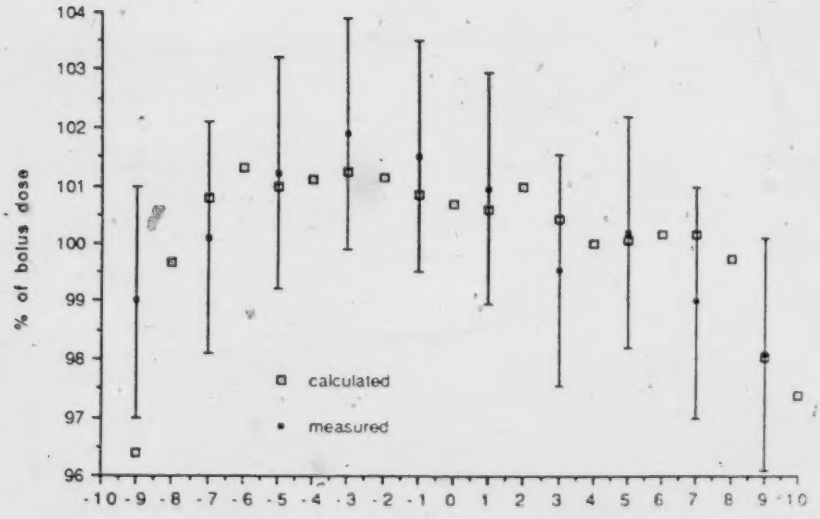

(b)

Figure 5.20 Percentage of bolus dose at layer #4 with the optimized compensator (comparison between measurement and calculation) (a) along the X-axis, (b) along the Y-axis.

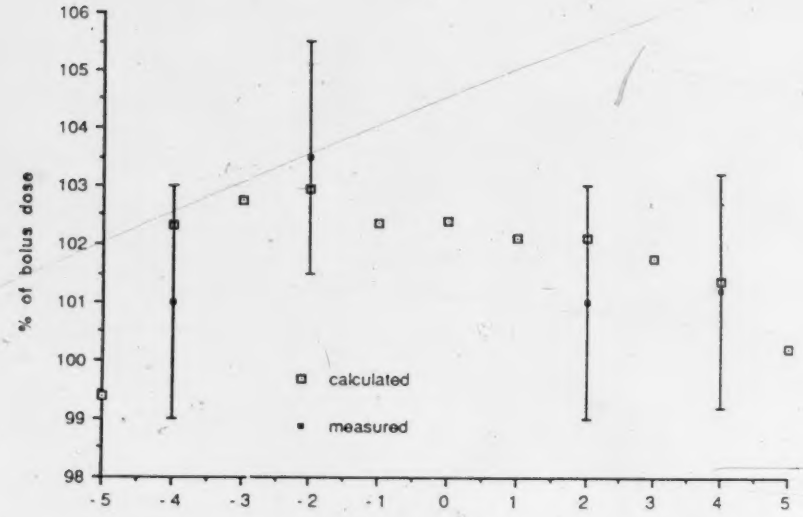

(a)

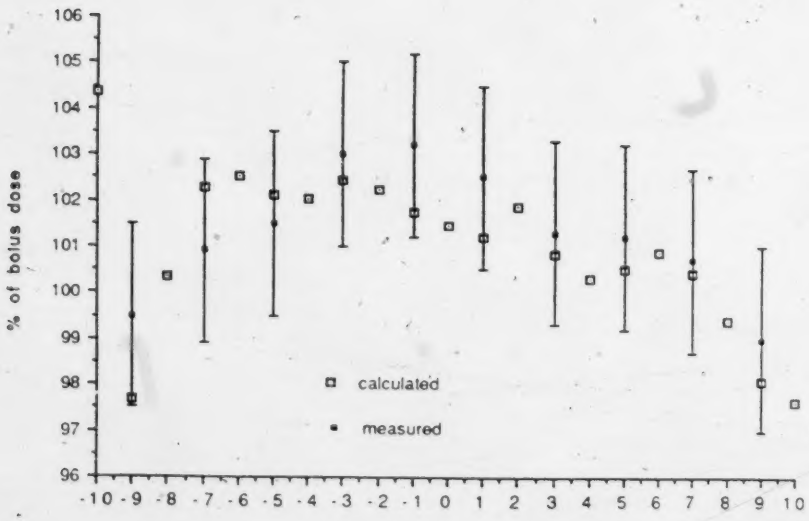

(b)

Figure 5.21 Percentage of bolus dose at layer #5 with the optimized compensator (comparison between measurement and calculation) (a) along the X-axis, (b) along the Y-axis.

Conclusions

The most incomprehensible thing about the world is that it is comprehensible.

Einstein

VI Conclusions

The experimental investigation of regular mathematically describable geometries has shown geometric compensators to be a good first approximation toward the restoration of bolus dose distribution. It has, however, also provided ample proof of the need for improvement in compensator design. The theoretical analysis presented in this thesis has provided a means by which compensators, which will accurately produce a desired dose distribution at a given depth both in regular and irregular geometries, may be designed. It is hoped that this work will contribute to the furtherance of quantitative analysis of beam modifying devices and improved clinical results when compensators are used.

REFERENCES

[1.1] Brahme, A., "Dosimetric Precision Requirements in Radiation Therapy", Acta Radiologica Oncology, 23, 379-391, (1984).

[1.2] "Code of practice for X-ray therapy linear accelerators", Medical Physics, 2, 110-121, (1975).

[1.3] Hubble, J.H., Photon Cross Sections, Attenuation Coefficeints, and Energy Absorption Coefficients from 10keV to 100GeV, NSRDA - NBS 29, U.S. Department of Commerce, 1969.

[1.4] Ibid.

[1.5] Johns, H.E., Cunningham, J.R., The Physics of Radiology, (Springfield: Charles C Thomas Publisher, 1983), p.147.

[1.6] Heitler, W., The Quantum Theory of Radiation, (New York: Oxford University Press, 1954).

[1.7] Nelms, A.T., Graphs of the Compton Energy-Angle Relationship and the Klein-Nishina Formula from 10keV to 500MeV, N.B.S. Circular, 542, U.S. Department of Commerce, 1953, p.38.

[1.8] Ibid, p.52.

[1.9] Ibid.

[1.10] Ibid.

[1.11] Hubble, loc. cit.

[1.12] Attix, F.H., Roesch, W.C., Radaition Dosimetry, Volume 1, (New York: Academic Press, 1968), p.97.

[1.13] Ibid, p.138.

[1.14] Ibid, p.142.

[1.15] Mott, N.F., Gonville, M.A., College, C., "The Polarization of Electrons by Double Scattering", Proceedings of the Royal Society of London, A135, 429-458, (1932).

[1.16] Bethe, H.A., "Moliere's Theory of Multiple Scattering", Physical Review, 89, 1256-1266, (1953).

[1.17] Berger, M.J., and Seltzer, S.M., "Evaluation of Collision Stopping Power of Elements and Compounds for Electrons and Positrons",

International Journal of Applied Radiation and Isotopes, 133, 1189-1218, (1982).

[1.18] Ibid.

[1.19] Brahme, loc. cit.

[1.20] Burkell, C. C., Watson, T.A., Johns, H.E., Horsley, R.J., "Skin Effects of Cobalt-60 Telecurie Therapy", British Journal of Radiology, 27, 171-176, (1954).

[1.21] Hendee, W.R., Medical Radiation Physics, (Chicago: Year Book Medical Publishers, 1973), p. 230.

[1.22] Ellis, F., Hall, E.J., Oliver, R., "A Compensator for Variations in Tissue Thickness for High Energy Beams", British Journal of Radiology, 32, 421-422, (1959).

[1.23] Hall, E.J., Oliver, R., "The use of Standard Isodose Distributions with High Energy Radiation Beams-The Accuracy of a Compensator Technique min Correcting for Body Counours", British Journal of Radiology, 34, 43-52, (1961).

[1.24] Feaster, G.R., Agarwal, S.K., Huddleston, A.L., Friesen, E.J., "A Missing Tissue Compensator", International Journal of Radiation Oncology Biology Physics, 5, 277-280, (1979).

[1.25] Laursen, J.F., Andersen, H.C., Hansen, H.P., "3D thin lead sheet compensating system", Medical Physics, 9, 741-745, (1982).

[1.26] Thomas, R.L., "Tissue compensation-difference compensators", British Journal of Radiology, 55, 859-861, (1982).

[1.27] Leung, P.M.K., Van Dyk, J., Robins, J., "A method of large irregular field compensation", British Journal of Radiology, 47, 805-810, (1974).

[1.28] Cohen, M., Burns, J.E., Sear, R., "Physical aspects of cobalt 60 teletherapy using wedge filters.2 Dosimetric considerations", Acta Radiologica, 53, 486-504, (1960).

[1.29] Ellis, F., Feldman, A., Oliver, R., "Compensation for tissue inhomogeneity in cobalt 60 therapy", British Journal of Radiology, 37, 795-798, (1964).

[1.30] Sundbom, L., "Individually Designed Filters in Cobalt 60 Teletherapy", Acta Radiologica, 2, 189-207, (1964).

[1.31] Huang, P.H., Chin, L.M., Bjarngard, B.E., "Scattered photons produced by beam-modifying filters", Medical Physics, 13, 57-63, (1986).

[1.32] Leung, loc. cit.

[1.33] Dixon, R.L., Ekstrand, K.E., Ferree, C., "Compensating Filter Design Using Megavoltage Radiography", International Journal of Radiation Oncology Biology, Physics, 5, 281-287, (1979).

[1.34] Jayaraman, S., Galinsky, D., Chung-Bin, A., Sollars, R., Williams, P., "Tissue Compensation and Uniformity of Dose in Mantle-Fields", American Association of Medical Dosimetrists Journal", 11, 11-14, (1986).

[1.35] Wilks, W.R., Casebow, M.P., "Tissue compensation with lead for Cobalt 60 therapy", British Journal of Radiology, 42, 452-456, (1962).

[1.36] van de Geijn, J., "The construction of individual intensity modifying filters in cobalt 60 teletherapy", British Journal of Radiology, 38, 865-870, (1965).

[1.37] Kahn, F.M., Moore, V.C., Burns, D.J., "An Apparatus for the Construction of Irregular Surface Compensators for Use in Radiotherapy", Radiology, 90, 593-594, (1968).

[1.38] Watkins, D.M.B., "A proposed method for making reduced wax compensators for use with high-energy radiation beams", British Journal of Radiology, 48, 760-762, (1975).

[1.39] Sorensen, N.E., " A simple Method for the Construction of Compensators for "missing Tissue"", Physics in Medicine and Biology, 13, 113-115, (1968).

[1.40] Renner, W.D., O'Conner, T.P., Amtey, S.R., Reddi, P.R., Bahr, G.K., Kereiakes, J.G., "The Use of Photogrammetry in Tissue Compensator Design", Radiology, 125, 505-510, (1977).

[1.41] Lerch, I.A., Barish, R.J., "Developement of optical process for accessing three-dimensional patient topology", Medical Physics, 5,546-549, (1978).

[1.42] Boyer, A.L., Goitein, M., "Simulator mounted Moire topography camera for constructing Compensating filters", Medical Physics, 17,19-25, (1980).

[1.43] Renner, W.D., "Photogrammetry applied to radiation therapy", Treatment Planning, 6, 10-17, (1981).

[1.44] Mok, E.C., Boyer, A.L., "Compensator filters made with compact Moire camera and computer", Medical Physics, 11,513-515, (1984).

[1.45] Ellis, F., Lescrenier, C., "Combined Compensation for Contours and Hetrogeneity", Radiology, 106, 191-194, (1973).

[1.46] Dixon, loc. cit.

[1.47] Renner, W.D., O'Conner, T.P., Bermudez, N.M., "An electronic device for digitizing radiotherapy films for the construction of tissue compensators", Medical Physics, 9, 910-916, (1982).

[1.48] Renner, W.D., O'Conner, T.P., Bermudez, N.M., "A note on designing tissue compensators for parallel opposed fields", Medical Physics, 10, 483-486, (1983).

[1.49] Lindskoug, B.A., Notter, G., "Design of flattening filters based on intercavitary absorbed dose measurements in external radiation therapy", British Journal of Radiology, 53, 976-980, (1980).

[1.50] Goitein, M., "Compensation for Inhomogeneities in Charged Particle Radiotherapy Using Computed Tomography", International Journal of Radiation Oncology, Biology, Physics, 4, 499-508, (1978).

[1.51] Flynn, M.J., "Dosimetric evaluation of automatic tissue compensator design", Medical Physics, 8, 558, (1981).

[1.52] Jackson, W., "Wax retraction as a technique for compensating the effect of surface irregularities in high-energy radiotherapy", British Journal of Radiology, 43, 859-867, (1970).

[1.53] Thomas, loc. cit.

[1.54] Van Dyk, J., "Broad beam attenuation of cobalt 60 gamma rays and 6-, 18-, and 25-MV x rays by lead", Medical Physics, 13, 105-110, (1986).

[1.55] Kubo H., "Dosimetry of Anterior chest treatment by 10MV X-rays using a tissue compensating filter", Radiotherapy and Oncology, 4, 185-192, (1985).

[1.56] Faddegon, B.A., Pfalzner, P., "Computer aided design and verification of megavoltage tissue compensators for oblique beams", Medical Physics, 15, 757-762, (1988).

[1.57] El-Khatib, E.E., Podgorsak, E.B., Pla, C., "Broad beam and narrow beam attenuation in Lipowitz's metal", Medical Physics, 14, 135-139, (1987).

[1.58] Huang, loc. cit.

[1.59] Robinson, D.M., Scrimger, J.W., "Megavoltage photon beam dose reduction with retracted tissue compensators", Physics in Medicine and Biology, 32 ,1031-1037 (1987).

[2.1] White, D.R., "The Photon Attenuation and Absorbtion Properties of Clear and White Polystyrene", British Journal of Radiology, 51, 379-380, (1978).

[2.2] Rikner, G., Silicon Diodes as Detectors in Relative Dosimetry of Photon, Electron and Proton Radiation Fields, (Uppsala: Acta Universitatis Upsaliensis, 1983), p. 1.21.

[2.3] Ibid, p. 4.7.

[3.1] Wong, J.W., Henkelman, R.M., Fenster, A., Johns, H.E., "second scatter contribution to dose in a cobalt-60 beam", Medical Physics, 8, (1981)

[3.2] Scrimger, J.W., Cormack, D.V., "Spectrum of the radiation from a cobalt 60 teletherapy unit", British Journal of Radiology, 36, 514-521, (1963).

[3.3] Johns, H.E., Cunningham, J.R., The Physics of Radiology, (Springfield: Charles C Thomas Publisher, 1983), p.184.

[3.4} Mackie, T.R., *****:Ph.D. thesis, University of Alberta, (1984).